FINAL REPORT

Exploiting EMI Signals During Active Transmission

SERDP Project MR-1659

AUGUST 2010

Gregory Schultz
Sky Research Inc.

SERDP
DOD ▪ EPA ▪ DOE

REPORT DOCUMENTATION PAGE

Form Approved
OMB No. 0704-0188

PLEASE DO NOT RETURN YOUR FORM TO THE ABOVE ORGANIZATION.

1. REPORT DATE *(DD-MM-YYYY)*	2. REPORT TYPE	3. DATES COVERED *(From - To)*
12-08-2010	Final Technical Report, V 2.0	02/12/2008-30/06/2010

4. TITLE AND SUBTITLE

Exploiting EMI Signals During Active Transmission
Final Technical Report

5a. CONTRACT NUMBER

W912HQ-09-C-0003

5b. GRANT NUMBER

5c. PROGRAM ELEMENT NUMBER

6. AUTHOR(S)

Dr. Gregory Schultz, Sky Research, Inc.
Jonathan Miller, Sky Research, Inc.
Dr. Leonard Pasion, Sky Research, Inc.

5d. PROJECT NUMBER

SERDP 1659

5e. TASK NUMBER

5f. WORK UNIT NUMBER

7. PERFORMING ORGANIZATION NAME(S) AND ADDRESS(ES)

Sky Research, Inc.
445 Dead Indian Memorial Road
Ashland, OR 9520

8. PERFORMING ORGANIZATION REPORT NUMBER

9. SPONSORING/MONITORING AGENCY NAME(S) AND ADDRESS(ES)

SERDP Program Office
Attn: Dr. Herb Nelson
901 North Stuart St.
Suite 303
Arlington, VA 22203

10. SPONSOR/MONITOR'S ACRONYM(S)

11. SPONSOR/MONITOR'S REPORT NUMBER(S)

12. DISTRIBUTION/AVAILABILITY STATEMENT

unlimited

13. SUPPLEMENTARY NOTES

14. ABSTRACT

Theoretically, signals measured during the transmit period (the "on-time") provide information about the instantaneous magnetization and current gathering in objects illuminated by a transmitter. In this SEED project, we examined the potential of on-time EMI data for improving the detection and discrimination of UXO and in rejecting clutter and noise. Through a combination of modeling and analysis of experimental data, we found that on-time data provide a number of theoretical and practical enhancements to aid in UXO characterization. This work also supported a more thorough understanding of the physical mechanisms being exploited by existing on-time instruments and their capabilities and limitations. We provide a theoretical basis that links our understanding of existing off-time pulsed induction and always-on frequency domain responses to the full waveform response. This approach provides for estimation of the magnetic properties of targets (e.g., demagnetization factors and bulk magnetic susceptibility) that are not obtainable with conventional off-time pulsed induction methods.

15. SUBJECT TERMS

electromagnetic induction sensors, on-time EMI transmitter signals, UXO

16. SECURITY CLASSIFICATION OF:			17. LIMITATION OF ABSTRACT	18. NUMBER OF PAGES	19a. NAME OF RESPONSIBLE PERSON
a. REPORT	b. ABSTRACT	c. THIS PAGE			Dr. Herb Nelson
unclassified	unclassified	unclassified	unclassified	144	19b. TELEPHONE NUMBER *(Include area code)* 703-696-8726

Reset

Standard Form 298 (Rev. 8/98)
Prescribed by ANSI Std. Z39.18

EXECUTIVE SUMMARY

This project was undertaken by Sky Research Inc. and the University of British Columbia Geophysical Inversion Facility to examine the potential of exploiting electromagnetic induction (EMI) signals during active transmission - the so-called on-time.

Summary

Recent advances in EMI sensor capabilities have incorporated sensing mechanisms to more fully exploit the spatial response of UXO targets. These next generation systems utilize multi-axis and multi-static transmitter and receiver configurations to increase the spatial sampling of the scattered magnetic field response from targets for improved characterization. Previous research also has shown that enhanced capability may be gained from extending the temporal or spectral information. For example, characterization of a target's shape, size, and orientation can be improved by considering very early or late time decay information. Additionally, in-phase responses from frequency-domain metal detectors include magnetization effects that are not present in conventional time-domain systems. Similar information is also available in the time-domain by sampling the receiver waveform during the full period of both current "on" and "off" times. Since the introduction of high-rate digital sampling technology in EMI data acquisition, the whole waveform of measured EMI responses has been made available. The airborne electromagnetics community, in particular, has utilized full waveform EMI data to improve models of ground conductivity and magnetic susceptibility. Theoretically, received signals measured during the transmit period provide information about the instantaneous magnetization and current gathering in objects within the presence of the illuminating field. Although some work has been conducted to examine designs that provide for on-time signal reception, very few, if any, efforts have been concentrated on optimal methodologies for processing associated signals.

In this SEED project, we examined the potential of on-time EMI data for improving the detection and discrimination of UXO and to aid in rejecting anthropogenic and soil-related clutter and noise. Through modeling and simulation combined with experimental data collection and analyses, we found that on-time data provide a number of theoretical and practical enhancements to aid in UXO characterization. This work also supported a more thorough understanding of the physical mechanisms being exploited by existing on-time instruments and their capabilities and limitations.

Findings and Recommendations

In this project we have concentrated on providing a thorough and applied understanding of the utility of on-time responses. Our results suggest that processing of full waveform data (during both the transmitter "on" and "off" times) yield a number of benefits and should be pursued further. We provide a theoretical basis that links our understanding of existing off-time pulsed induction and always-on frequency domain responses to the full waveform response. This approach provides for estimation of the magnetic properties of targets (e.g., demagnetization factors and bulk magnetic susceptibility) that are not obtainable with conventional off-time pulsed induction methods. As has been shown previously, a comparison of on- and off-time signals lead to opposing polarity for purely ferrous and purely conductive objects - a simple, yet practical indicator of bulk material magnetization. In addition, we have shown that on-time

signals may also yield important added information through their spatial response. For example, off-time responses over simulated spheres reveal an improved ability to resolve small, shallow targets relative to on-time. Conversely, on-time data are able to resolve deep, large targets, suggesting they are less influenced by surface ground clutter and provide added information for separating shallow and deep targets in a single region of interest.

Based on our preliminary findings, we recommend conducting a more thorough analysis of on-time signals and developing a test instrument to fully assess the utility of on-time data in target detection and discrimination. More work must be conducted on the analysis of both laboratory and field data to elucidate and validate the veracity and uniqueness of features extracted from on-time data. Physics-based features extracted from full waveform temporal signatures as well as their spatial evolution over targets will likely lead to better discrimination based on target size and aspect ratio as well as material composition and demagnetization effect.

Although a handful of on-time instruments exist, no current system fully leverages the potential advantages of full waveform EMI data. To do this, we suggest that advanced full waveform sensors be investigated, and, if warranted, developed into testable prototypes. In an idealized system, the current waveform would have the properties that maximize the magnetization effect on a target. Comparisons of basic waveforms lead to the suggestion of a linear ramp current excitation and rapid cessation as an ideal source for a full waveform system. This excitation characterizes the combined effect of a bipolar electromotive force (i.e., the electromotive force rapidly changes polarity as the ramp-on period transitions to the shut-off period) and a linear magnetic field applied to the target. The contrasting effects of the electromotive force and the magnetizing field produce a unique response that is a function of target features such as geometry, conductivity, and magnetic susceptibility.

The results of this project also suggest that an idealized system would likely utilize a current waveform with multiple ramp durations. The implementation of different ramp durations may allow for at least two different excitation periods. This approach provides certain advantages by: 1) enabling baseline excitation for comparing magnetization responses, 2) creating discrete energy states from which the secondary response decays, and 3) yielding needed information for cancelling the viscous magnetization effects of mineralized soils.

Perhaps the most critical design consideration for full waveform data acquisition is the ability to precisely null or cancel the primary magnetic field from the transmitter. Previous and on-going work on nulling designs for frequency-domain EM systems as well as digital cancellation methods applied to airborne EM survey data have strong leveraging potential. Geometric nulling using precise receiver positioning or gradient configurations have been used to cancel the primary field in frequency-domain EM instruments. Others have used digital cancellation methods by removing the component of the response that is aligned in phase with the transmitter. It is also common to use various modes of absolute field calibration for removing primary field effects. All of these methods have limitations, and we advocate an intelligent combination of methods that minimizes the impacts on sensitivity and dynamic range. Overlapping coil arrangements along with absolute calibration and balancing combined with digital cancellation and fine tuning with a Q-coil are likely the optimal choice for removing the primary field. We

found that gradient configurations are less optimal due to their inherent fall-off in sensitivity with range.

TABLE OF CONTENTS

LIST of TABLES

LIST of FIGURES

ACRONYMS

AEM	Airborne Electromagnetic
Amp	Amperes
AWGN	Additive White Gaussian noise
BUD	Berkeley UXO Discriminator
cm	Centimeter
DC	Direct Current
DGPS	Differential Global Positioning System
EM	Electromagnetic
EMI	Electromagnetic Induction
EMF	Electromotive Force
ESTCP	Environmental Security Technology Certification Program
FPGA	Field Programmable Gate Array
GMR	Giant Magnetoresistive
Hz	Hertz
LR	Inductive Resistive
LRC	Inductance (L), Resistance (R), and Capacitance (C)
μs	Microsecond
m	Meter
MHz	Megahertz
mm	Millimeter
MPV	Man Portable Vector
ms	Milliseconds
mS/m	MilliSiemens/meter
nT	nanoTesla
NVE	Non-volatile Electronics
PRF	Pulse Repetition Frequency
PRN	Pseudo-random Noise
RC	Resistive Capacitive
S/m	Siemens/meter
SAM	Sub Audio Magnetics
SERDP	Strategic Environmental Research and Development Program
STMR	Single Transmit Multiple Receive
SVD	Singular Value Decomposition
USGS	United States Geological Survey
UXO	Unexploded Ordnance
VLF	Very Low Frequency

ACKNOWLEDGEMENTS

This technical report for project MM-1659, *"Exploiting EMI Signals During Active Transmission"*, documents the results of theoretical studies and laboratory measurements undertaken to test the utility of electromagnetic induction data acquired during the transmitter "on-time".

The work was performed by Sky Research, Inc and the University of British Columbia Geophysical Inversion Facility (UBC-GIF). Dr. Gregory Schultz from Sky Research was the principal investigator. Jonathan Miller of Sky Research conducted laboratory experiments and supported numerical modeling and analysis, Dr. Lin-Ping Song from UBC-GIF supported the analysis and inversion of ALLTEM data. Dr. Leonard Pasion supported development of analytical on-time models.

Dr. Ben Barrowes of the US Army Corps of Engineers, Engineer Research and Development Center, loaned the Man Portable Vector sensor that was used extensively in the laboratory experiments.

Funding for this project was provided by the Strategic Environmental Research and Development Program Office. We wish to express our sincere appreciation to Dr. Jeffrey Marqusee, Dr. Anne Andrews, Dr. Herb Nelson, and staff of the SERDP Office for providing support and funding for this project.

This report was prepared under contract to the Department of Defense Strategic Environmental Research and Development Program. The publication of this report does not indicate endorsement by the Department of Defense, nor should the contents be construed as reflecting the official policy or position of the Department of Defense. Reference herein to any specific commercial product, process, or service by trade name, trademark, manufacturer, or otherwise, does not necessarily constitute or imply its endorsement, recommendation, or favoring by the Department of Defense.

1. INTRODUCTION

This SEED project addressed the unexploded ordnance (UXO) Statement of Need MM-SEED09-01 "Advanced Technologies for Detection, Discrimination, and Remediation of Military Munitions". The objective was to provide the information required to understand, process, and evaluate the potential of on-time signals and to quantify the value that associated data parameters add to current advanced technology. While the quest for optimal electromagnetic induction (EMI) discrimination capabilities can take many different directions, the scope of our project was limited to the physics and application of existing time-domain induction technology while a transmitter is on.

The objective of this project was to develop a thorough understanding of the potential of EMI signals during active transmission. As such, we set out to answer the following questions:

1. What physical mechanisms are being exploited by current systems that receive during transmission? How does the instantaneous magnetization response vary with transmitter waveform, transmitter coil parameters, and various target & host media scenarios? What are the limits or constraints of these responses?
2. Which sensor designs are best suited for optimal exploitation of on-time signals? What receiver coil designs, transmitter ramp functions, and data acquisition methods maximize the use of on-time signals?
3. What would be required to sample on-time signals using EMI sensor configurations currently in-use?
4. What new processing methods are needed to fully take advantage of on-time signals? To what level is the information unique and useful in discrimination/classification or inversion algorithms?

Specific technical objectives were to:

1. Develop models that represent the responses from different current ramps and on-time waveforms for objects and ground. We considered target and clutter objects and grounds having a range of material properties, shapes and sizes, and configurations along with existing data to compare with and validate our model results. Such comparisons are useful for indicating the gaps that may exist in our fundamental understanding of on-time responses. The results provide a baseline from which we can extend the current theory to better predict responses.
2. Develop a testbed for controlled experiments based on the results of our modeling and simulation effort. These experiments were used to assess the practical limitations of the available on-time measurement configurations. We also investigated potential modifications to currently used conventional and advanced EMI systems. The results of this investigation yielded constraints on the extent of development necessary to incorporate these measurements into existing data acquisition methods.
3. Examine the existing processing methods currently used for sampling, post-processing, filtering, and inversion and/or discrimination of on-time data. Signal processing techniques were used to transform the data into some suitable form based on a physical understanding of the underlying signal phenomenology. The results from this task

provide a better understanding of the constraints of current off-time processing methods for dealing with the on-time signals and will produce new methods for exploiting on-time signal features.

4. Prepare this report detailing a synthesis of the modeling and simulation and experimental work conducted and recommend future research, including the hardware, software and logistical requirements to develop an optimized full waveform (on- and off-time) sensor based-system that can meet the required performance specifications.

Each of these objectives was met. Some constraints were placed on the level of completeness possible in examining inversion and deconvolution methodologies due to limited availability of relevant on-time field data.

1.1. Motivation for the Project

The critical need to implement new EMI technologies capable of improved detection and discrimination of UXO in order to reduce the cost of site characterization and cleanup is well documented. Current EMI sensors used in UXO detection consist of time- or frequency-domain instrumentation. Recent advances in EMI sensor capabilities such as multi-axis array technology, advanced time and frequency domain acquisition and filtering methods (multi-gate, multi-frequency), and tight coupling with high-accuracy navigation and positioning information have all increased the potential for discrimination. These recent advances have added features that expose researchers and practitioners alike to a greater range of information that is ripe for discrimination.

Following on research that quantified the limitations of traditional single-component (single-axis) two-coil sensors (e.g., Strategic Environmental Research and Development Program [SERDP] projects MM-1310, UX-1355, UX-1356, and CU-1121), the SERDP developed a number of new multi-component, multi-receiver EMI sensors. These systems have shown promising improvements in both target localization and discrimination. In concert with advanced analysis methods, these systems have been capable of detecting nearly all UXO items at live test sites that contain relatively simple geology and low levels of clutter (Billings, 2008). These recent successes have been attributed primarily to more complete spatial interrogation of scattered EMI responses from targets, and lead directly to more complete characterization of object principal axis polarizabilities. This approach attempts to maximize the information content available from spatial sampling of the scattered magnetic field.

To expand the “parameter space” from which we can extract unique information about targets, clutter, or background geology, researchers have been pushing not only the spatial, but also temporal sensing capabilities of EMI detectors. In doing so, we have learned that there is useful information in parts of the spectral band that we have yet to fully exploit. For example, it appears that useful information exists in the magnetic field ratios above the very low frequency (VLF) band usually sampled by frequency-domain systems (Shubitidze et al, 2004). Similarly, in the time domain, there has been a growing interest in exploiting relatively early and or late-time responses (Pasion, 2007). In fact, a number of innovative time-domain electromagnetic (EM) sensors now have the capability to sample receivers during the transmitter on-time. None of these sensors have been developed specifically for on-time measurements; however, many have claimed advantages from the signal received during transmission of the primary magnetic field.

Theoretically, received signals measured during the transmit period provide information about the instantaneous magnetization and current gathering in objects within the presence of the illuminating field. Although some work has been conducted to examine designs that provide for on-time signal reception, very few, if any, efforts have been concentrated on optimal methodologies for processing associated signals. As part of this research effort, we conducted several experiments to assess the veracity of on-time EMI signals in aiding the detection and discrimination of UXO.

1.2. Report Organization

Through a series of linked studies, this report characterizes the potential of full waveform EMI sensing, with particular emphasis on the relevant theoretical and practical implications to UXO detection and discrimination. This report is organized into 9 chapters that include:

- Introduction and perspective on the motivation for utilizing on-time signals;
- Background on physics and phenomenology of on-time EMI, theoretical and numerical modeling of target responses under various scenarios; and
- Investigations into data collection and design alternatives and associated data processing methodologies.

Chapter 2 provides information on existing on-time capable systems and parallel work in airborne electromagnetics. Chapters 3 and 4 describe the theoretical basis and numerical modeling, and analysis of simulated on-time responses to various target parameters. Chapter 5 focuses on deconvolution and inversion approaches for decomposing the on-time signal and extracting useful features. Chapter 6 details design considerations including waveforms, sensor types and configurations. Chapters 7 and 8 outline the major conclusions and recommendations for follow-on research.

2. BACKGROUND: ON-TIME ELECTROMAGNETIC PHENOMENOLOGY

Since the introduction of high-rate digital sampling technology in EMI data acquisition, the whole waveform of measured EMI responses has been made available. The airborne electromagnetics community, in particular, has utilized full waveform EMI data to improve models of ground conductivity and magnetic susceptibility. In the mid-to-late 1990's, airborne EM survey systems such as the QUESTEM, GEOTEM, AeroTEM, and VTEM (Figure 1) began integrating measurements of their receivers during the transmitter on-time (Smith and Annan, 1997; Witherly, 2009). This has become particularly more common when the target of airborne EM (AEM) investigations are high conductance ore bodies and/or massive sulfide bodies such as nickel sulfide deposits (Sattel, 1998). Because these economic sized bodies do not decay in the normal time windows of conventional off-time periods, full waveform data acquisition has been suggested. This leverages the on-time portion of the signal to detect so-called non-decaying responses (Macnae and Mutton, 1997). Here, the on-time information can be used to deconvolve for the effect of the shape of the transmitter pulse and produce a band-limited step or impulse response to highly conductive terrain.

In AEM surveys where the detection of poor conductors with decay rates so fast that the response is over before the first off-time measurement can be made, Annan et al. (1996) suggested that on-time responses can be used to determine conductivity structure. In this type of terrain, the on-time response is orders of magnitude larger than the off-time response, so the response of weakly conductive (ground conductivities as low as 25 milliSiemens/meter [mS/m] were reported by Smith and Annan [1997]) can be mapped. These field examples show that on-time data have exhibited utility in AEM detection of both ”off-scale" resistivity and "off-scale" conductivity features (i.e., "off-scale" relative to normal off-time measurement windows).

Figure 1. (Left) GEOTEM (Fugro Airborne Surveys) fixed wing airborne EM system. (Center) AeroTEM (AeroQuest Surveys) helicopter-based airborne time-domain EM system, (Right) VTEM (GeoTech Ltd.) helicopter-borne AEM system. All three of these systems acquire data during the on-time for large geo-electromagnetic mapping.

2.1. Basic Physics of On- and Off-time EMI

All EMI systems rely on a time-varying electromagnetic field to induce the flow of electrical currents in targets or the ground. These time-varying fields are achieved by either production of short pulses or by smoothly varying sine waveforms. Time-domain systems utilize a time-

varying waveform that is repeated with a characteristic pulse repetition frequency (PRF). In frequency-domain detectors, an integrated circuit measures the induced voltage generated by sine waves transmitted at one or more independent frequencies. The secondary response from conductors in the ground also produces a sinusoidal waveform of the same frequency; however, the amplitude and phase of the secondary waveform are modulated in accordance with the electromagnetic properties of the ground conductors (Figure 2). In these instruments, measurements are made from received sinusoids that are in-phase and quadrature-phase with respect to the transmitted signal (shifted in phase by $\pi/2$).

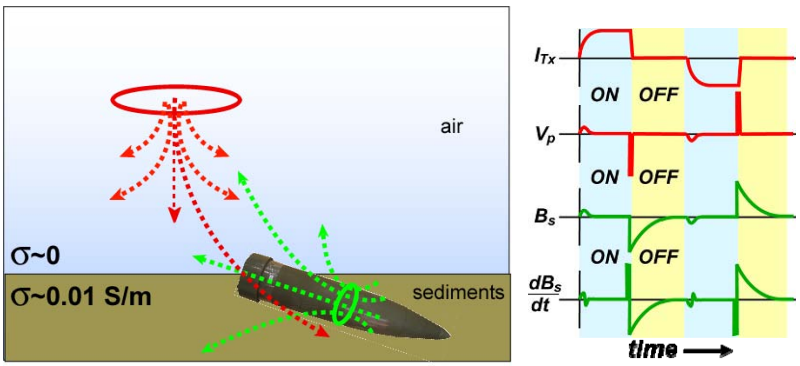

Figure 2. Schematic of the time-domain electromagnetic response from a buried UXO object. The temporal signal response in a receiver attempts to separate the primary magnetic field (red) from the transmitter from the secondary field (green) scattered from conductive targets. The off-time signal is generally what is measured by modern conventional pulsed-induction electromagnetic instruments. This is measured while the transmitter has been turned off. Useful and unique information may also be obtained while the transmitter is on.

Time-domain EMI measurements are made at certain times after each pulse – this is the so-called "off-time". A primary magnetic field is ramped up and then rapidly decreased. In many designs, the receive circuit is switched off completely or actively damped, to avoid being swamped by the primary field. The resultant time-varying magnetic field generates an electromotive force (EMF) that induces eddy currents in nearby conductive objects. The primary field is damped such that its effect decays within the first few microseconds following the primary voltage shutoff, but the secondary magnetic fields induced in conductive objects or ground may last for tens or even hundreds of microseconds. Additionally, this primary field magnetizes ferromagnetic objects that are in close proximity to the transmitter. During the off-period of the transmit pulse cycle, the eddy currents decay to produce a time-varying secondary magnetic field. In most conventional pulsed-induction EMI sensors, the detection circuit reads the coil voltage after the direct effect of the primary field has ceased. Receiver coils measure the voltages induced by the secondary fields over select time windows following the termination of each exciting pulse. Amplified receiver signals are integrated over the windows, low-pass filtered, and digitized. For a given coil configuration and sensor electronics, the strength and temporal form (decay time constant) of the response produced by an object depends on its electrical properties as well as its size, shape, position, and orientation with respect to the coils. Pulsed induction detectors avoid the instantaneous response of the ground (characterized by the real part of the magnetic susceptibility) but still suffer from the delayed or remnant response (characterized by the imaginary part of the magnetic susceptibility).

During transmission – the so called "on-time", current flows through the transmitter coil to produce an increasingly intense field (depending on the transmitter current ramp function). This primary magnetic field then interacts with conductive and magnetic bodies such as volumes of the ground and metallic clutter or UXO (Figure 3). As the transmitted field increases in intensity it induces an EMF in conductive material. This EMF drives currents that produce secondary magnetic fields in the object. The secondary magnetic fields tend to oppose the direction and magnitude of the primary inducing field. The transmit field is then extinguished very rapidly, thus reversing the direction of the secondary fields in the surrounding conductive objects. These secondary fields are produced by eddy currents that gradually diffuse and decay with time (Grant and West, 1965). When the same process occurs in the presence of ferromagnetic material, magnetic moments become aligned with the external primary field. This instantaneous magnetization occurs through the movement of magnetic domain walls and has been well studied in the geophysics community (e.g., Pasion et al., 2003). As the field decreases when the transmitter current is critically damped, the magnetic moments remain aligned with the primary field and decrease proportionally to the primary field excitation. Although this instantaneous magnetic response will reduce to essentially zero as the primary field goes quiet, remnant magnetization in ferromagnetic materials may persist.

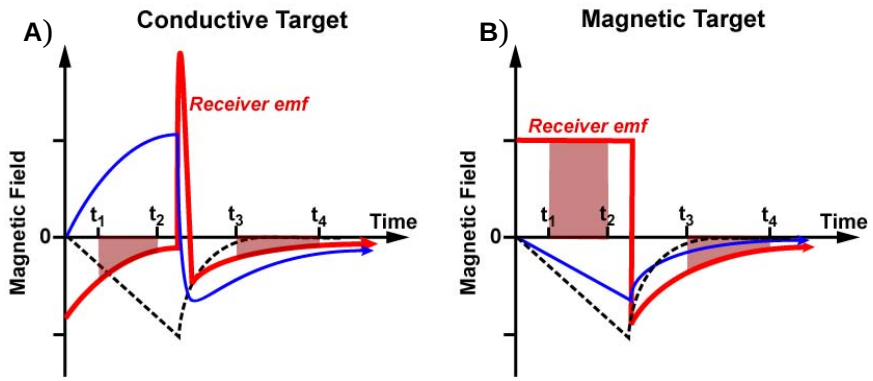

Figure 3. Schematic of the time-domain on- and off-time responses of a transmitted magnetic field over (A) conductive (non-ferrous) and (B) magnetic (ferrous) targets. The intensity of the transmitted field (black dashed curve) is proportional to the current in the transmitter coil. For a magnetic target, as the transmitter field increases, so does the field from the magnetic target (blue curve). For a conductive target, as the transmitter field increases, eddy currents develop and, according to Lenz's law, these currents are such that their concomitant magnetic field will oppose any change in the applied field. At the end of the application of the transmitter voltage the magnetic target emanates a field in the same direction as the transmitter field. For the conductive target, rapid decay of the transmitted magnetic field produces currents that are in the opposite sense to those produced during the transmitter stage.

There are two primary physical phenomena at work during the on-time. As the transmitted field increases in intensity it induces an EMF in conductive and permeable objects leading to secondary scattered magnetic fields. During this ramp up period, eddy currents develop and, according to Lenz's law, these currents are such that their concomitant magnetic field will oppose any change in the applied field. For permeable targets, magnetostatic excitation generates an induced magnetic field in the same direction as the primary field during current ramp-up in the transmitter (Figure 4). At the end of the application of the transmitter voltage, the magnetic target emanates a field in the same direction as the transmitter field. For conductive targets, rapid

decay of the transmitted magnetic field produces currents opposing the primary field. The phenomena compete against each other during the on-time to dominate the transient response.

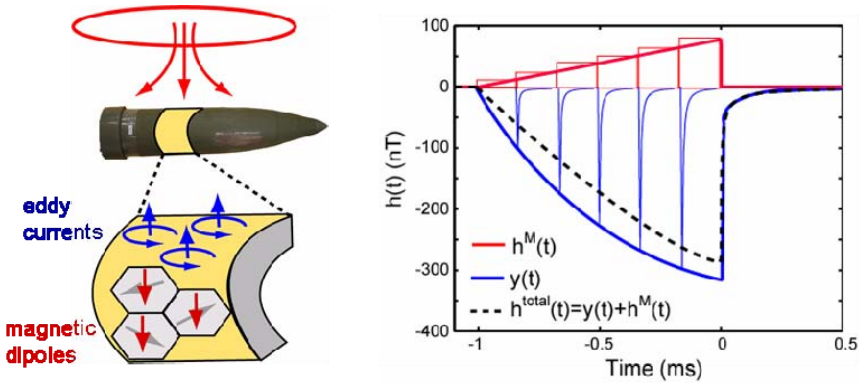

Figure 4. LEFT-Schematic representation of the tradeoff between transient inductive (eddy-current) decay *y(t)* and magnetostatic excitation $h^M(t)$. For conductive targets, the inductive decay signal opposes any changes in the primary field. For purely permeable (non-conducting) targets, the alignment of magnetic dipoles tends to orient the magnetic field in the same direction as the applied primary field. For conductive and permeable targets, these two phenomena compete to form the net scattered field response during the on-time. RIGHT - Example on-time magnetic field signal response for a postive linear ramp current excitation. The total response (dashed line) can be approximated by the superposition of step or impulse function responses. These are shown schematically for both the inductive (blue) and magnetostatic (red) components. The inductive component is represented by an integration of differential impulse responses opposing the primary field (approximated by exponential decay functions) and the magnetostatic component as an integration of DC excitations aligned with the primary field. The staircase fucntion approximation represents a series of finite steps, and, assuming the discrete time intervals are very small, the summation will pass into an integral as detailed further in Section 3.1.

2.2. Waveforms In-Use and Their Effectiveness

The primary excitation in a time-domain EM system is determined by the current pulse waveform and the characteristics of the transmitting system (including the charging circuit utilized and induction antenna, i.e., coil, used). Current waveforms can have any shape: step, ramp, saw-tooth, square, trapezoidal, Gaussian, half-sinusoidal or pseudo-random noise (PRN). There are certain advantages to different pulse shapes, but, in general, time-domain electromagnetic systems employ some form of a strictly periodic waveform with equally spaced pulses having alternating polarity but identical shape. This is because such a waveform has only odd harmonic components and all the information that is contained in the transient responses lies only at these odd harmonic frequencies (Guptasarma et al., 1976). Coherent sampling of the received waveform (e.g., once every half-cycle) allows for rejection of noise contributions at all frequencies other than the signal frequencies.

At one extreme of current waveforms is the always-on sinusoidal (as used in frequency-domain systems – a special class of on-time instrumentation), sawtooth, square-wave, and pulse modulated waveforms. A more common set of waveforms, found especially in AEM systems, contains both on-time and off-time periods. Examples of current on-time systems and their waveforms are summarized in Table 1.

Table 1. On-time capable systems.

System	Waveform	Type	On Time
ALLTEM (USGS)	Triangular Sawtooth	Ground	11 ms
SAM (GAP Geophysics)	Square wave	Ground	125 ms
STMR (Minelab)	Linear ramps	Ground	24 μs and 125 μs
GEOTEM	Half-sine	AEM	2 or 4 ms
QUESTEM	Half-sine	AEM	2 ms
AeroTEM	Triangular ramp-on/off	HEM	11 ms
VTEM	Polygonal	HEM	4.5-7 ms

ms=milliseconds
μs=microseconds

The most common waveform utilized for conventional pulsed induction EM systems is the exponential ramp-on. This form is extremely convenient from an engineering perspective because it represents the form of a natural charging circuit. For example, the exponential nature of the change (of charge or voltage) in a resistive capacitive (RC) circuit with time results from applying Kirchoff's voltage rule and the definition of current as the rate of change of charge with time. Once the circuit has sufficiently approached the maximum current (or voltage), the circuit is abruptly turned off to produce an effective step-off response.

Among the most pervasive pulse shapes utilized for AEM is a half-sinusoid. This waveform is used in the QUESTEM and GEOTEM systems with base operating frequencies between 300 Hertz (Hz) and 25 Hz. However, any other waveform with a rise or fall of the current pulse is relatively abrupt can serve as an approximate step pulse. Triangular ramp-on/ramp-off functions are also used in systems such as the UTEM (Lamontange Geophysics) and the SPECTREM AEM systems. Geotech Ltd. uses a complicated waveform which has been optimized to use as much of the helicopter's spare electrical power as possible. The effect of different transmitter waveforms on target responses is discussed further in Section 3.2.

2.3. Existing On-time Capable Systems

2.3.1. ALLTEM

In SERDP project MM-1328, a number of field tests have been conducted to evaluate the United States Geological Survey (USGS) ALLTEM EMI system for UXO detection (Figure 5). This system uses induction receiver coils in differential gradiometer pairs or orthogonal transmit and receive coils to effectively null the primary field during transmission. Early observations of data recorded during the ramp-up of the transmitter loop current responded very strongly to shallow subsurface objects (Wright et al., 2000).

Figure 5. (Left) The USGS ALLTEM array operating at the Yuma Proving Ground calibration area. (Right) The ALLTEM sensor array showing the horizontal dipole (vertical coils) receivers. Three orthogonal transmitters are used along with 19 differential receiver combinations.

2.3.2. STMR

The Minelab Single Transmit Multiple Receive (STMR) array system (Figure 6) (Schultz et al., 2007; Stametescu and Schultz, 2007) includes both figure-8 shaped (quadrapole) and monoloop (dipole) receive coils encircled by a large transmitter. The opposing lobes of the "8"-shaped coil act to null the net primary field from the transmitter and, thus permit reception both during and after each pulse transmission. Comparison of the on-time and off-time signals has led to on-the-fly ferrous/non-ferrrous discrimination for landmine detection using this system.

Figure 6. (Left) The Minelab Ltd. Single-Transmit Multiple-Receive (STMR) EMI array containing both quadrapole (figure-8 shaped) and dipole (monoloop) coil receivers. They array houses the ten monoloop receivers across the width layered directly on top of the ten quadrapole receivers. (Right) The STMR array mounted on a HUMVEE by the U.S. Army Night Vision and Electronic Sensors Directorate Countermine Branch.

2.3.3. SAM

Sub-audio Magnetics (SAM) (Figure 7) is a technology developed to acquire both time-domain electromagnetic induction and total field magnetic data. The transmitter is composed of a large induction loop carrying a time varying square wave current with 50% duty cycle and maximum of 15 Amperes (Amps). The square wave pulse repetition frequency is nominally 8 Hz, and is thus sub-audio. The receiver is a total field optically pumped Cesium vapor magnetometer capable of measuring 1 nanoTesla (nT) resolution at 8 kHz (Stanley and Griffin, 2002). Mobile total field magnetometers are used to receive low frequency changes in the ambient (i.e., Earth's

field) and synthetic (i.e., those produced by the transmitter) magnetic fields simultaneously with the changing Earth- and locally-generated electromagnetic fields. This on-time signal is split into low-pass and high-pass channels. The lowest frequencies provide information related to the magnetization response of the ground, while data obtained from higher frequencies capture the effects of transient currents and viscous remnant magnetization.

Under the Environmental Security Technology Certification Program (ESTCP) project MM-0322, Gap Geophysics (GAP; formerly GTek) demonstrated near-direct current (DC) low frequency technology called SAM for UXO detection. GAP has developed a custom magnetic field receiver system for SAM, the TM-4, which interfaces multiple total field magnetometers with differential global positioning system (DGPS). The TM-4 also utilizes a custom frequency counter implemented through an FPGA (Field Programmable Gate Array) with a 20 megaHertz (MHzMHz) reference clock that is capable of converting the Larmor frequency produced by an atomic magnetometer to magnetic field readings of 0.2 nT resolution at 400 Hz. Feasibility studies revealed detection using the TM-4 SAM system has been effective against UXO.

Figure 7. GAP custom magnetic field receiver system for SAM, the TM-4, which interfaces multiple total field magnetometers with DGPS.

3. THEORETICAL AND NUMERICAL MODELING

The transient full waveform response of a system can be determined through several different representations. In this Section we describe the formulation of both analytical and numerical methods for simulating the full waveform response to various targets and grounds. An input pulse is defined over a certain finite interval of time and has a zero value at all other times. Starting from Maxwell's equations, the continuous-time full waveform response to certain input waveforms can be solved for directly using closed form analytical solutions. These solutions assume that the target of interest can be represented by a linear system and an associated causal EM field impulse response. The impulse response (or step response) can be represented in either the time or frequency domain. If the system is represented in the frequency domain, the time-domain full waveform representation can be obtained by Fourier and/or Laplace transform methods. For simple axi-symmetric targets, such as spheres, rods, disks, and spheroids, we utilize time or frequency domain analytical formulations for the target impulse response. Targets can be further simplified by an equivalent circuit representation.

3.1. Full Waveform Response Model

The response of a linear, time invariant system to transient excitation can be described by the convolution integral:

$$y(t) = \int_{-\infty}^{\infty} h(t-T)x(T)dT \quad , \qquad \textbf{(1)}$$

where the output magnetic field time series *y(t)* lags the time series of current excitation *x(t)* by *T*, and $h(t-T)$ is the system impulse response function. We can equivalently utilize the step response by recognizing that the time derivative of the step response is the impulse response: $h_{imp}(t) = -\frac{\partial h_{step}(t)}{\partial t}$. In this case, the convolution integral becomes:

$$y(t) = \int_{-\infty}^{\infty} h_{imp}(t-T)I(T)dT = -\int_{-\infty}^{\infty} \frac{\partial h_{step}(t-T)}{\partial t} I(T)dT \quad , \qquad \textbf{(2)}$$

where *I(t)* is the transmitter current. It is sometimes more useful to think of the EMF as the driving function that induces current in a target, where the EMF, ε, is proportional to the negative of the time derivative of the transmitter current scaled by the mutual induction. Therefore, invoking the derivative theorem of convolution (which simply states that a linear system invokes linear operations such that the derivative of a convolution is the convolution of either of the functions with the derivative of the other; Bracewell, 1986):

$$y(t) = -\int_{-\infty}^{\infty} \frac{\partial h_{step}(t-T)}{\partial t} I(T)dT = -\frac{\partial}{\partial t}\int_{-\infty}^{\infty} h_{step}(t-T)I(T)dT = -\int_{-\infty}^{\infty} \frac{\partial I(t-T)}{\partial t} h_{step}(T)dT \quad . \qquad \textbf{(3)}$$

Defining the input function over the interval from *0* to t_1 and the impulse response over the interval from *0* to ∞ and applying the differentiation in (3), we can rewrite the equation as:

$$. y(t) = -\int_0^t \frac{\partial I(t-T)}{\partial t} h_{step}(T)dT \qquad 0 \le t \le t_1 \tag{4}$$

$$y(t) = -\int_0^{t_1} \frac{\partial I(t-T)}{\partial t} h_{step}(T)dT \qquad t > t_1$$

The output magnetic field response can be differentiated to give a proportional voltage response as would be observed in an induction coil receiver:

$$\frac{\partial y(t)}{\partial t} = -\int_0^t \frac{\partial^2 I(t-T)}{\partial t} h_{step}(T)dT \qquad 0 \le t \le t_1 . \tag{5}$$

$$\frac{\partial y(t)}{\partial t} = -\int_0^{t_1} \frac{\partial^2 I(t-T)}{\partial t} h_{step}(T)dT \qquad t > t_1$$

The voltage in the receiver due to the target is thus proportional to the second order time derivative of the transmitter current. These equations (1-5) express the EM response of a target (i.e., the system) to a general input current waveform in terms of a unit step function or delta impulse function. In other words, *y(t)* or *dy(t)/dt* can both be regarded as the superposition of the fundamental response to either an impulse or step function - the choice to implement one or the other primarily depends on which method provides a simpler convolution integral.

If *x(t)* and *y(t)* in Equation (1) are stochastic second order stationary processes, these time series can be written as orthogonal processes $dZ_x(\omega)$ and $dZ_y(\omega)$ using the Fourier-Stieltjes integrals $x(t) = \int_{-\infty}^{+\infty} e^{i\omega t} dZ_x(\omega)$ and $y(t) = \int_{-\infty}^{+\infty} e^{i\omega t} dZ_y(\omega)$. $dZ_x(\omega)$ and $dZ_y(\omega)$ are complex Fourier incremental amplitudes of the current excitation and the receiver coil response, respectively. Because $dZ_x(\omega)$ is an orthogonal process, its relationship to the expected value operator *E[ ]* and autospectral density function $S_{xx}(\omega)$ or spectrum of *x(t)* is:

$$E[dZ_x(\omega_1)dZ_x^*(\omega_2)] = S_{xx}(\omega)d\omega \quad \forall \ \omega_1 = \omega_2 , \tag{6}$$

$$E[dZ_x(\omega_1)dZ_x^*(\omega_2)] = 0 \quad \forall \ \omega_1 \neq \omega_2 , \tag{7}$$

where the asterisk denotes the complex conjugate, and $\omega=2\pi f$ represents the radian frequency. In the frequency domain, convolution may be described using a spectral representation $dZ_y = \Gamma(\omega)dZ_x$, where $\Gamma(\omega)$ is the Fourier transform of the impulse response function of the system, also referred to as the frequency response. The frequency response is complex-valued and contains information about amplitude attenuation and phase at the frequencies represented in the input and output time series.

The convolution operation and equivalent Fourier transform relationships provide powerful methods to relate magnetic field response data to a model of a linear, time invariant electromagnetic system. For example, consider the impulse response of an EM field incident on a metallic target with a system response function obtained via the Fourier transform operator:

$$f(t) = \frac{1}{2\pi}\int_{-\infty}^{\infty} F(\omega)e^{i\omega t}d\omega \quad \Leftrightarrow \quad F(\omega) = \frac{1}{2\pi}\int_{-\infty}^{\infty} f(t)e^{-i\omega t}dt\,. \tag{8}$$

The real and imaginary parts are even and odd functions of frequency, respectively. The impulse response can be formed by the inverse sine transform:

$$h_{imp}(t) = \frac{-2}{\pi}\int_{0}^{\infty} \mathrm{Im}[H(\omega)]\sin(\omega t)d\omega\,. \tag{9}$$

Similarly, the causal step-off response can be derived from the inverse cosine transform:

$$h_{step}(t) = \frac{-2}{\pi}\int_{0}^{\infty} \mathrm{Im}[H(\omega)]\cos(\omega t)d\omega\,. \tag{10}$$

According to the convolution theorem, we can then express the output function $H(\omega)$ as a product of the Fourier transform of the current waveform $I(\omega)$ and the system response function $H_{imp}(\omega)$, such that:

$$H_{step}(\omega) = I(\omega)H_{imp}(\omega) = -i\omega I(\omega)H_{step}(\omega)\,,$$

$$\text{and } H_{step}(\omega) = \left(\frac{-1}{i\omega} + \pi\delta(\omega)\right)H_{imp}(\omega)\,. \tag{11}$$

These equations are sufficiently general for computing the response during the off-time as well as the on-time for arbitrary waveforms. The Sections that follow discuss particular implementations (both analytical and numerical) of these formulations.

3.2. Analytical Models for Axi-Symmetric Targets

For simplified representations, including those for axi-symmetric targets, it is possible to solve Equation (2) directly using closed-form analytical expressions. To illustrate the method, we present a few simple examples.

First, consider the magnetic field response of a target exhibiting a natural exponential decay step response to different excitation voltage (emf, ε) waveforms. For example the result of the convolution of a unit rectangular step voltage function over duration $0 \le t \le t_1$ with the exponential decay is described by the following equations:

$$h(t) = \int_{0}^{t} e^{-(t-T)/\tau}dT = \tau(1-e^{-t/\tau})\ ,\ \ \forall\ 0 \le t \le t_1\text{, and} \tag{12}$$

$$h(t) = \int_{0}^{t_1} e^{-(t-T)/\tau}dT\ = -\tau e^{-t/\tau}(1-e^{t_1/\tau})\ ,\ \ \forall\ t > t_1\,.$$

The analytical full waveform response is shown in Figure 8 . Note that the response for t<0 is zero and that the only time dependent terms are exponentials. After reaching a maximum, the magnetic field response decays with the same time constant as that of the impulse response. The on-time signal is defined over the duration of $0 \le t \le t_1$, and the off-time signal for $t>t_1$.

Another simple, but illustrative example, is the convolution of the exponential decay impulse response with the truncated linear ramp waveform of duration t_1. The magnetic field output response is given by:

$$h(t) = \int_0^t e^{-(t-T)/\tau} T dT = \tau t - \tau^2 \left(1 - e^{-t/\tau}\right), \quad \forall\ 0 \le t \le t_1, \text{ and} \tag{13}$$

$$h(t) = \int_0^{t_1} e^{-(t-T)/\tau} T dT = \tau e^{-t/\tau} \left(e^{t_1/\tau}\left(t_1 - \tau\right) + \tau\right), \quad \forall\ t > t_1,$$

Figure 8 below shows the full waveform response produced by the analytical solution to the convolutions previously described.

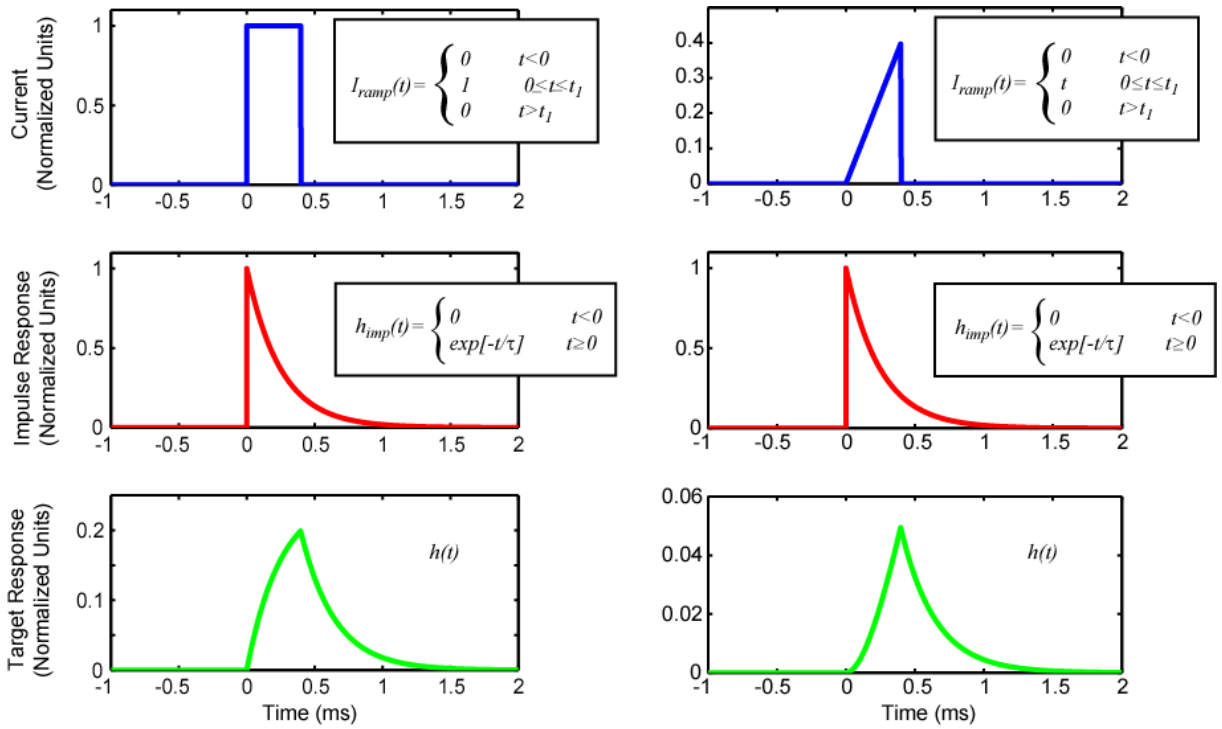

Figure 8. Examples of analytical convolution for simple waveforms: rectangular (LEFT) and linear ramp (RIGHT).

Lastly, we convolve the exponential decay step response with an exponential ramp transmitter waveform. In this case, the output response can be derived to give:

$$h(t) = \int_0^t e^{-(t-T)/\tau}(1 - e^{-T/a})dT = \tau(1 - e^{-t/\tau}) - \frac{\tau a}{a-\tau} e^{-t/\tau}\left(e^{(a-\tau)t/(\tau a)} - 1\right), \quad \forall\ 0 \le t \le t_1, \text{ and} \tag{14}$$

$$h(t) = \int_0^{t_1} e^{-(t-T)/\tau}(1 - e^{-T/a})dT = -\tau e^{-t/\tau}(1 - e^{t_1/\tau}) - \frac{\tau a}{a-\tau} e^{-t/\tau}\left(e^{(a-\tau)t_1/(\tau a)} - 1\right), \quad \forall\ t > t_1$$

As shown in Figure 9, as the ramp-on constant *a* becomes small, the response tends toward that of the step solution. Conversely, as the ramp-on constant increases, the response looks more like the ramp response.

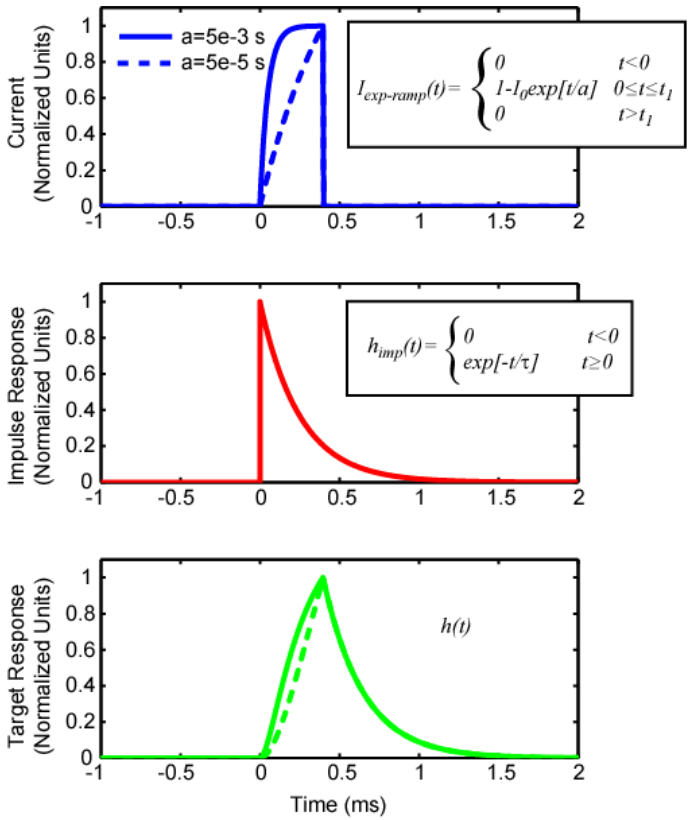

Figure 9. Examples of analytical convolution for simple exponential ramp-on waveform. Two different ramp-on constants are shown - a short ramp constant produces a current waveform that tends to look like a linear ramp and long ramp constant produces a waveform that approaches a rectangular waveform.

In many cases, analytical solutions or approximate solutions for the magnetic field response from axi-symmetric targets are provided in the frequency domain. In this case, the Laplace transform provides an effective technique to obtain transient solutions. Solutions in the time domain require an inverse Laplace transform, which has been extensively described in the literature for circuits and engineering systems analysis. In this case, both the excitation current pulse function and the impulse response are defined in the Laplace domain $s=i\omega$. The multiplication of these functions is equivalent to the convolution operation in the time domain, and, therefore, by taking the inverse Laplace transform of the product of the frequency responses, we can obtain the equivalent full waveform solution. The Laplace transforms for some common current waveforms are given in Table 2.

Table 2.Table of on-time waveforms and their Laplace transforms.

Waveform	Laplace Domain	Time Domain	Region
step	$\frac{1}{s}$	$u(t)$	$0 \le t \le t_0$
rectangular	$\frac{A}{s^2}(e^{st_0} - e^{-st_0})$	A	$-t_0 \le t \le t_0$
ramp	$\frac{1}{s^2}$	t	$0 \le t \le t_0$
exponential ramp	$\frac{(1/a)}{s(s+1/a)}$	$(1-e^{-t/a})$	$0 \le t \le t_0$
triangular	$\frac{1}{s^2}\frac{A}{t_0}(e^{st_0} - e^{-st_0})$	$A(1-\frac{\lvert t \rvert}{t_0})$	$-t_0 \le t \le t_0$
sine	$\frac{\omega}{\omega^2 + s^2}$	$\sin(\omega t)$	$t > 0$
half-sine	$\frac{\omega}{\omega^2 + s^2}(1+e^{-st_0/2})$	$\sin(\omega t)$	$0 \le t \le t_0/2$

Several researchers have utilized this method to derive time-domain responses for spherical targets and homogeneous soil (e.g., Wait, 1951; Patra and Mallick, 1980; Lee, 1984; Billings et al., 2003; and Das, 2004). Patra and Mallick (1980) consider the example of a conducting sphere of radius *R* excited by a half sine waveform. The current waveform is defined over the duration $0 \le t \le t'$ corresponding to half of the period for the complete sine wave $t_0/2$. Therefore, $I(t) = I_0 \sin\left(\frac{2\pi}{t_0} t\right) \quad \forall \ 0 \le t \le t_0/2$, and $I(t) = 0 \quad \forall \ 0 > t$. The Laplace transform of *I(t)* during the on-time is $I(s) = I_0 \int_0^{t_0/2} \sin\left(\frac{2\pi}{t_0} t\right) e^{-st} dt = \frac{I_0 \omega}{\omega^2 + s^2}(1+e^{-st_0/2})$, where $\omega = 2\pi/t_0$. The steady state magnetic field response is given by Wait (1951). The scattered magnetic field is:

$$H(s) = G(r)\left[\frac{1}{3} + \frac{1}{\beta^2 s} - \frac{1}{\beta\sqrt{s}}\coth(\beta\sqrt{s})\right] I(s) \qquad (15)$$

$$H(s) = G(r)\left[\frac{1}{3} + \frac{1}{\beta^2 s} - \frac{1}{\beta\sqrt{s}}\coth(\beta\sqrt{s})\right]\left[\frac{I_0 \omega}{\omega^2 + s^2}(1+e^{-st_0/2})\right],$$

where *G(r)* is geometrical factor that accounts for the offset between the sphere center and the location of the sampled magnetic field, and $\beta^2 = \sigma\mu R^2$ is the dimensional size response parameter for conductivity σ and magnetic permeability μ. The inverse Laplace transform of (15) will then give the full waveform transient solution:

$$\frac{h(t)}{I_0 G(r)} = L^{-1}\left\{\left[\frac{1}{3}\frac{\omega}{\omega^2 + s^2} + \frac{1}{\beta^2 s}\frac{\omega}{\omega^2 + s^2} - \frac{1}{\beta\sqrt{s}}\coth(\beta\sqrt{s})\frac{\omega}{\omega^2 + s^2}\right](1+e^{-st_0/2})\right\} \qquad (16)$$

By expanding the third term into the series expansion for the hyperbolic tangent, Wait (1951) presents an approximate inverse transform:

$$\frac{h(t)}{I_0 G(r)} = L^{-1}\left\{\left[\frac{1}{3}\frac{\omega}{\omega^2+s^2} + \frac{1}{\beta^2 s}\frac{\omega}{\omega^2+s^2} - \frac{1}{\beta\sqrt{s}}\frac{\omega}{\omega^2+s^2} - 2\frac{\omega}{\omega^2+s^2}\sum_{n=1}^{\infty}\frac{e^{-2n\sqrt{s}}}{\beta\sqrt{s}}\right](1+e^{-st_0/2})\right\} \quad (17)$$

where each term yields a transformed component:

$$L^{-1}\left\{\frac{1}{3}\frac{\omega}{\omega^2+s^2}\right\} = \frac{1}{3}\sin(\omega t)$$

$$L^{-1}\left\{\frac{1}{\beta^2 s}\frac{\omega}{\omega^2+s^2}\right\} = \frac{1}{\omega\beta^2}(1-\cos(\omega t))$$

$$L^{-1}\left\{\frac{1}{\beta\sqrt{s}}\frac{\omega}{\omega^2+s^2}\right\} = \frac{1}{\omega\beta\sqrt{\pi t}}\sum_{n=1}^{\infty}(-1)^{n-1}\frac{(2\omega t)^{2n}}{1\cdot 3\cdot 5\ldots(4n-1)}$$

$$L^{-1}\left\{2\frac{\omega}{\omega^2+s^2}\sum_{n=1}^{\infty}\frac{e^{-2n\sqrt{s}}}{\beta\sqrt{s}}\right\} = \sum_{n=1}^{\infty}\left[(-1)^{n-1}\frac{i\omega^{2n-1}}{\beta}\sum_{m=1}^{\infty}(4t)^{(2n-1)+4}\,erfc\left(\frac{n\beta}{\sqrt{t}}\right)\right].$$

A similar approach has been taken by Smythe (1950) and Baum (1999) to derive an equivalent dipole model for simple compact metallic targets. A brief review of the dipole model is warranted to place the solution in context. The dipole model can be described as:

$$h(t) = \vec{M}(t) * (3\vec{r}\vec{r} - \boldsymbol{I}) = \frac{1}{4\pi r^3}\left(\frac{3(\vec{M}(t)*\vec{r})\vec{r}}{r^2} - \vec{M}(t)\right), \quad (18)$$

where $\vec{M}(t) = \boldsymbol{P}(t) * \vec{H}_0(t)$ for primary field H_0 and polarizability dyadic tensor:

$$\boldsymbol{P}(t) = \begin{bmatrix} p_1(t) & 0 & 0 \\ 0 & p_2(t) & 0 \\ 0 & 0 & p_3(t) \end{bmatrix}. \quad (19)$$

The general form of the step response representation of the magnetic polarizability is given by:

$$p_i(t) = p_0 - \sum_{n=1}^{\infty} p_n \exp\left(\frac{-t}{\tau_n}\right). \quad (20)$$

This contains a low frequency limit response corresponding to the DC or low frequency component and a transient component associated with induction. The sum of exponentials function is a general form that has been validated against numerous data and related directly to the analytical physical model for spheroidal and other compact conductive and permeable objects. The derivative of the step response polarizability function gives a basic form for the impulse response:

$$m_i(t) = -m_\infty \delta(t) - \sum_{n=1}^{\infty}\frac{m_n}{\tau_n}\exp\left(\frac{-t}{\tau_n}\right). \quad (21)$$

The first term corresponds to the high-frequency limit. The derivative of the magnetic field response produces a dipole model that will be proportional to the measured voltage on an induction coil receiver:

$$\frac{dh(t)}{dt} = \frac{d\vec{M}(t)}{dt} * (3\vec{r}\vec{r} - \boldsymbol{I}) = \frac{1}{4\pi r^3}\left(\frac{3(\frac{d\vec{M}(t)}{dt} * \vec{r})\vec{r}}{r^2} - \frac{d\vec{M}(t)}{dt} \right). \quad (22)$$

The solution for magnetic polarizability of a sphere has been detailed in many publications (e.g., Baum, 1999; Ward and Hohmann, 1987, Raval and Rao, 1973):

$$p_i(t) = \int_{-\infty}^{t} m_i(T)dT = 2\pi a^3 \left[2\frac{\mu_r - 1}{\mu_r + 2} - 6\mu_r \sum_{n=1}^{\infty} \frac{\exp\left(\frac{-\delta_i^2 t}{\mu\sigma a^2} \right)}{(\mu_r + 2)(\mu_r - 1) + \delta_i^2} \right] u(t). \quad (23)$$

This solution is derived by representing the frequency response in the Laplace domain as a ratio of analytic functions (Baum, 1999) and invoking the Laurent expansion as described by Patra and Mallick (1980). Due to symmetry the magnetic polarizability components are equal: $p_1(t) = p_2(t) = p_3(t)$. Similarly, the integral of the magnetic polarizability components $m_i(t)$ are also equivalent, where:

$$m_i(t) = 2\pi a^3 \left[-\delta(t) - 6\mu_r \sum_{n=1}^{\infty} \frac{\left(\frac{-\delta_i^2 t}{\mu\sigma a^2} \right) \exp\left(\frac{-\delta_i^2 t}{\mu\sigma a^2} \right)}{(\mu_r + 2)(\mu_r - 1) + \delta_i^2} \right] u(t). \quad (24)$$

The induced dipole moment associated with the magnetic field response (b-field response) is given by the convolution: $\vec{M}(t) = \int_{-\infty}^{\infty} p(t-T)\boldsymbol{I}\vec{H}_0(T)dT = g(r)\int_{-\infty}^{\infty} p(t-T)I(T)dT$, where $H_0(t)$ represents the transient nature of the incident primary magnetic field. For the *db/dt* response, we can represent the time derivative of the magnetic moment as $\frac{\partial \vec{M}(t)}{\partial t} = \int_{-\infty}^{\infty} m(t-T)\boldsymbol{I}\vec{H}_0(T)dT$.

For a linear ramp current waveform normalized to the maximum current such that $I(t)=1/t_0$ for an on-time $0 \le t \le t_0$, we can utilize Equation (20) to derive the magnetic dipole moment as:

$$M(t) = g(r)\left[\frac{p_0}{t_0}t + \sum_{n=1}^{\infty} \frac{p_n \tau_n}{t_0}\left(\exp\left(\frac{-t}{\tau_n} \right) - 1 \right) \right], \quad (25)$$

and its time derivative as:

$$\frac{dM(t)}{dt} = g(r)\left[\frac{p_0}{t_0} - \sum_{n=1}^{\infty} \frac{p_n}{t_0} \exp\left(\frac{-t}{\tau_n} \right) \right] = \frac{g(r)}{t_0} p_i(t). \quad (26)$$

Therefore, the db/dt response for a linear ramp current waveform is simply the step response. This formulation is intuitive since the derivative of the ramp waveform is the step waveform.

During the off-time (after the linear ramp has been terminated), the time derivative of the dipole moment is:

$$\frac{dM(t>t_0)}{dt} = g(r)\left[\sum_{n=1}^{\infty}\frac{p_n}{t_0}\exp\left(\frac{-t}{\tau_n}\right)\left(\exp\left(\frac{t_0}{\tau_n}\right)-1\right)\right]. \quad (27)$$

Comparing Equation (26) for the on-time response to the off-time described by Equation (27) tells us that the on-time contains a low frequency component not apparent during the off-time.

3.3. Numerical Convolution Models

3.3.1. Circuit Theory Approach

The use of circuit analysis to approximate the first order response of conductive objects has been applied to both frequency domain and transient electromagnetic applications (Riggs and Mooney, 2001; Miller et al., 2010). The behavior of simple objects, such as rings and coils, can be described completely by a single set of parameters that characterize the self-inductance and resistance of the object and determine the phase and magnitude of induced currents. The transient response of a conducting target can be obtained directly from Maxwell's equations utilizing the vector potential *A* and neglecting displacement currents. This yields the Helmholtz equation:

$$\nabla^2 A = \sigma\mu\frac{\partial A}{\partial t}, \quad (28)$$

where σ is the conductivity and μ is the magnetic permeability. If we approximate the transient response as a superposition of exponential functions, *A* can be expressed as:

$$A = \sum_{j=1}^{\infty} a_j e^{-b_j t}. \quad (29)$$

Wait and Spies [1969] and Weichman [2003] present solutions for a conducting sphere following this approach. Das [2006] develops similar solutions for permeable soils and conducting spheres embedded in permeable soils. Das et al. [1984] and Raval and Rao [1973] have considered layered spheres.

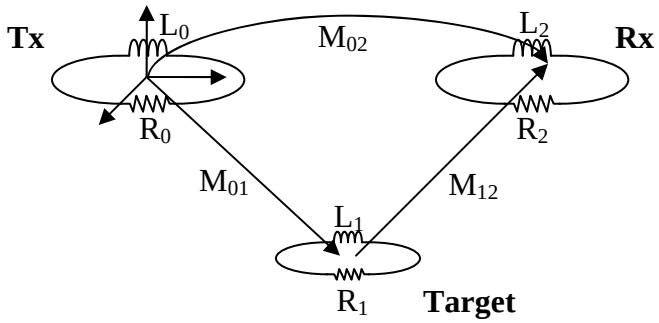

Figure 10. Schematic diagram of simple equivalent circuit used to model the full waveform (on- and off-time) transient response of a target.

The simplest approach to obtaining the full waveform response is to utilize an equivalent circuit model. Here we represent a target of interest (e.g., ground or UXO) as an equivalent (inductive-

resistive) LR circuit that is excited by a transient primary field driven by transient currents in a coil winding, as shown in Figure 10. By combining the potentials induced in the target from the current $I_0u(t)$ in the transmitter and the current generated in the circuit $I_1(t)$, we have:

$$-\left(R + L\frac{d}{dt}\right)I_1(t) = M_{01}I_0\frac{d}{dt}u(t)\ , \tag{30}$$

where the induced current in the target during the ramp on is:

$$I_1(t) = -\frac{M_{01}I_0}{R\tau_1} + Ae^{-Rt/L} \tag{31}$$

During the ramp-off is:

$$I_1(t) = -\frac{M_{01}I_0}{R(\tau_1 - \tau_2)} + Be^{-Rt/L} \tag{32}$$

And decays during the off-time as:

$$I_1(t) = Ce^{-Rt/L}\,. \tag{33}$$

L and R are the inductance and resistance, M_{01} is the mutual coupling between the transmitter coil and target, and t_1 and t_2 are the durations of the linear ramp-on and ramp-off periods, respectively. Figure 11 shows a schematic representation.

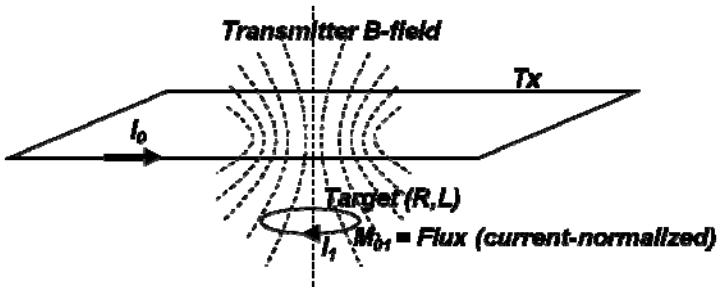

Figure 11. Schematic representation of the equivalent circuit model where the target LR circuit is inductively coupled to the transmitter emf.

The forms of the current waveform during the ramp-on, ramp-off, and decay periods are:

$$u(t) = t/\tau_1 \text{ (ramp on)}, \tag{34a}$$

$$u(t) = \frac{t - \tau_2}{\tau_1 - \tau_2} \text{ (ramp off)}, \tag{34b}$$

$$u(t) = 0\,. \tag{34c}$$

By applying the transmitter current waveform to the circuit model we can determine the current induced on the target I_1 for each phase of the waveform using continuity at boundaries to determine constants A, B, C in Equations (31)-(33). The induced current I_1 can then be used to determine secondary field generated by a coil target. The time rate of change of the secondary field is proportional to the measured voltage in the receiver coil. Thus, the voltage induced in a receiver coil can then be determined from:

$$v_p = -M_{02} I_0 \frac{d}{dt} u(t) \tag{35}$$

$$v_s = -M_{12} \frac{d}{dt} I_1(t) . \tag{36}$$

This solution is sufficient for deriving the full waveform response of an equivalent circuit, but has limited utility for modeling realistic metallic targets that contain both eddy current and magnetic polarizability responses. In this case, the equivalent magnetic circuit can be formed as a function of the size, shape, orientation, and magnetic properties of the target object:

$$v_{DC} = -NA\mu_0 \frac{d}{dt} h_{DC}(t) . \tag{37}$$

3.3.2. Discrete Linear Time-Invariant System Analysis

In the analysis presented in Section 3.2, we considered every current waveform and system response to be a continuous function over a given duration. Alternatively, in the Laplace domain, we represented the waveforms as a continuous sum of sinusoidal waveforms spread over a frequency band. In this section, we consider the implications of expressing the convolution integral in a discrete linear time-invariant system approach. In this case, we consider the current waveform as a piecewise linear function (i.e., straight line segments between provided sample points). Responses to any energizing waveform can be obtained by approximating the waveform as a superposition of step functions (or unit impulse functions). This is equivalent to discrete-time convolution of the impulse (or step) response with the transmitter current waveform.

The convolution sum is $y(n) = x[n] * h[n] = \sum_{k=-\infty}^{\infty} x[k]h[n-k]$, where k and n are integer indices into discrete arrays. This is the discrete equivalent of Equation (1). The causal form of a length-m input signal and causal finite length-k linear time-invariant impulse response is $y(n) = x[n] * h[n] = \sum_{i=0}^{m-1} x[i]h[n-i]$, which can be represented in the generalized form for the z-transform as $y(n) = \sum_{k=-\infty}^{\infty} x[n-k]h[k] = \sum_{k=-\infty}^{\infty} h[k]z^{n-k}$ (the z-transform being the discrete analogue of the continuous Laplace transform).

The discrete form of the system response function can be formulated in either the time or frequency domain with the discrete Fourier transform mapping them from one domain to the other. Because the desired time domain response function rises quickly and decays slowly it is desirable to sample it with small abscissa values (time intervals) during the rapid changing portions and at increasing intervals during later times. In discrete Fourier analysis, the transform is computed at equi-spaced sampling points (frequencies) over the signal bandwidth, where the inverse transform is: $h(n) = \frac{1}{N} \sum_{k=0}^{N-1} H[k] \exp\left(i \frac{k 2\pi n}{N} \right)$, where $t = n\Delta t$. Various methods have been presented to extend the equi-spaced sampling in forward and inverse Fourier transforms to logarithmic sampling. These methods include fitting the response function with a set of

functions for which the analytical Fourier transforms are known (Palacky and West, 1973; Hostetter, 1982), exact analytical Fourier transform expressions of logarithmically sampled functions (Talman, 1978; Haines and Jones, 1988), and segmented Fourier transforms (Asten and Verma, 1978).

For its versatility and simplicity we utilize the digital filtering method of Anderson (1983), where the time-domain function is approximated by a cubic spline between any two discrete sample times: $y(n) = y_0 + a_1 n + a_2 n^2 + a_3 n^3$ where $n = \log(t') - \log(t_i)$ for interpolated times t' given known values of $y(n)$ at time t_i. The spline coefficients are given by a_i. Therefore, the log-transformed integration can be represented by:

$$\int_{x=a}^{b} y(\log(t'))dx = \int_{\log x=\log a}^{\log b} y(\log(t'))t'\,d[\log(t')] = t_i \int_{n=\log a-\log t_i}^{\log b-\log t_i} y(n)\exp(n)dn\,. \qquad (38)$$

As an example, we take the numerical convolution starting from the frequency response for sphere. This forms the discrete convolution analogue to the continuous Laplace transform described in Equations (15)-(17) in Section 3.2. The use of numerical convolution permits modeling of the response to any discrete current waveform. The frequency response for a conductive and permeable sphere at $r = \sqrt{x^2 + y^2 + z^2}$ in a uniform alternating magnetic field is well known (Ward, 1951):

$$H_z(\omega) = \frac{-3}{2} R^3 H_0(\omega)\left[M + iN\right]\left(\frac{3z^2}{r^5}\right), \qquad (39)$$

$$\left[M + iN\right] = \frac{2\mu_1\left(\sinh(\alpha) - \alpha\cosh(\alpha)\right) + \mu_2\left(\sinh(\alpha) - \alpha\cosh(\alpha) - \alpha^2\sinh(\alpha)\right)}{2\mu_1\left(\sinh(\alpha) - \alpha\cosh(\alpha)\right) - 2\mu_2\left(\sinh(\alpha) - \alpha\cosh(\alpha) - \alpha^2\sinh(\alpha)\right)}, \qquad (40)$$

where $\alpha = R\sqrt{i\omega\sigma_1\mu_1 - \omega^2\varepsilon_1\mu_1}$, and μ_1, σ_1, ε_1, and R are the magnetic permeability, electrical conductivity, dielectric permittivity, and radius of the sphere, μ_2 is the magnetic permeability of the host medium (soil). The associated magnetic moment for a dipole can be represented by: $m = -2\pi R^3 H_0(\omega)\left[M + iN\right]$.

The cosine and sine transforms of this function are then computed by the Anderson (1983) filtering routine described above, such that the cosine transform yields the step response and the sine transform corresponds to the impulse response, both logarithmically spaced in time. The time-domain representation of the time-derivative current waveform is then convolved with that for the sphere step response using numerical integration, such that:

$$h^T(t) = -\int_0^t \frac{\partial I(t-T)}{\partial t}\left[-\frac{2}{\pi}\int_0^\infty \mathrm{Im}\left[H(\varpi)\right]\cos(\omega t)d\omega\right]dT\,. \qquad (41)$$

The convolution sum can then be calculated using the generalized Gauassian quadrature numerical integration algorithm:

$$h_t(t) = \int_0^{\Delta t} I'(t-T)h_{step}(T)dT \approx \Delta t\int_0^1 I'(t-u\Delta t)h_{step}(u\Delta t)du\,, \text{ and}$$

$$h_t(t) = \Delta t \sum_{i=1}^{N} w_i I'(t - u_i \Delta t) h_{step}(u_i \Delta t) du \text{, where}$$

w_i are the weights defined by a set of orthogonal polynomials such as the Legendre polynomials or Gauss-Chebyshev polynomials (Ueberhuber, 1995).

To this convolution sum we add the magnetostatic response h^M from the zero-frequency excitation, such that $h^{total}(t) = h^T(t) + h^M(t)$, where:

$$h^M(t) = \frac{1}{4\pi}\left(\frac{3(\vec{m}(t)\cdot\vec{r})\vec{r}}{r^5} - \frac{\vec{m}(t)}{r^3}\right). \quad (42)$$

Here the magnetic dipole moment, *m(t),* is linearly related to the primary field H_0, such that $\vec{m}(t) = VkH_0(t) = V\vec{M}(t)$:, where the demagnetization coefficients, *k*, depend on the shape, orientation, and material properties of the object, but not its volume, *V*. When combined with the primary field, these terms form the magnetization dyadic *M(t)*. For the case of a sphere,

$$\vec{m}(t) = \frac{4}{3}\pi a^3 \left(\frac{\chi}{1+\chi/3}\right)\vec{H}_0(t) \ , \quad (43)$$

where χ is the magnetic susceptibility and *a* is the radius of the sphere. In this case the magnetic field response can be expressed as:

$$h^M(t) = \frac{-2}{\pi}\int_0^{\infty} \mathrm{Im}[k(r)a^3 H_0(\omega)\left(\frac{\chi}{\chi+3}\right)]\cos(\omega t) d\omega. \quad (44)$$

For simple spheroidal objects Pasion [1999] gives the formula for internal magnetic induction B_i in terms of three axial demagnetization factors D_1, D_2, D_3, where $B_i = \mu_0 H_0\left[1 + (1 - D_i)\frac{\chi}{1 + D_i\chi}\right]$.

For a given aspect ratio $q=a/b$, the demagnetization factor for a prolate spheroid ($q>1$) is:

$$D_a = \frac{1}{q^2-1}\left\{\frac{q}{(q^2-1)^{0.5}}\ln\left[q + (q^2-1)^{0.5}\right] - 1\right\} \text{ and } D_b = \frac{1}{2}(1 - D_a), \quad (45)$$

where D_a is the demagnetization factor for *a* and D_b along *b*. For a sphere $D_a = D_b = \frac{1}{3}$.

It should be noted that our formulations assume that the permeability of ferrous objects is a constant value over varying field strengths. A more realistic representation accounts for the nonlinear relationship between the impinging primary magnetic field and the magnetic flux for ferromagnetic objects. The assumption that magnetization is linearly related to the magnetic field is only valid for incident field strengths of ~1 A/m (Sower, 1998). However, almost every EM system of interest produces primary fields well in excess of this. Therefore, during a transmitter excitation period, the effective permeability of an object may change by as much as 25 times its original value. The permeability is also, to some extent, frequency dependent. Resonance and relaxation spectral behavior has been noted for ferrous objects where permeability decreases above ~5 kHz to the free space value at frequencies >100 kHz.

4. SIMULATED ON-TIME RESPONSE ANALYSIS

To develop an understanding of the various drivers that influence on-time responses, we generated simulations under various scenarios. The purpose of these models was to evaluate the performance that may be possible with field instrumentation, and to provide a comparison for the eventual data.

4.1. Limitations and Assumptions of the Model

The model makes the following assumptions about the physics and characteristics of particular targets:

- The physical system representing a target response is assumed to form a linear causal time-invariant system.
- The model evaluates the field produced by a perfect dipole source at each sensor in the absence of any other fields.
- The model does not consider the impact of any limitations of the measurement extraction techniques.
- The model considers additive white Gaussian noise (AWGN) in a fixed bandwidth with no other interference sources.

4.2. Effect of Varying Waveform

Both the duration and the shape of the current waveform affect the full waveform response. Figure 12 shows that the form of the current waveform influences the scattered magnetic field during both the on- and off-times. The modelled responses are for the case of conductive and permeable sphere 0.5m directly below a 1m x 1m transmitter. The properties of metallic spheres are of interest both because their response can be analytically calculated (with help of numerical integration techniques), and because they are used as calibration targets.

The box car or rectangular waveform response mimics that of a step off response for on-time durations where the impulse response decay is significantly shorter than the on-time period. The same is true for the linear ramp-on function. The triangular and half-sine waveforms have similar responses.

As stated previously, it is well-known that the magnetic field response for a step current source can be expressed as a sum of exponential time functions (Kaufman, 1978). A single exponential decay is equivalent to assuming that the target is a simple wire loop as demonstrated in the Section 4.3.1 for equivalent circuits. For a step current transmitter, the voltage in an induction receiver due to current induced in a loop is:

$$v_{step} = G(r)\left[\delta(t) - \frac{I_0}{\tau}\exp\frac{-t}{\tau}u(t)\right], \qquad (47)$$

where *u(t)* is a unit step function and $\delta(t)$ is the dirac delta function or the derivative of *u(t)*. $G(r)\delta(t)$ is often referred to as the inductive limit term and is important in calculating the target response when the transmitter is turned on. *G(r)* accounts for the geometry of the system.

Figure 13 shows the response to the same conductive and permeable sphere case described in the previous example. The model responses exhibit the effect of varying the duration of a linear ramp-on current waveform from 0.5 milliseconds (ms) to 5ms. Both the on-time and off-time are affected by the duration of the current ramp on period.

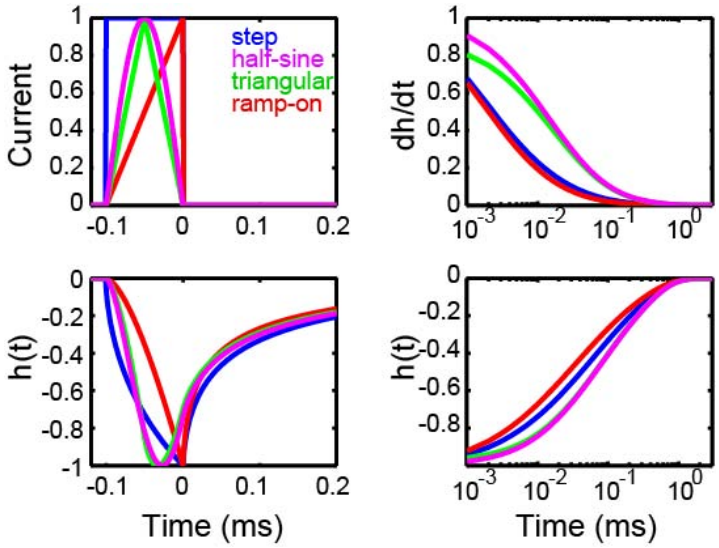

Figure 12. Response to various on-time current waveforms. The target magnetic field (h(t)) and its time rate of change are plotted against logarithmic time on the right. On the left, the transmitter emf waveforms and the linear time response of the target magnetic field are shown.

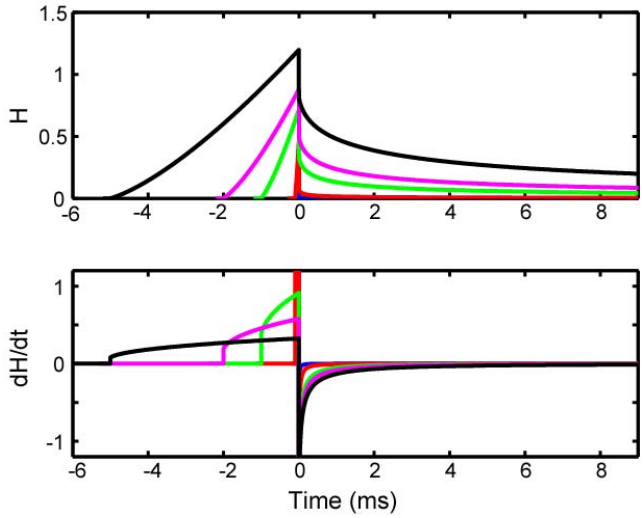

Figure 13. Response to linear current ramp-on waveforms of varying duration between 1 and 5 ms.

During the off-time after cessation of a rectangular pulse with linear ramp-off time, the inductive limit term is suppressed. In Figure 14 we compare the analytical solution for a step-off excitation with the full waveform response for a given linear ramp-off duration. In this example, we model

the response from a 5 centimeter (cm) diameter conductive and permeable sphere 50 cm from an induction loop transmitter. We also compare the step-off responses for a conductive half-space. In both cases, we see that as the ramp-off duration is shortened the response tends to that of the true step-off response.

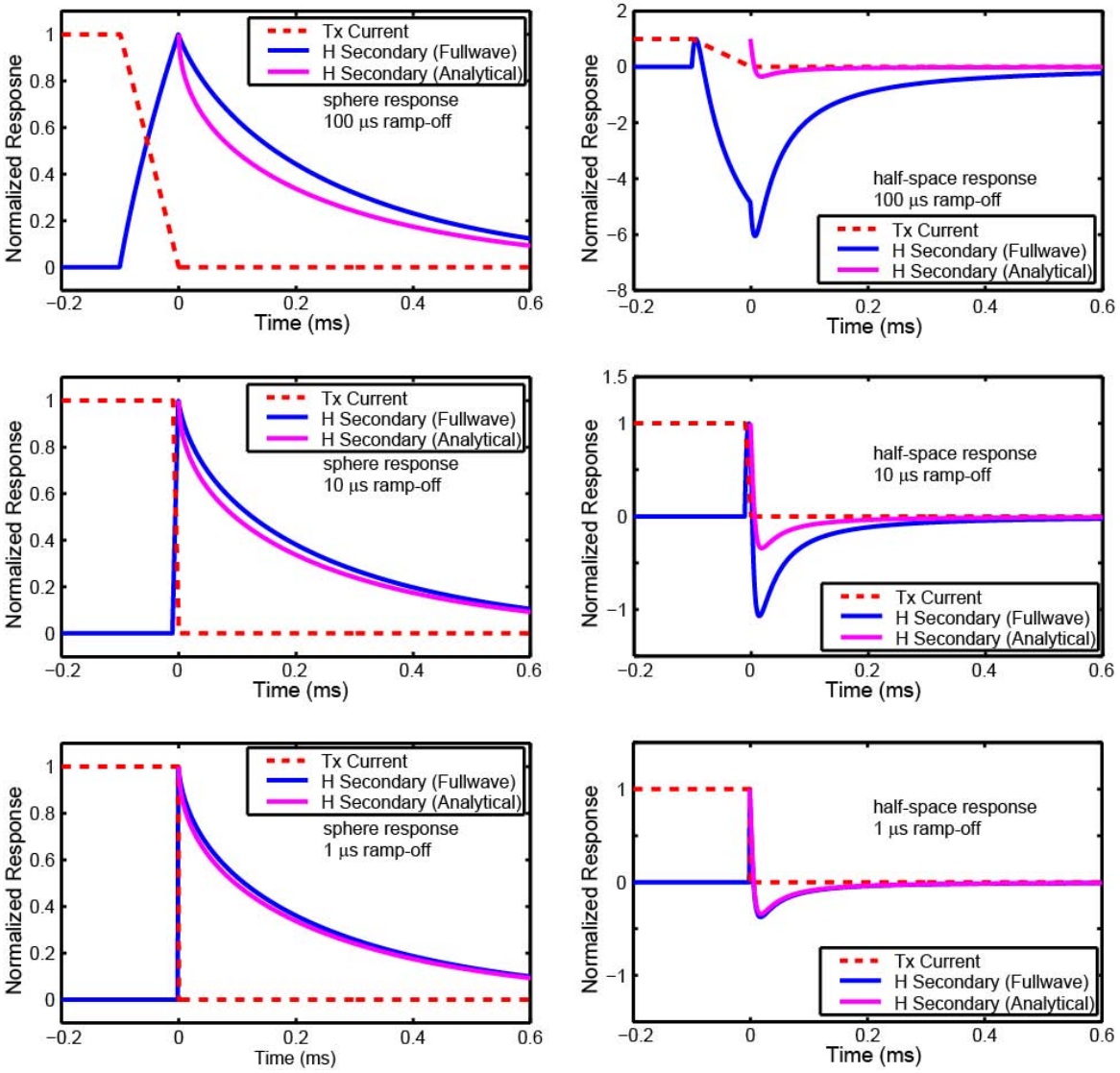

Figure 14. Response to a linear current ramp-off of varying duration. (Left) The analytical off-time response for a conductive and permeable sphere is compared with the corresponding full waveform response. (Right) Comparison of the off-time step-off response to that from the full waveform response to a conductive half-space.

4.3. Target Size and Depth Sensitivity

We demonstrate the sensitivity of on-time responses to target size and depth. A conductive and permeable steel sphere is used for the target embedded in a permeable half-space. Steel is modelled with a conductivity $\sigma=3.5\text{x}10^6$ Siemens/meter (S/m) and permeability $\mu=150\mu_0$. A 1.0 meter square transmitter with a linear ramp current excitation is used to generate both on- and off-time response as shown in Figure 15. We see that the magnetic field response varies with size and depth of the target. In particular, the off-time magnetic field response for a small (2 cm

diameter) sphere shallowly buried (z=20 cm) is larger than the on-time response relative to that for a deeper, larger sphere. This effect is very much dependent on the times during the on- and off-time for which the magnetic field response is sampled. We choose t_{on}=-0.31 ms and t_{off}=0.1 ms relative to the shut off time (t=0). The full waveform response was computed using the formulations described in Equations (39)-(45).

The stronger response in the on-time for a deep, large sphere relative to the off-time is predominantly due to the influence of the mass of the object on its magnetization response. The asymmetry in the responses reveals the influence of the Earth's magnetic field on the magnetic field response.

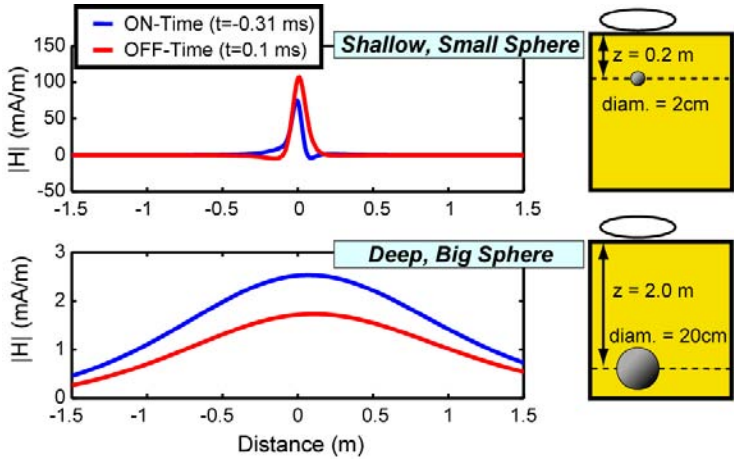

Figure 15. Response to varying duration linear current ramp-off functions. A 1.0 meter square transmitter with a linear ramp current excitation is used to generate both on- and off-time responses

4.4. Responses to Varying Shape, Size, and Composition

The tradeoff between the influence of the induction and magnetization responses during the on-time is evident when comparing the on- and off-time response of objects of different size. In the example shown in Figure 16, we model the time-domain magnetic field response for spheres of varying size. The on- and off-time signals are compared. For small spheres, the target surface area overwhelms the amount of available mass for magnetization and, thus, the off-time induction signal dominates. As the diameter of the sphere increases, the magnetization response has an increasing influence relative to the induction response, and the on-time signal dominates.

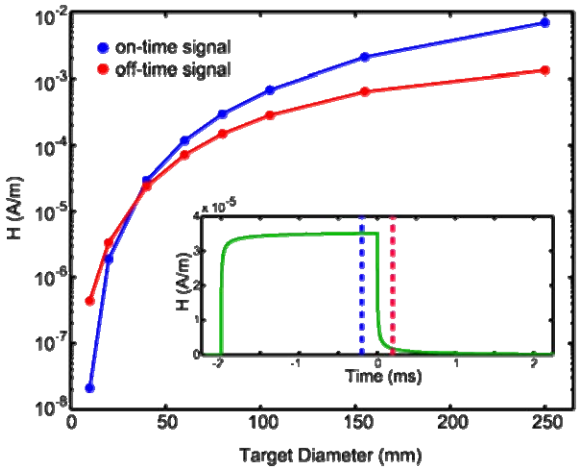

Figure 16. Response to varying duration linear current ramp-off functions. Model results for the time-domain magnetic field response for spheres of varying size

In order to gain some intuition on the influence of varying the aspect ratio of spheroidal objects, we combined a dipole induction model with a formulation for the magnetization response from prolate or oblate spheroids. The spheroidal magnetization response is computed using the magnetic dipole equation (Equation (18)) by incorporating ellipsoidal demagnetization factors as described by Cronemeyer [1991].

Figure 17 compares the on- and off-time *dH/dt* responses over spheroids with varying aspect ratios. A differential horizontal gradient receiver configuration was simulated. During the off-time, the form of the anomaly does not change regardless of the aspect ratio *a/b*. During the on-time, the sphere (*a/b*=1) as well as the prolate spheroidal-shaped objects (*a/b*<1) generate responses that are in opposition to the corresponding off-time signals. It is also noticeable that the on-time signal appears to have a greater sensitivity to variations in the aspect ratio relative to the off-time signal. This is likely due to the influence of the magnetization factors corresponding to the shape of the object. The magnetization response, in general, is very dependent on the configuration of available magnetization volume within the object. The induction response may be more influenced by the total surface area available for currents to set up on.

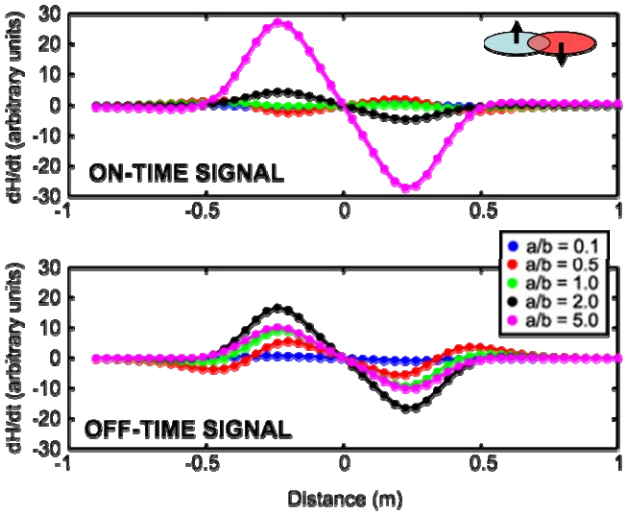

Figure 17. Comparison of the on- and off-time *dH/dt* responses over spheroids with varying aspect ratios.

5. DECONVOLUTION AND INVERSION APPROACHES

5.1. Full Waveform Inversion Methods

5.1.1. Effective In-phase/Quad-phase Decomposition

Assuming that measured responses during the on-time are due to a single body we can model it accurately using the linear systems approach. While the generation of forward full waveform models has great utility in understanding the phenomenology of on-time responses, the most practical use is in extracting model parameters using an inverse model. By deconvolving the system transfer function from the received voltage waveform we can estimate the location, size, shape, and material properties of a target anomaly. These deconvolution methods are based upon statistical models and are implemented in a least-squares inversion. The details of the nonlinear least squares inversion approach are described in Pasion and Oldenburg [2001], Aster et al. [2005], and Schultz and Ruppel [2005]. Inverted parameters for a spherical test target are presented in Section 3.

Another method of deconvolution involves removing the primary field from the total field response in order to yield only the induced scattered component of the response. The full waveform response is decomposed into two parts, which are referred to as the time-domain "in-phase" and "quadrature-phase" components. The time-domain in-phase component reflects the transient behavior of the primary field. The time-domain quadrature-phase component is derived solely from the scattered field response to eddy currents induced in nearby conductors.

The method used to decompose the received transient signal is based on the deconvolution approach described by Stolz and Macnae [1998]. We assume that the measured response (whether measured as *H* or *dH/dt*) is composed of both primary field H_0 and a scattered field H_s components: $H_{total}(t) = H_{\varnothing}(t) + H_S(t)$. The scattered field, in-turn, is composed of a component that is purely in-phase and a component that is out-of-phase (quadrature-phase) with respect to the primary field: $H_S(t) = I_S(t) + Q_S(t)$. By definition, the in-phase scattered field is a scaled version of the primary field, such that the residual component of scattered field yields the quadrature-phase component: $Q_S(t) = H_S(t) - aH_P(t)$. Therefore, the decomposition reduces to finding the scaling factor via a least-squares approach that minimizes the objective function:

$$\Phi = \left[\sum_{i=1}^{N} (H_S(t_i) - aH_0(t_i))^2 \right]^{1/2} . \qquad (48)$$

An example of this procedure is shown in Figure 18 for the response to a 10 cm diameter steel sphere. The scattered field is represented by a linear combination of in-phase and quadrature-phase components. The total in-phase component contains both system geometry and the magnetostatic scattered field response. In the absence of any conductive or permeable material, the in-phase component of the scattered field will be non-existent and the procedure will yield the primary field transient behavior exactly.

In order to compare the character of the transient full waveform in-phase and quadrature-phase components with their frequency-domain analogs, we have computed the response to a conductive and permeable sphere with varying conductivities and magnetic susceptibilities. The results for 4 different conductivity-susceptibility cases are shown in Figure 18A-D. We assume

a 10cm radius sphere located 50cm directly beneath a circular transmitter coil, and estimate the full waveform response at a position 1m offset from the transmitter. The scattered field response clearly shows the tradeoff between responses dominated by the magnetostatic effect (magnetization) and those dominated by eddy current decay (Lenz's law). Examination of the responses for permeable spheres with conductivities that vary from essentially non-conducting (σ=10^{-4} S/m) to infinitely conducting (σ=10^{6} S/m) yields the equivalent resonant-relaxation frequency response.

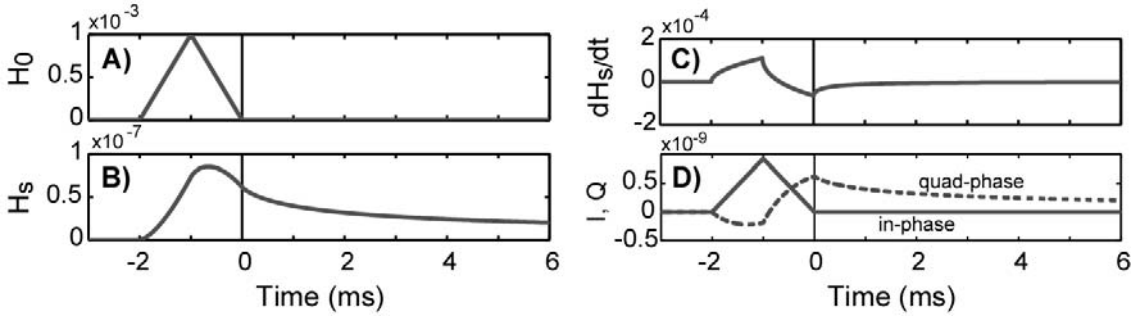

Figure 18. Separation of in-phase and quad-phase scattered field components. A) The primary field is generated from a 2ms triangular current waveform. A steel sphere with σ=10^{6} S/m and χ=1000 were assumed. B) Scattered magnetic field. C) The time derivative of the scattered field in is proportional to the expected voltage signal in a receiver coil. D) Decomposition of the scattered field into the equivalent in-phase (I) and quad-phase (Q) components.

Figure 19 shows the values of the sampled transient response during the on-time (at -1.5ms), early off-time (at 4.0 μs), and at late off-times (at 1.8ms). By modeling the decomposed full waveform signal at various conductivities (i.e., induction numbers), we observe a systematic resonant response in the quadrature-phase portion of the scattered field.

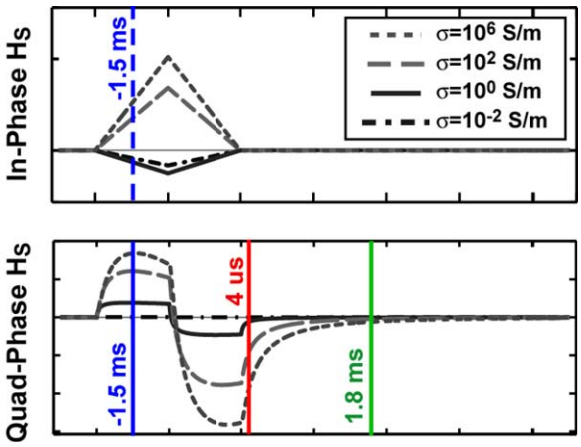

Figure 19. Example full waveform scattered field response for conductive and permeable spheres.

Figure 20 illustrates the analog frequency-domain response computed from the frequency-domain solution for a conductive and permeable sphere. The separation of the in-phase and quad-phase components facilitates an analogue to the conventional frequency domain response for sinusoidal excitation. The residual transient (quadrature) off-time response is similar to the quadrature frequency-domain response and the in-phase on-time response is also similar to the in-phase frequency-domain conductivity spectra. The early off-time quad-phase response reveals its relatively high frequency analog. In airborne electromagnetics (e.g., Annan et al.,

1996 and Smith, 1998), the on-time quadrature-phase component has been used to estimate the apparent conductivity of ground.

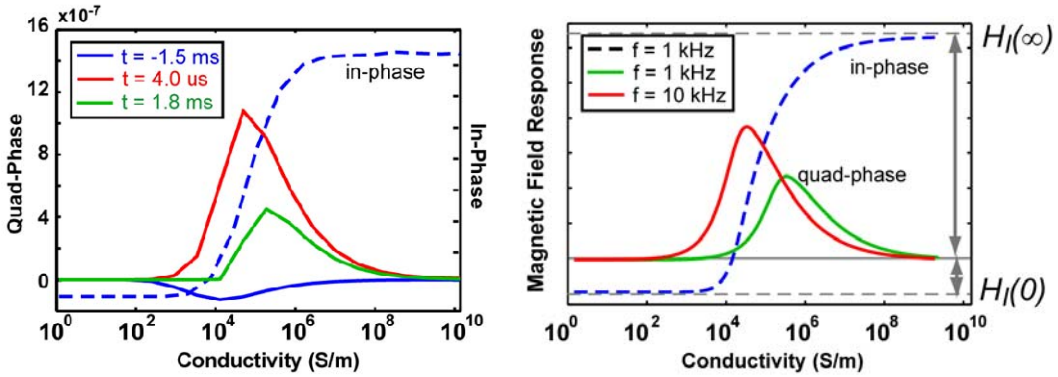

Figure 20. Analog frequency-domain response computed from the frequency-domain solution for a conductive and permeable sphere

5.1.2. Resitive and Inductive Limits

For UXO applications, the limits of the in-phase and quadrature-phase responses may be of particular interest. For example, the frequency-domain in-phase and quadrature-phase responses for a metallic sphere are represented in Figure 21. The behavior of the complex response function as described by Equation (39) from Section 3.3.2 is shown as a function of frequency. In the limit as the frequency approaches infinity, the response tends to an asymptotic value of 1. This is the inductive limit and is purely in-phase (Grant and West, 1965). The inductive limit is equivalent to the zero time amplitude relative to a step-off current excitation in the time domain. Physically, the inductive limit represents the stage in the induction process where all the secondary currents are concentrated on the surface of an object in order to oppose the change in the normal component of the primary field. At the equivalent time, no current has penetrated into the object and the inductive limit is only dependent on the geometry of the object. (Note that the inductive limit as defined here is not the same as the "early time" limit defined elsewhere).

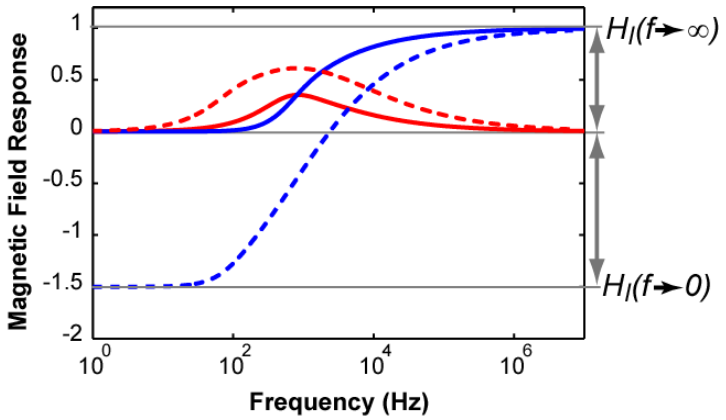

Figure 21. Frequency-domain response function of a sphere in a uniform alternating field. The blue curves represent the in-phase component of the response and red curves are the quadrature phase. The solid curves are for $\mu=\mu_0$ and the dotted curves are computed responses for $\mu=10\mu_0$ to illustrate the magnetization effect for sinusoidal excitation as in frequency-domain EM systems. The example is meant to illustrate the resistive (low frequency asymptote) and inductive (high frequency asymptote) limits, both of which are obtainable from on-time EM measurements.

At the other end, as the frequency approaches DC, the slope of the response function approaches a finite value. In the time-domain, the limit is equivalent to the total area under the decay of a step response. Here, the induced currents have fully penetrated the object and material composition (bulk conductivity) as well as geometry affect the value.

When $\mu=\mu_0$ the response is very similar to that for the simple induction loop described in Section 3.3.1. The main difference being that the transition between the inductive and resistive limits occurs over a wider frequency range for a sphere because the sphere's volume permits the potential of induced currents to redistribute whereas they are confined to a loop in the coil case. For magnetically permeable objects ($\mu>\mu_0$), the dipole moment is composed of a static component and a transient component. The static component is in-phase and co-aligned with the primary field. At the resistive limit, Grant and West [1965] define the limiting magnetic moment:

$$m(f\rightarrow 0)=\left[4\pi R^3\left(\frac{\mu-\mu_0}{\mu+2\mu_0}\right)-2\pi R^3\left(\frac{i\omega\sigma\mu_0R^3}{15}\right)\left(\frac{3\mu_0}{\mu+2\mu_0}\right)\right]H_0(\omega), \qquad (49)$$

where the first term represents the magnetization and the second term indicates the initial induction barrier. During the off-time, the transition between being dominated by magnetization to that of being dominated by the transient induction response is controlled by the modal eigenvalue. During the on-time, this transition is modified by a factor that is directly related to the bulk demagnetization $D=\dfrac{m(f\rightarrow\infty)}{m(f\rightarrow\infty)-m(f\rightarrow 0)}$. Physically, this factor describes how the object responds to the excitation from the primary magnetic field. As a permeable object becomes magnetized, the magnetic domains distort and deform as their dipoles rotate to align with the impinging field. The net (magnetometric) build up of magnetic poles on either end of the object creates a demagnetizing field (aligned with the primary field outside the object and opposing the primary field inside the object). In Figure 20 and Figure 21, the limiting magnetic

field responses H_I at both low and high frequencies, are proportional to the demagnetization factor such that: $D = 1 - \dfrac{H_I(0)}{H_I(\infty) - H_I(0)}$.

5.1.3. Matrix Pencil Decomposition

In order to estimate the effective resistive and inductive limit responses from on-time data, we apply the deconvolution method of Stolz and Macnae (1998). Here, the decomposition of a response to any excitation waveform is achieved through the use of exponential basis functions pre-convolved with a particular system's current waveform. It follows from the theory of optimal experimental design that a singular value decomposition can be used to assess which specific waveforms provide superior resolution of a range of exponential decay constants that can be related to a targets size, shape, and material composition. Moreover, this formulation permits estimation of the inductive and resistive limit responses, which are related to the bulk demagnetization.

As described in Equations (20)-(24), we can expand the step-off response as a sum of pure exponentials $d_n(t) = p_0 - \sum_{m=1}^{\infty} p_m \exp\left(\dfrac{-t}{\tau_m}\right)$. The effective inductive limit can be computed by summing the amplitude coefficients $p(f \to \infty) = \sum_{m=1}^{M} p_m$, and the resistive limit by $p(f \to 0) = \sum_{m=1}^{M} p_m \tau_m$. The resistive limit is defined in the frequency domain as the slope of the response function as frequency approaches a zero value (Grant and West, 1965) and is thus similarly defined as the area under the step response decay curve in the time-domain. To extend the simple step-off response to any current waveform excitation, we convolve each of the *M* exponential terms of associated discrete time constants with the transmitter waveform. For a system of measurements at *N* times and a set of *M* basis functions, we have

$$\begin{bmatrix} d_1 \\ \vdots \\ d_n \\ \vdots \\ d_N \end{bmatrix} = \begin{bmatrix} 1 & I(t_1)*e^{-t_1/\tau_1} & \cdots & I(t_1)*e^{-t_1/\tau_M} \\ 1 & \vdots & I(t_n)*e^{-t_n/\tau_m} & \vdots \\ 1 & I(t_N)*e^{-t_N/\tau_1} & \cdots & I(t_N)*e^{-t_N/\tau_M} \end{bmatrix} \begin{bmatrix} p_0 \\ p_1 \\ \vdots \\ p_M \end{bmatrix}, \qquad (50)$$

where "*" indicates numerical convolution. This leads to a simple linear matrix formulation ***d=Gp***. The deconvolution of this system yields the time constants represented by a particular target. Deconvolution methods using least squares inversion of this system are highly unstable. Although, the real exponential functions do not form a stable set of basis function for inversion, this method provides stable estimates of the resistive and inductive limits. This is because of the nature of the exponential basis functions. These functions are known to have a tendency to produce non-unique solutions because of their sensitive to the number of discrete model parameters preselected for the system kernel matrix (Stolz and Macnae, 1998).

To estimate the discrete time constants by analyzing the exponential bases, we use singular value decomposition (SVD). SVD has been used extensively in system design, geophysical inversion, and optimization to generate an orthonormal factorization of a system of equations (Menke, 1989; Golub and Van Loan, 1996; Strang, 1998). The SVD of $\boldsymbol{G}$, $\boldsymbol{\Phi=U\Lambda V^T}$ allows us to form an inversion, such that we can solve for $\boldsymbol{p=(V\Lambda^{-1}U^T)d}$. By retaining only the most significant diagonal elements of $\boldsymbol{\Lambda}$, we can avoid singularities and unstable solutions. Performing general singular-value decomposition also allows us to assess the conditioning and resolution of $\boldsymbol{\Phi}$. The $\boldsymbol{\Lambda}$ matrix contains the nonzero square roots of the eigenvalues λ_i shared by $\boldsymbol{\Phi\Phi^T}$ and $\boldsymbol{\Phi^T\Phi}$ and is useful for evaluating the available information and the rank deficiency of the transformation matrix.

To assess this method we generated a synthetic data set using a 2ms linear ramp current waveform. Gaussian noise was added to the synthetic data such that the lowest signal response values magnified the noise the most. This is typical of time-domain EM systems.

We consider the case of significantly overdetermined decay constants (where the number of data far exceeds the number of decays to be estimated). The solution via SVD yields coefficients (weights) p_m for each decay constant. We found, as expected, that the actual values of the estimated decay constants became increasingly unstable as the number of discrete coefficients increased. Figure 22 (Left) shows the results of inverting for 18 decay constants over the range of τ_i=0.001 to 10 ms. The synthetic model for this case consisted of a single decay constant of 0.01 ms. Although, the recovered transient signal fits the data equally well when we use either the full waveform or off-time only data, the estimated decay constants are significantly different. For a given number of decay constants the full waveform model is able to reproduce the synthetic decays much better than using an off-time only model. Figure 22 (Right) shows the total error for synthetic cases represented by a single decay constant over a range of decays.

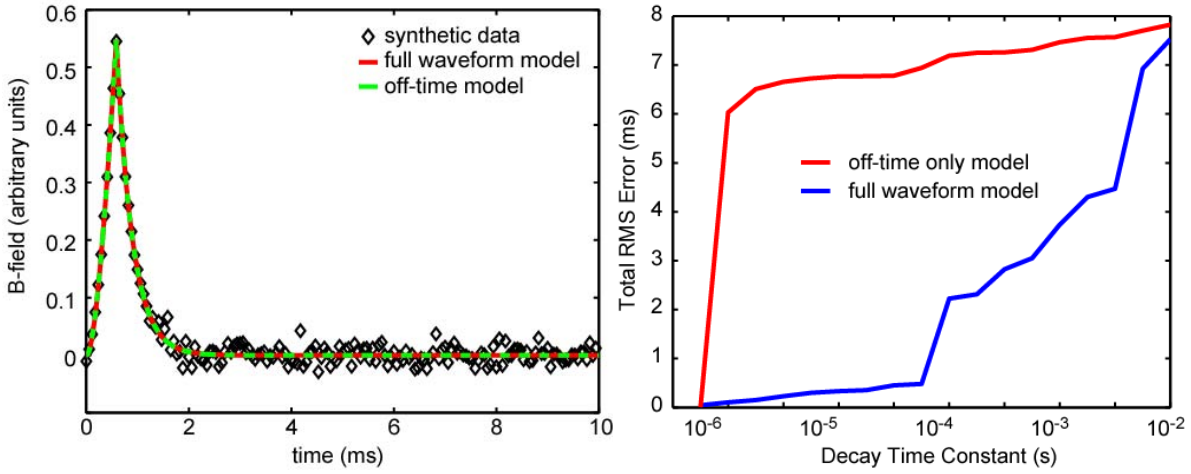

Figure 22 . (Left) Example application of the SVD-based Matrix Pencil inversion. The synthetic data were generated by adding Gaussian noise scaled to the signal level. Model parameters recovered via inversion of full waveform and off-time only data generate equally good fits to the original synthetic data. (Right) The total error in decay time constant obtained with off-time data and full waveform data for various decays.

Although, the estimated decays generated by SVD of discrete exponential bases are unstable for any model other than a highly overdetermined one, estimates of the inductive and resistive limits appear to remain stable over a range of values. This is useful for estimating the demagnetization factor for permeable targets. Figure 23 compares the synthetic inductive and resistive limit values with those estimated from recovered decays.

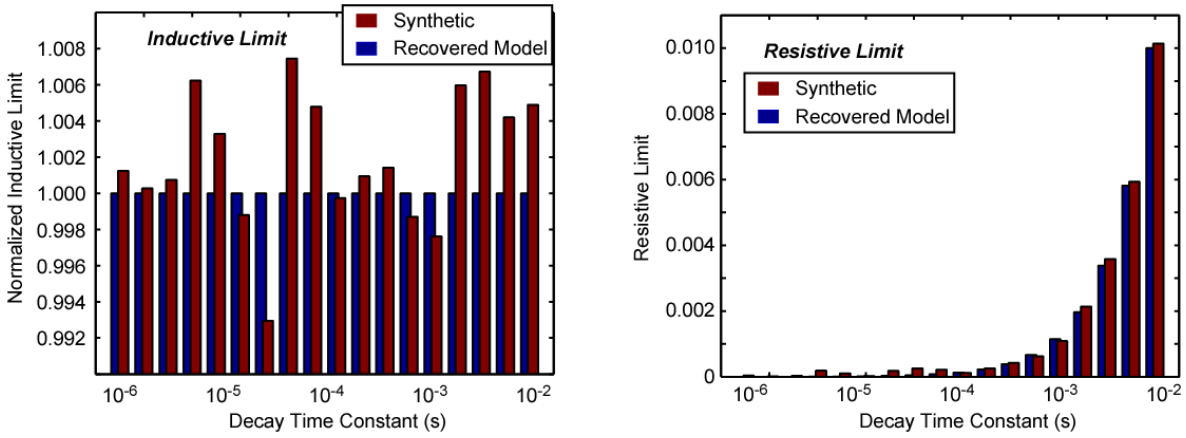

Figure 23. (Left) Comparison of the equivalent synthetic (known) inductive limit response and those estimated by matrix pencil inversion. (Right) The corresponding synthetic and estimated resistive limit values. Both the inductive and resistive limits can be robustly determined by application of this method.

5.2. ALLTEM Data Inversions

The ALLTEM is a prototype system that utilizes a triangular saw-tooth excitation waveform through 3 tri-axial transmitters. Multi-axis differential receiver pairs acquire full waveform data at all times during the continuous excitation. The current waveform is an always-on triangular sawtooth with a full period of 11ms. Figure 24 shows a schematic of the basic coil configuration for the ALLTEM system and a comparison of ALLTEM calibration data with the modeled full-waveform response to a 10 cm steel sphere.

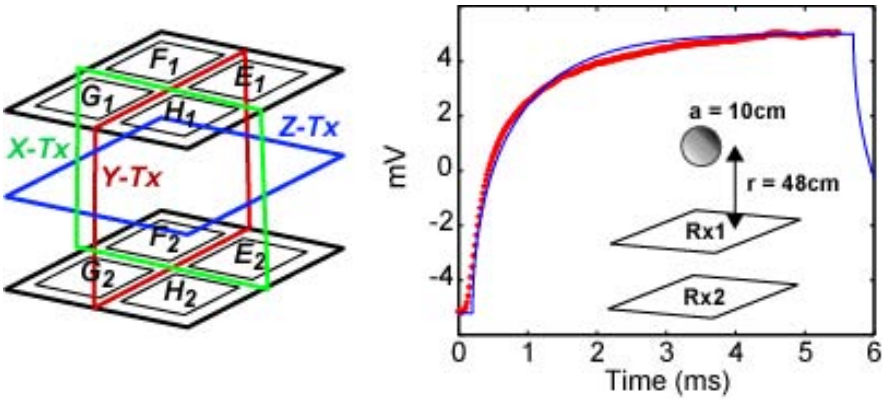

Figure 24. Schematic of the basic coil configuration for the ALLTEM system (left). The measured voltages (solid circles) from a differential pair of square loop receivers reveals the response to 10cm radius steel sphere placed 48 cm from the array (right). Modeled full waveform response fits the data well throughout the on-time period.

For compact metallic objects, the forward model can be approximated by a dipole moment induced in the target by the primary field (Pasion and Oldenburg, 2001). We use the solution derived by Wait [1951] for the quasi-static transient response of a conducting and permeable sphere. We utilize the relationship between the induced dipole and the primary field to characterize the magnetic polarizability dyadic (Raval and Rao, 1973), where the triple degeneracy of the polarizability tensor reflects the symmetry of the sphere.

Inversions are accomplished by application of a regularized least-squares optimization method. These methods are well-documented (e.g., Farquharson and Oldenburg, 1998; Pasion and Oldenburg, 2001; Schultz and Ruppel, 2005) and have been shown to reproduce data for various target types and scenarios. To solve the global nonlinear optimization problem, we use an iterative procedure based on the truncated Taylor's series expansion, $\boldsymbol{F}(\boldsymbol{m}+\boldsymbol{\delta m}) = \boldsymbol{F}(\boldsymbol{m}) + \boldsymbol{J}\boldsymbol{\delta m}$, where $\boldsymbol{F}(\boldsymbol{m}+\boldsymbol{\delta m})$ is the forward model after perturbation $\boldsymbol{\delta m}$ of the initial model parameters $\boldsymbol{m}$, and $\boldsymbol{J}$ denotes the Jacobian (sensitivity) matrix. The k^{th} iteration of the model that minimizes the updated model parameters for the nonlinear problem is given by the Levenberg-Marquadt scheme

$$\boldsymbol{m}_{est}(\eta)_{k+1} = \boldsymbol{m}_k + \boldsymbol{\delta m} = \left[(\boldsymbol{W}\boldsymbol{J}_k)^T \boldsymbol{W}\boldsymbol{J}_k + \eta^{-2}\boldsymbol{R}^T\boldsymbol{R} \right]^{-1} (\boldsymbol{W}\boldsymbol{J}_k)^T \boldsymbol{W}\boldsymbol{d}_k . \quad (51)$$

The regularization matrix $\boldsymbol{R}$ takes the form of an M x N roughness matrix that constrains the model structure, and the regularization parameter η balances the influence of the least-squares and roughness components of the objective. The data weighting matrix is given by $\boldsymbol{W}=\boldsymbol{I}(1/\boldsymbol{s})$, where $\boldsymbol{I}$ denotes the N x N identity matrix, and $\boldsymbol{s}$ is a length N column vector containing uncertainties in the data. Assuming that errors in the data are uncorrelated and equivalent for every observation, s represents the sample standard deviation. It should be noted that the L_2 norm is particularly sensitive to presence of outliers.

An example inversion for magnetic polarizabilities utilizing the full waveform model is shown in Figure 25. We see in this example that the inverted polarizabilities are relatively consistent over the duration of the triangular current waveform (positive and negative ramps are aligned and averaged to form the processed data shown on the Leftmost panels in Figure 25). Full waveform inversions predict the target location and polarizability for an axi-symmetric spherical target. The inverted location for the 10cm solid steel sphere is accurate to within 2cm in x, y, and z.

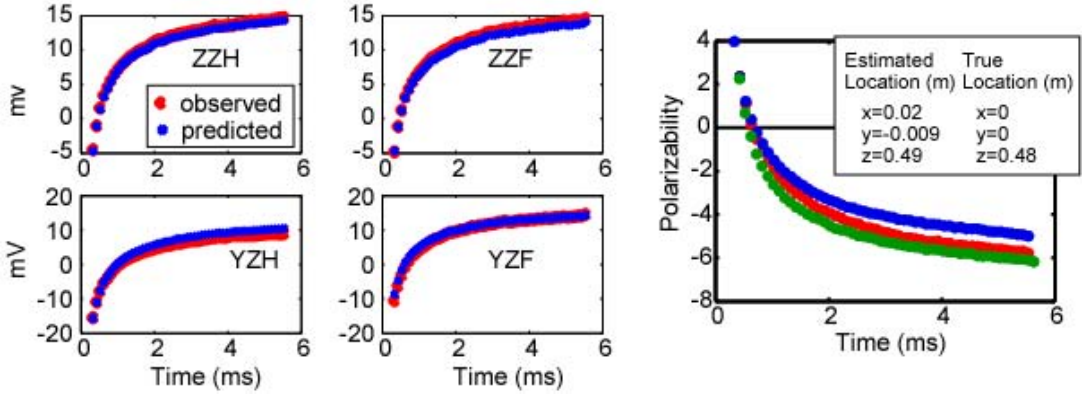

Figure 25. Inversion results for the polarizability response model applied to data from different transmitter excitation (both Y- and Z-oriented – see Figure 25) and differential receiver pairs (H_2-H_1 and F_2-F_1 – see Figure 25). Note the primary and secondary polarizabilities converge as expected for the spherical target.

In this example, we only utilized 4 transmitter and receiver pairs. Potential errors associated with calibration of the instrument may contribute to the separation between axial polarizabilities. Inversions applied to data from subsequent tests utilized all 12 combinations of transmitters and receivers and yielded more reliable polarizabilities. Figure 26 shows the polarizabilities resulting from inversions of ALLTEM calibrations data taken over a steel sphere. The estimated polarizabilities converge throughout the measurement duration and are reproducible for multiple data sets. Figure 27 shows inversion results from data collected over a 81millimeter (mm) mortar oriented at different angles.

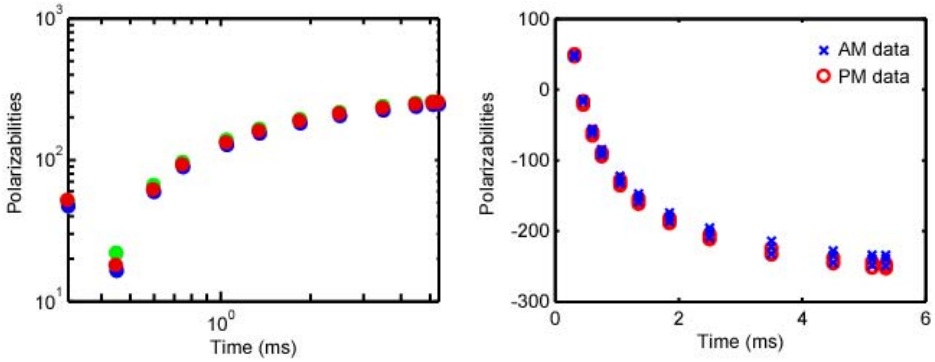

Figure 26. (Left) Comparison of the three primary polarizabilities estimated from a full waveform inversion of ALLTEM calibration data over a steel sphere. The red, blue, and green symbols represent the p_1, p_2, and p_3 axial polarizabilities, which converge to nearly the same value for the case of the axially symmetric sphere. (Right) Inverted polarizabilities over the duration of the half-waveform period from two different data collections over a steel sphere: AM and PM.

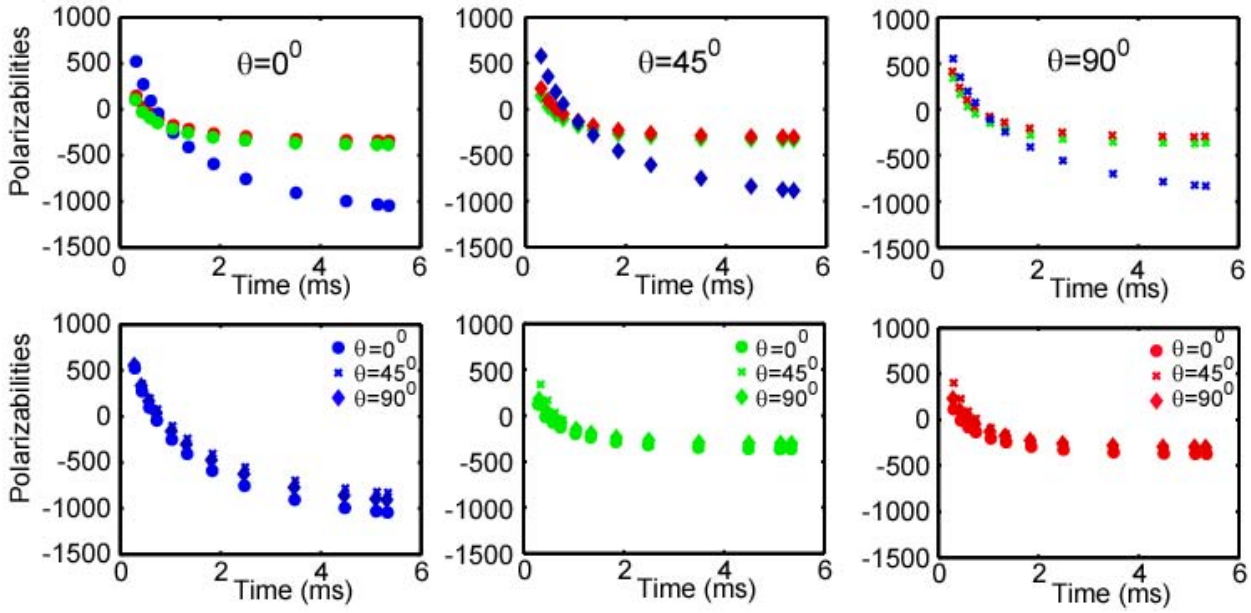

Figure 27. Inverted polarizabilities from ALLTEM data collected over a 81 mm mortar. The top panels show the estimated axial polarizabilities for different orientations of the test object. The bottom panels compares estimated polarizabilities at various orientations grouped by the same primary, secondary, and tertiary terms.

5.3. STMR On-Time Data Analysis

The STMR uses a pulse train of both short- and long-duration ramp-on waveforms with durations of 24 ms and 120 ms, respectively. These are followed by quiet, off-time periods. An array of figure-8 shaped quadrapole receivers acquire data during active transmission (the "X" channel) and during the off-time (the "G" channel). This allows for useful comparisons of the on- and off-time signals.

By comparing the on- and off-time channel response directly, we can ascertain some simple inference about nature of ferrous material present in a target. For example, Figure 28 shows the relative amplitude of the on- and off-time data channels from the STMR over various UXO targets. For predominantly non-permeable targets (e.g., small rockets and practice grenades), which are mostly composed of aluminum casings and components, the on- and off-time channels are strongly anti-correlated. In contrast, targets that have significant portions of ferrous material, such as thick projectile or mortar shell casings (e.g., 155 mm projectile and 81mm mortar) exhibit strongly correlated on- and off-time signals, as expected. The correlations are generally the strongest and most coherent when the receiver array is directly over the target. There also are likely some differences in the correlation of the signals as the distance from the target is increased. Therefore, there is likely information in the relative differences in the spatial evolution of these signals that may be useful in characterizing aspects of UXO.

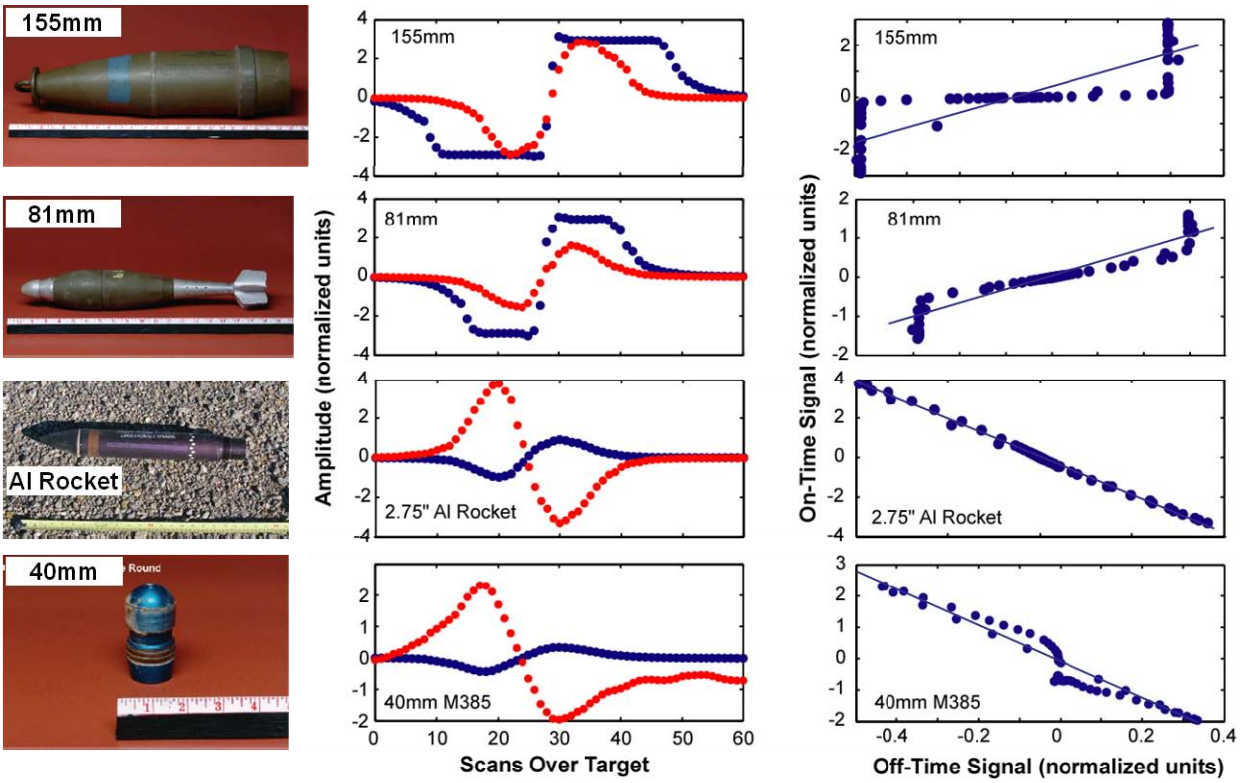

Figure 28. Spatial correlation of on- and off-time signals over various UXO targets. (Left) UXO targets with varying amounts of ferrous components. (Middle) Normalized responses from the STMR on-time (red) and off-time (blue) data channels. Note the strong correlation (Right) for targets with significant ferrous material and the anti-correlation for targets with little ferrous material (from Schultz et al., 2008).

Because the STMR acquires data across a 2m array width, it enables interpretations of the two-dimensional spatial evolution of the on-time signal. For example, Figure 29 shows the spatial response for the on- and off-time channels from STMR data collected over buried steel and aluminum cylinders. These data were collected in support of a US Army assessment of vehicle-based electromagnetic arrays (Miller et al, 2010; Marble and McMichael, 2010). Additional examples of on-time data collected over variable size calibration targets buried at different depths are shown in Appendix A. The evolution of the signal response as the STMR traverses a target appears as the spatial derivative since we are using a differential receiver coil. The off-time channels have similar responses with different amplitudes for the aluminum and steel cylinders. We expect for a significantly ferrous target such as the solid steel cylinder that the polarity of the response would completely flip between the on and off times. In this example, the spatial response is more complex and reflects the tradeoff between induction and magnetization of the object.

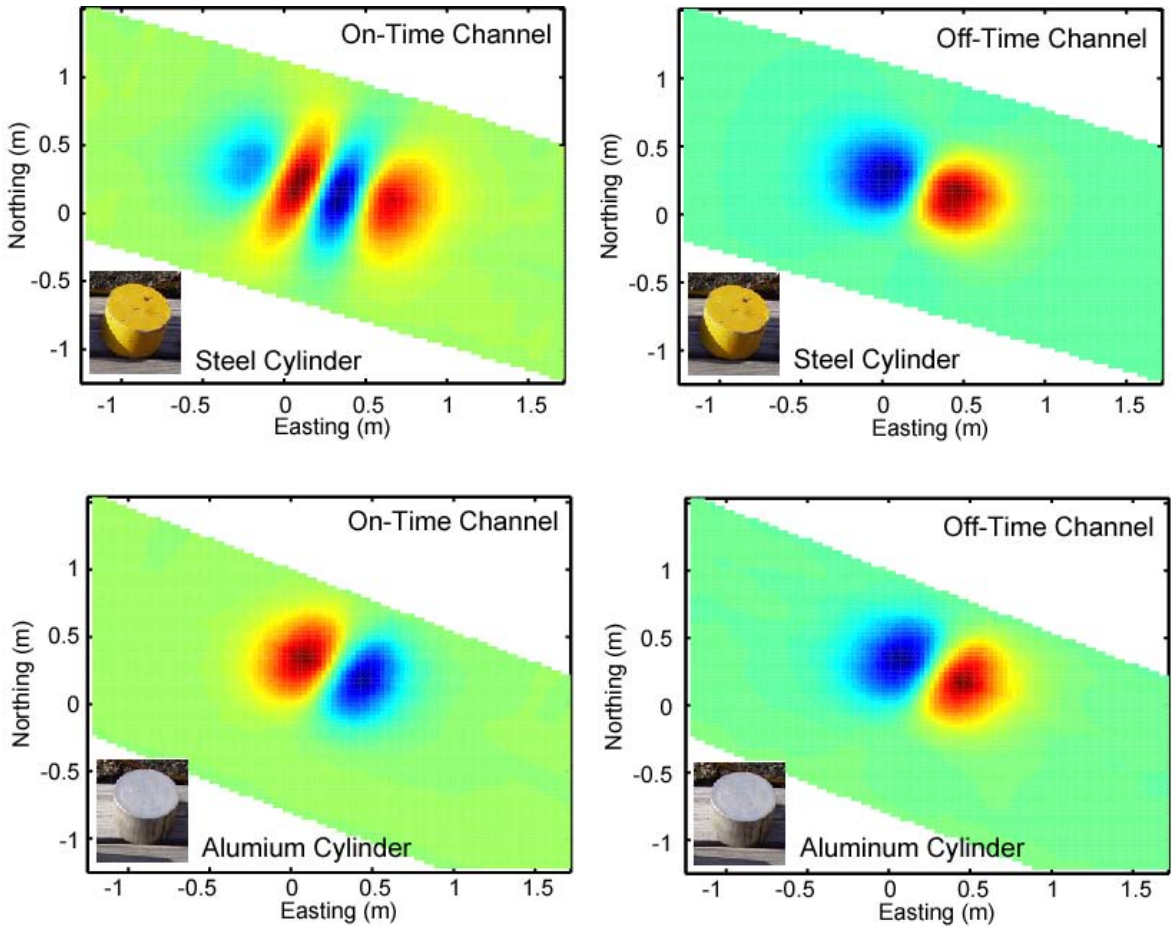

Figure 29. Two-dimensional spatial responses for integrated on-time (Left) and off-time (Right) data windows. STMR data were acquired over canonical test objects during assessments of US Army vehicle-based electromagnetic induction systems.

Full waveform inversions predict the target location and polarizability for a solid ferrous and non-ferrous axi-symmetric metallic objects such as spheres, cylinders, and disks. Specifically, Figure 30 shows an example of the full waveform model fit to field data acquired with the STMR array. It is interesting to note the complex form of the spatial response of the on-time signal (integrated time window during on-time) as the differential receiver coil traverses the ferrous target in Figure 30. Variability in the tradeoff between the target magnetization in the same direction as the primary magnetic field and eddy current decay in opposition to the primary magnetic field is exhibited in this response. This complexity reveals characteristics of the steel target DC magnetization response when the excitation field is oriented off of the target axis and then shifts to eddy current decay as the impinging field increases and becomes aligned with the target axis.

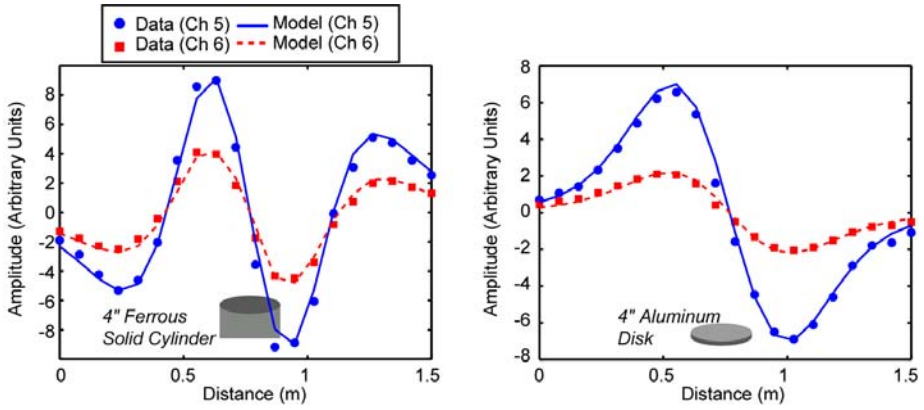

Figure 30. Field data and model representing the on-time data channel from the STMR array over a steel cylinder (Left) and Aluminum disk (Right). Data used for inversions were taken from the two middle differential receiver pairs (denoted channel 5 and 6).

To better understand the spatial evolution of the on-time signal (relative to the off-time), we performed a series of simulations using our full waveform for a spheroidal target. The objective was to gain some intuition on how the target parameters effect the correlation or anti-correlation between on- and off-time integrated time windows. Figure 31 and Figure 32 show examples of synthetic data and inverted responses. Figure 31 compares the on and off time responses over a modeled aluminum disk. Select on-time and off-time integration windows were selected and the signal response was summed over those windows to produce on-time and off-time data channels.

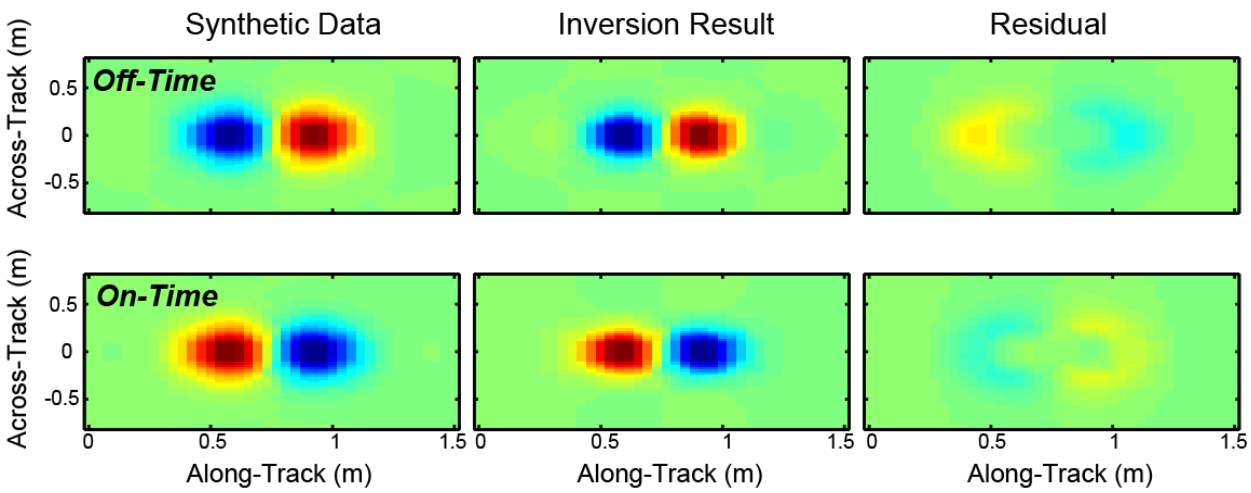

Figure 31. Inversion results generated from application of the full waveform model to synthetic data representing the modeled response for the STMR array over an aluminum disk. Random noise was added to the synthetic data.

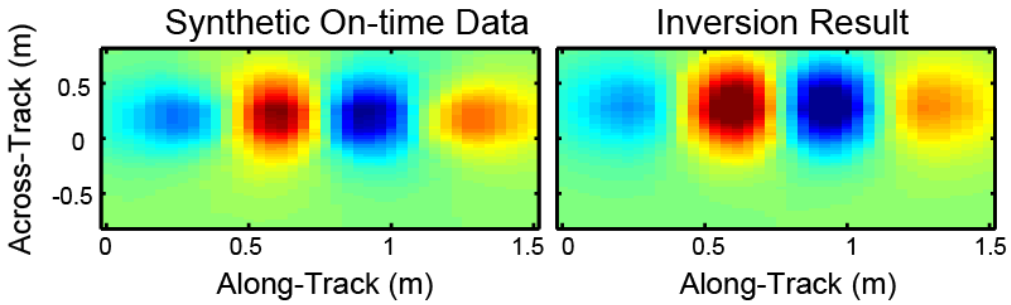

Figure 32. Inversion results generated from application of the full waveform model to synthetic data representing the modeled response for the STMR array over a metallic sphere.

We performed of simulations of the full waveform response corresponding to the STMR geometry and current waveform characteristics. Simulations were carried out for a 10 cm solid metallic sphere that ranged in conductivity from 10^5 S/m to 10^8 S/m. The ratio of the on-to-off time response was computed to determine the cross-over point correlated and anti-correlated responses. We found that for a range of conductivity values consistent with steel, the on-to-off ratios transitions between negatively correlated to positively correlated values. Further simulations with different size spheres at different standoff distances affected the conductivity of the cross-over point.

Figure 33 shows that the on-time response for the sphere in our example transitions from negative on/off-time ratios at conductivities associated with certain types of steel to positive values for slightly higher conductivities. This effect is also influenced by the object size and depth, but predicts the complex spatial pattern observed in STMR field data (as in Figures 29 and 30).

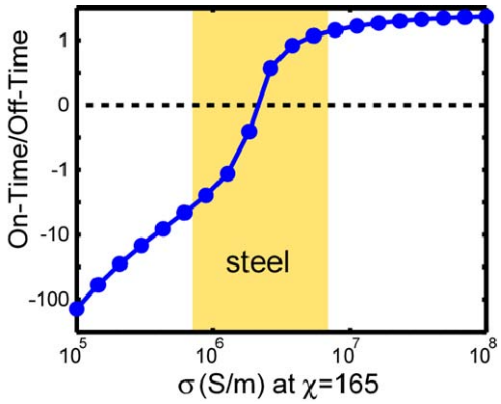

Figure 33. Inversion results generated from application of the full waveform model to synthetic data representing the modeled response for the STMR array over steel cylinder. Random noise was added to the synthetic data. The form of the on-time spatial response is dependent on the object size, depth, and material composition.

This effect is exemplified in the results of simulations shown in Figure 34. In this example, we modeled a 10 cm diameter sphere beneath the STMR array. Simulations used a conductivity of 10^5 S/m in each case, but varied the target's magnetic susceptibility. The spatial response varies as the susceptibility changes. Not only does it trend from negatively correlated with the off-time response (at low permeability or susceptibility) to positively correlated, but as also shown in Figure 32, the spatial response becomes complex at intermediate susceptibilities. Although we may generally think of a steel sphere as a magnetically permeable object, in the context of the tradeoff between induction and magnetization associated with the polarity of the on/off-time ratio, steel spheres appear to be in the transition between the two.

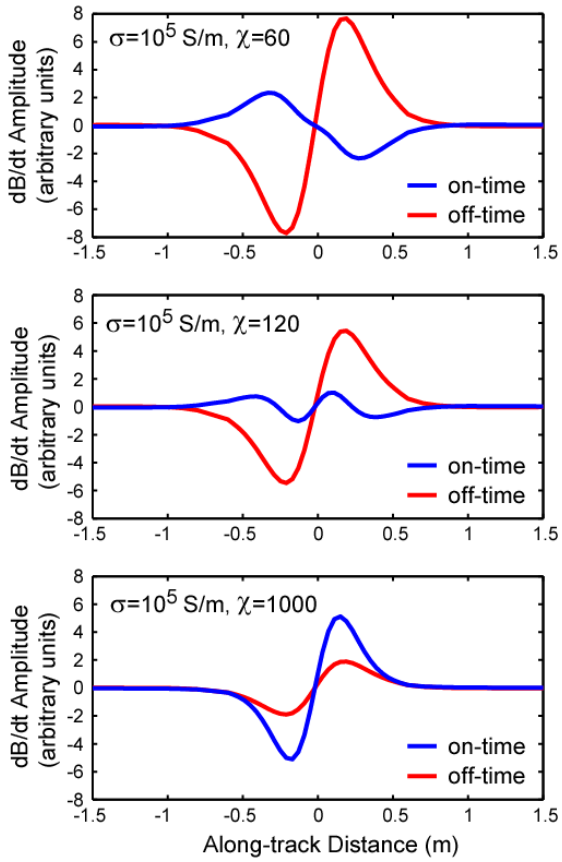

Figure 34. Full waveform model simulation results for a 10 cm diameter sphere located 50 cm below the STMR transmitter. These model results expemplify the variability in the form of the on-time response with changeing magnetic susceptibility of the sphere. For conductivity and permeability values representative of steel, the spatial form of the response is somewhat complex relative to the correlated or anticorrelated differetial response resulting from higher or lower permeabilities.

6. SENSOR DESIGN CONCEPTS

The purpose of this study was to provide an experimental basis for comparison and validation of the full waveform models and to assess the practical limitations of the most promising on-time measurement configurations.

6.1. Laboratory Experiments

We performed a series of measurements to sample full waveform (both on- and off-time periods) responses from various targets. Targets included well-characterized coils of wire of varying gauge, number of turns, coil diameter, and associated inductance, resistance, and capacitance. The inductance (L), resistance (R), and capacitance (C) were measured using an LRC-meter. Analytical and empirical methods of estimating L, R, and C values match the measured coil parameters providing well-characterized standard targets. Examples of the coils used for these experiments are shown in Figure 35.

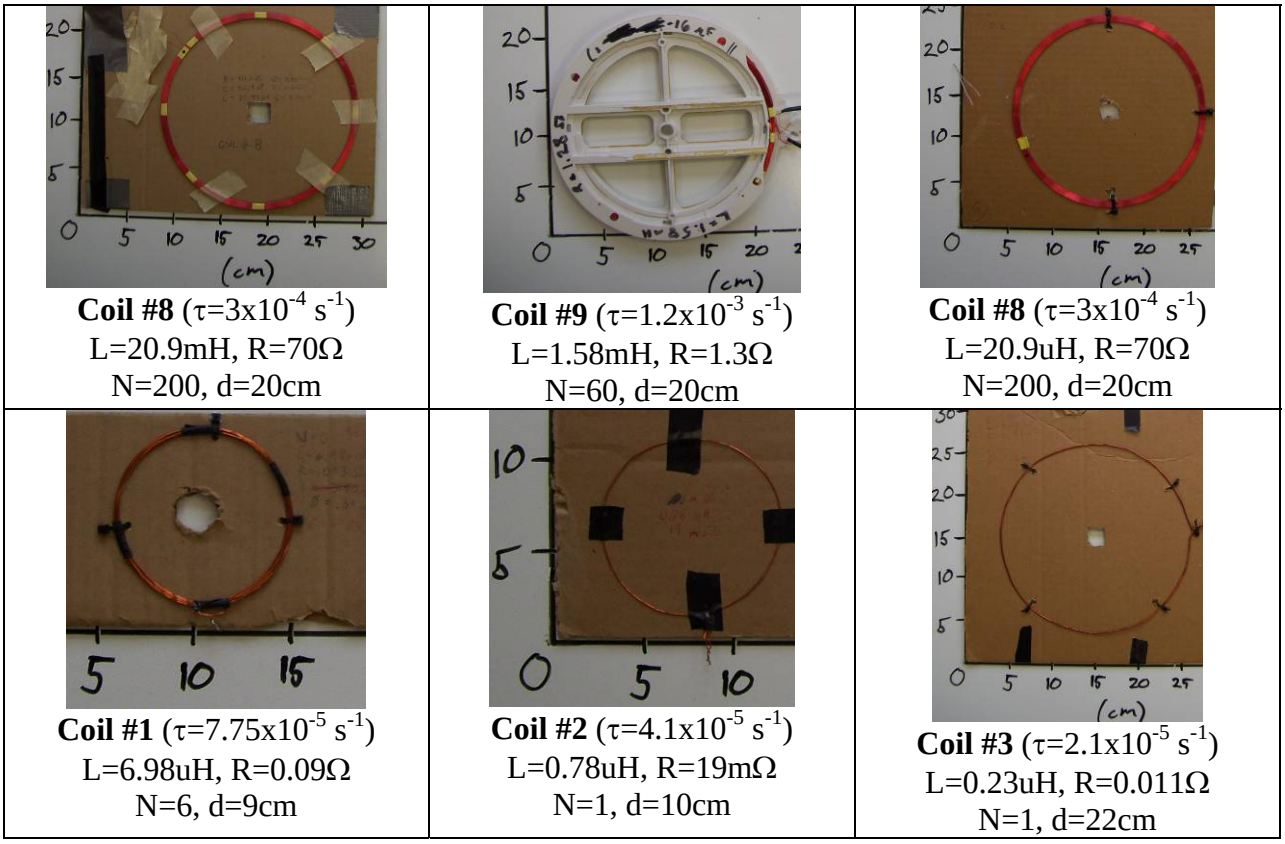

Coil #8 (τ=3x10^{-4} s^{-1})
L=20.9mH, R=70Ω
N=200, d=20cm

Coil #9 (τ=1.2x10^{-3} s^{-1})
L=1.58mH, R=1.3Ω
N=60, d=20cm

Coil #8 (τ=3x10^{-4} s^{-1})
L=20.9uH, R=70Ω
N=200, d=20cm

Coil #1 (τ=7.75x10^{-5} s^{-1})
L=6.98uH, R=0.09Ω
N=6, d=9cm

Coil #2 (τ=4.1x10^{-5} s^{-1})
L=0.78uH, R=19mΩ
N=1, d=10cm

Coil #3 (τ=2.1x10^{-5} s^{-1})
L=0.23uH, R=0.011Ω
N=1, d=22cm

Figure 35. Examples of the coils used experiments to measure full waveform (both on- and off-time periods) - responses from various targets

Additional targets used in these experiments consisted of solid steel, aluminum, and copper disks, rods, and cylinders. Examples of these standard axi-symmetric targets and inert UXO items used as targets are shown in Figure 36.

Figure 36. Solid steel, aluminum, and copper disks, rods, and cylinders used as targets (left), and other targets comprise a subset of inert UXO test items such as 37mm, 60 mm, and 81mm projectiles.

The majority of the data collections were conducted outside in a controlled environment and away from any known or significant noise sources. The basic set-up is shown in Figure 37. We utilized a number of different transmitters with varying on-time waveforms combined with different receivers. Overall geometry was dependent on the transmitter-receiver configuration and type of primary field nulling used. Further details of the data collection geometries and instruments used are given in the Sections that follow.

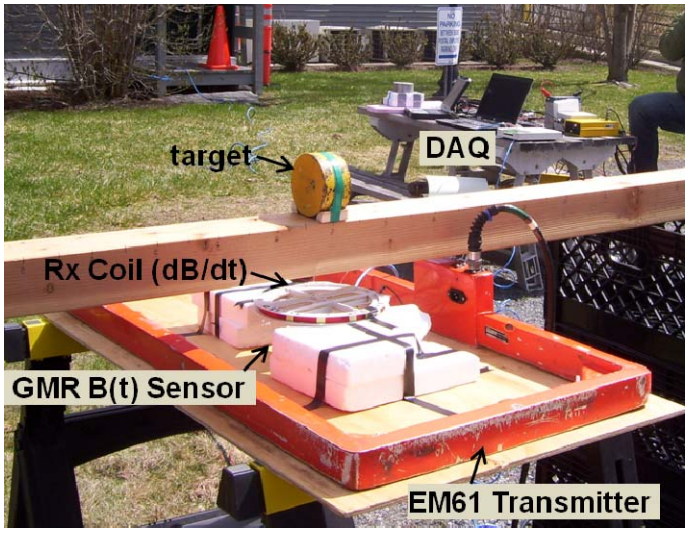

Figure 37. Basic set-up for controlled data collection of on-time data using existing instrumentation. Various transmitters and receivers were used to represent existing and potential on-time EMI measurement geometries. In this experiments exemplified in this photo we used an EM-61 MkII transmitter and sampled both a small induction coil receiver and a GMR B-field sensor using a National Instruments data acquisition system.

6.1.1. B and dB/dt Measurement Methods

Our experimental setup included sensors that measure the B-field (wideband magnetic sensors) and those that sense the time rate of change of the magnetic field, or dB/dt, sensors (induction coils). For sensing dB/dt, coils of wire are used as the sensing elements to provide simple, low power, high-sensitivity at frequencies above a few hundred Hz. At lower frequencies, their sensitivity is reduced. Asten and Duncan (2007) list a number of potential benefits of B-field measurements including a higher sensitivity to large deep items compared to small shallow items. Our objective was not to rigorously determine the tradeoffs between B and dB/dt measurements during the on-time, but to provide example responses for both modalities.

B-field measurements were made with commercially-available giant magnetoresistive (GMR) magnetic field sensors. Magnetoresistive sensors use changes in resistance caused by an external magnetic field expressed as the percentage change in resistance per unit field or in voltage change out per volts in Oersteds. Magnetoresistance magnetometers are very attractive for low cost applications because they are simply energized by applying a constant current and the output voltage is a measure of the magnetic field. GMR sensors use layered metals consisting of thin ferromagnets that sandwich a thin conductor and an anti-ferromagnet to form a resistive bridge (specifically known as a spin valve). The technique relies on the ability of electrons to travel more easily either parallel to or perpendicular to the layers if the magnetizations of the two ferromagnets are parallel to each other. When the magnetizations are parallel, electrons undergo less scattering when going from an electronic band structure state in one of the ferromagnets into a similar state in the other ferromagnet.

We used the AA series analog GMR sensors from Non-volatile Electronics (NVE). The GMR sensor was combined with a small magnet to bias the measurement floor in order to overcome the Earth's field. Both the dB/dt coils and B-field GMR sensors were simultaneously logged with a National Instruments multi-channel data acquisition system with 16 bit resolution at sample rates up to 1.25 MHz. In general, raw data are displayed, although in some cases a simple low-pass filter has been applied to remove high frequency noise.

6.1.2. MPV Data

The Man-Portable Vector (MPV) instrument was used to collect data during both the transmitter on-time and after its rapid shut-off. This instrument was developed under SERDP MM-1443 project and is currently undergoing further enhancements. The MPV represents the next-generation of handheld UXO sensors and is unique in its ability to acquire multi-static and multi-component measurements over a programmable range of time channels. Details of the MPV instrument can be found in previous SERDP reports and literature (e.g., Barrowes et al, 2009).

During our experiments, MPV data was collected at Sky Research test facilities in Hanover, NH and in Vancouver, BC. The instrument was positioned off the ground on non-metallic stands in a benign area (minimum noise). A photograph of the basic test set-up is shown in Figure 38.

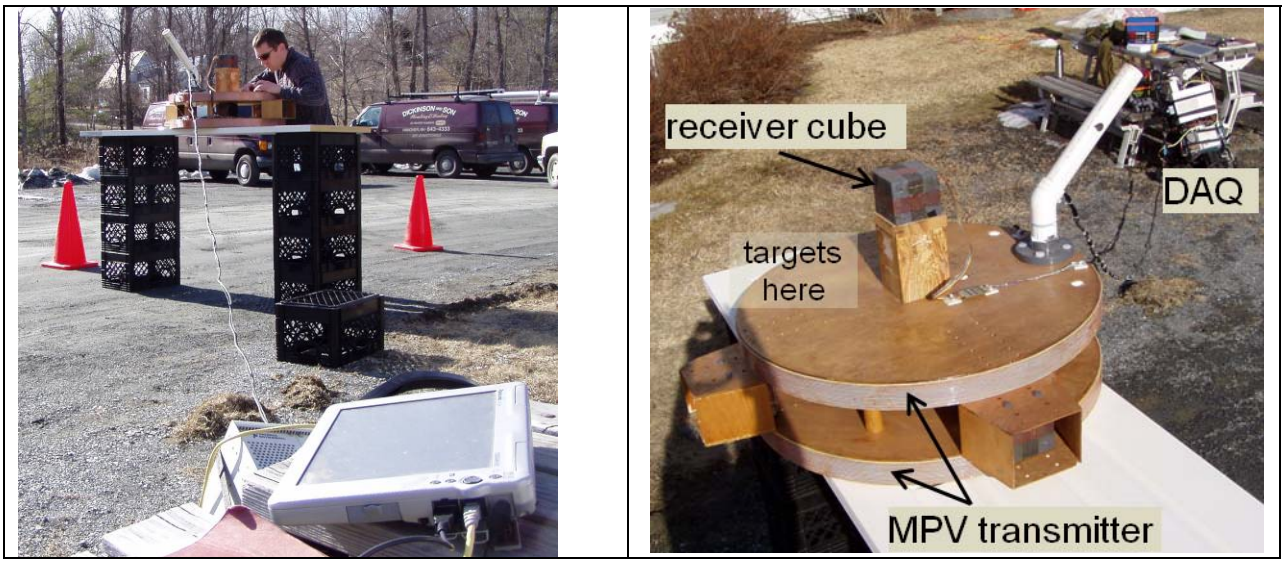

Figure 38. MPV data collection setup.

The primary field of the transmitter was reduced significantly (effectively nulled) by placing axi-symmetric targets in the approximate line of the maximum horizontal magnetic flux and acquiring measurements along the corresponding horizontal component receiver. A standard calibration procedure was also followed to correct for instrument drift and further cancellation of the primary field. The calibration background measurements were acquired often throughout our experiments. The transmitter generates an exponential on current with ramp on constant τ_a of ~5.5×10^{-4} s^{-1}. The ramp on time of the waveform reflects the charging circuit resistance and capacitance $\tau_a = RC$. For our data collection we utilized a 25 ms current on-time.

The first set of targets investigated consisted of coil loops of copper wire for which the L, R, and C parameters have been measured (Coils 1, 3, 8, and 9 - see Figure 29 above). The raw data as logged by the MPV are shown in Figure 39 (left side) over both the on- and off-time durations. The off-time behavior is as expected and reported elsewhere - the larger time constant loops exhibit longer decay, with generally predictable forms. The on-time signals yield the inductive response of the loops while the transmitter is ramping up current. Because the induced voltage in the receiver is proportional to emf in the coil, the on-time signals tend to reflect the time-derivative of the scattered field, which has a form that reflects the time-derivative of the current waveform.

Application of the analytical convolution model compares favorably with the measured MPV waveforms (Figure 39, right side). The current waveform was represented by an exponential ramp on with time constant of 5.5×10^{-4} s^{-1}. Both the on-time and off-time responses from the coil with the smallest time constant ($\tau = 7.8 \times 10^{-5}$ s^{-1}) were not predicted with same level of accuracy as the other coils.

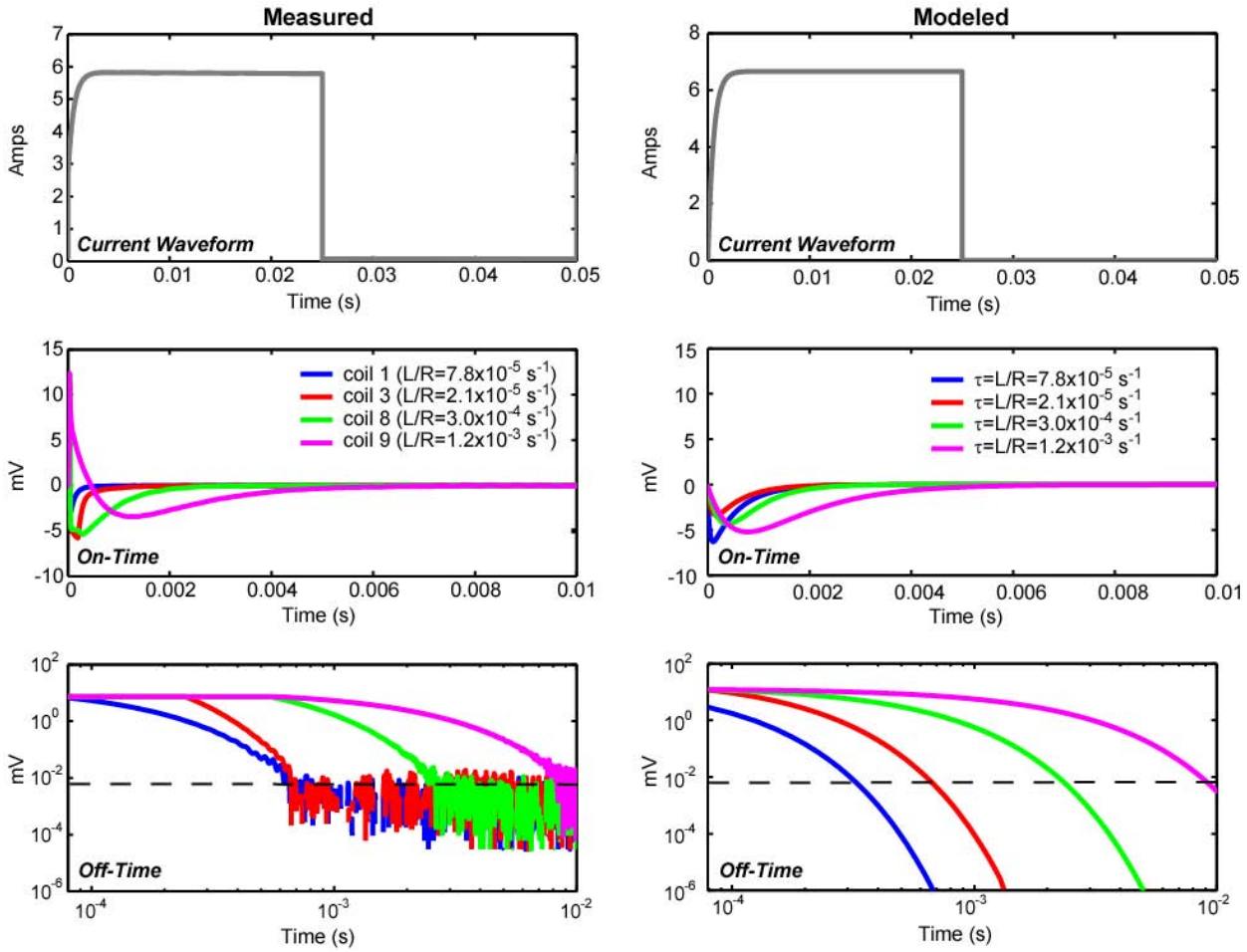

Figure 39. Measured (left) and modeled (right) on- and off-time responses from standard copper coil targets with varying time constants. The coil parameters are described in detail in Figure 30. In general, the convolution of a simulated exponential ramp on current waveform with a single time constant exponential decay impulse response predicts the on-time behavior.

Further MPV data were collected with solid aluminum and steel discs and cylinders. Targets were again placed where the z-component of the primary magnetic field was minimized. This provided an approximate primary field nulling in order to capture on-time responses. The corresponding on- and off-time responses are shown in Figure 40. The on-time responses for the solid cylinders (Figure 40-left-center) reveal opposing polarities as expected for targets dominated by inductive or magnetostatic effects. Similarly, but less obvious, the solid aluminum and steel discs (Figure 40-right-center) also exhibit opposing polarity during the on-time. This implies that the magnetic properties of the steel objects influence their on-time response. The disc-shaped objects have a decreased on-time response amplitude, further implying that volume magnetization is contributing significantly to the response.

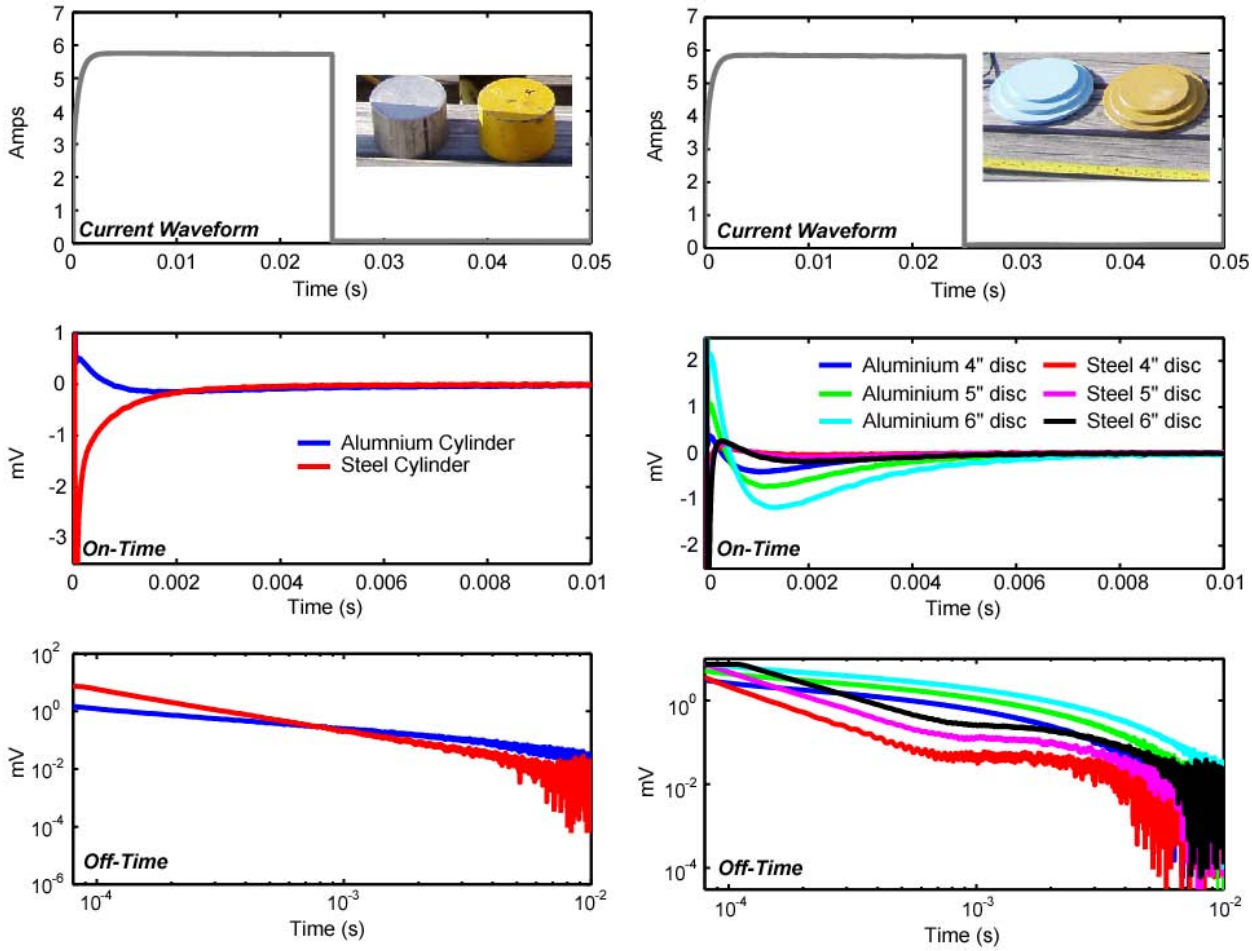

Figure 40. Measured current waveform (top panels), on-time responses (middle panels), and off-time responses (bottom panels) from solid axi-symmetric steel and aluminum objects. Comparisons between steel and aluminum cylinders (right) and thin discs (left) reveal the influence of volume magnetization on the on-time response.

In addition to the data acquired with cylindrical and disc-shaped objects, we also tested the MPV on-time response to varying orientation of a small steel rod (Figure 41- left). As expected, the steel rod generated the largest response along the axis of the strongest coupling with the primary field. Although, the object was positioned to remove the direct influence of the z-component (vertical) of the primary field, a z-oriented on-time response is still noticeable.

Experiments were also conducted with the MPV over the ground near the Sky Research test facilities in Hanover, New Hampshire. Although the soils are relatively benign with respect to mineralization or soil conductivity, a measureable response was observed by varying the height of the MPV over the ground. The on-time responses are shown in Figure 41 (right). The MPV was positioned on the ground and at increasing heights while recording its response during both on- and off-time durations. The strongest signal is observed when the sensor is located effectively on the ground and the signal decreases rapidly with standoff. We attempted to minimize the primary field by subtracting the response from the sensor elevated 1.10 meters (m) above the ground, forming an effective a simple, free-space calibration. Although the decay

times are very short over the ground, the plot of the off-time response does not reveal a decay even at early times.

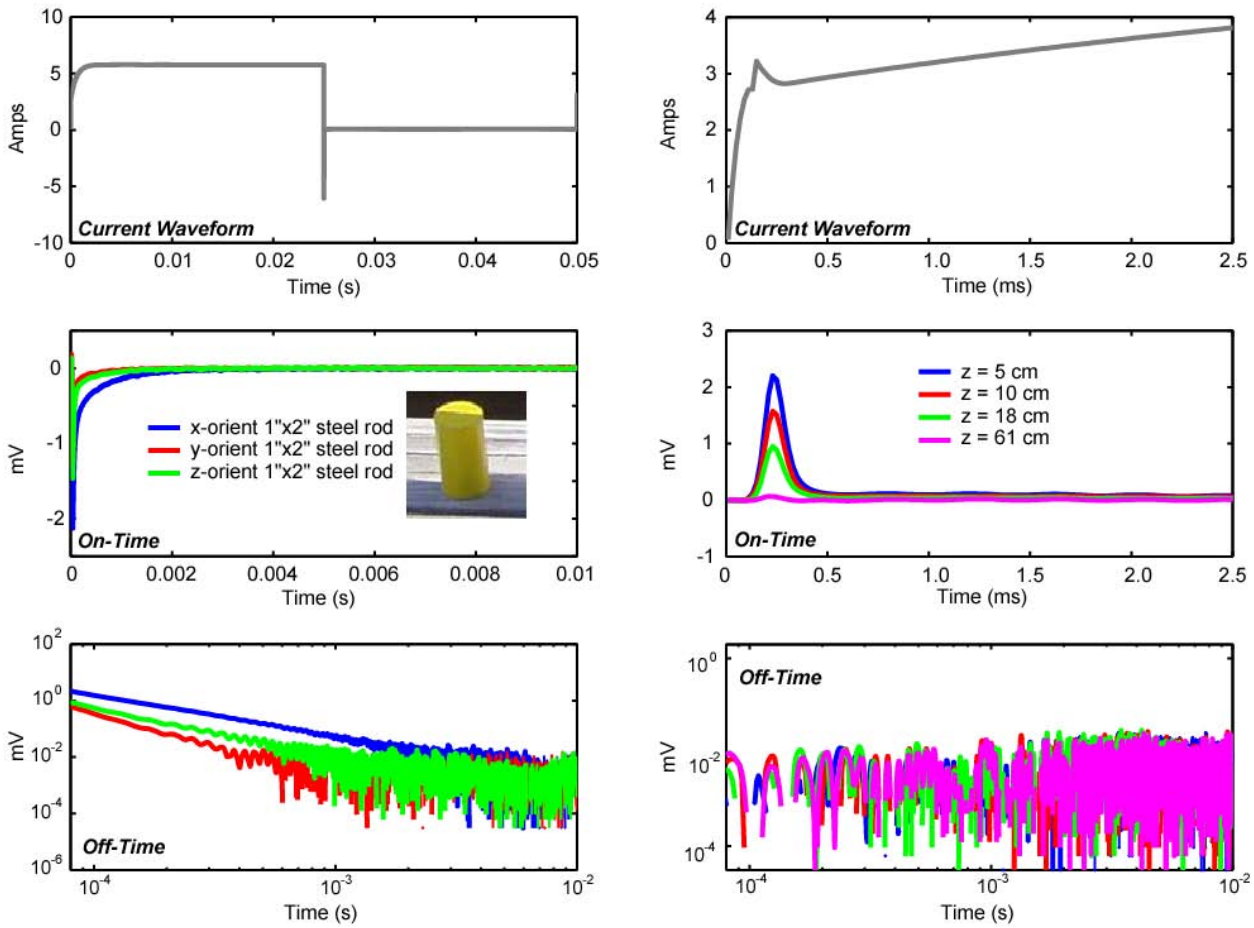

Figure 41. Measured current waveform (top panels), on-time responses (middle panels), and off-time responses (bottom panels) from a small solid steel rod (left) and over compacted soil (right). Slight differences between orientations of the steel rod are observable in both the on- and off-time responses. The maximum response is oriented along the primary coupling x-axis. Variable standoff from the soil generates a systematic on-time response, but is not noticeable in the off-time response. The time axis plotted for current waveform and on-time response correspond to the very short decay of the ground. Although, the current waveform has an anomalous current spike at ~200us, the soil response appears to react to only the driving emf and not the current spike.

A series of MPV on-time data were collected to assess the potential to discern solid metal cylinders from hollow ones. The experimental set-up is shown in Figure 42. The data are shown in Figure 43. Vertically oriented targets had a slightly stronger response. A small difference is observed between solid and hollow cylinders for both horizontally- and vertically-oriented targets.

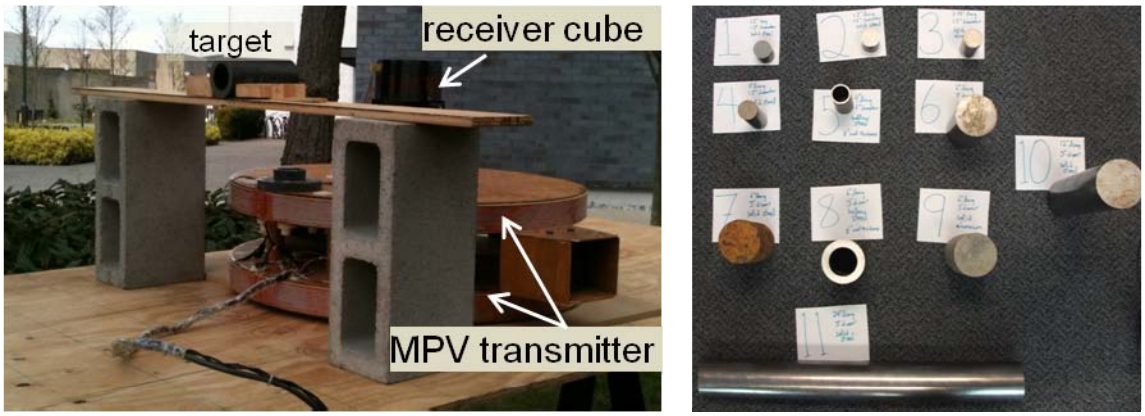

Figure 42. MPV data collection set-up for comparison of hollow and solid metal cylinders (left). Photograph of the targets used (right).

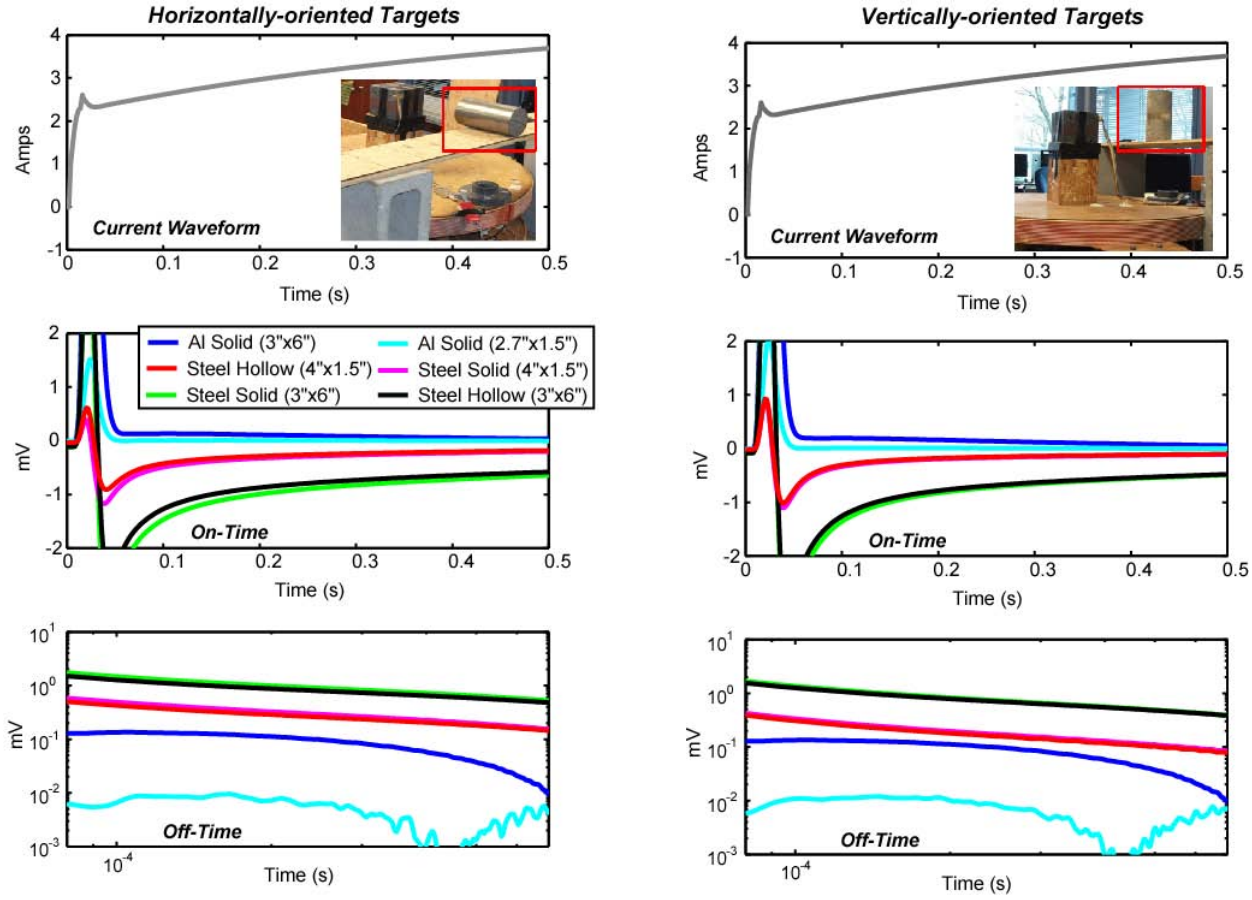

Figure 43 MPV data collection set-up for comparison of hollow and solid metal cylinders (left). Photograph of the targets used (right).

6.1.3. EM-61 Data

Controlled on-time data collection was also conducted using the Geonics EM-61 MkII transmitter. Like the MPV instrument, the EM-61 is a pulsed induction time-domain electromagnetic sensor utilizing and exponential current ramp-on waveform. The EM-61 MkII represents one of the most common commercial EM instruments used for UXO remediation. Therefore, it is of interest to assess how its current waveform and other features might be used to acquire on-time data.

The EM-61 current waveform has a duration of about 3.1 ms and a exponential ramp on constant τ_a of ~6.2×10^{-4} s^{-1}. The transmitter pulse repetition frequency is 75 Hz and peak power output is about 50 Watts with 25 Watts being the average power. Our initial set-up utilized a small 20 cm diameter winding of 200 turns of 22 gauge copper wire as a receiver. In addition, we also collected data with a GMR B-field sensor. No attempt was made to cancel the primary field. The basic experimental set-up is shown in Figure 44.

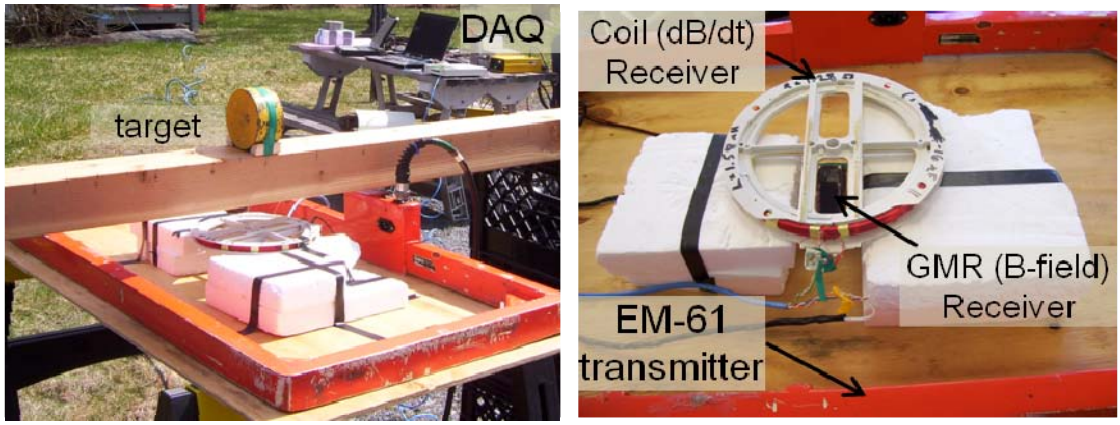

Figure 44. EM-61 data collection set-up with induction coil and GMR B-field sensor receivers.

Figure 45 and Figure 46 show the GMR (B-field) on-time response to the EM-61 transmitter excitation. Without any nulling of the primary field there is a distinguishable change in the signal when a metal cylinder is placed close to the receivers. The aluminum target appears to respond strongly to the transient emf during both the ramp-on and ramp-off periods relative to the background calibration data.

On-time data were also acquired with a differential receiver array allowing for cancelation of the primary field. A small frequency-domain array system containing 3 quadrapole receivers was used. The receiver pairs are wound in opposing directions and were centered inside the EM-61 transmitter. The experimental set up is shown in Figure 46 (right).

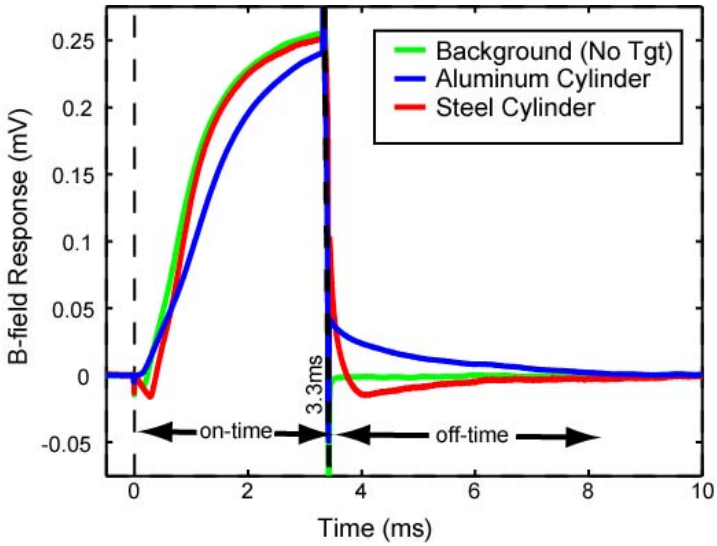

Figure 45 B-field response during excitation of the EM-61 transmitter. The total field is represented since no attempt was made to cancel the primary field. Despite the presence of the primary field, a relatively strong anomaly is observable during the on-time.

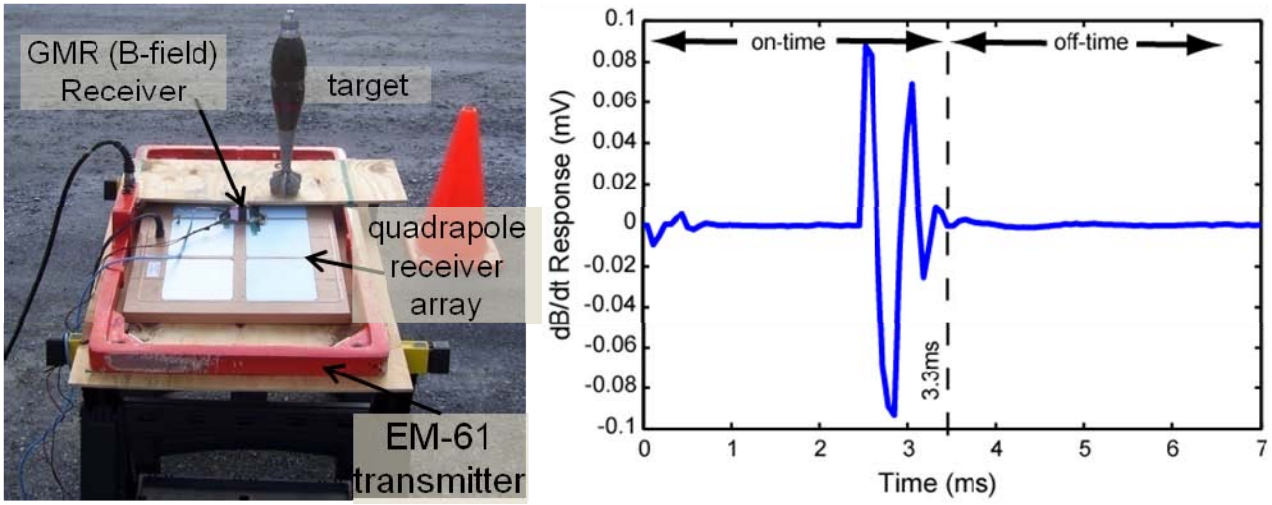

Figure 46. (left) Data collection configuration for EM-61 transmitter with quadrapole differential receiver array and GMR sensor. The quadrapole array was carefully positioned in the center of the EM-61 loop so as to effectively null the primary field from the transmitter. (right) The background signal from the center quadrapole receiver channel. The primary field during the on-time (between 0.6 and 2.4 ms) duration is nulled due to the geometry of the horizontal differential receivers.

As shown in Figure 46 (right), the primary field is effectively removed (nulled to zero) during the on-time period between 0.6 and 2.4 ms. The strong transients during ramp-on and ramp-off of the current waveform produce some residual signal. This background residual primary signal is subtracted from the receiver data when targets are present.

As shown previously, Figure 47 shows the opposing B and dB/dt signal polarity during the on-time for ferrous (steel) and non-ferrous (aluminum) objects. The offset in the B-field data before

and after the on-time period is likely due to the influence of Earth's magnetic field on ferrous target. This magnetostatic (DC) excitation is similar to what is measured with a magnetometer. During the on-time, the influence of the Earth's field is superposed with the magnetostatic excitation in response to the primary magnetic field from the transmitter.

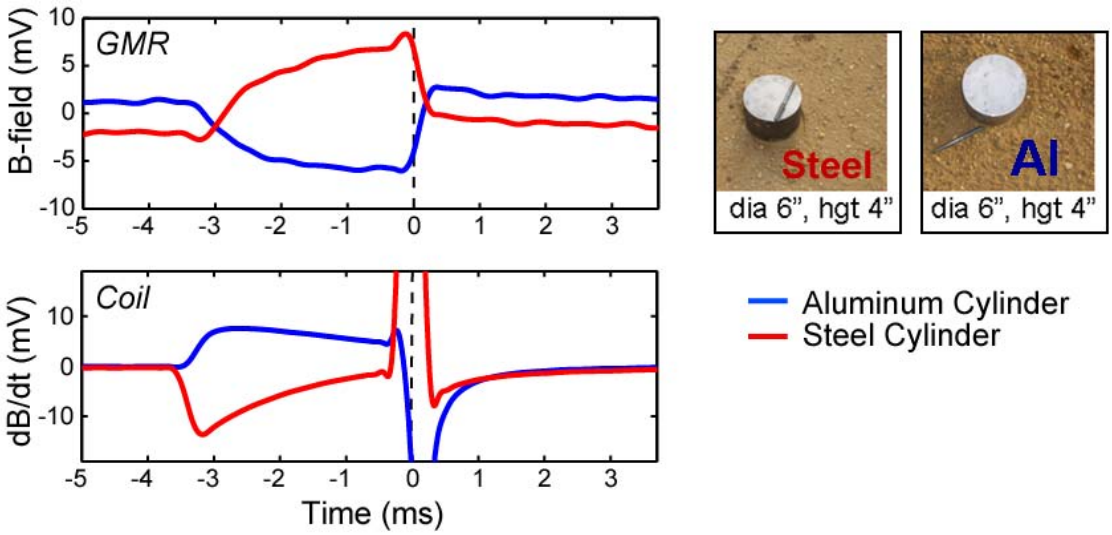

Figure 47. Responses to the EM-61 exponential ramp-on energizing waveform in the presence of ferrous (steel) and non-ferrous (aluminum) cylinders.

We repeated this measurement procedure while moving standard axi-symmetric objects and inert UXO objects over the sensor array. By sampling the B and dB/dt responses at particular times through both the on- and off-time periods we form effective target response transects. These are shown in Figure 48 (A and B) for a 37mm and 81mm UXO. Both targets display opposing on- and off-time signals. The 37mm is composed primarily of steel and thus exhibits a strong ferrous response. The 81mm is considered more of a composite object with a ferrous head and non-ferrous tail, although its signal appears to be dominated by the ferrous components in that the on- and off-time signals are strongly anti-correlated. Compiling the results for various types of UXO and a steel cylinder and copper disc, Figure 48C shows the absolute signal amplitude sampled at one position and one time for both the on- and off-time signals. The amplitudes are nearly the same for the copper disk, as a consequence of the on and off times sampled.

Traverses over the aluminum and steel cylinders are represented in Figure 49. Here we compare the on- and off--time amplitudes to the show the strong correlation of signals for the non-ferrous (aluminum) cylinder and anti-correlation for the ferrous (steel) cylinder. The differential configuration of the receiver coils yields zero signal when the target is directly under the centerpoint of the receiver pair.

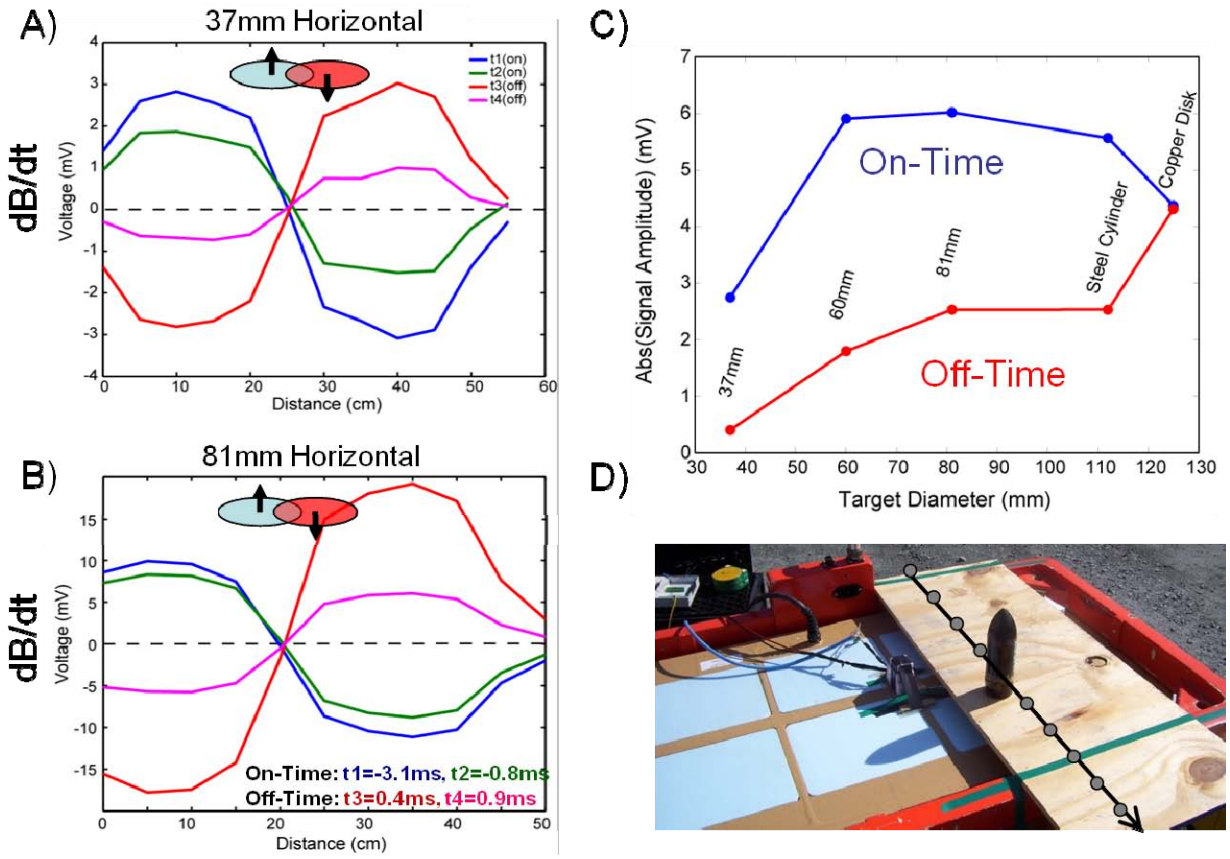

Figure 48. A) Voltage (dB/dt response) measured from the quadrapole induction coil receiver array as a 37mm projectile was placed at different positions across the EM-61 transmitter. The spatial response of the on-time data channels (blue and green) is opposing that of the off-time data channels (red and magenta). On- and off-time data channels were selected at times (t_1[on-time]=-3.1ms, t_2[on-time]=-0.8ms, t_3[off-time]=0.4ms, t_4[off-time]=0.9ms) during the respective periods such that the responses were approximately equivalent. B) Voltage (dB/dt response) from an 81mm mortar. C) Comparison of the on-time (t[on]=-3.1ms) and off-time (t[off]=0.9ms) for various types of targets. The absolute signal amplitude was retrieved from data collected while targets were placed at 15cma long the transect. D) Photograph of the data collection lay out with a 37mm target oriented vertically along the transect. The blue foam occupies the gaps in the centers of the quadrapole differential loops.

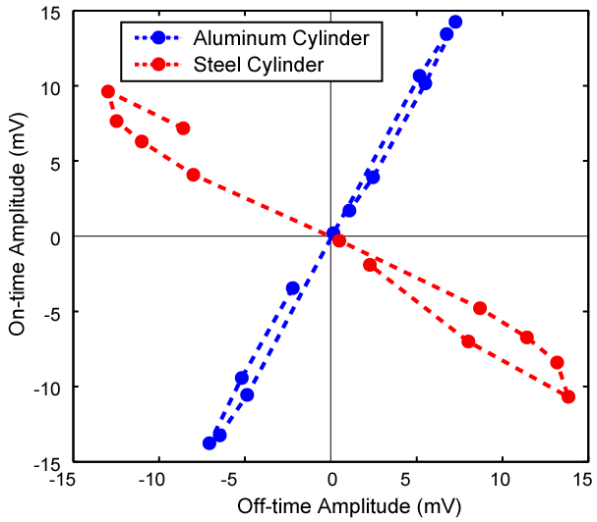

Figure 49. Comparison of the on-time and off-time signal amplitudes across a limited portion of the array. The signal amplitudes go from positive to negative across the differential receivers, with the null (essentially zero amplitude for both on- and off-time amplitudes) when the target is directly over the centerpoint between the two coils in the pair.

6.1.4. STMR Data

In order to test the veracity of full waveform models using the equivalent circuit and linear systems approaches, we performed a series of measurements with simple targets. We utilized the large moment transmitter from the Minelab STMR array along with wide-band GMR sensors to measure the magnetic field response from well-characterized coil targets. The current waveform consists of both long- (t=120us) and short-duration (t=24us) current ramps of opposite polarity. Centering the GMR magnetic field sensor in the array, we measured the response to a set of well-characterized (in terms of area, number of turns, inductance, resistance, and capacitance) shorted coil windings. The experimental set-up is shown in Figure 50A.

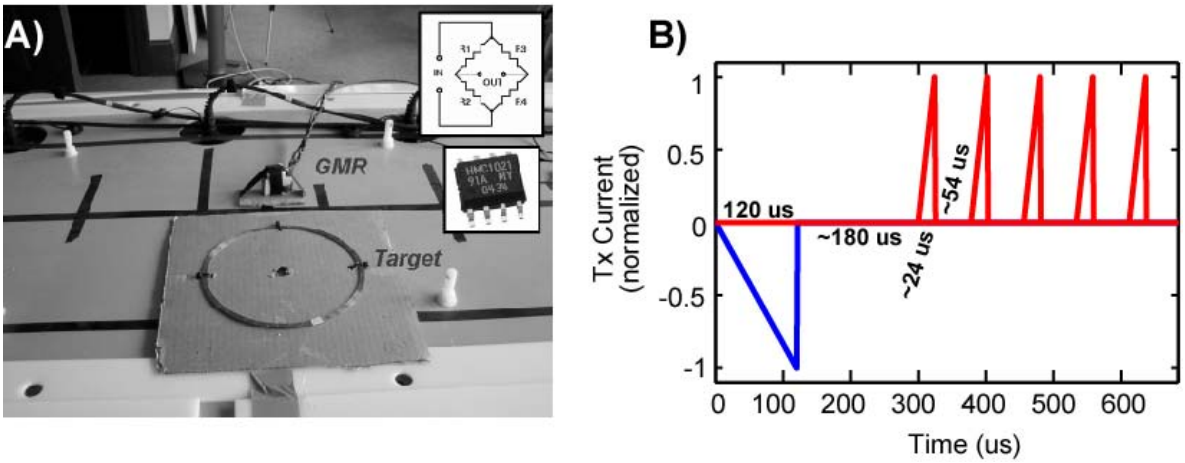

Figure 50 A) Photograph of the experimental set-up for *B* and *dB/dt* on-time laboratory measurements. B) STMR transmitter current function consisting of both long- and short-duration linear ramp waveforms.

Using the full waveform analytical model derived from equivalent circuits, we predict the response to coil targets with various time constants $\tau=L/R$. Even though the ramp-off period is

affected by a parasitic transient response from the GMR circuit, we are able to predict the full waveform response for all portions of the excitation period (Figure 51). The baseline difference of ~35μV is attributed to bias in the GMR circuit.

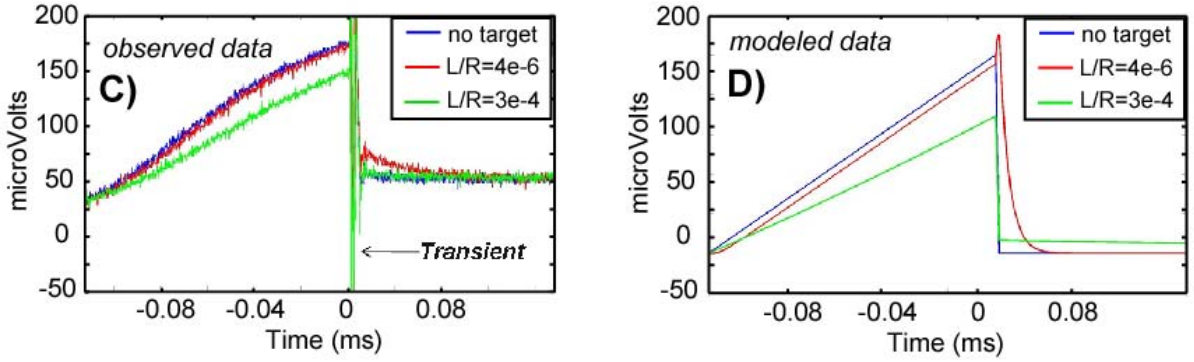

Figure 51. A) Measurements from a GMR magnetic field sensor at the center of the STMR transmitter with shorted coil windings emplaced nearby as test targets. Nonlinear bias and measurement noise in the form of a strong transient signal mask the decay during the off-time, but variations during the on-time are clearly observed. B) Results of simple circuit theory model for the full waveform response show agreement with observed data.

Data also were collected by sampling the STMR quadrapole coil receivers directly using a National Instruments data acquisition system sampling at 1.25 MHz. The horizontal gradient receiver pairs tend to null much of the primary field excitation. Figure 52 shows the response from coil windings to the shorter duration (24 μs) linear current ramp on and shut-off. The coils were placed approximately 20 cm horizontally and 15 cm vertically from the center of the receiver pairs. When the coils are positioned in vertical orientation only the background transient signal is observed. Figure 53 shows a comparison between STMR data and full waveform equivalent circuit model. Figure 54 and Figure 55 show full waveform responses for steel and aluminum cylinders, and a test grenade and 60mm projectile, respectively.

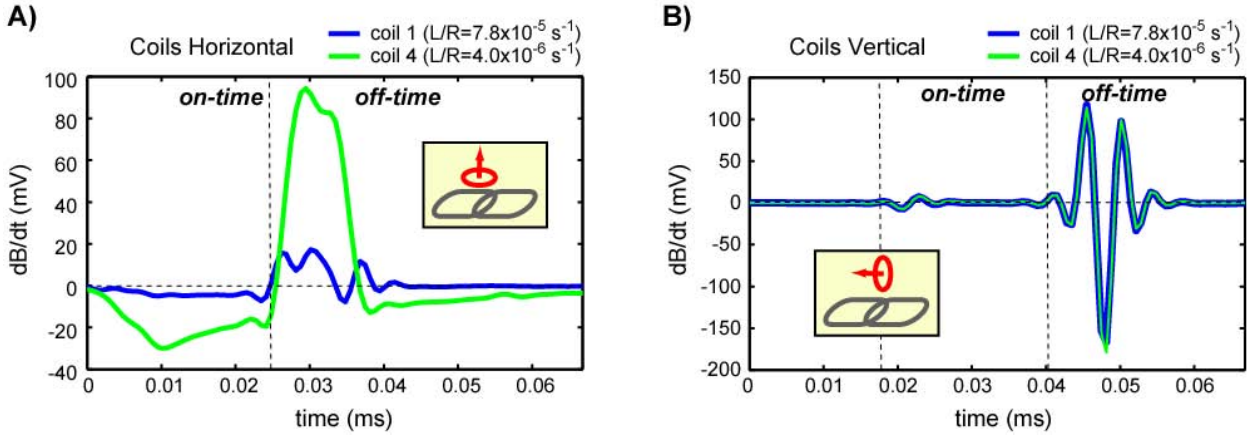

Figure 52 Full waveform STMR data collected with a National Instruments data acquisition system by sampling the differential quadrapole coils. A) Response from Coil 1 and Coil 4 oriented horizontally with corresponding characteristic time decays of 7.8×10^{-5} s^{-1} and 4.0×10^{-6} s^{-1}. B) Responses from Coil 1 and Coil 4 oriented vertically (horizontal dipole). Due to the position and geometry of the coil near the receivers there is essentially no response.

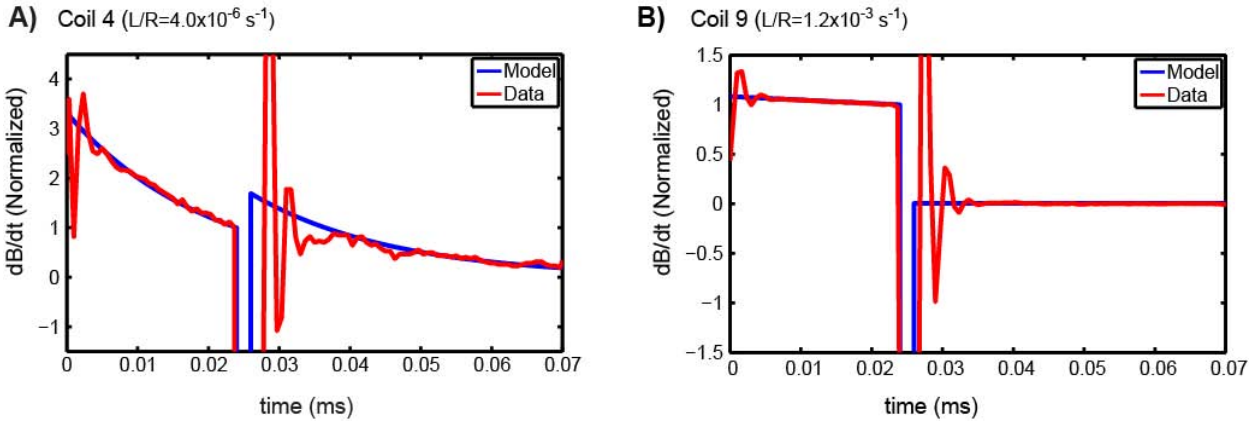

Figure 53. Comparison between STMR data and full waveform equivalent circuit model. A) Data and model fit for Coil 4. B) Data and model fit for coil 9.

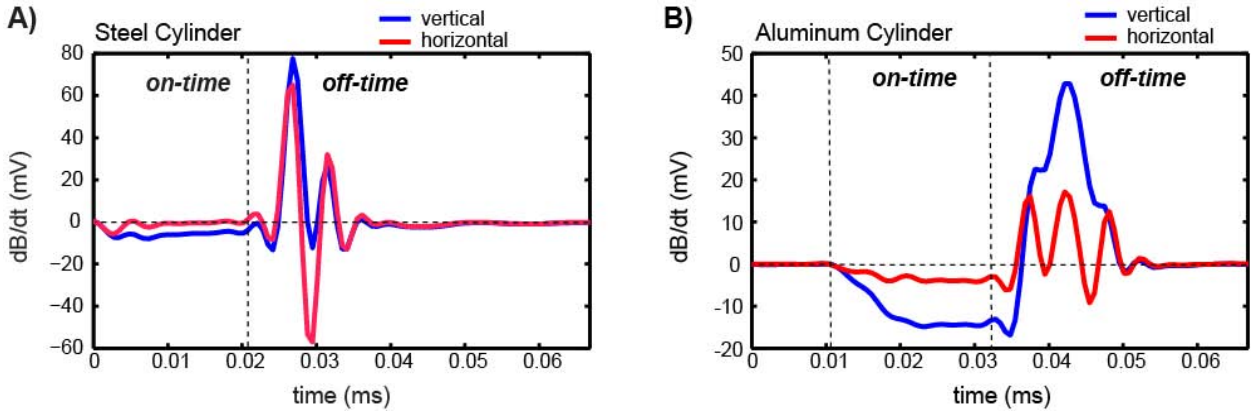

Figure 54. Full waveform responses for A) steel cylinder and B) aluminum cylinder. Although the off-time signal is difficult to interpret, the on-time signals are evident for both targets.

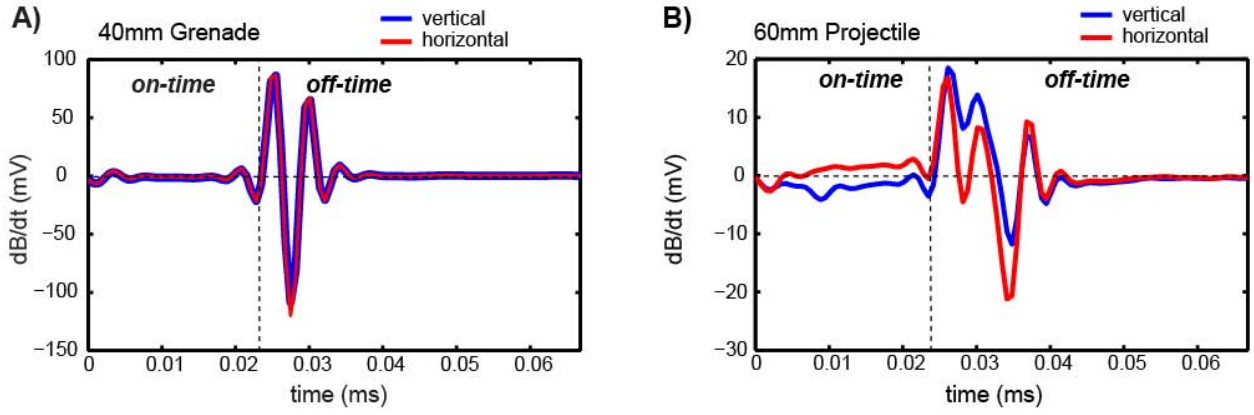

Figure 55. Full waveform responses for A) 40mm practice grenade and B) 60mm projectile. The on-time signal for the 40mm grenade is masked by the background signal, but the 60mm projectile exhibits a clear on-time response.

6.2. Primary Field Nulling Configurations

A key common characteristic among all of the available on-time systems is that they attempt to minimize the effects of the primary field. During the on-time, receiver circuitry is flooded by the effects of direct coupling of the receiver coil with the transmitter. Detection of the secondary magnetic fields is challenging since they can be as much as six orders of magnitude smaller than the primary field. Therefore, procedures that remove the effect of the primary field are critical to effective measurement of on-time data. Fortunately, the same problem has existed for frequency-domain EMI systems since their inception (e.g., Won, 1980). A number of nulling methods have been devised, tested, and implemented. In this section, we will briefly examine their utility for removing on-time primary field effects. Nulling is defined as a significant reduction in the net primary field relative to the expected amplitude of the scattered magnetic field.

In general, nulling of the primary field is accomplished through one of or a combination of the following methods:

1. Absolute Field Nulling
2. Geometric Nulling
3. Shielding
4. Tailored Transmitter or Receiver Designs

Absolute field nulling can be achieved through calibration methods or via total field decomposition. Calibration methods include both one-time equivalent free space calibration measurements as well as dynamic calibration. An equivalent free space calibration is usually conducted by suspending an instrument well above the ground and away from the influences of any nearby conductors or EM radiators. The assumption is that the only contribution to measured voltages on an instrument's receivers are from the primary field and any small secondary fields associated with electronics or conductors contained within the instrument. Therefore, this calibration is thought to produce an effective system transfer function describing the intrinsic self signature of the instrument. By removing this effective free space primary field from all subsequent measurements, the resulting signals are attributed only to external sources such as scattered fields from conductive and permeable targets.

To fine tune this one-time free space calibration, instruments often also employ a dynamic calibration through the use of a quality coil (Q-coil). These have been implemented in many forms, but, in general, they consist of an induction coil with similar (although often scaled) characteristics to the induction receivers. Q-coils act as a third coil (in addition to transmitter and receiver) and are often called bucking coils (as in frequency-domain electromagnetics). In many cases, they are placed halfway between the transmitter and receiver in a maximum-coupled configuration. The dipole moment of the bucking coil is tuned such that the inducted voltage from the primary field is equal to that inducted in the receiver coil. The bucking and receiver coils are wound in opposite directions so that the primary field at the preamplifier is nulled to within some tolerance. The remaining signal from the primary field can be furthered nulled electronically by small adjustments in the receiver circuits. The combination of coarse absolute field calibration (via free space or Q-coil methods) and fine adjustments in circuitry are commonly applied when the transmitter and receiver are separated by more than a coil diameter (e.g., terrain conductivity instruments such as the EM-31, EM-38, and EMP-400 Profiler). One

challenge associated with this method is that the bucking coil also reduces the signal from secondary fields and relies on rigid geometry between the transmitter, receiver, and bucking coil (e.g., Won et al., 1996).

Another potential method for nulling the primary field during the on-time is through use of geometry. By arranging transmitters and receiver in particular configurations, it is possible to cancel out the majority of the primary field signal in the receiver(s). This method has been thought to be particularly effect for multi-static and multi-axis EM instruments. Null-coupling can be achieved by different means: 1) offset gradient configurations, 2) concentric configurations, 3) orthogonal transmitter and receiver arrangements, and 4) overlapping transmitter and receiver coils. The concentric bucking arrangement has been implemented by Geophex in their GEM-3 instrument and is well documented (e.g., Won et al., 1997; 1998; 2001). Offset gradient configurations have also been used in a number of systems such as the Berkley UXO Discrimination (BUD) System, ALLTEM, STMR, and others. Horizontal co-planar and vertical gradient configurations have been used. In fact, patents for these designs have been identified as early as the 1930's in the United States (Hedden, 1936 - Patent US 2129058) and Germany (Ambronn, 1930 - Patent 494831). Schematic illustrations of some of these configurations are shown in Figure 56.

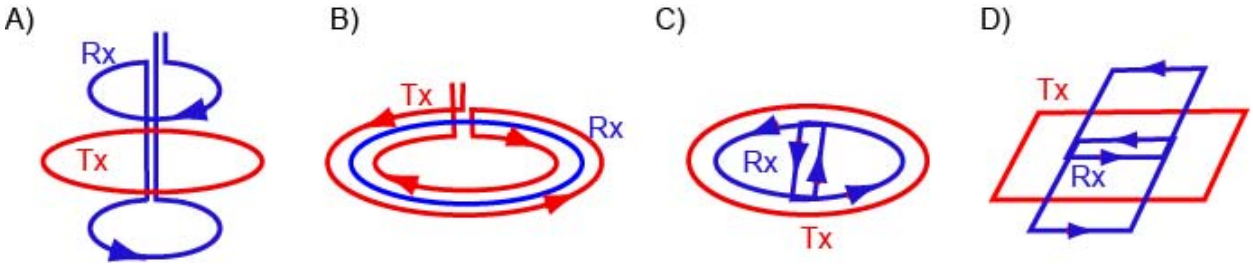

Figure 56. Examples of nulled gradient transmitter-receiver configurations for on-time EMI instruments. A) Vertical gradient receiver configuration (e.g., GEM-5). B) Concentric bucking configuration (e.g., GEM-3). C) Concentric double-D configuration (e.g., Minelab and Foerester metal detectors). D) Overlapping and gradient oval, rectangular, or "race-track" shaped coil configuration (e.g., Minelab STMR).

The orientation of particular gradient configuration is important to its effectiveness. For example, coaxial gradient pairs have to be balanced if their relative distance to a target is significantly different (such as the vertical gradient pairs used in the ALLTEM). Coplanar horizontal gradient pairs are less susceptible to these imbalances, because they attempt to retain symmetry between transmitter, receivers, and the target of interest (such as the figure-8 qudrapole receivers used in the STMR). These differential setups produce signals that are symmetric but of opposite polarity as shown for the STMR array (e.g., Figure 28 and Figure 29). This enables pinpointing (localizing the center by identifying the signal zero crossing) and aids in background suppression. An alternate to the gradient designs shown in Figure 56 are the use of orthogonal and overlapping transmitter and receiver arrangements. By positioning receivers so that half of the available flux area (coil area) is inside the transmitter circumference and half is outside of the transmitter, the primary field from the transmitter may be cancelled. This arrangement is sensitive to positional errors, but will provide better depth sensitivity than the gradient configuration.

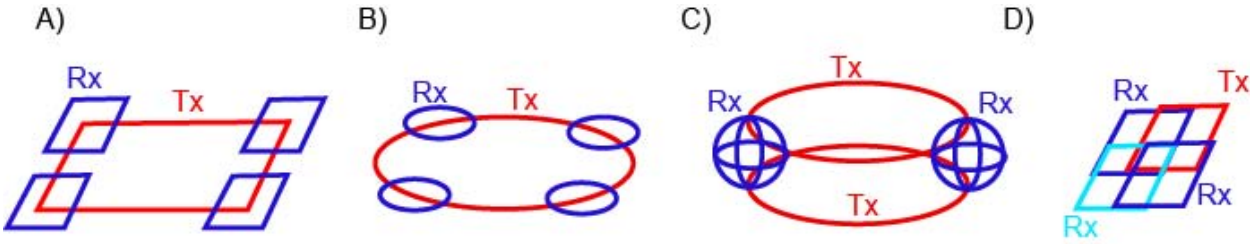

Figure 57. Examples of overlapping transmitter-receiver configurations for nulling the primary field. Both monostatic and multi-static configurations are conceivable. A) Rectangular arrangement. B) Circular arrangement. C) Three-axis receiver nulling through multiple transmitters and overlapping circular coils. D) Multi-static concept. Each receiver also acts a transmitter as combinations of Tx-Rx pairings are sequenced.

To better understand the tradeoffs between various nulling configurations we conducted a simple analysis of the sensitivity of two coil arrangements to variability in their configuration. For example, First, we looked at the horizontal coplanar configuration (similar to that used in the STMR array), which we represented as two circular differential receiver coils encompassed by a larger circular transmitter. The receivers consist of oppositely wound loops of wire and are allowed to have a small overlap to adjust for any imperfections and corresponding residual primary field. We specifically investigated the case where the coils were slightly different in diameter (2mm or 2% difference). As shown in Figure 58, the magnetic flux was integrated over the area of each coil and differenced to produce a nulled current normalized residual primary field. For this example, the field is perfectly nulled with the larger receiver positioned at 0.115m from the center. At this point the positional sensitivity is 0.1 nT/cm (Figure 59).

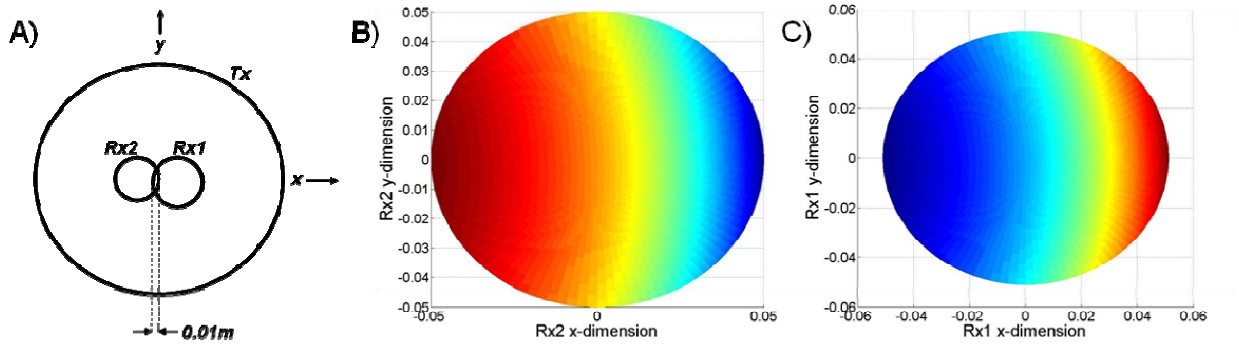

Figure 58. Horizontal differential gradient receiver set up for nulled primary field on-time measurements. A) Circular transmitters and receivers were used for simplicity in modeling. B) The flux density over the area of the smaller receiver Rx2. C) The flux density over the area of the slightly larger Rx1. Small differences in coil size (i.e., magnification errors) as well as deviations in linear and angular displacement can lead to residual primary fields that effect on-time measurements. The flux density full scale color range extends from 2.5 to 4.0 microTeslas for calculations over both Rx1 and Rx2 in this example.

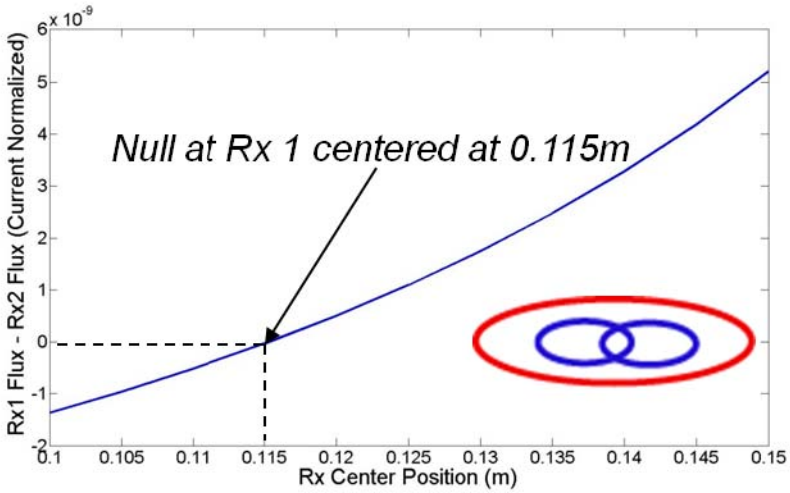

Figure 59. The residual magnetic flux associated with the primary magnetic field coupling between the transmitter and receivers. The difference signal is sensitive to deviations in the both the position and size of the receiver coils.

In another example, we model a simple overlapping coil arrangement (Figure 60). In this case, the receiver has overlapping areas on either side of the transmitter to create equal and opposite magnetic flux. This acts to cancel the primary field coupling from the transmitter. In this configuration, the receiver is able to sense transient magnetic fields from any external source such as scattering from metallic UXO. In Figure 61 we show the sensitivity in positional errors associated with this configuration. The normalized flux is zero (perfectly nulled) when the receiver center is offset 26.06 cm from the center. This put slightly more area of the receiver outside of the transmitter to account curvature of the transmitter and the nature of the primary field near the transmitter windings. We note this nulling arrangement is more sensitive to positional errors

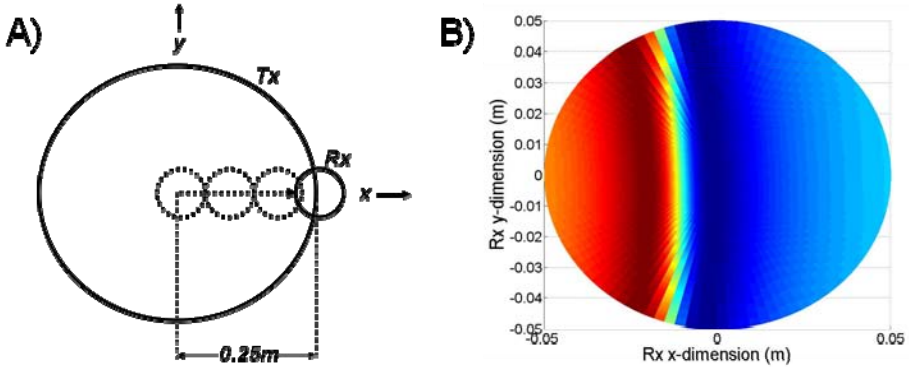

Figure 60. Overlapping transmitter and receiver to null the primary field during the on-time. A) A circular receiver is positioned to straddle the transmitter providing equal flux opposing each side of the transmitter. B) The flux density over the area of the receiver (red is positive flux, blue is negative flux). Slightly more area must overlap outside of the transmitter to create equal flux due to the curvature of transmitter and nature of the primary field very near the transmitter coil. The flux density full scale color range shown in (B) extends from -8.5 to 12 microTeslas for this example.

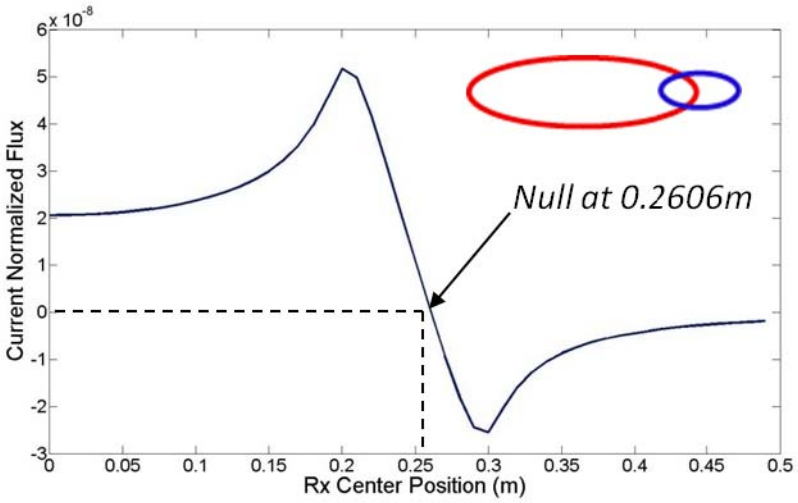

Figure 61. The total current normalized magnetic flux associated with the primary magnetic field coupling between the transmitter and receiver. Perfect cancellation occurs when the receiver coil is offset 26.06 cm. The receiver coil center is at 25cm, so a slightly greater portion of the receiver extends outside the transmitter coil to achieve the nulling. This is due to the curvature of the transmitter and the nature of the primary field near the transmitter windings.

7. CONCLUSIONS

7.1. Summary

A synthesis of the results of our investigation in this exploratory phase suggests that a handheld prototype full waveform system that combines the best designs and methods can be quickly developed. We also initiated a number of integrated system design tradeoffs that compare candidate configurations and quantify performance and suitability with respect to maximizing the information content from on-time signals as well as cost and logistical considerations. Time- and frequency-domain electromagnetic induction and magnetic data processing and inversion strategies were evaluated and tested to better understand the challenges associated with the collection and analysis of low-noise data and UXO detection. Comparisons of available on- and off-time data provide simple, yet potentially powerful information for target discrimination. Both data and theory provide evidence that there is potential to extract useful and unique information about targets and ground from on-time signals. In particular, new processing methods show potential to improve target detection and discrimination, especially when on-time and off-time signals are used in conjunction with each other.

7.2. Primary Conclusions

In addition to providing detailed investigations of potential on-time capable systems, this work has advanced the current understanding of the challenges associated with acquiring and processing full waveform EMI data. Results of our evaluation suggest that although various modes exist to sample on-time data, no one method has been proven superior.

During this project we investigated various waveforms, receiver configurations, and modes for nulling the primary field. Among the major contributions are:

- The physical representation of full waveform responses can be simplified by using an analytical equivalent circuit theory approach. We show that this model is equivalent to the inverse Fourier transform of the corresponding frequency domain response convolved with the current waveform. Laboratory magnetic field responses from various wire loop targets collected with a wideband giant magnetoresistive sensor are used to verify the model results.
- Investigations of deconvolution approaches exhibited their utility in removing the primary in-phase component from on-time responses. We show that the total full waveform magnetic field response can be decomposed into primary and secondary components. The secondary response contains a signal that is completely in-phase with the transmitter and reflects the system geometry and the magnetization effect on any targets in the presence of the transmitter field. By subtracting a scaled version of the primary field from the total full waveform response, we extract the out-of-phase (or equivalent quadrature phase) component during the transmitter on-time. Sampling these deconvolved in-phase and quadrature-phase secondary fields generated from our simulations over a range of target conductivities yields conductivity spectra analogous to spectral plots of magnetic field ratios for frequency-domain responses. The in-phase response, in particular, yields information that is directly related to the bulk volume demagnetization factors for simple canonical objects. This equivalence between the time

and frequency domains further supports the utility of on-time signals in elucidating magnetic properties consistent with in-phase or instantaneous parameters.

- Simulations of various target scenarios such as varying diameter, size, depth, and aspect ratios contrast the sensitivity and resolvability of on-time signals to off-time responses. Responses to different diameter spheres were modeled and show that the on-time response has greater sensitivity to large diameter objects relative to off-time. Further simulations for particular object size and depth combinations revealed that the on-time signal is better suited for resolving deep, large targets whereas comparable off-time response resolves small, shallow targets.

- Both simulations and data acquired with on-time systems reveal a complex interplay between target magnetization and inductive responses with varying angle and offset of an inductive loop transmitter source. The degree of complexity of the spatial evolution of the on-time responses depend on target orientation such that targets with the majority of their surface area normal to the inducing field are appropriately dominated by inductive responses. Conversely ferrous targets that extend their long axis parallel to the incident primary field tend to be dominated by magnetization effects. Simulations of both on- and off-time responses that account for the shape of spheroids were used to compare sensitivities to oblate and prolate aspect ratios. As expected, oblate targets oriented with their long-axis perpendicular to the incident primary field generate a response dominated by inductive effects (scattered field opposing the primary), and prolate objects oriented parallel with the incident field have stronger magnetization responses (magnetic field aligning with the primary).

- On-time data collection with existing pulsed induction EM instruments was made possible with nulled receiver configurations. A variety of axi-symmetric objects and UXO targets were used to measure the responses to both the exponential and linear rise of charging currents in various transmitters. Measurements were made with the Minelab Single Transmit-Multiple Receive (STMR) array system, the EM-61 transmitter with custom receivers, and the Man-Portable Vector array instrument. Both B-field (via GMR sensor) and dB/dt temporal signatures were acquired to yield expected responses for ferrous, non-ferrous, and composite targets.

- Analysis of field data collected with two on-time capable survey instruments, the USGS ALLTEM and Minelab STMR arrays, exemplified both the capabilities and limitations of the current fieldable systems. The “always on” ALLTEM system sawtooth-shaped waveform generated predictable results for calibration data over steel spheres. Combining a well-established dipole model with the triangular waveform (using a linear systems convolution approach) provided stable and nearly identical polarizabilities over the duration of the 11ms ALLTEM waveform cycle. Inversions of an integrated (over time) on-time data channel reproduced a model that closely matched STMR field data over steel and aluminum disks, rods, and cylinders.

- An investigation of sensor design considerations identified primary field nulling, waveform selection, and sensor type and spatial arrangement as the key factors in optimal design of full waveform EM systems. Preliminary investigations of nulling configurations led us to the conclusion that overlapping receiver coils under the outer winding of the transmitter may provide an alternate to conventional gradient coil

configurations. Gradient coil pairs have inherent depth sensitivity limitations relative to single coil receivers. Our first-order analysis suggests that a combination of geometric nulling (avoiding gradient configurations, if possible) combined with digital cancellation and dynamic calibration are likely adequate for effectively removing the primary field.

- A limited analysis of waveform shapes, durations, repetition frequencies, and mark/space characteristics shed light on new possibilities for on-time target excitation. Generally, charging circuits in EMI instrumentation are designed to reach steady state quickly and hold a stable current that is terminated as quickly as possible. When on-time data are desired there may be certain advantages to choosing one waveform over another and in using multiple types or ramp durations. Specifically, we suggest that repeated waveforms of differing ramp (e.g., linear ramp) duration could be used to separate the effects of mineralized ground from target responses. We noted that there is also potential to generated cumulative charge in targets by repeating short duration current ramps spaced closely together in time (closer than the effective target time constant). This effect may lead to "pumping charge" into a target in order to increase the total energy in the system and yield higher signal-to-noise ratios. In addition, we recommend investigations of alternates to conventional charging circuits that include digital control (and, perhaps, dynamic control) of current waveform shape and power. Recent work on pulse generator circuits using nanosecond switching silicon controlled rectifiers may be leveraged for pulse width modulation waveform generation. This allows for digital control of the current waveform and the potential for varying the waveform during acquisition.

7.3. Utility of On-time Information

The key feature of an on-time or full waveform system is the capability to provide both frequency domain (on-time) and time domain (off-time) information from one instrument. The on-time portion of the signal contains inherent information about the target response to a wide spectrum of frequencies. This information is obtained without the necessity of high-precision phase measurements required in frequency domain systems. Furthermore, these on-time data can provide a wideband response with only one excitation waveform (rather than stepping through a band of continuous wave frequencies). This wideband excitation enables greater sampling rates and alleviates the difficulties associated with phase measurement. At the same time, the off-time portion of the signal provides insight into the target parameters (e.g., decay constant) typically recovered in transient EM data.

Another important utility is the potential to estimate the resistive and inductive limits or the equivalent low- and high-frequency asymptotes from on-time data. We have shown that these values can be reliably estimated using a simple sum of exponentials model and leads to quantification of a target's bulk magnetization. Aspects of this type of information have been estimated from very early and very late off-time behavior, but the sampling of data during those periods in the off-time have proven particularly challenging. Improved signal-to-noise ratio sampling during the on-time may provide an alternate method for obtaining this information. Furthermore, when the off-time signal is used as a reference, relatively straightforward analysis of on-time signals and their spatial evolution yield first-order estimates of bulk material characterization.

8. FUTURE WORK RECOMMENDATIONS

8.1. Key Questions for Future Research

While on-time instruments exist, there is no system that fully leverages the potential advantages of full waveform data. The work we started in this project has led to a subset of key questions that should be addressed to complete the assessment of on-time EMI capability for UXO applications:

1. *Can we formulate processing methods to extract unique properties of demagnetization (e.g., demagnetization factor, magnetic cross-over, resistive and inductive limits)?* The integration of physically-complete models with existing linear systems analysis approaches can be used to quantify the full waveform response for realistic targets and scenarios. In particular, a more complete understanding of the tradeoffs between transient inductive and magnetization mechanisms are needed (especially regarding spatial variability and responses to composite targets).

2. *What are the key mechanisms driving on-time spatial responses?* Full validation of the models developed during this SEED project should be conducted using controlled data collection. This should also lead to a more thorough understanding of the complex interplay of transient and magnetostatic effects.

3. *Do field data from existing on-time capable systems support the extraction of physics-based features identified in theoretical and numerical simulation studies?* We suggest that SERDP conduct a complete analysis of field data acquired with the ALLTEM and other on-time capable systems of interest. This analysis will not only allow for verification of models, but will also test the constraints on on-time signal acquisition, noise influences, and the parameterization of unique features that better characterize targets, clutter, and ground.

4. *What are the best performing methods for extracting features from full waveform data? What are the barriers to acquiring and analyzing these types of data? Is there unique information in these signals to exploit for discrimination?* These questions can be answered through the implementation and comparison of deconvolution and inversion approaches for laboratory and field data. A complete assessment of on-time data features can be compared to off-time features to determine the added value they provide in discrimination. Receiver-operator-curve analysis procedures and tests of model-feature sensitivity and robustness can be tested through quantitative analyses.

   More work must be conducted on the analysis of both laboratory and field data to elucidate and validate the veracity and uniqueness of features extracted from on-time data. Physics-based features extracted from full waveform temporal signatures as well as their spatial evolution over targets will likely lead to better discrimination based on target size and aspect ratio as well as material composition and demagnetization effect.

5. *What nulling configuration and methods are best suited for various on-time performance metrics?* A combination of model simulation and experiments can be conducted to

assess the tradeoffs of nulling methods. It is suggested that on-going work by SERDP to develop next-generation handheld instrumentation (e.g., MM-1658) as well as new work on nulled configurations (e.g., MM-1711) should be leveraged to support on-time system assessments. Geometric nulling, digital cancellation methods, and various modes of absolute field calibration have been used for removing primary field effects. All of these methods have limitations, and we advocate an intelligent combination of methods that minimizes the impacts on sensitivity and dynamic range. Overlapping coil arrangements along with absolute calibration and balancing combined with digital cancellation and fine tuning with a Q-coil are likely the optimal choice for removing the primary field. We found that gradient configurations are less optimal due to their inherent fall-off in sensitivity with range.

6. *What utility do wideband B-field sensors provide for on-time data acquisition?* There are clear advantages in using B-field sensors in place of, or to augment induction coil (dB/dt) data collection. An investigation into the role of the B-field sensors and best configurations for primary field cancellation in the context of full waveform EMI should be considered.

7. *What overall design is optimal for a tailored full waveform sensing unit?* Once the previous questions have been answered, we should consider the development of an integrated prototype. Complete evaluation of design tradeoffs is warranted in order to optimize the design of next generation full waveform systems (e.g., sensors, primary field cancellation, waveform design). The performance of the system can be quantified and compared to expectations from modeling and preliminary experimental work.

   Although a handful of on-time instruments exist, no current system fully leverages the potential advantages of full waveform EMI data. To do this, we suggest that advanced full waveform sensors be investigated, and, if warranted, developed into testable prototypes. In an idealized system, the current waveform would have the properties that maximize the magnetization effect on a target. Comparisons of basic waveforms lead to the suggestion of a linear ramp current excitation and rapid cessation as an ideal source for a full waveform system. This excitation characterizes the combined effect of a bipolar electromotive force (i.e., the electromotive force rapidly changes polarity as the ramp-on period transitions to the shut-off period) and a linear magnetic field applied to the target. The contrasting effects of the electromotive force and the magnetizing field produce a unique response that is a function of target features such as geometry, conductivity, and magnetic susceptibility.

   The results of this project also suggest that an idealized system would likely utilize a current waveform with multiple ramp durations. The implementation of different ramp durations may allow for at least two different excitation periods. This approach provides certain advantages by: 1) enabling baseline excitation for comparing magnetization responses, 2) creating discrete energy states from which the secondary response decays, and 3) yielding needed information for cancelling the viscous magnetization effects of mineralized soils.

9. REFERENCES

Ambronn, R., 1930, German patent 494831: “Verfahren zur elektrischen bodenerforschung mittels dem untergrund induktiv zugeführter wechselströme und aumessung des elliptisch ploarisierten magnetischen feldes durch suchspulen”, German patent office.

Anderson, W.L., 1979, “Numerical integration of related Hankel transforms of orders 0 and 1 by adaptive digital filtering”, Geophysics, 44, 1287-1305.

Annan A.P., Smith, R.S., Lemieux, J.O., O’Connel, M.D., and R.N. Pederson, 1996, “Resistive-limit, time-domain AEM apparent conductivity”, Geophysics, 61, 93-99.

Asten, M.W., and A.C. Duncan, 2007, “Fast approximate EM induction modeling of metallic and UXO targets using a permeable prism,” Jour. Applied Geophysics, 61, 235-242.

Asten, M.W., and S.K. Verma, 1978, “Conversion of wideband EM frequency response to transient response using segmented transformation,” Geophysics 43, 189-193.

Aster, R.C., Borchers, B., and C.H. Thurber, 2005, "Parameter Estimation and Inverse Problems", Elsevier International Geophysics Series, 90, London, 301 pp.

Baum ,C.E., 1999, “Low-frequency near-field magnetic scattering from highly but not perfectly, conducting bodies”, in Detection and Identification of Visually Obscured Targets, C.E. Baum, Ed., New York: Taylor and Francis, Ch 6., pp. 163-218.

Billings, S. Pasion, L. Oldenburg, D. And J. Foley, 2003, “The influence of magnetic viscosity on electromagnetic sensors,” in Proc. of EUDEM-SCOT2, International Conference on Requirements and Technologies for the Detection, Removal, and Neutralization of Landmines and UXO, Brussels, 123-130.

Billings, S.D., 2004, “Discrimination and classification of buried unexploded ordnance using magnetometry”, IEEE Transactions on Geoscience & Remote Sensing, 42, 1241-1251.

Bracewell, R., 1986, “The Fourier Transform & Its Applications”, 2nd edition: McGraw Hill.

Candy, B.H., 1990, US Patent 4894618: “Metal detector using cross-correlation between components of received signals”, United States Patent Office.

Cronemeyer, D.C., 1991, “Demagnetization factors for general ellipsoids,” Jour. Applied Physics, 70, 2911-2915.

Das, Y., 2004, “A preliminary investigation of the effects of soil electromagnetic properties on metal detectors," in Proc. SPIE Conference on Detection and Remediation Technologies for Mines and Mine-like Targets IX, 5415, pp. 677{690, (Orlando, FL, USA), April 2004.

Das, Y., 2006, "Time-domain response of a metal detector to a target buried in soil with frequency-dependent magnetic susceptibility", in Proc. SPIE Conference on Detection and Remediation Technologies for Mines and Minelike Targets XI. Edited by Broach, J. Thomas; Harmon, Russell S.; Holloway, John H., Jr.. Proceedings of the SPIE, Volume 6217, pp. 621701 (2006).

Das, Y., McFee, J.E., and R.H. Chesney, 1984, "Time domain response of a sphere in the field of a coil: Theory and experiment", IEEE Trans. Geoscience & Remote Sensing, 22(4), 360-367.

Farquharson, C.G. and Oldenburg, D.W., 2000, “Simultaneous one-dimensional inversion of electromagnetic loop-loop data for both magnetic susceptibility and electrical conductivity”, GeoCanada 2000, Expanded Abstracts, 1-4.

Golub, G.H.; Van Loan, C.F.,1996, “*Matrix Computations”* 3rd ed., Johns Hopkins, ISBN 978-0-8018-5414-9.

Grant, F.S., and West, G.F., “Interpretation Theory in Applied Geophysics”, McGraw-Hill Book Company, New York, St. Louis, San Francisco, Toronto, London & Sidney, 485-546, (1965).

Guptasarma, D., Maru, V.M., and G. Varadarajan, 1976, “An improved pulsed transient airborne electromagnetic system for locating good conductors”, Geophysics, 41, 287-299.

Haines, G.V, and A.G. Jones, 1988, “Logarithmic Fourier transforms,” Geophysical Journal, 92, 171-178.

Hedden, 1936, US Patent 2129058: “Transformer for a metal detector”, US Patent Office.

Hostetter, G.H., 1982, “Recursive discrete Fourier transformation with unevenly spaced data, IEEE, Trans. Acoustics, Speech, Signal Processing, ASSP 31, 206-209.

Kaufman, A.A., 1978, “Frequency and transient response of electromagnetic fields created by currents in confined conductors,” Geophysics, 43, 1002-1010.

Kaufman, A.A. and Keller, G.V., “Inductive Mining Prospecting: Part 1: Theory: Methods in Geochemistry and Geophysics”, Elsevier Science Ltd., 195-205, (1985).

Lee, T., 1984, “The effect of a superparamagnetic layer on the transient electromagnetic response of the ground,” Geophysical Prospecting, 32, 480-496.

Macnae, J.C. and Mutton, A., 1997, “Can massive sulphides be distinguished from conductive slates? A case history at Dugald river,” Exploration Geophysics, 29, 535-542.

Marble, J. and I. McMichael, 2010, “Dual-EMI system for object classification,” in Detection and Sensing of Mines, Explosive Objects, and Obscured Targets XV, Proceedings of SPIE, Vol. 7664, 7664-0B.

Menke, W., 1984, “Geophysical data analysis – Discrete inversion theory”, Academic Press, Inc.

Miller, J.S., Schultz, G.M., Shubitidze, F., and J.A. Marble, 2010, "Target localization techniques for vehicle-based electromagnetic induction array applications" in Detection and Sensing of Mines, Explosive Objects, and Obscured Targets XV, Proceedings of SPIE, Vol. 7664, 7664-06.

Miller, J., Shubitidze, F., Schultz, G., Pasion, L., and Marble, J., 2010, "Surface magnetic charge model for source localization", IEEE Geoscience and Remote Sensing, in review.

Palacky, G.J., and G.G. West, 1973, “Quantitative interpretation of INPUT AEM measurements”, Geophysics, 38, 1145-1158.

Pasion, L.R., Billings, S.D., Oldenburg, D.W., Sinex, D., and Y. Yi, 2003, “Evaluating the Effects of Magnetic Susceptibility in UXO Discrimination Problems”, SERDP SEED Project UX-1285 Final Report, 37 pp.

Pasion, L.P., 2007, “Inversion of Time Domain Electromagnetic Data of Unexploded Ordnance”, University of British Columbia Ph.D. Thesis, 289 pp.

Pasion, L.R. and Oldenburg, D.W., 1999, “Locating and determining dimensionality of UXO’s using time domain electromagnetic induction. “ in Symp. Applications of Geophysics to Engineering and Environmental Problems, Oakland, March, 1999, pp. 763-772.

Pasion, L.R. and Oldenburg, D.W., 2001, “A discrimination algorithm for UXO using time domain electromagnetics,” Journal of Environmental & Engineering Geophysics, 28(2), 91-102.

Pasion, L.R., and D.W. Oldenburg, "Locating and determining dimensionality of UXO using time domain electromagnetic fields", J. Environ. Eng. Geophys., 6, 91-102, (2001).

Patra, H.P., and Mallick, K., “ Geosounding principles, 2”, Elsevier Science Publishers, (1980).

Raval, U., Rao, K.N.N., "Quasi-stationary electromagnetic response of covered permeable conductors to some pulses of spatially uniform magnetic field", Pure and Applied Geophysics, 104, 553-565, (1973).

Riggs, L.S. and Mooney, J.E., “Identification of metallic mine-like objects using low frequency magnetic fields,” IEEE Trans. Geoscience & Remote Sensing, 39(1), 56-65, (2001).

Sattel, D., "Improving conductivity models using on-time EM data", Exploration Geophysics, 29, 605-608, (1998).

Schultz, G., Miller, J., Stamatescu, L., and K. Kingdon, 2007, “Applications of a robotic multi-sensor UXO detection system”, in Symp. Applications of Geophysics to Engineering and Environmental Problems, Denver, March 2007.

Schultz, G.M., Miller, J.S., Song, L-P., and L. Pasion, 2010, "Transient electromagnetic responses during the transmitter on-time" in Detection and Sensing of Mines, Explosive Objects, and Obscured Targets XV, Proceedings of SPIE, Vol. 7664, 7664-05.

Schultz, G. and C. Ruppel, "Inversion of inductive electromagnetic data in high induction number terrains", Geophysics, 70, G16-G28. (2005).

Shubitidze, F., ONeill, K., Keli Sun, Paulsen, K.D., 2004, ” Investigation of broadband electromagnetic induction scattering by highly conductive, permeable, arbitrarily shaped 3-D objects**,”** IEEE Transactions on Geoscience and Remote Sensing, 42, 540 – 556.

Smith and Annan, 1997

Smith, R.S., 1998, “On the effect of arying the pulse width to detect high conductance bodies”, Exploration Geophysics, 29, 42-45.

Smythe, W.R., 1950, “Static and Dynamic Electricity”, 3rd Ed., McGraw Hill: New York, 345 pp.

Song, L-P., Shubitidze, F., Pasion, L.R., Oldenburg, D.W., and S.D. Billings, 2009, "Computing transient electromagnetic responses of a metallic object using a spheroidal excitation approach", IEEE Trans. Geoscience & Remote Sensing, 5, 359-363.

Sower, G., 1998, “Eddy current responses of canonical metallic targets,” in Detection and Identification of Visually Obscured Targets, C.E. Baum, Ed., New York: Taylor and Francis, Ch 8., pp. 243-282.

Stamatescu, L., and G.M. Schultz, 2007, “Minelab’s advanced EMI array”, UXO/Countermine/Range Forum 2007, Orlando.

Stanley, J.M, and S.M. Griffin, 2002, “Sub-audio magnetic: Miniature sensor technology for simultaneous magnetic and electromagnetic detection of UXO”, in EUDEM SCOT 2002.

Stolz, E.M., and J.C. Macnae, "Evaluating EM waveforms by singular-value decomposition of exponential basis functions", Geophysics, 63, 64-74, (1998).

Strang, G., 1998, "Introduction to Linear Algebra," 3rd ed., Wellesley-Cambridge Press.

Talman, J.D., 1978, “Numerical Fourier and Bessel transforms in logarithmic variables,” Jour. Computational Physics, 29, 35-48.

Ueberhuber, C.W., 1995, “Numerical computation: Methods, software, and analysis,” Springer-Verlag: Berlin, 442 pp.

Wait, J.R., 1951, “A conducting sphere in a time varying magnetic field,” Geophysics, 16(4), 666-672.

Wait, J.R., and K.P. Spies, "Quasi-static transient response of a conducting permeable sphere", Geophysics, 34, 789-792, (1969).

Ward, 1951

Ward, S.H., & G.W. Hohmann, “Electromagnetic Theory for Geophysical Applications”, in Electromagnetic Methods in Applied Geophysics: vol. 1, M.N. Nabighian (ed.), 131–311, Society of Exploration Geophysicists, Tulsa, Oklahoma, (1987).

Weichman, P.B., "Universal early-time response in high-contrast electromagnetic scattering", Phys. Rev. Lett, 91, 4pp., (2003).

Witherly, K., 2009, “Results of various airborne EM systems over a target of high conductance,” in Australian Society of Explor. Geo. Extended Abstaracts for PSEA conference 20009, Adelaide, 1-4.

Won, I. J. Keiswetter, D. Hanson, D. Novikova, E. and T. Hall, 1997, “GEM-3: a monostatic broadband electromagnetic induction sensor,” Jour. of Environmental and Engineering Geophysics, 2, 53–64.

Won, I.J., Keiswetter, D., and T.H. Bell, 2001, “Electromagnetic induction spectroscopy for clearing landmines,” IEEE Trans. Geoscience and Remote Sensing, 39, 703-709.

Won, I.J. 1980, “A wideband electromagnetic exploration method - Some theoretical and experimental results,” Geophysics, 45, 928-940.

Won, I.J., Keiswetter, D., and Novikova, E., 1998, “Electromagnetic induction spectroscopy ” Jour. of Environmental and Engineering Geophysics, **3**, 27-40.

Won, I.J., Keiswetter, D.A., Fields, G.R.A., and Sutton, L.C., 1996, “GEM-2: A new multifrequency electromagnetic sensor”, Jour. of Environmental and Engineering Geophysics, **1**, 129-138, (1996).

Wright, D.L., and W.C. Chew, 2000, “Enhancements to and Characterization of the Very Early Time Electromagnetic (VETEM) Prototype Instrument and Applications to Shallow Subsurface Imaging at Sites in the DOE Complex”, U.S. Dept. of Energy EMSP Project Number: 60162 Final Report, 69 pp.

APPENDIX A: STMR ON-TIME DATA

15.25 cm diameter steel cylinder, 30 cm depth

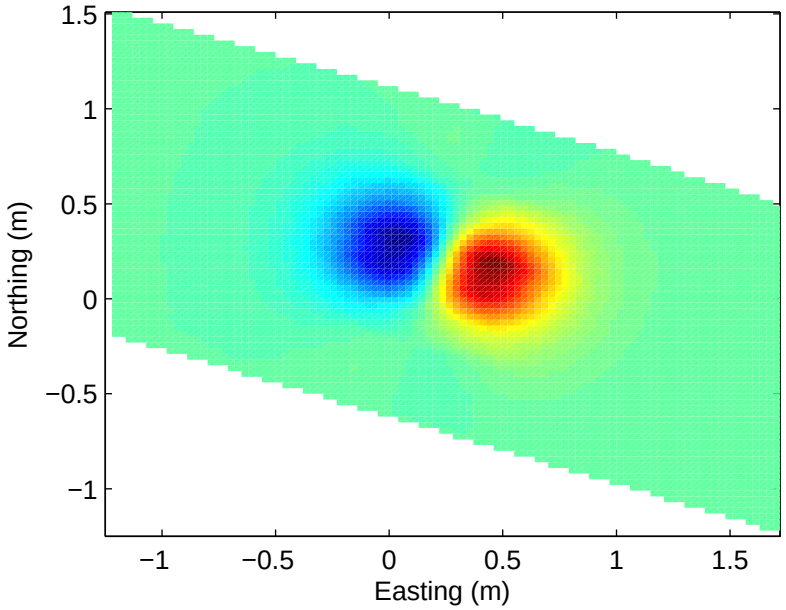

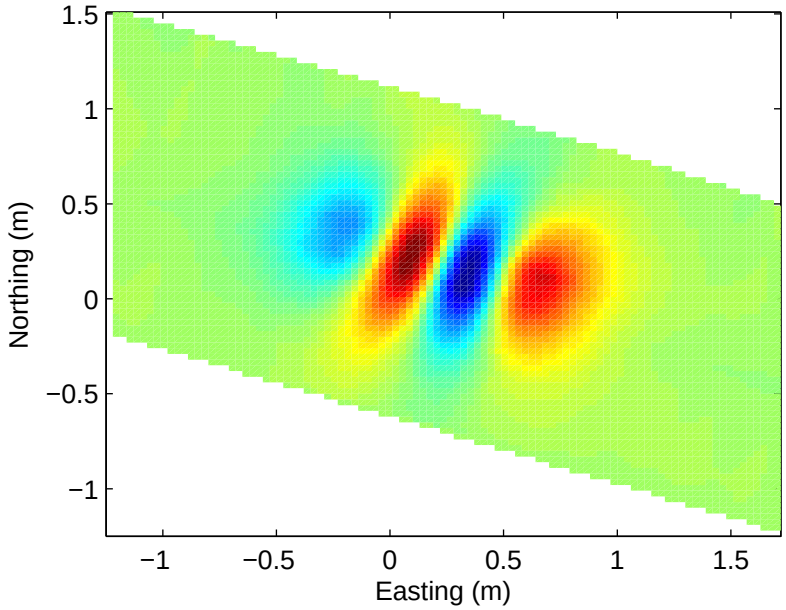

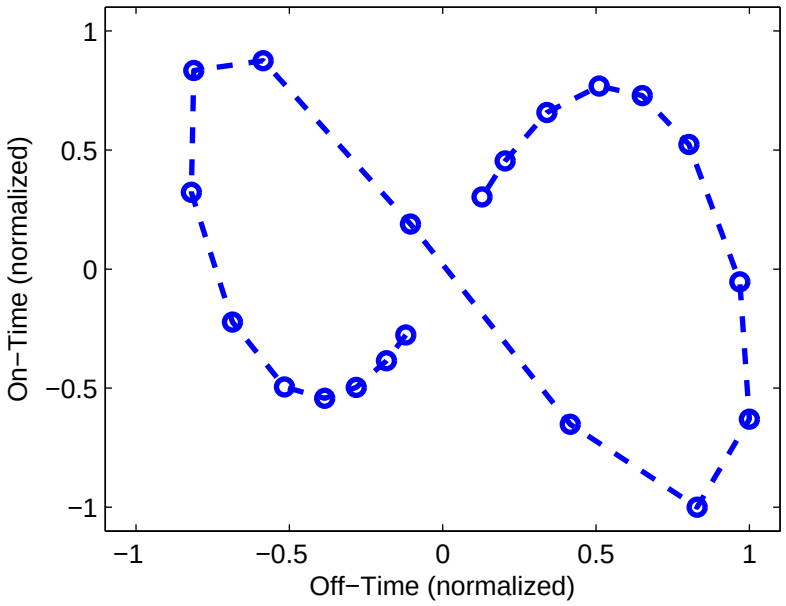

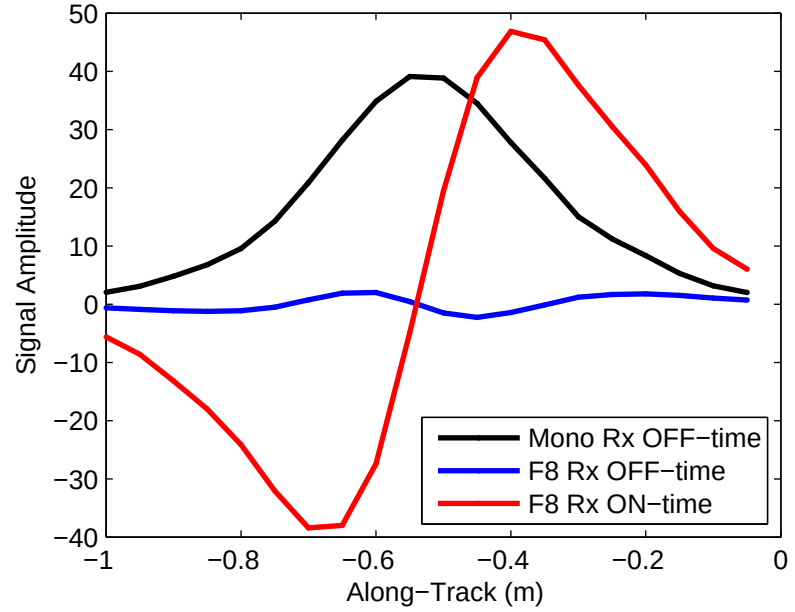

11.5 cm diameter steel cylinder, 30 cm depth

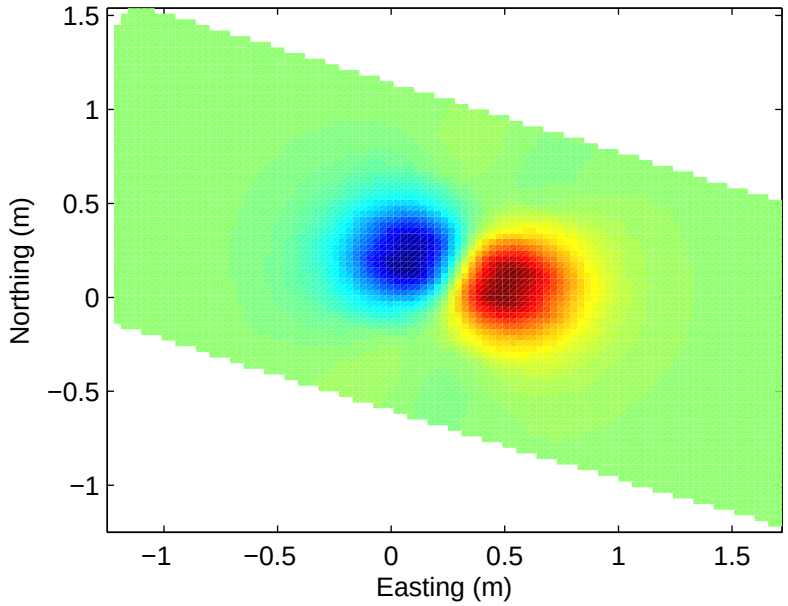

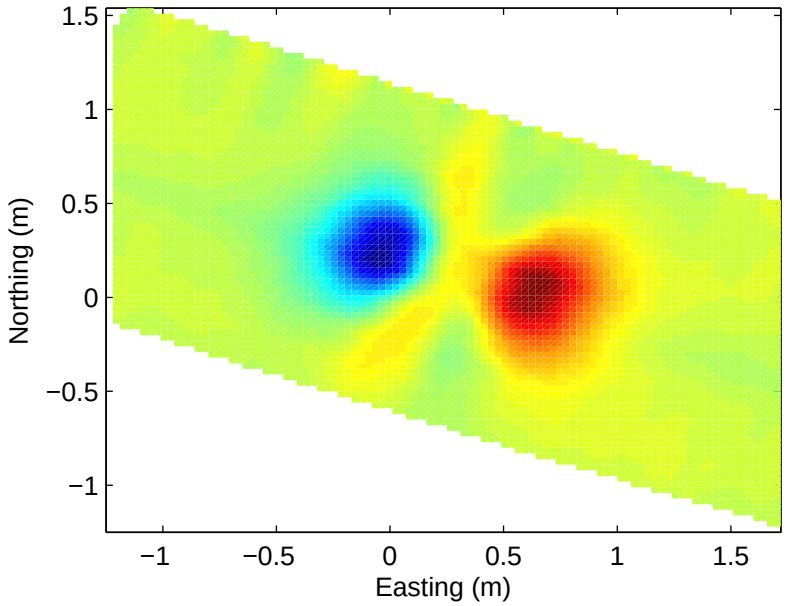

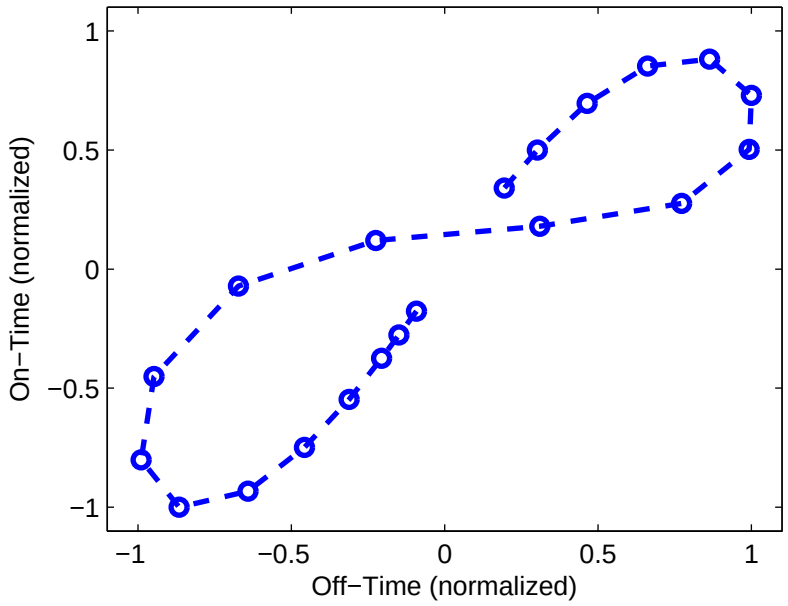

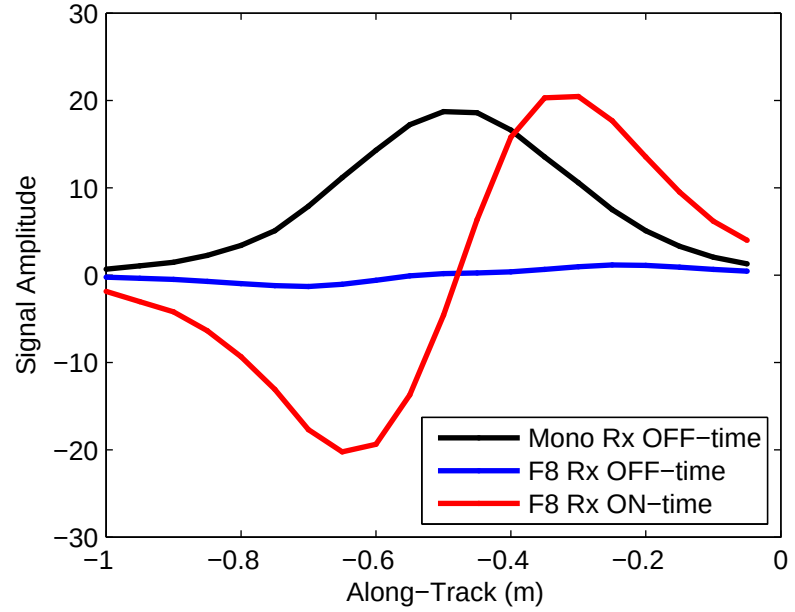

7.6 cm diameter steel cylinder, 30 cm depth

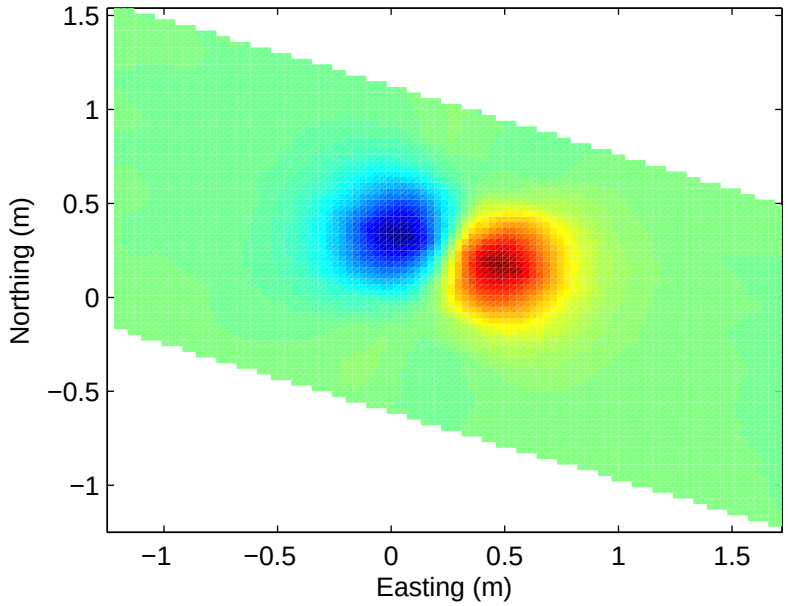

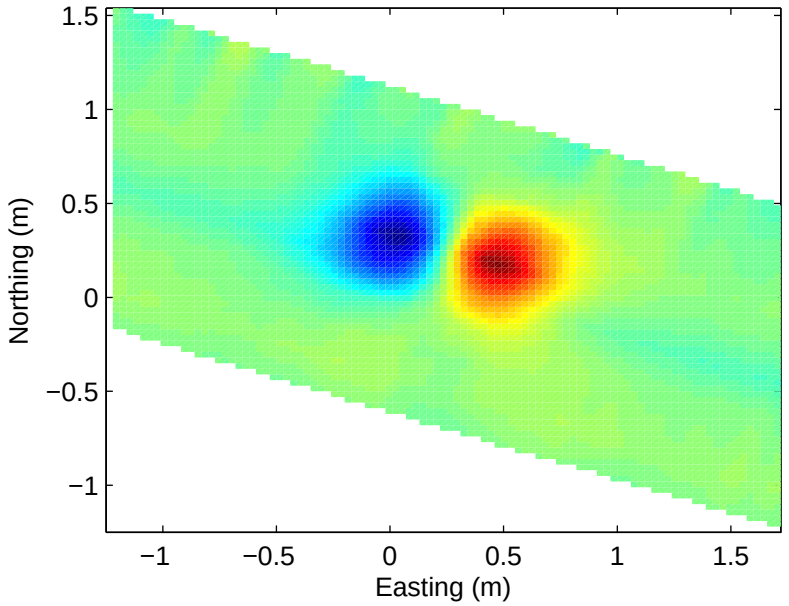

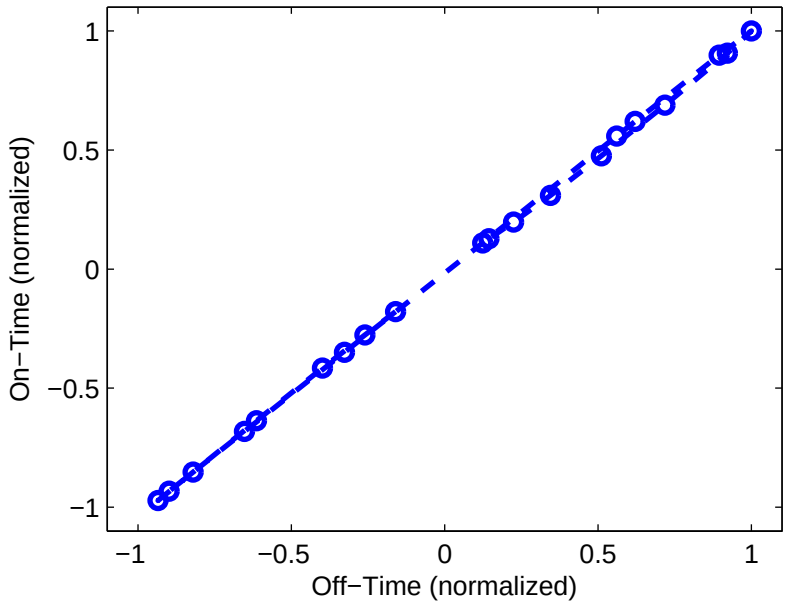

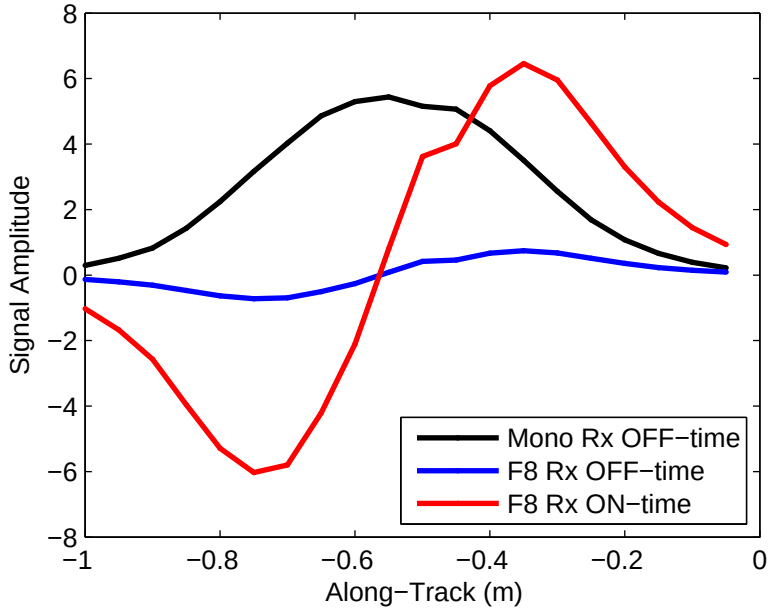

15.25 cm diameter steel disc, 30 cm depth

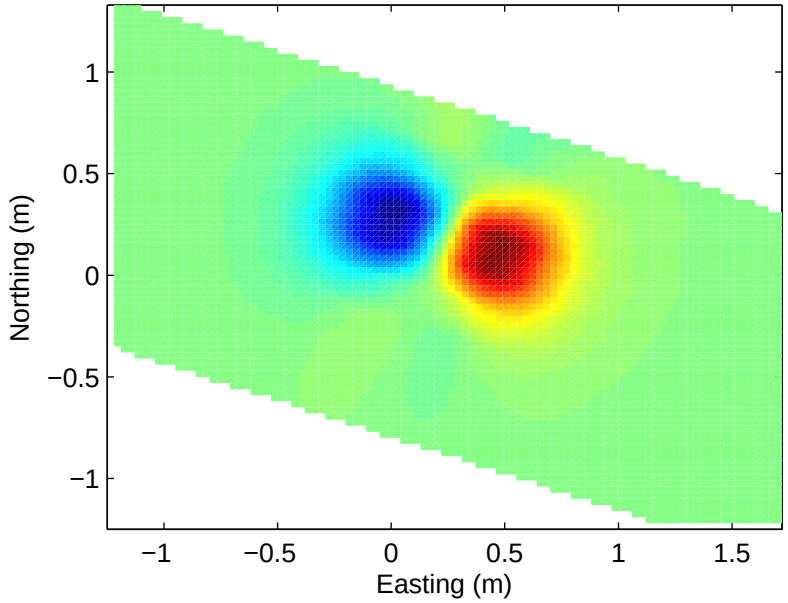

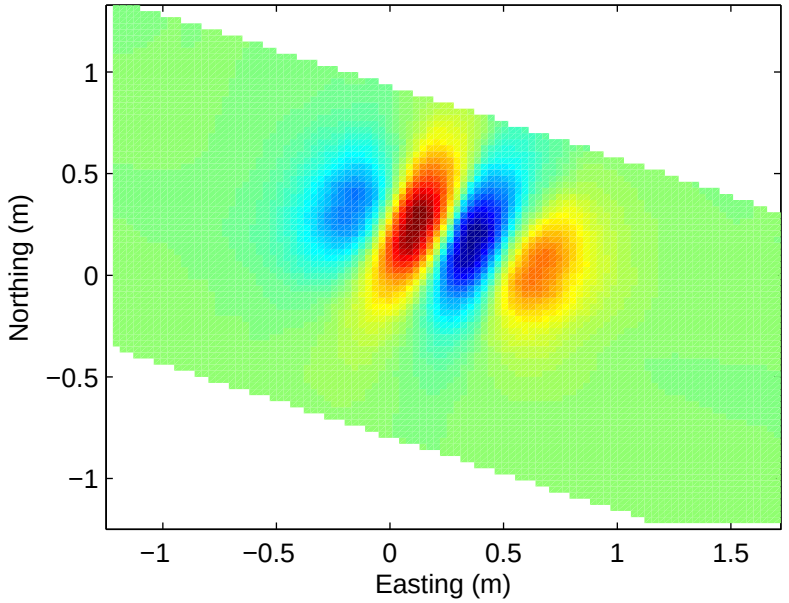

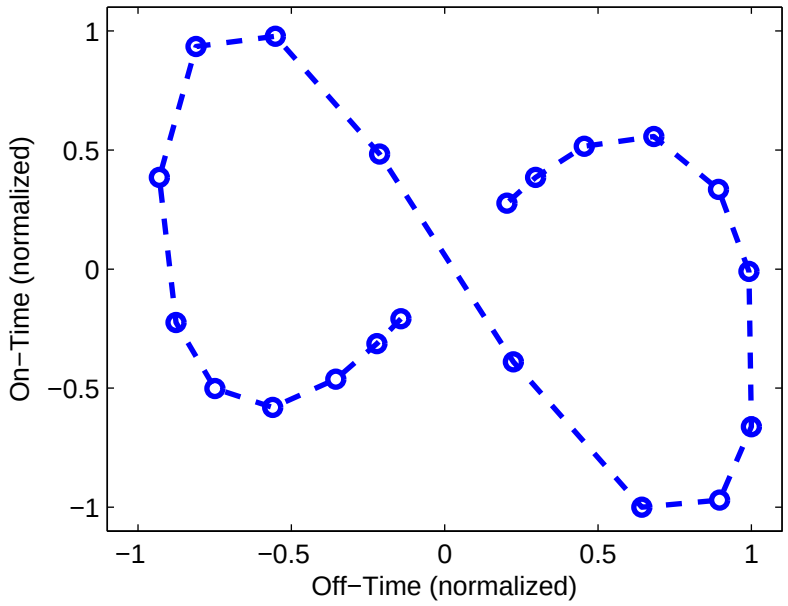

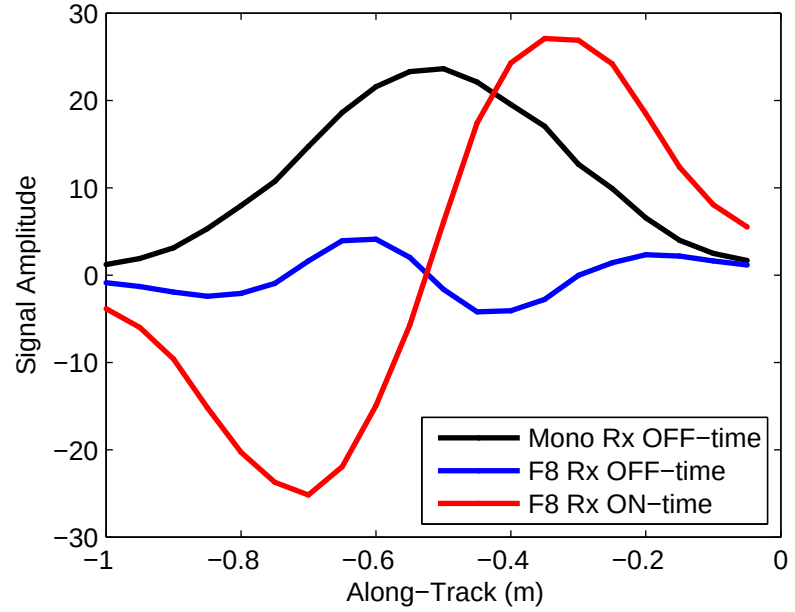

11.5 cm diameter steel disc, 30 cm depth

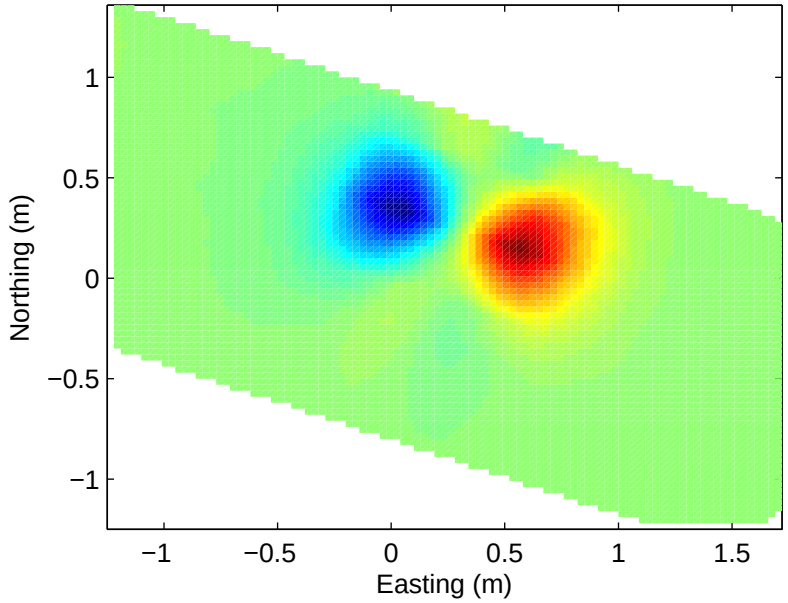

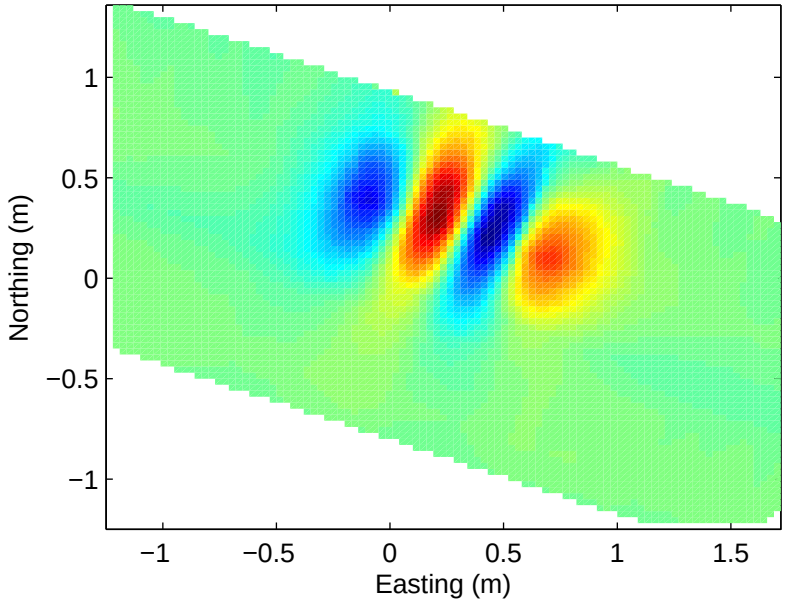

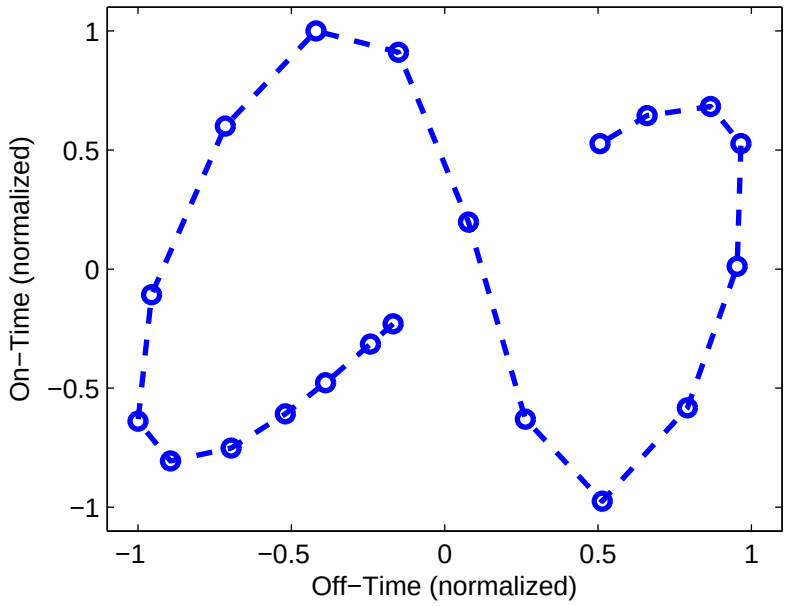

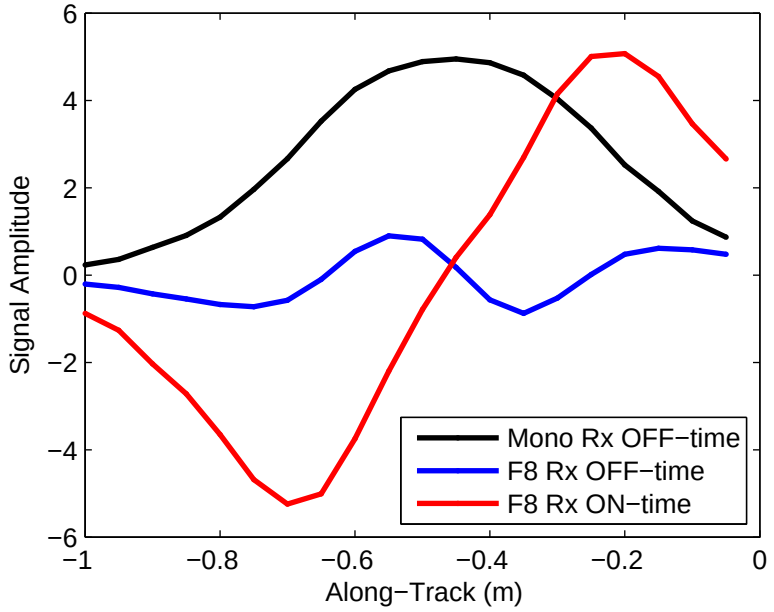

7.6 cm diameter steel disc, 30 cm depth

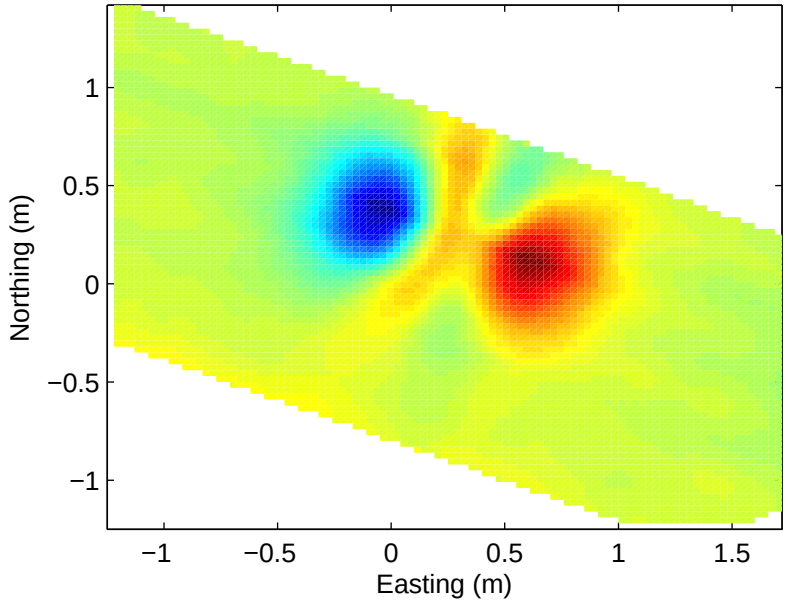

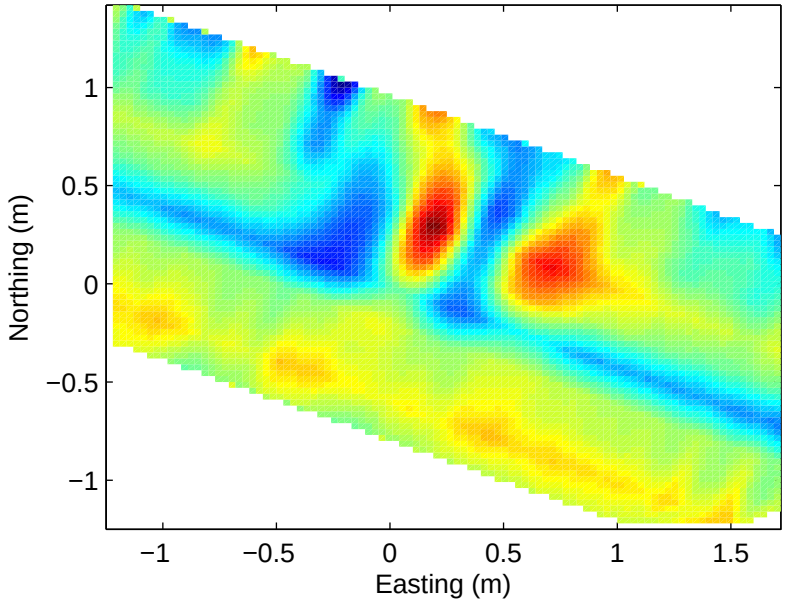

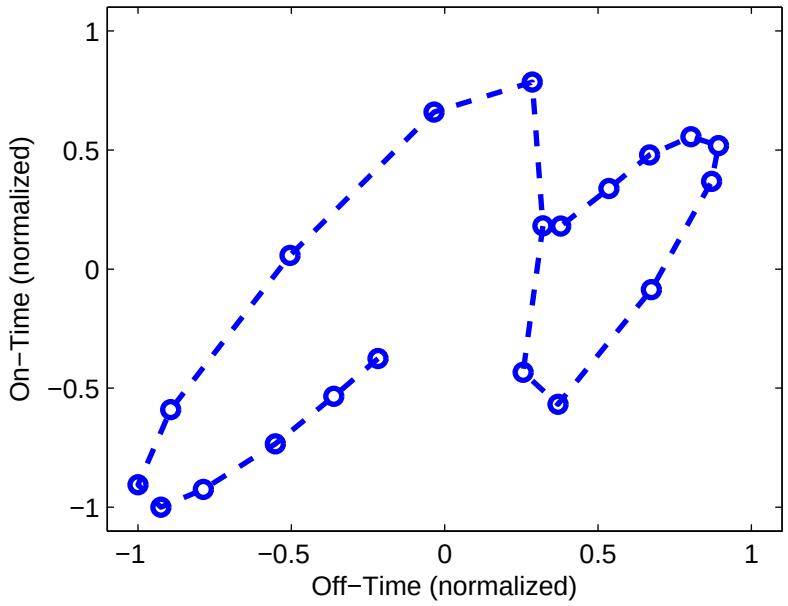

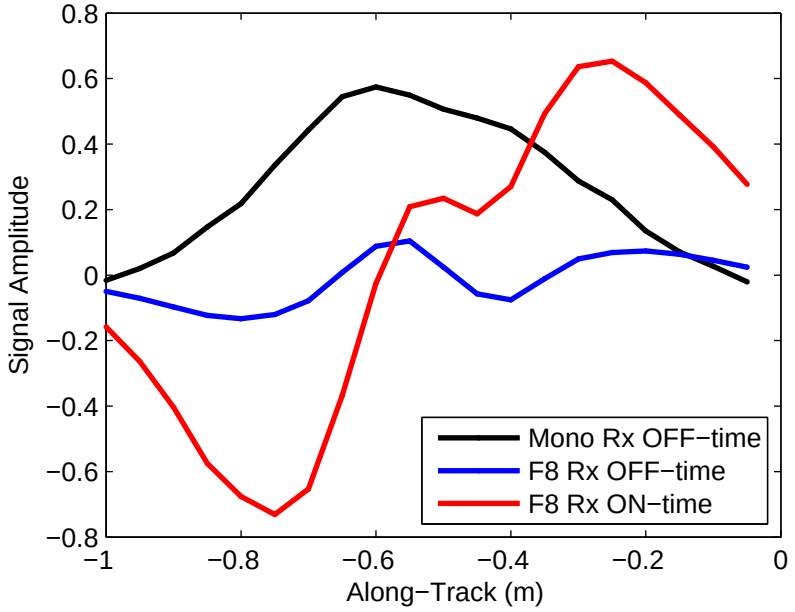

2.54 cm diameter steel rod, 30 cm depth

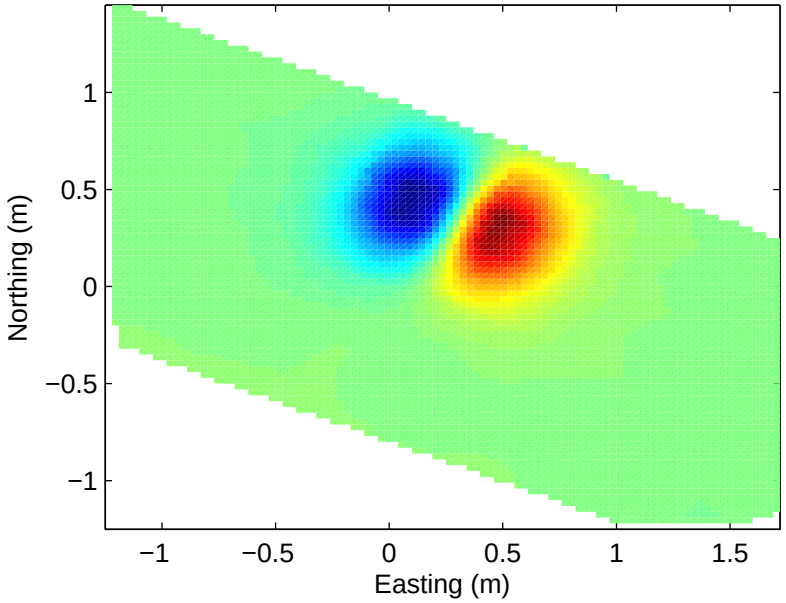

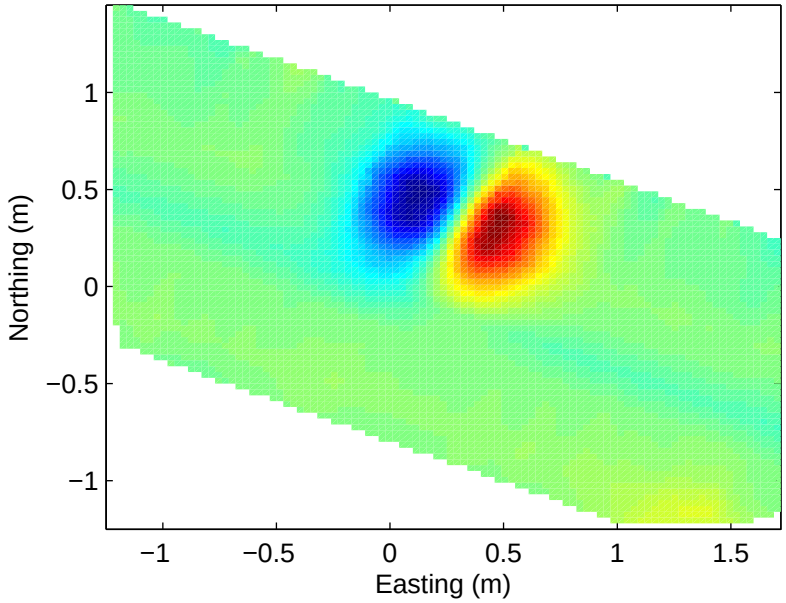

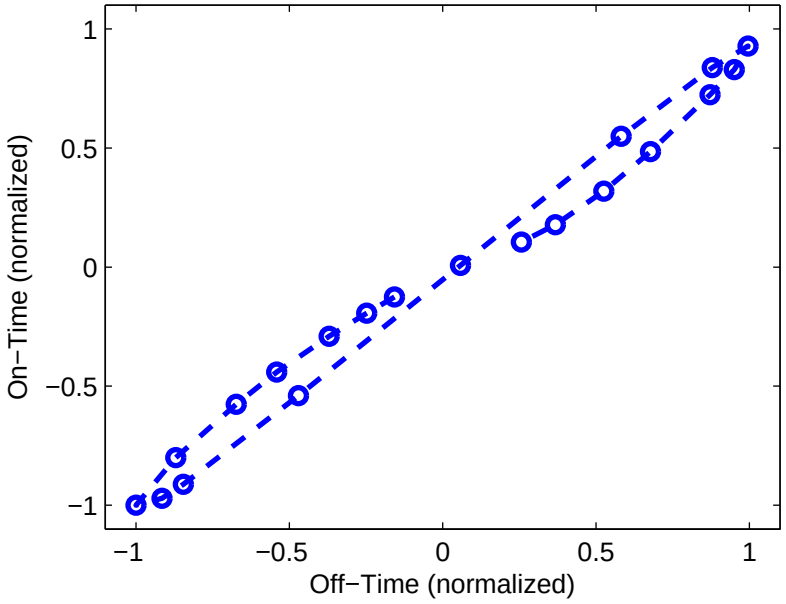

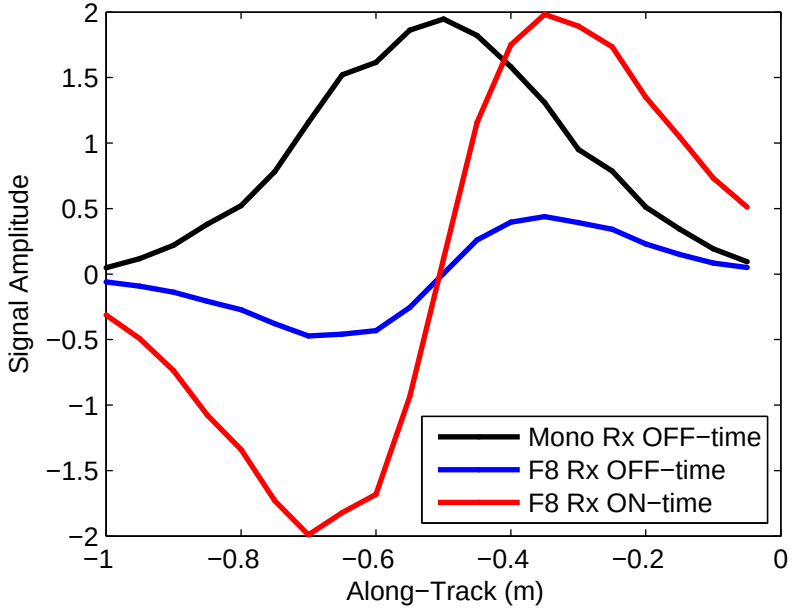

2.54 cm diameter steel rod, 30 cm depth

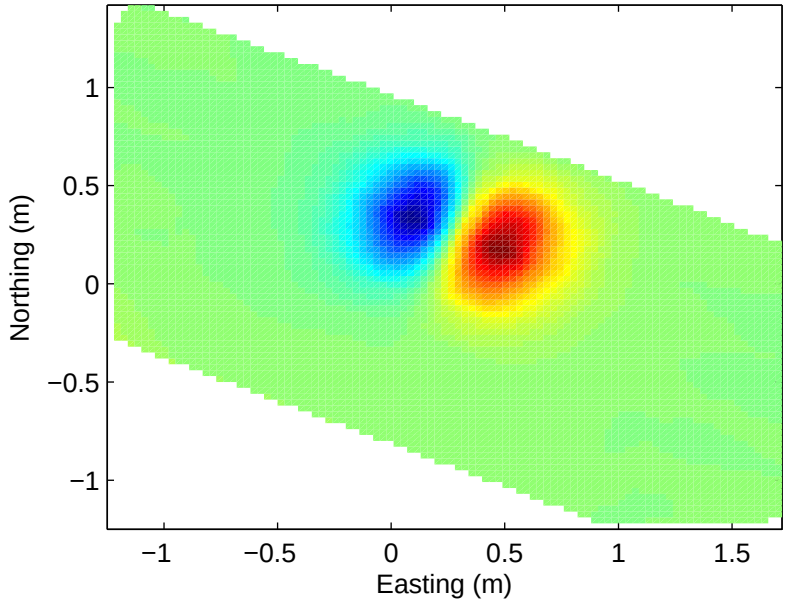

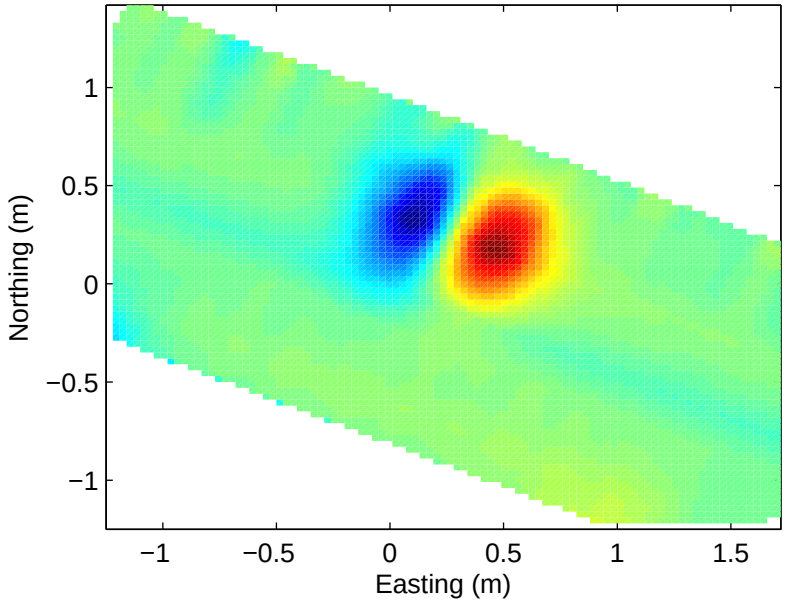

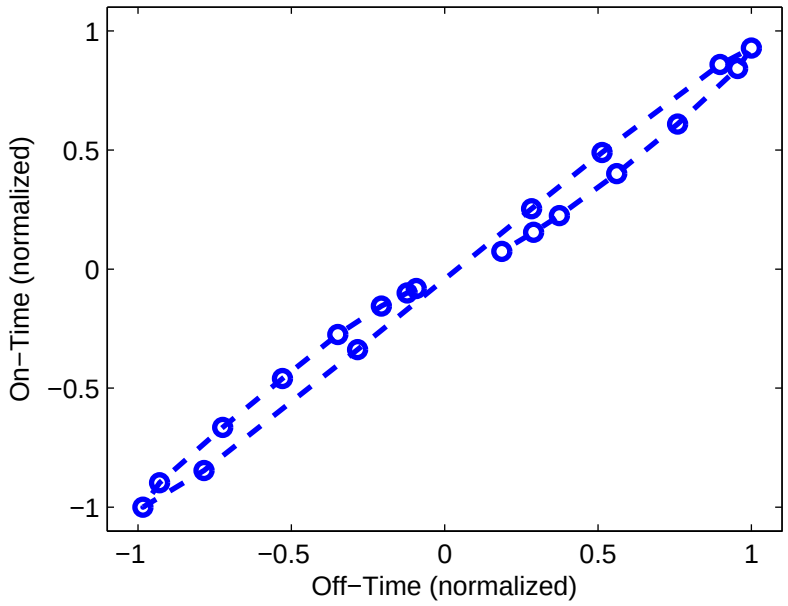

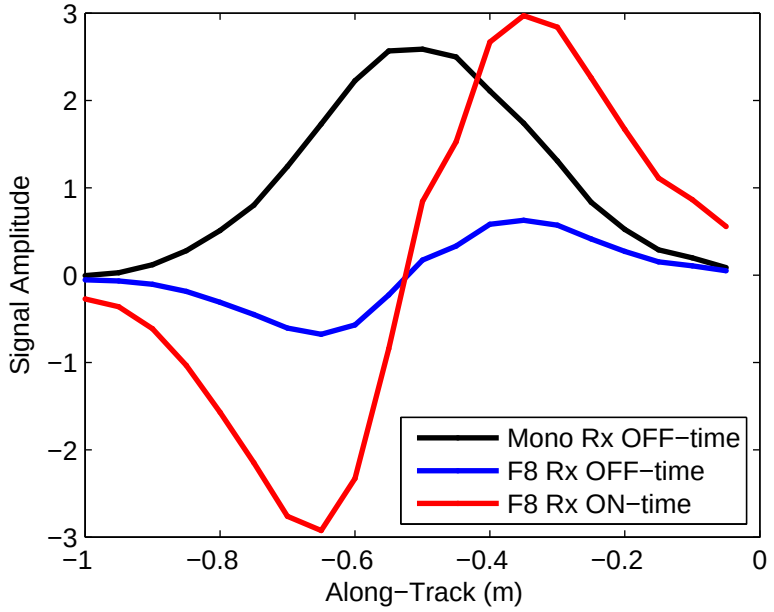

2.54 cm diameter steel rod, 30 cm depth

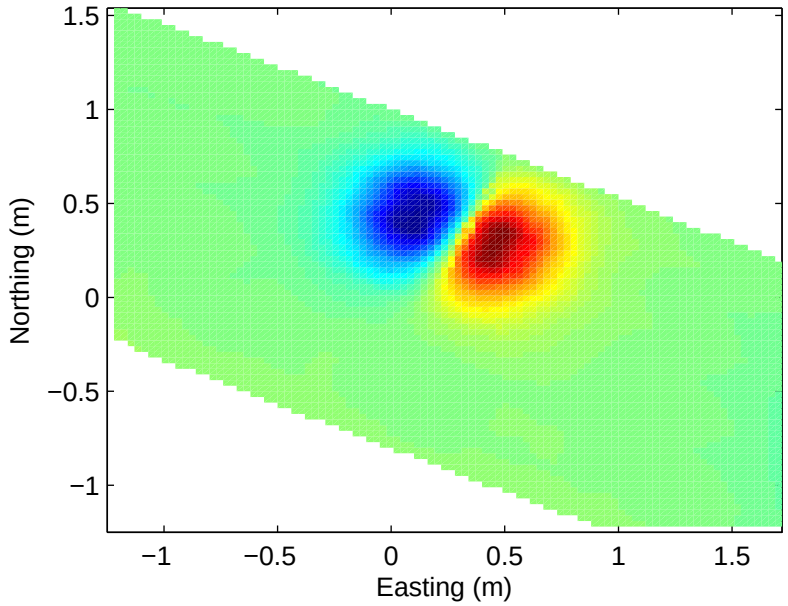

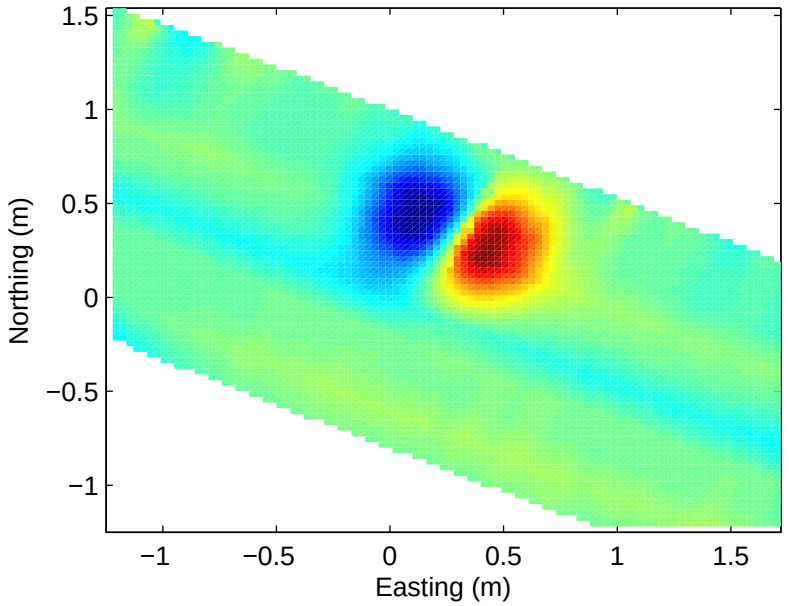

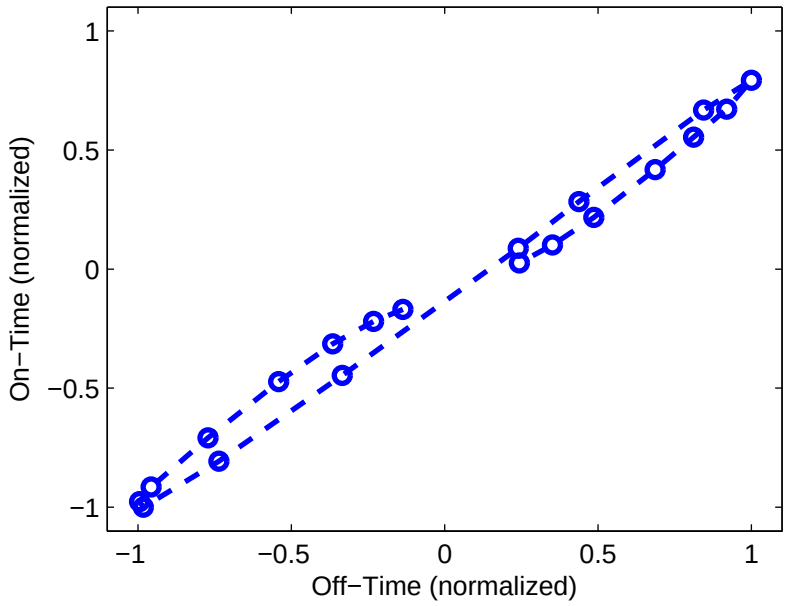

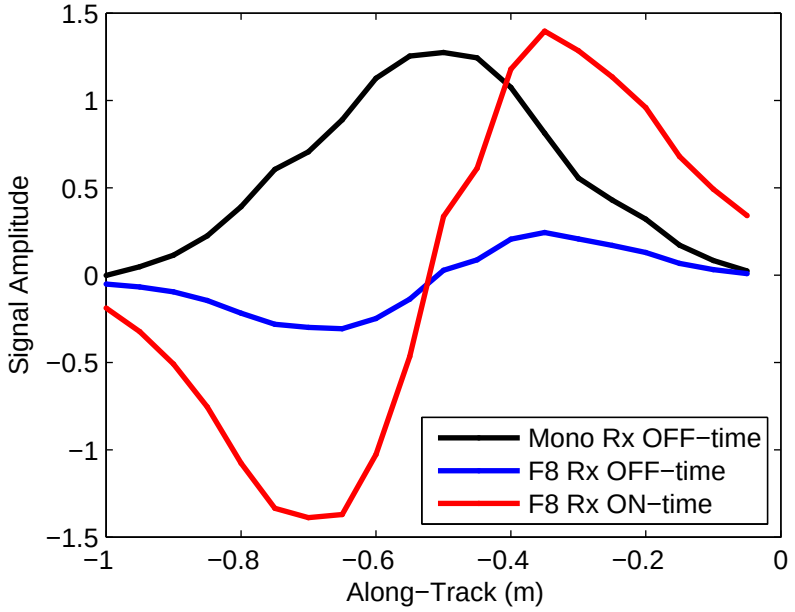

15.25 cm diameter steel cylinder, 45 cm depth

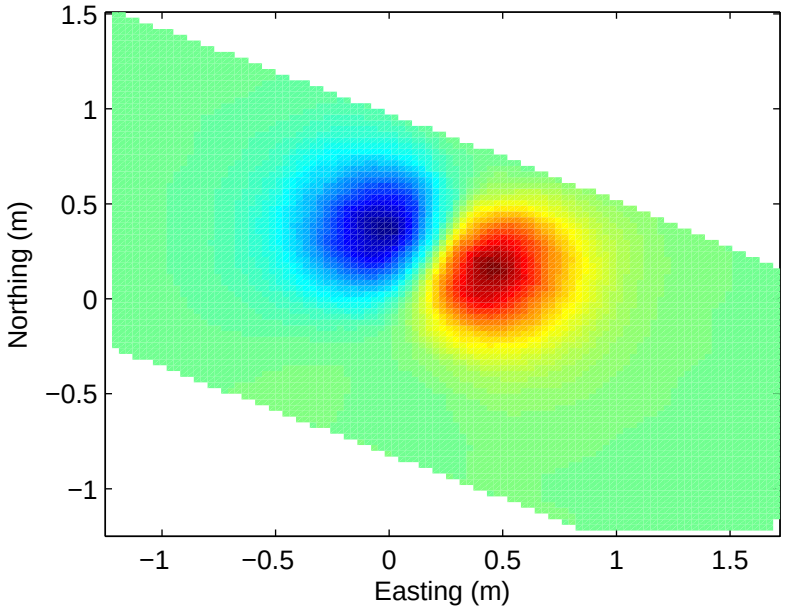

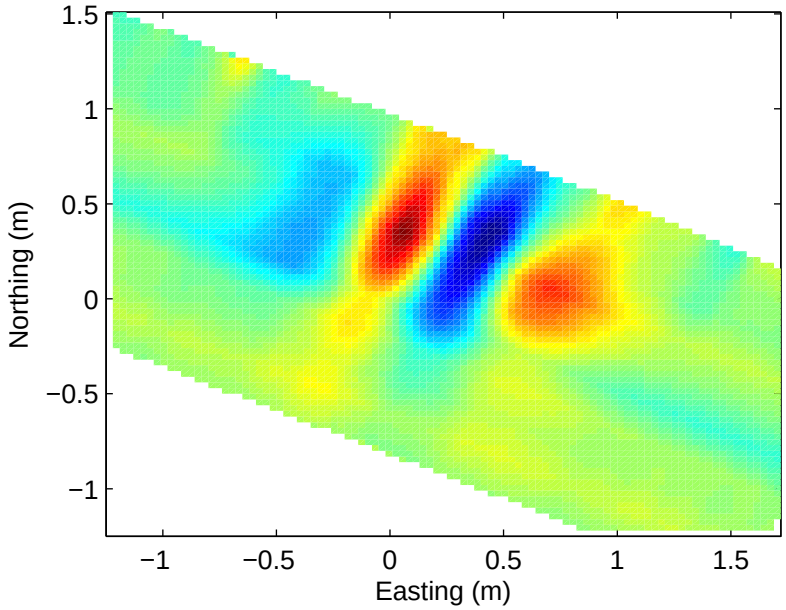

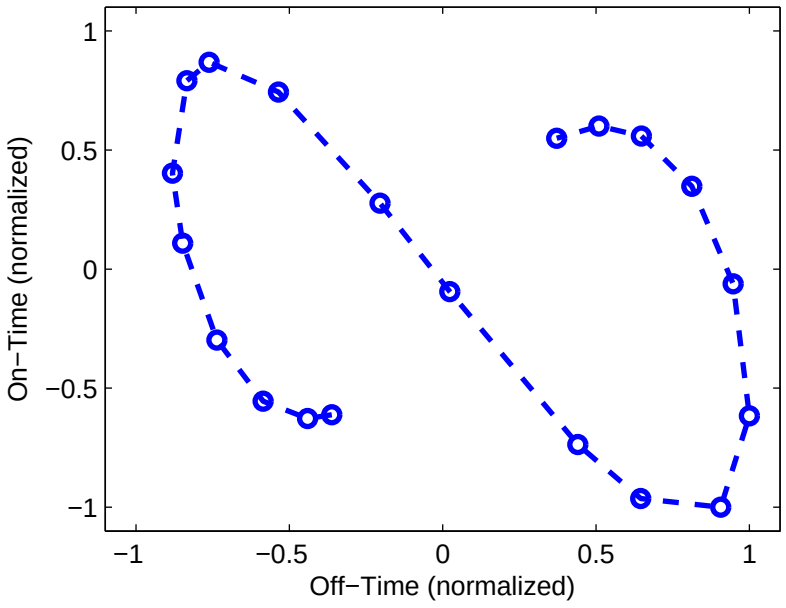

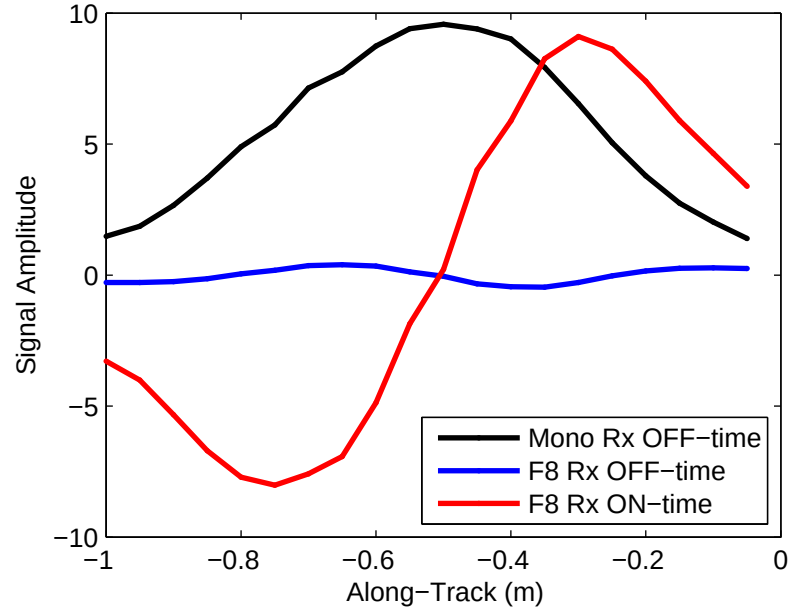

11.5 cm diameter steel cylinder, 45 cm depth

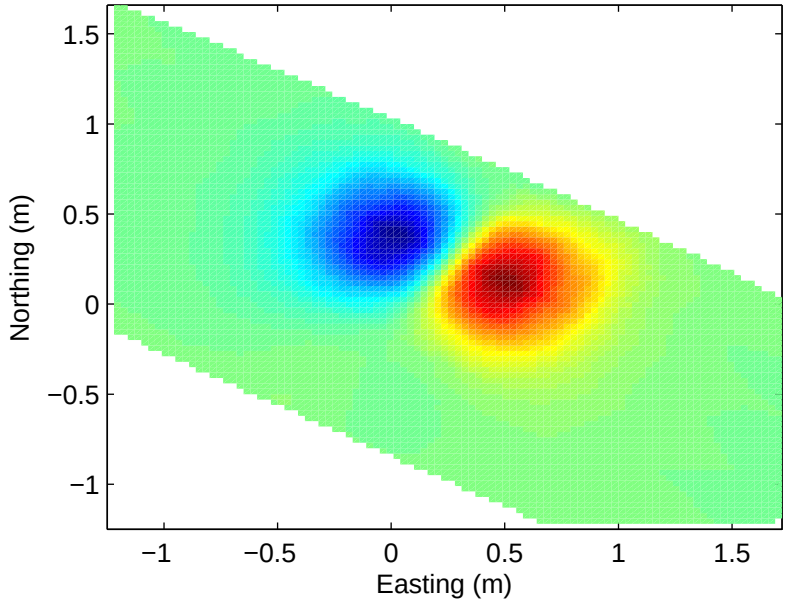

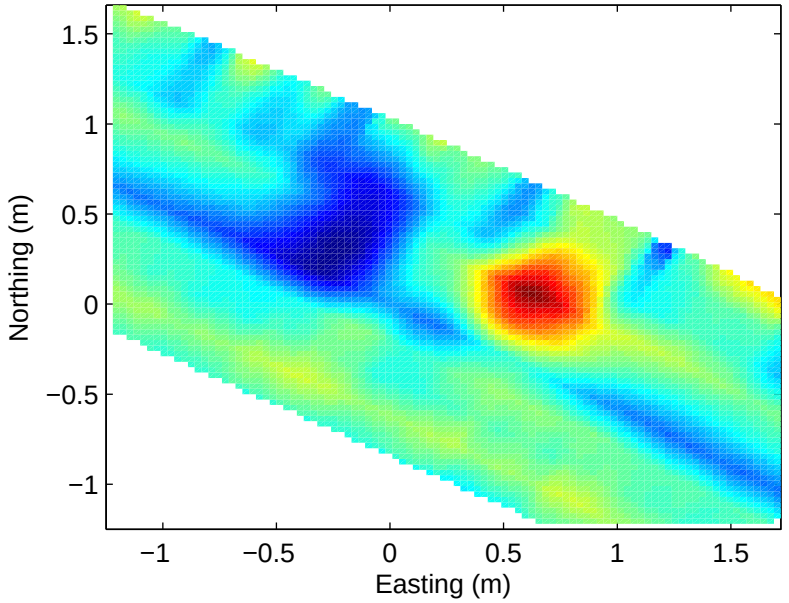

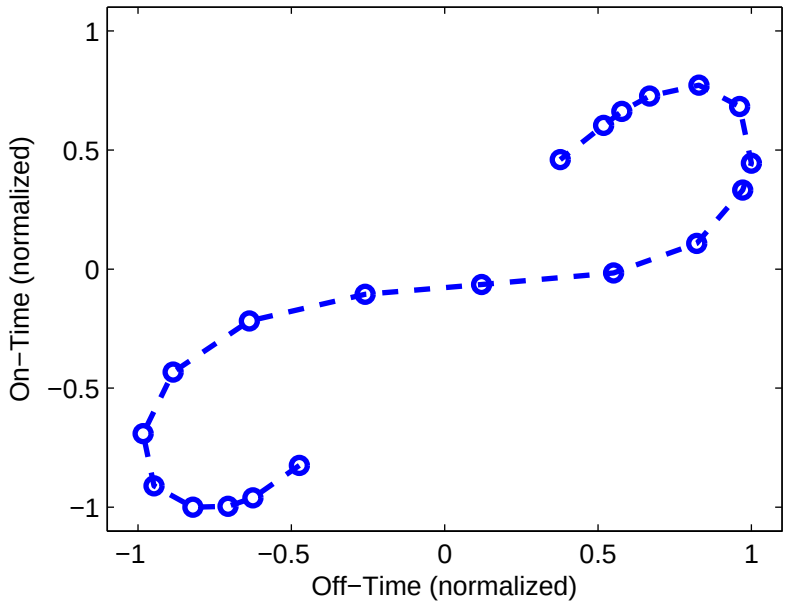

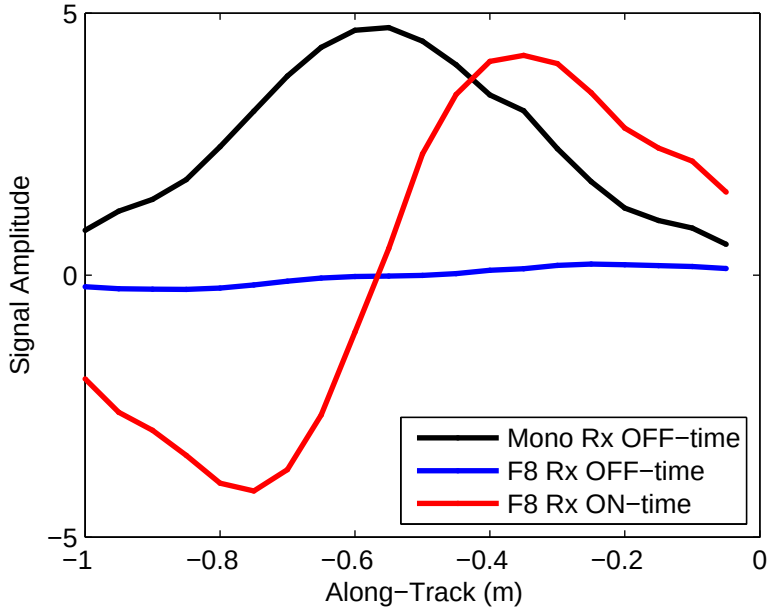

7.6 cm diameter steel cylinder, 45 cm depth

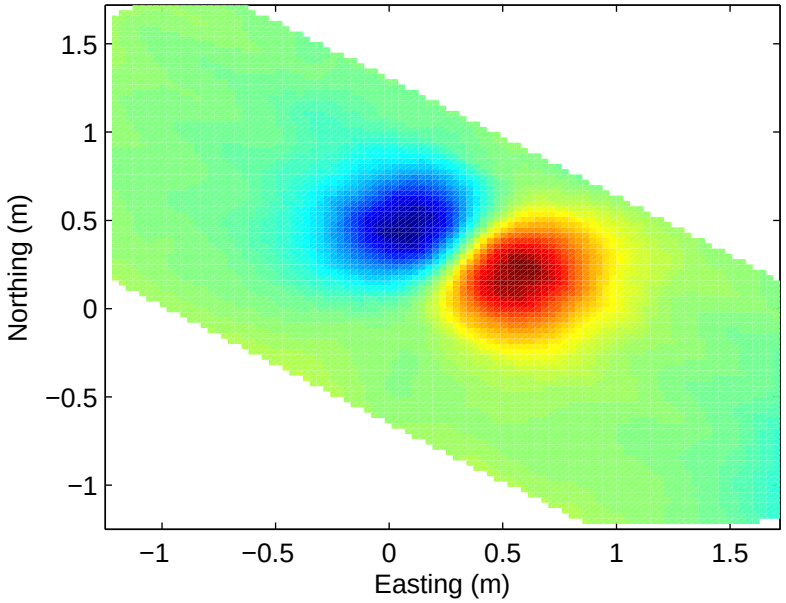

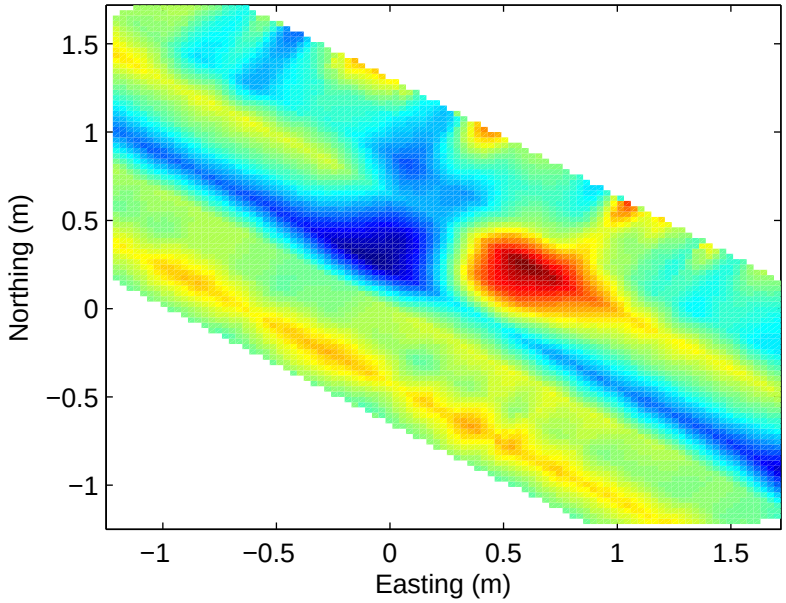

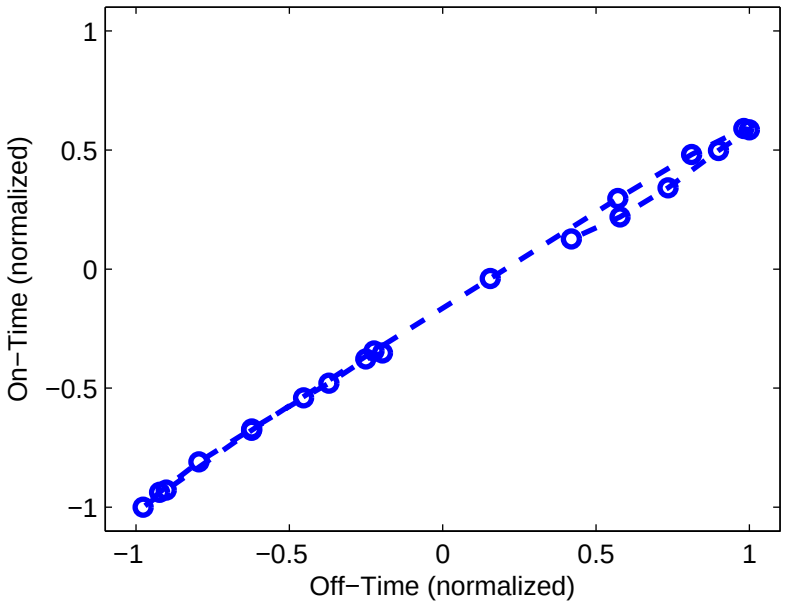

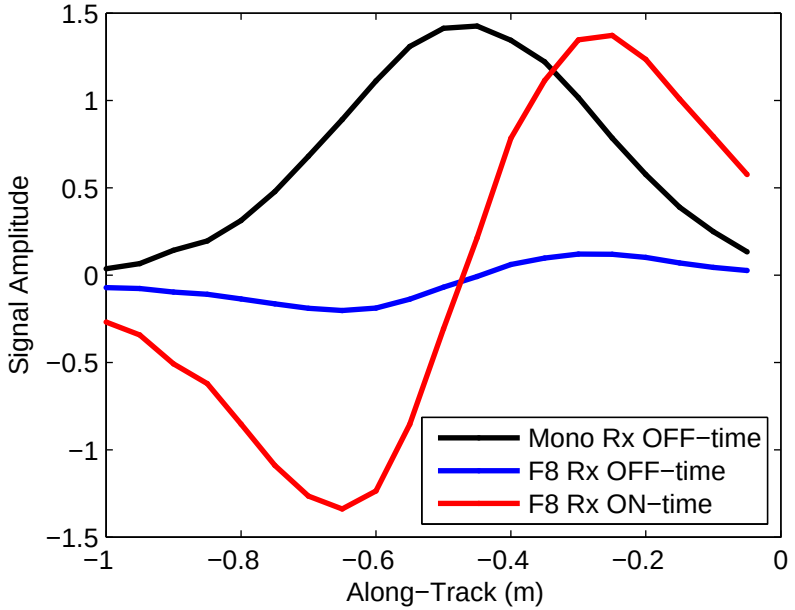

15.25 cm diameter steel disc, 45 cm depth

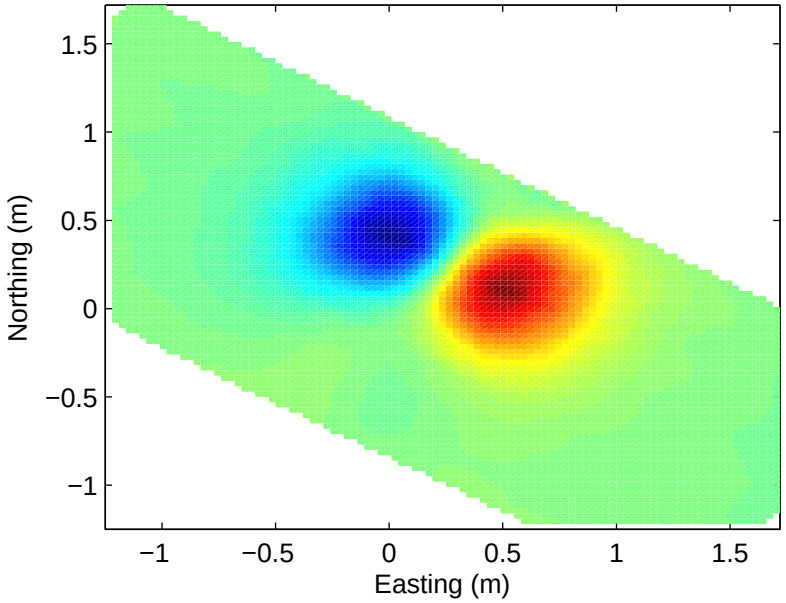

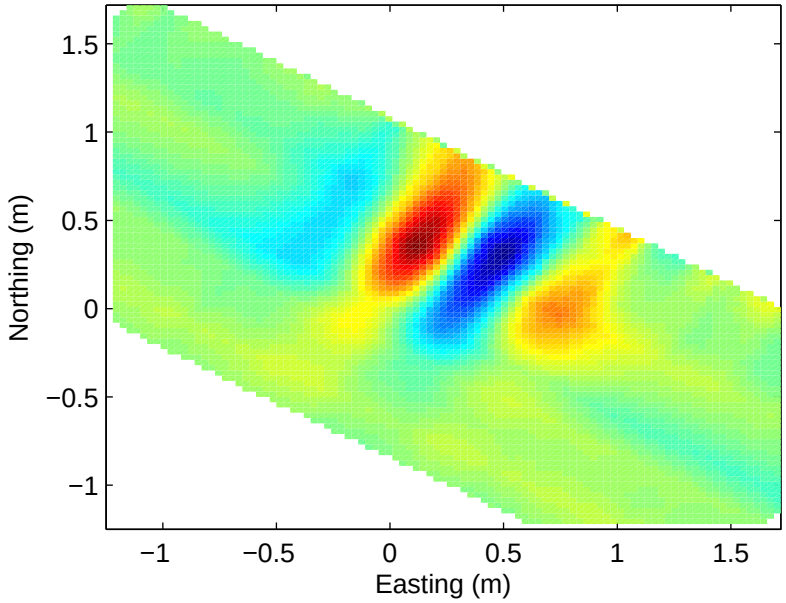

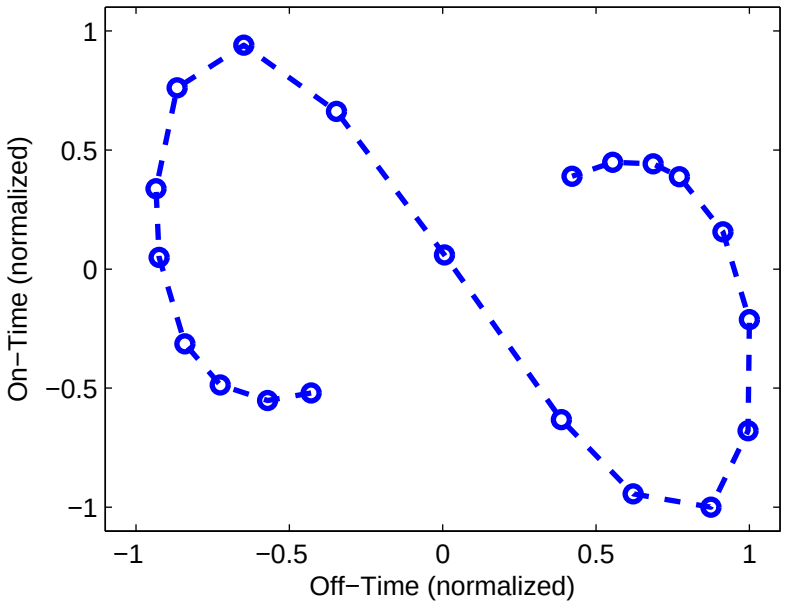

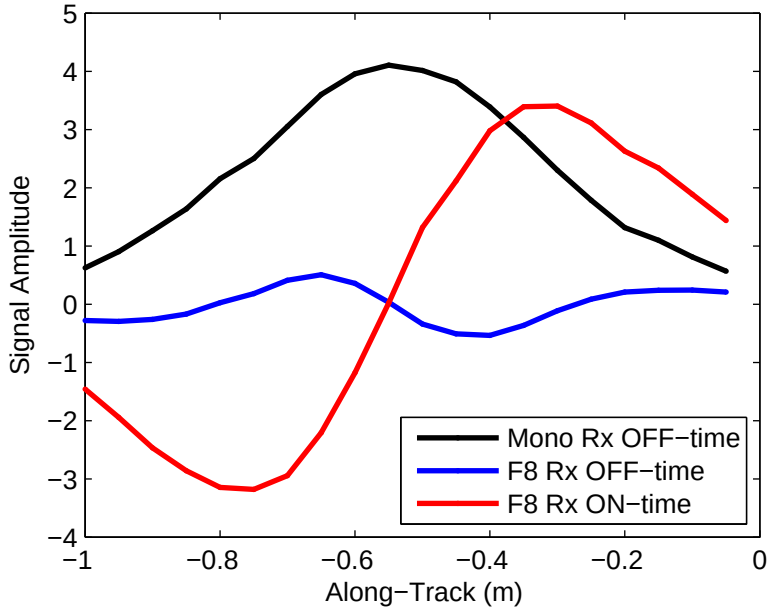

11.5 cm diameter steel disc, 45 cm depth

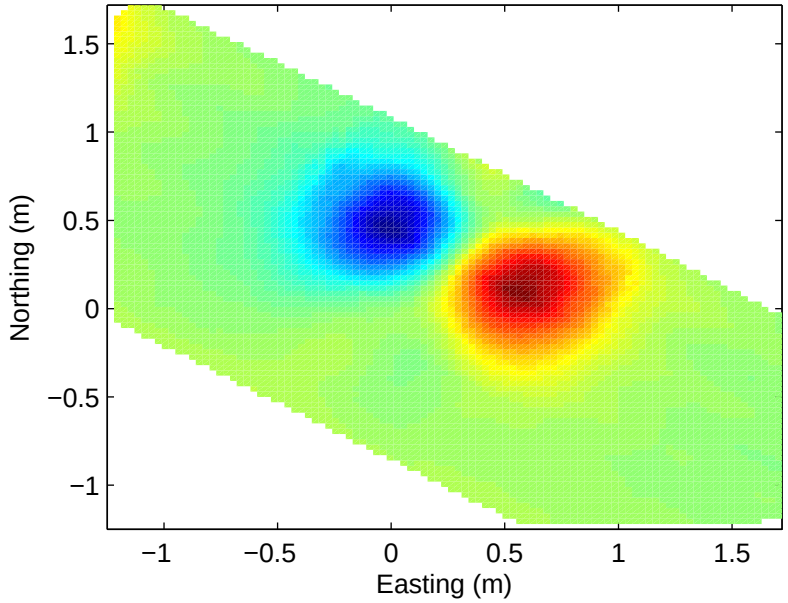

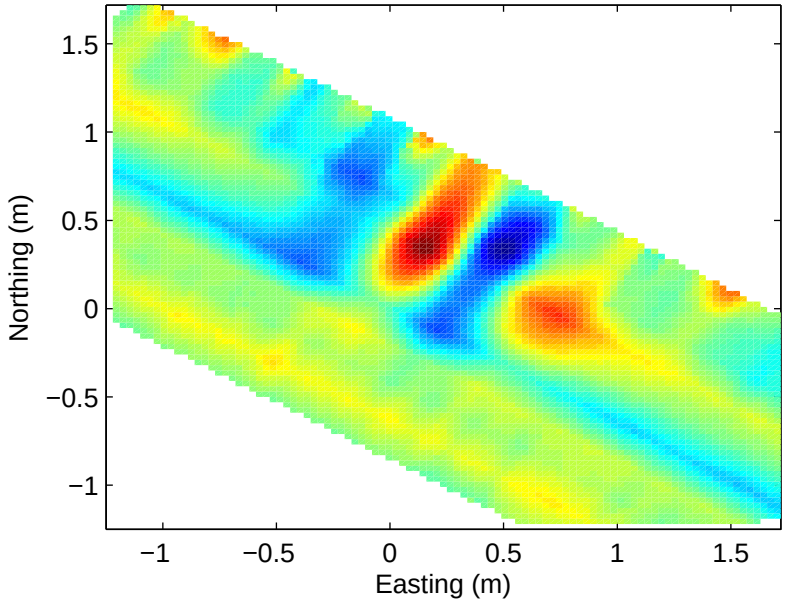

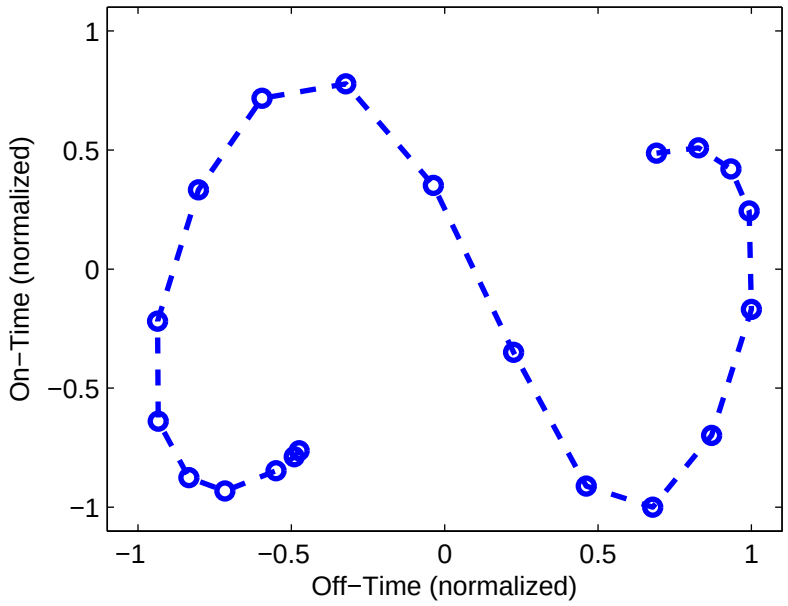

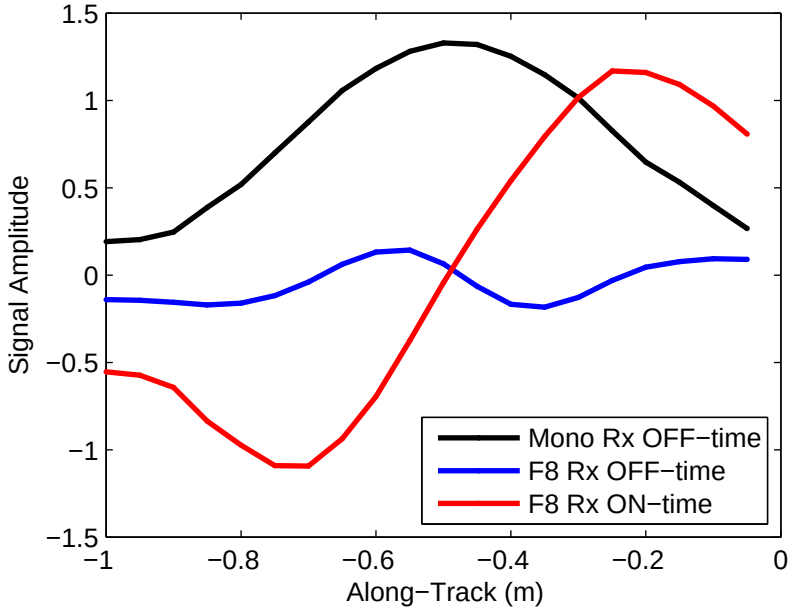

7.6 cm diameter steel disc, 45 cm depth

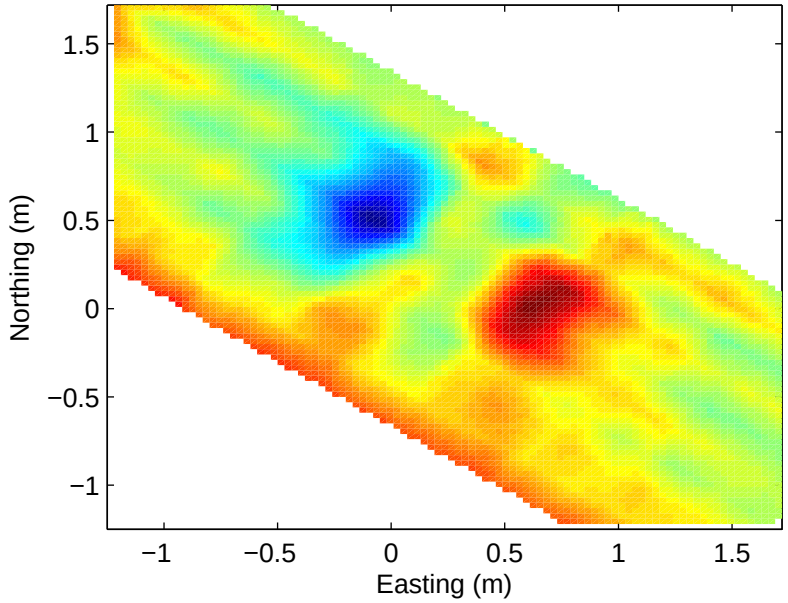

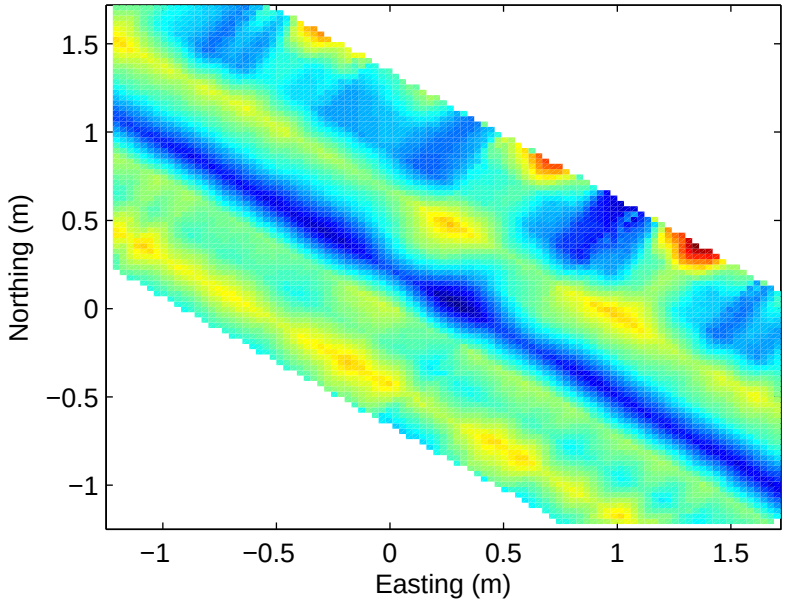

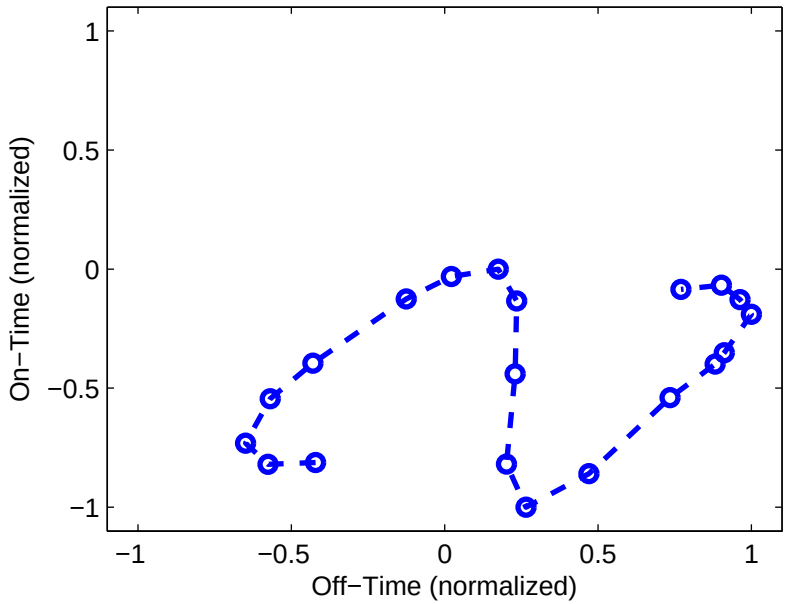

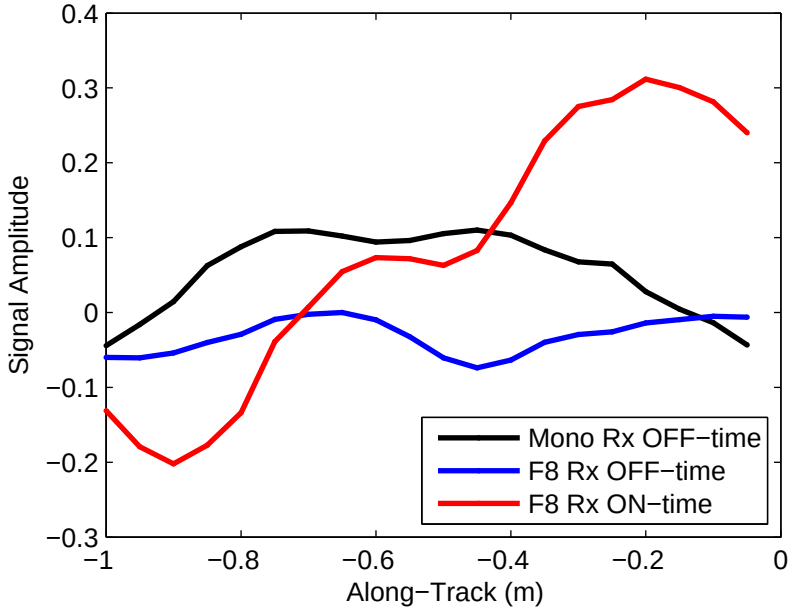

2.54 cm diameter steel rod, 45 cm depth

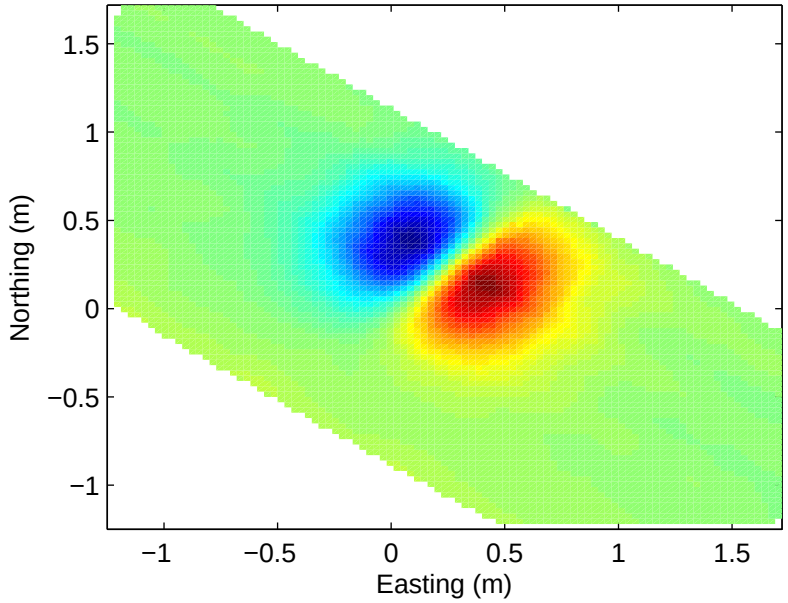

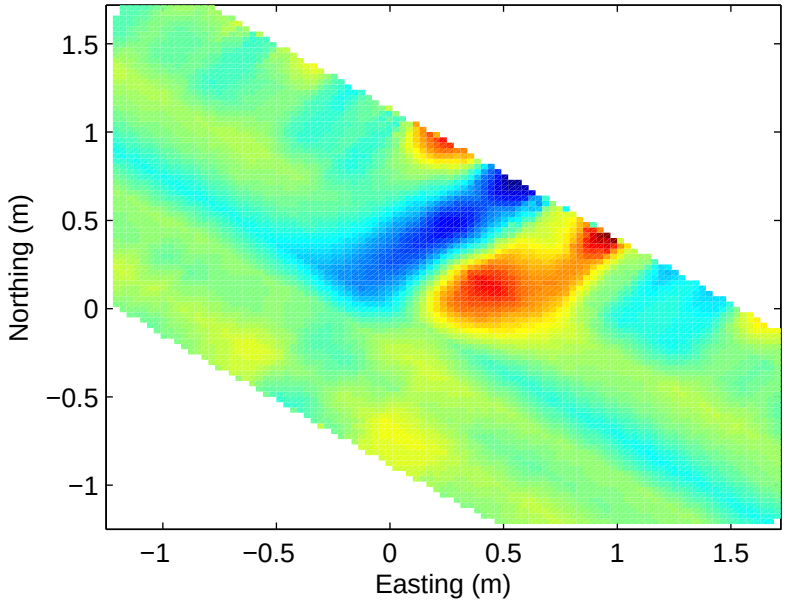

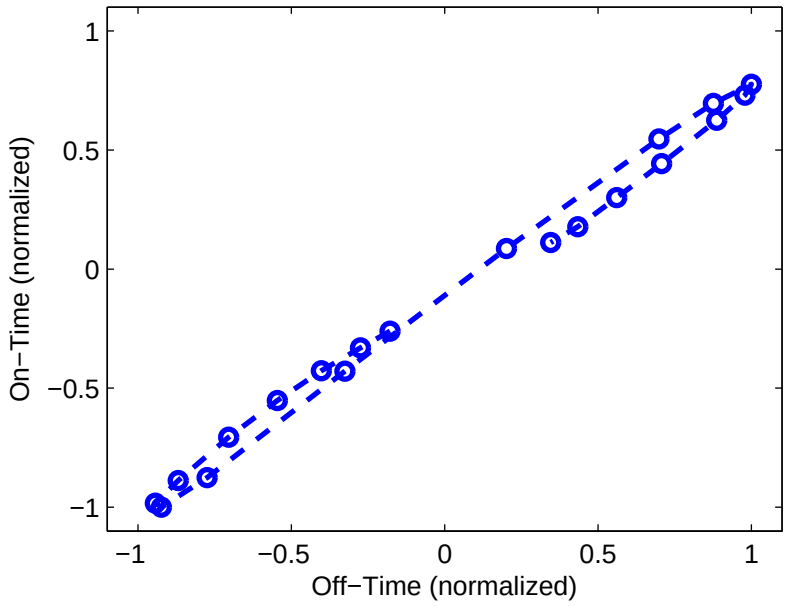

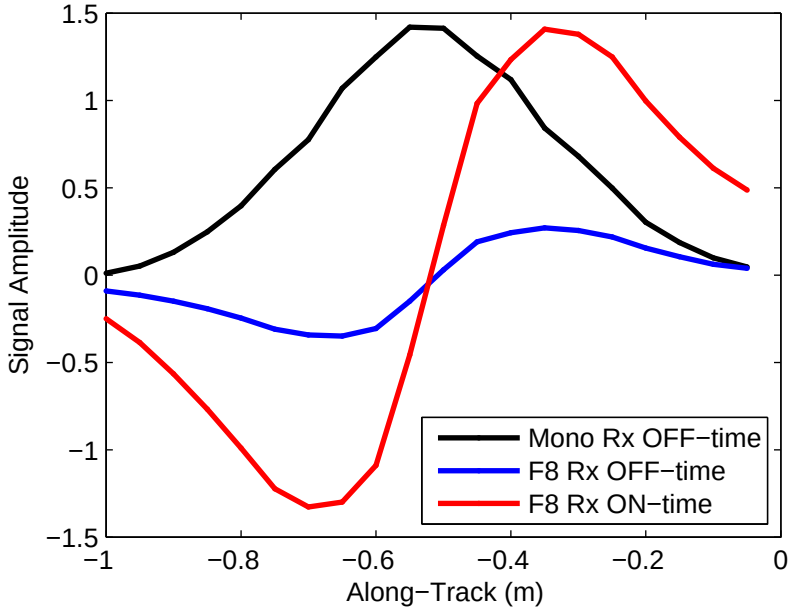

2.54 cm diameter steel rod, 45 cm depth

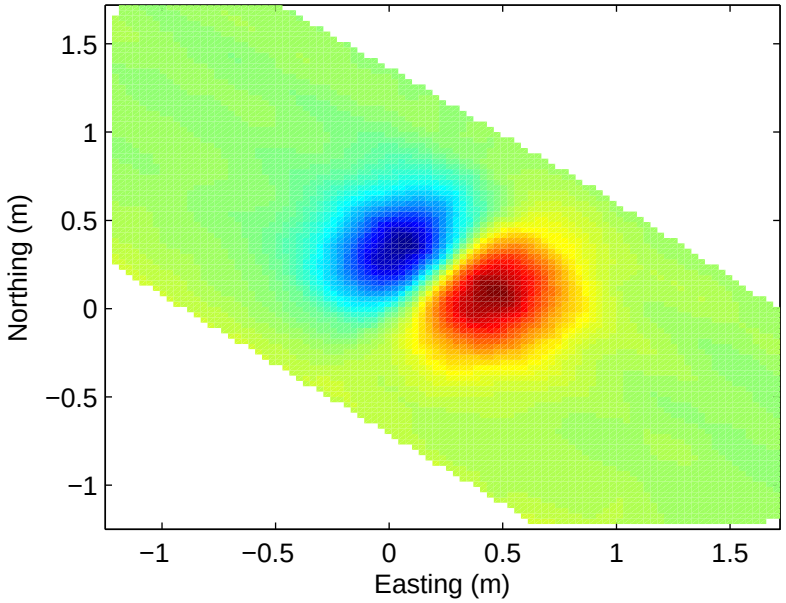

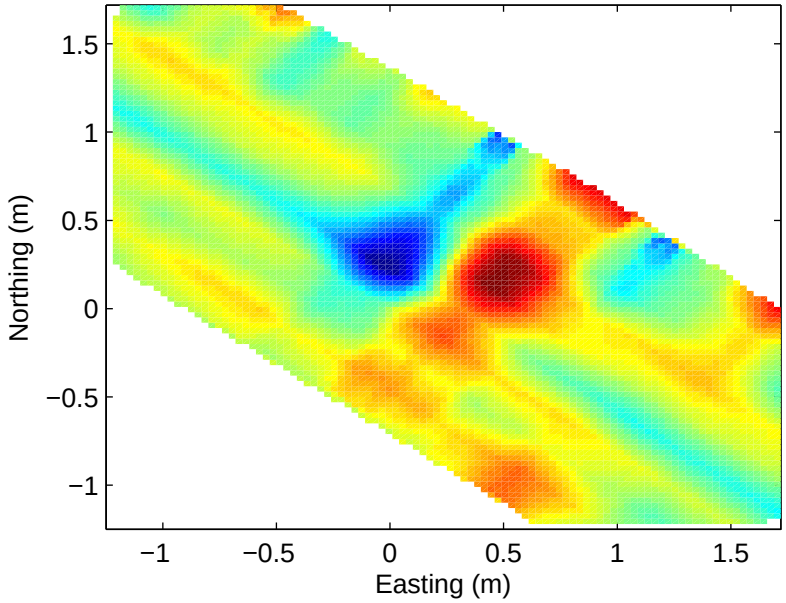

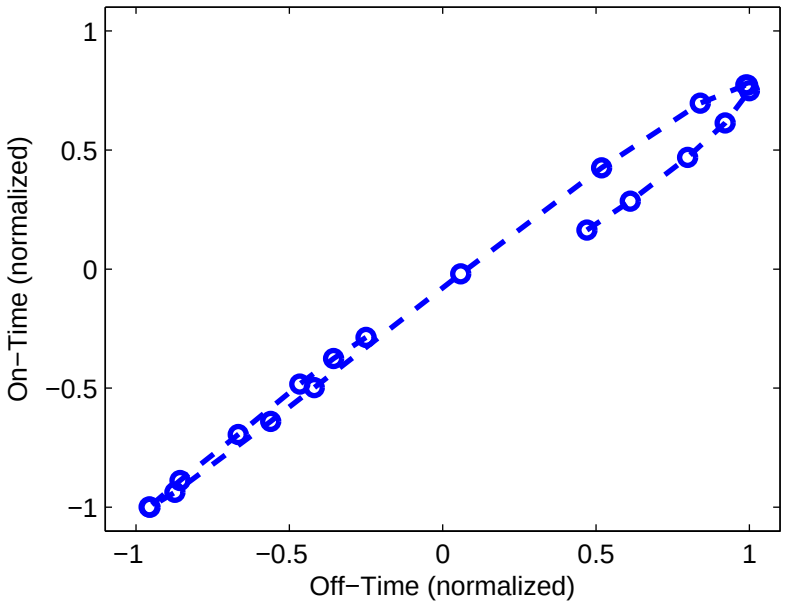

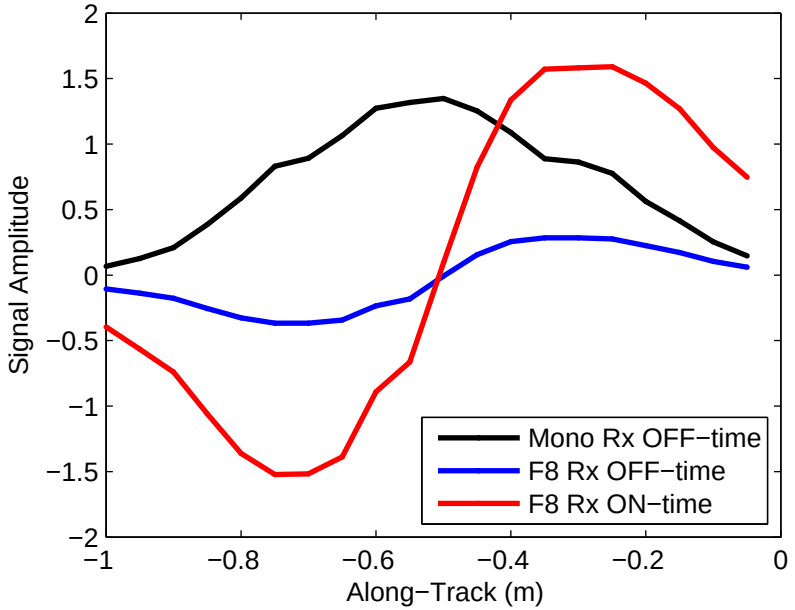

2.54 cm diameter steel rod, 45 cm depth

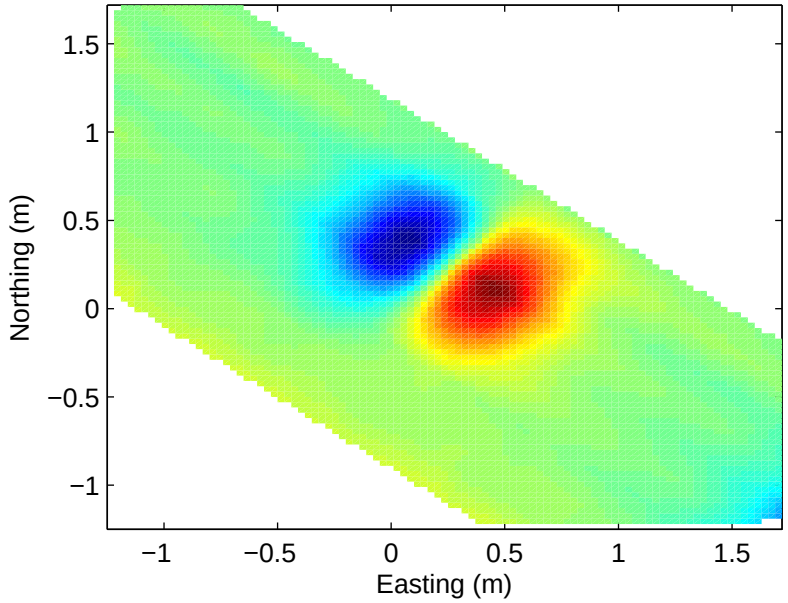

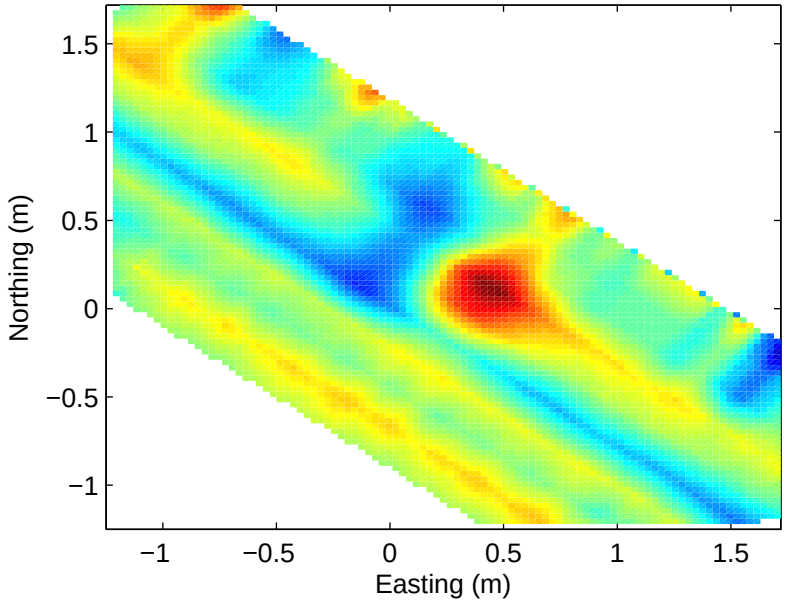

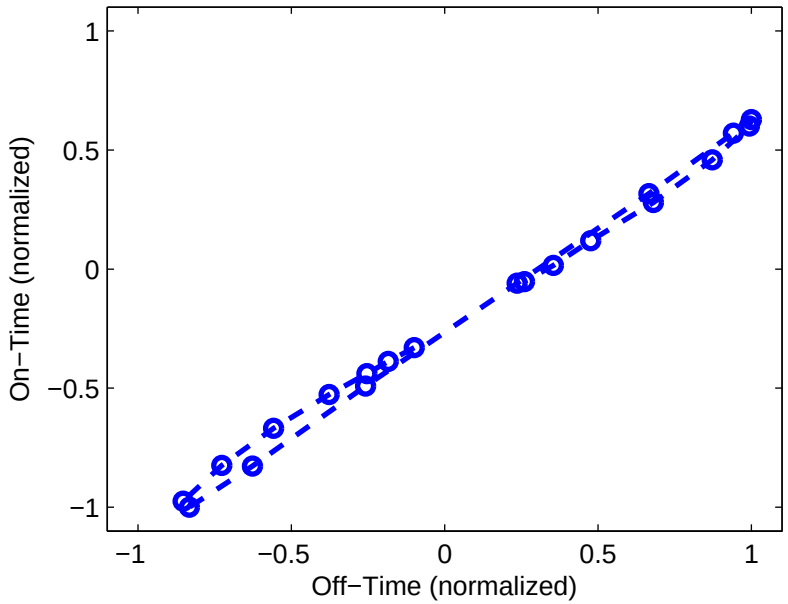

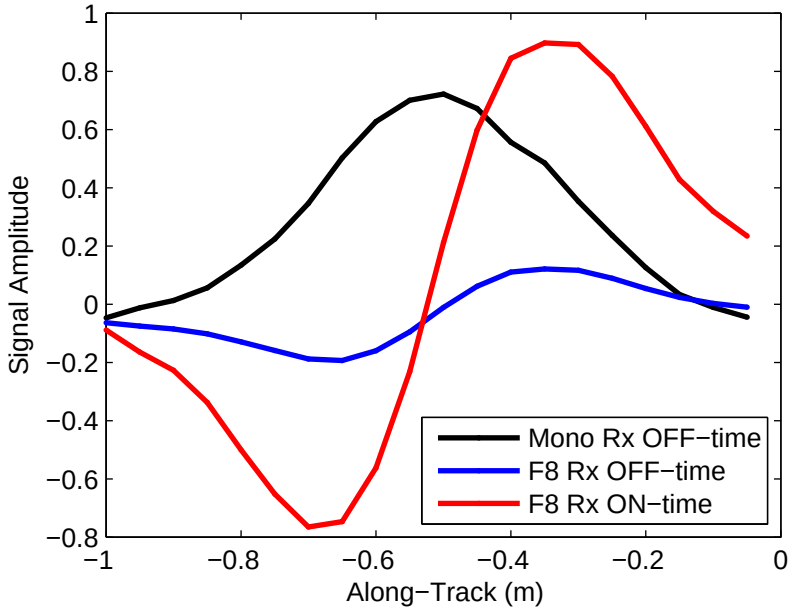

15.25 cm diameter steel cylinder, 60 cm depth

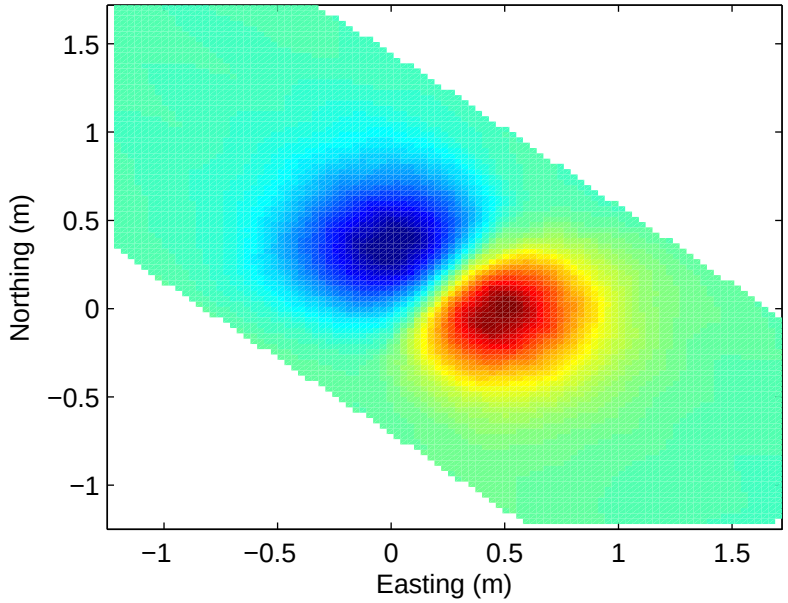

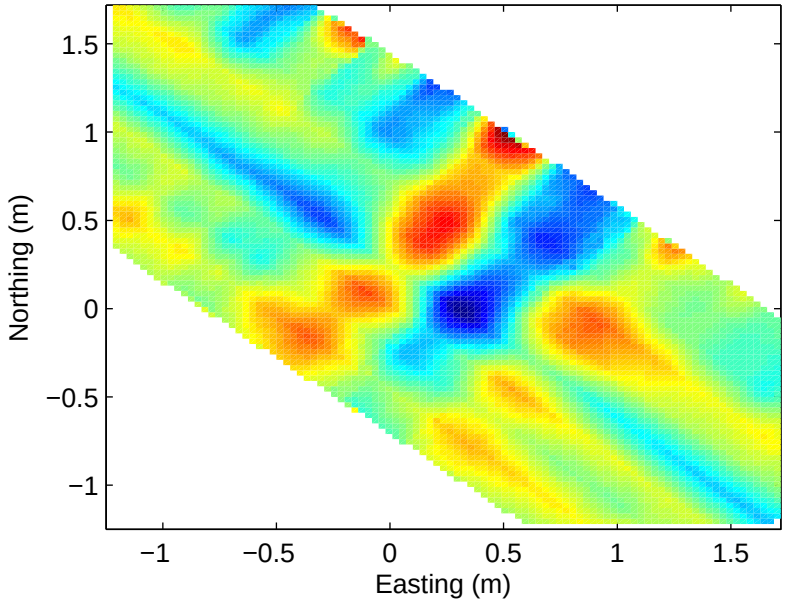

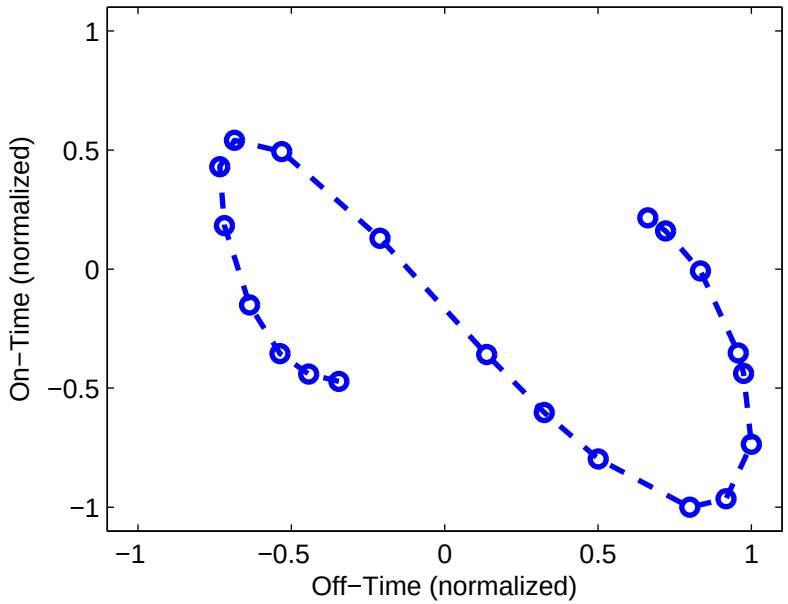

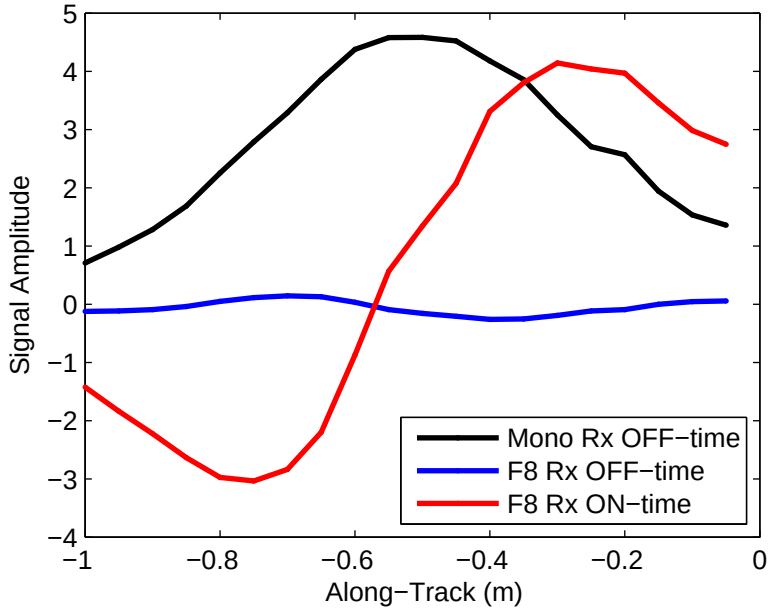

11.5 cm diameter steel cylinder, 60 cm depth

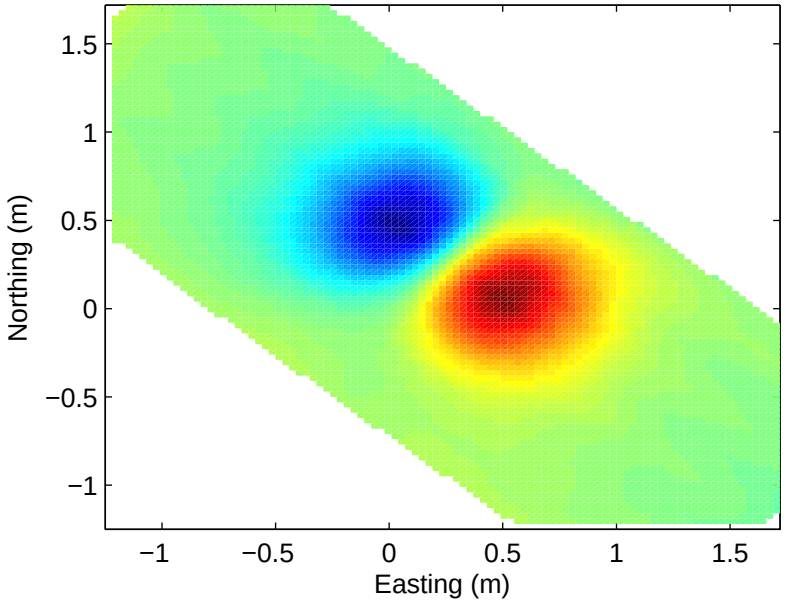

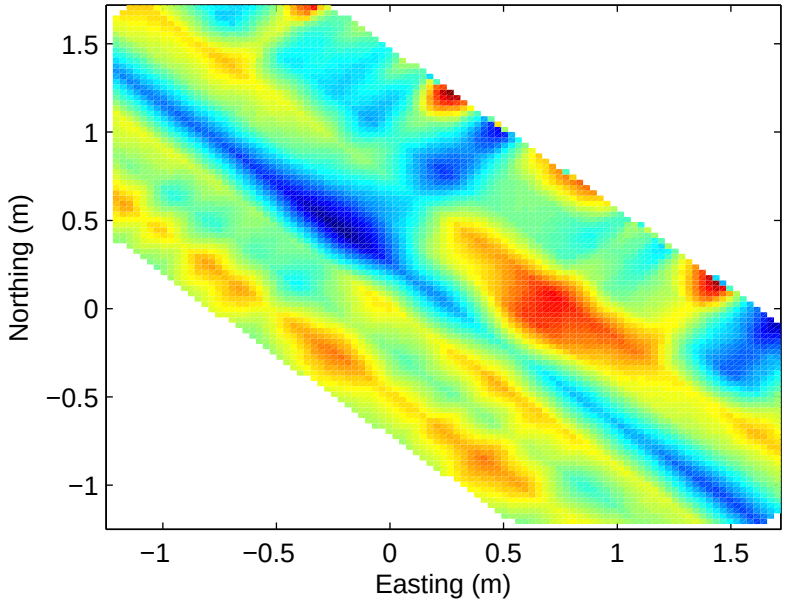

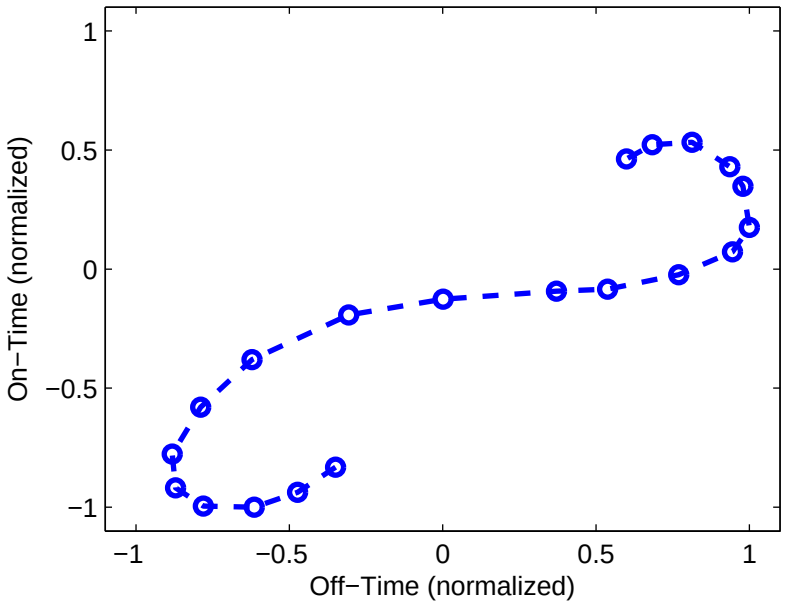

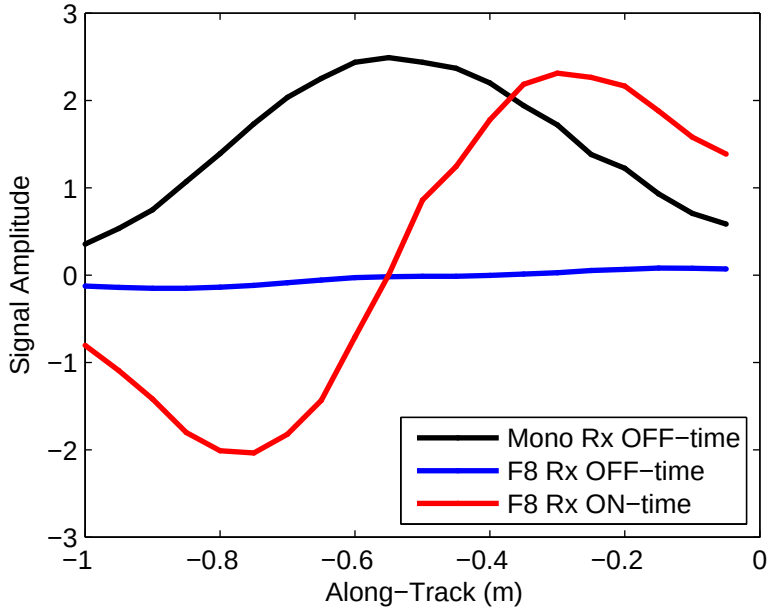

7.6 cm diameter steel cylinder, 60 cm depth

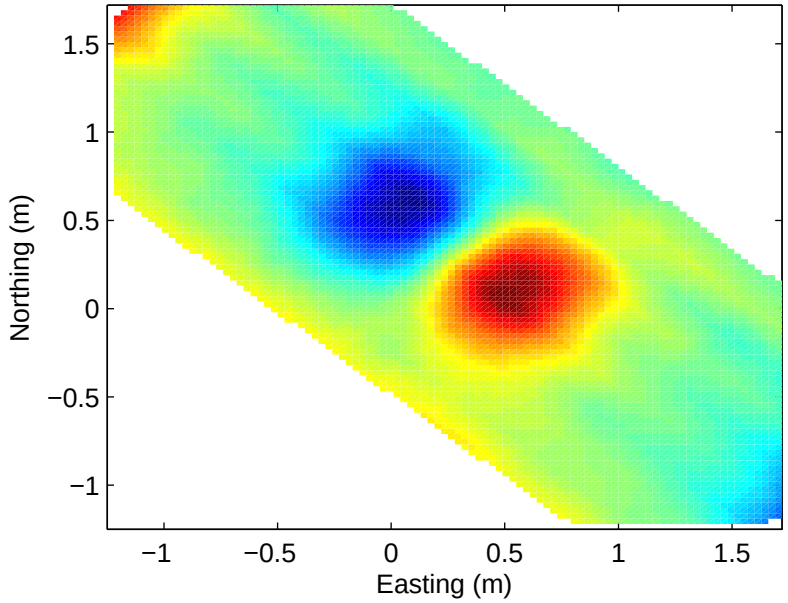

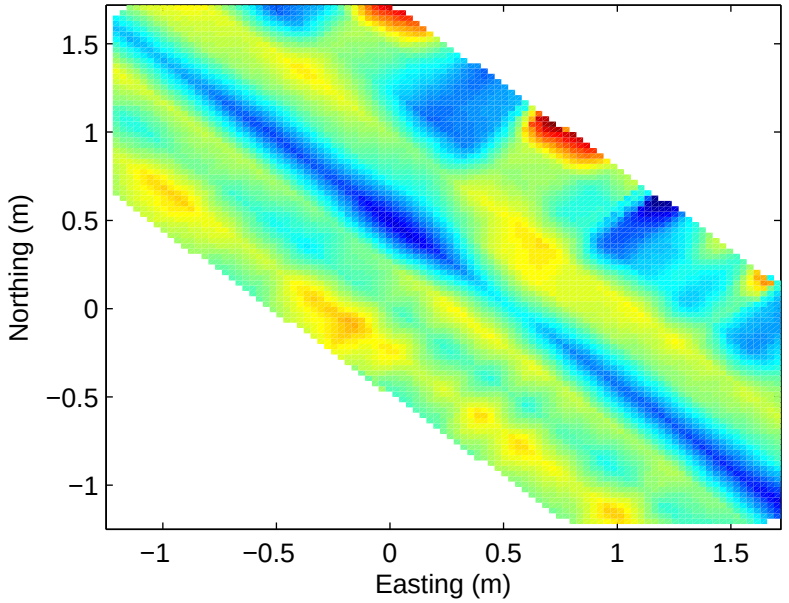

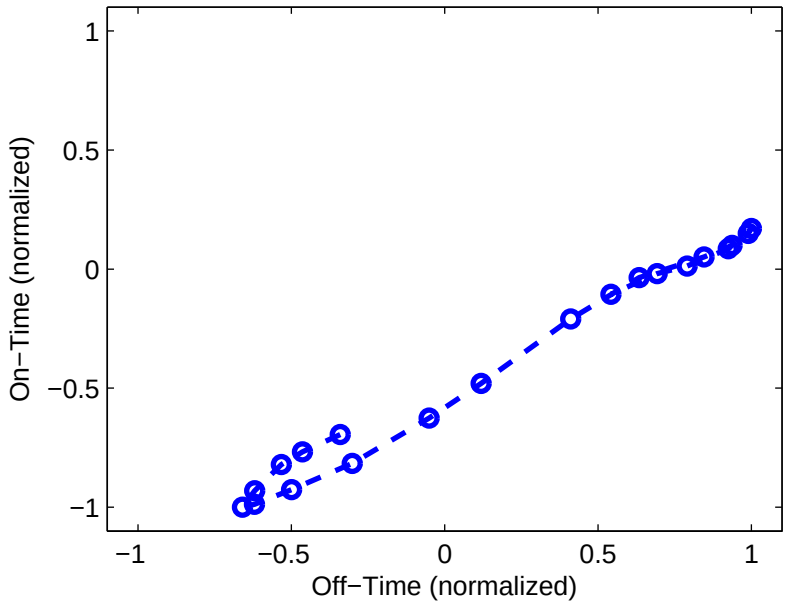

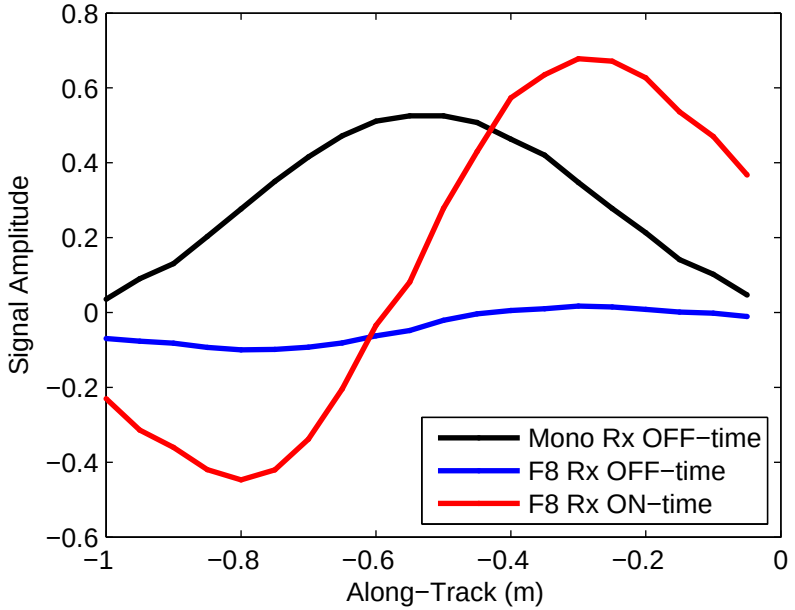

15.25 cm diameter steel disc, 60 cm depth

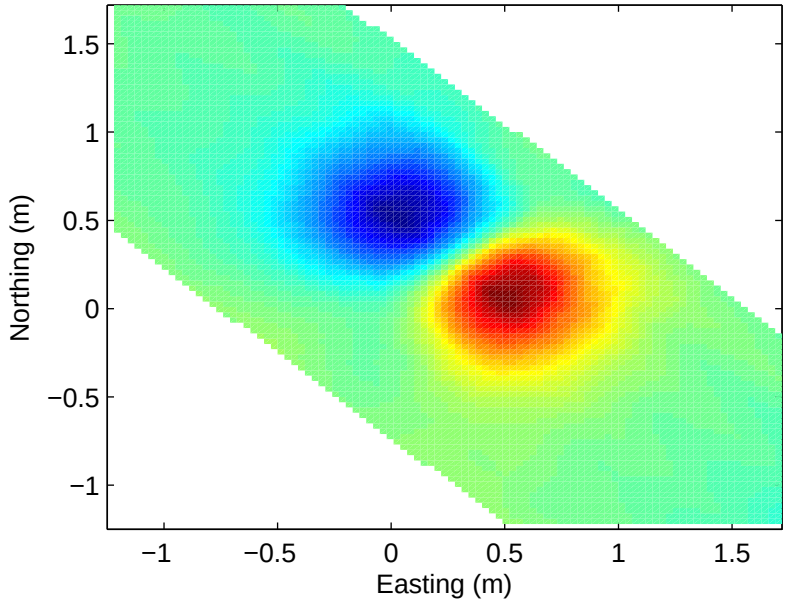

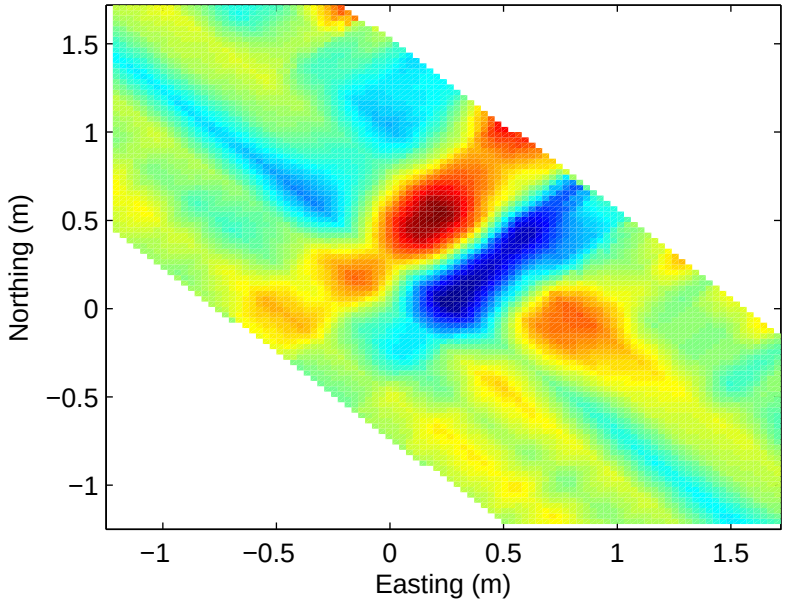

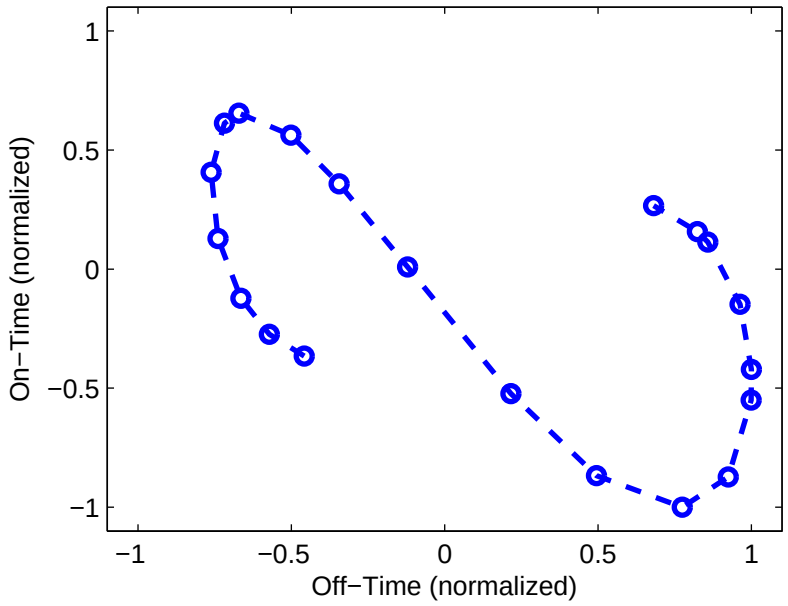

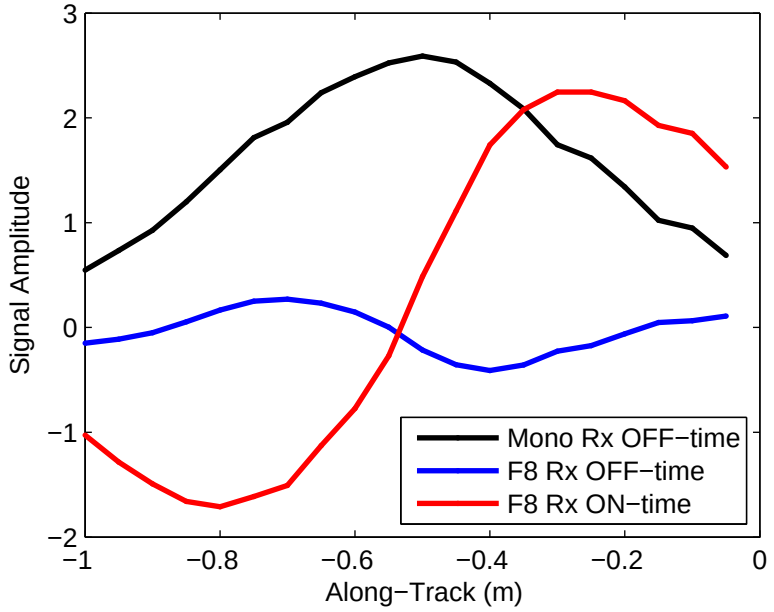

11.5 cm diameter steel disc, 60 cm depth

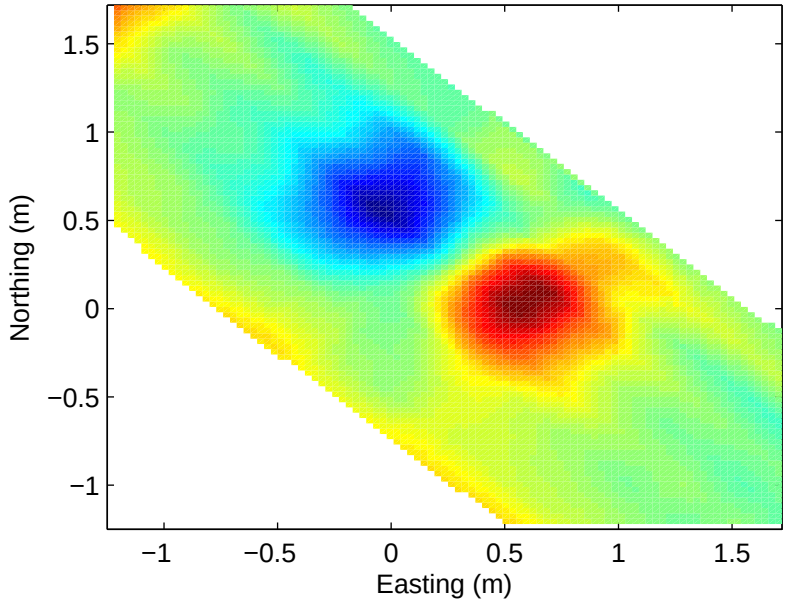

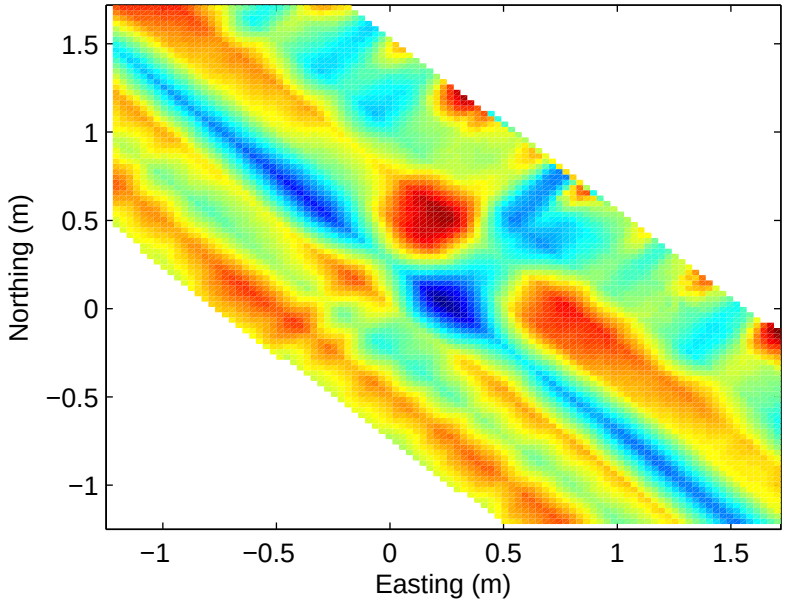

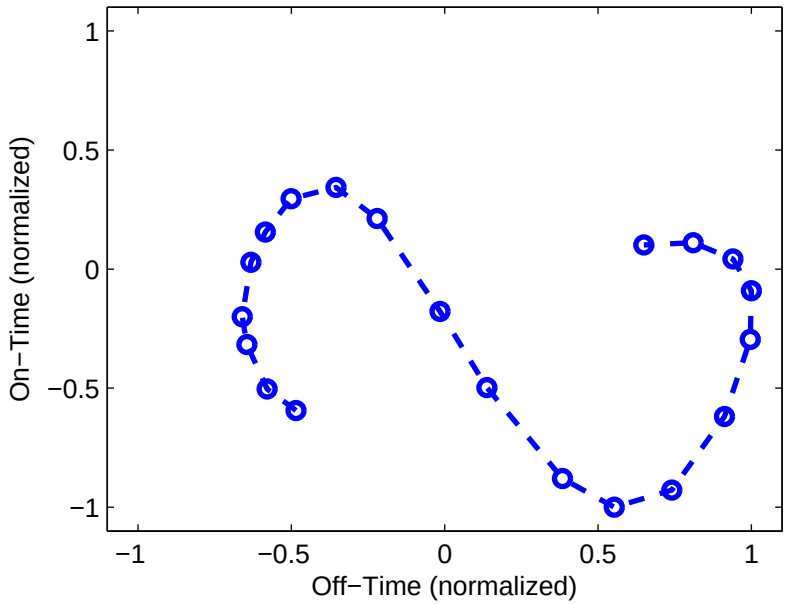

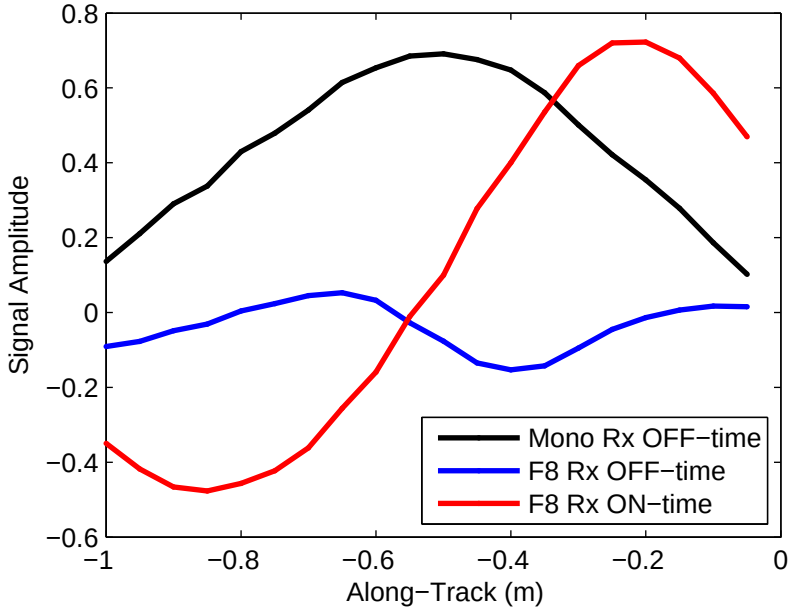

7.6 cm diameter steel disc, 60 cm depth

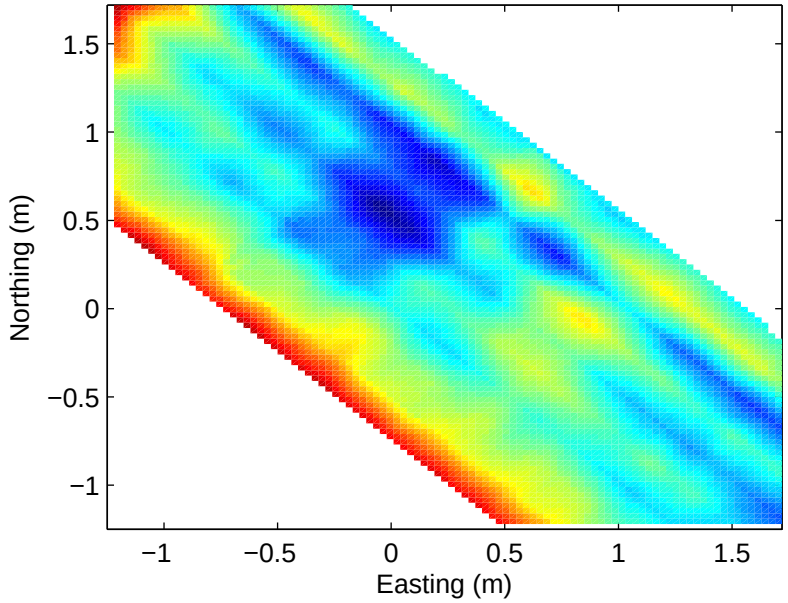

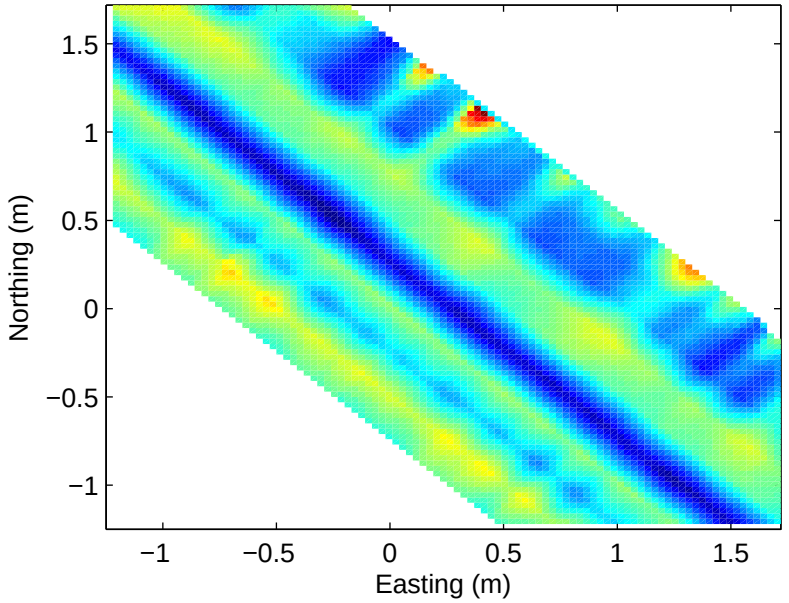

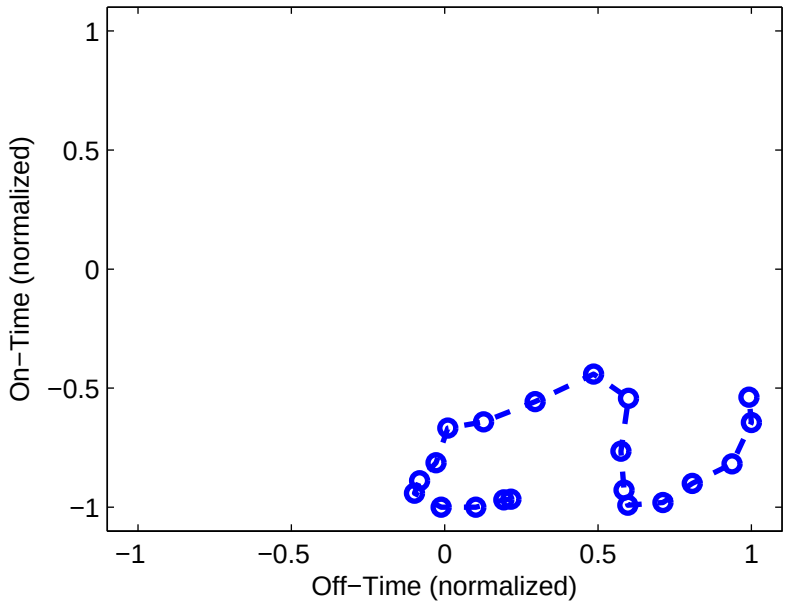

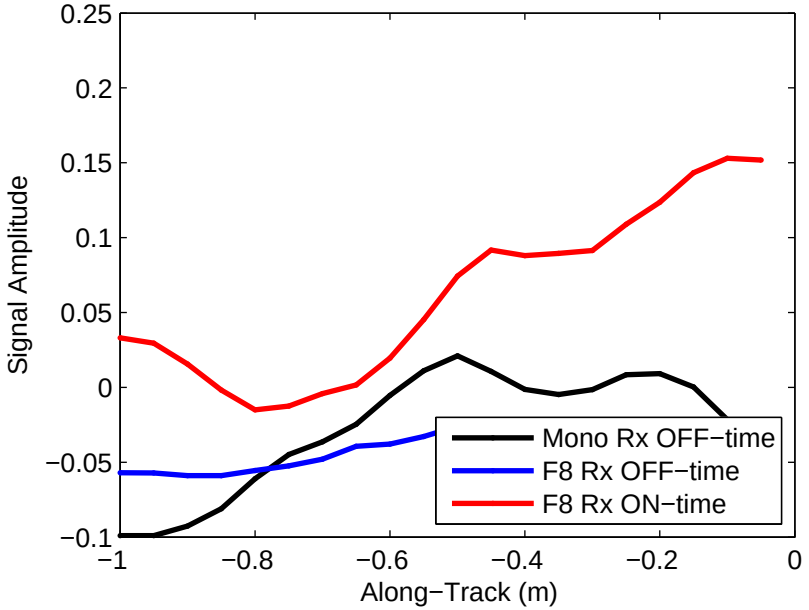

2.54 cm diameter steel rod, 60 cm depth

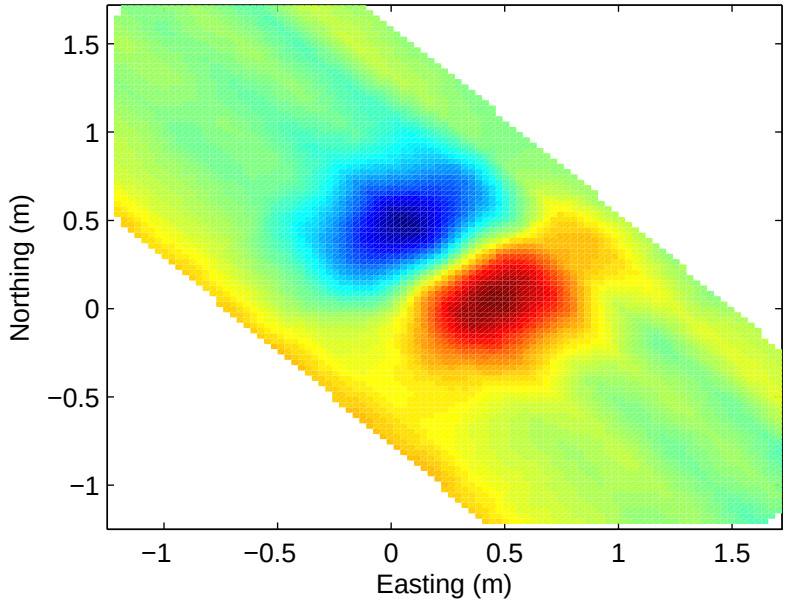

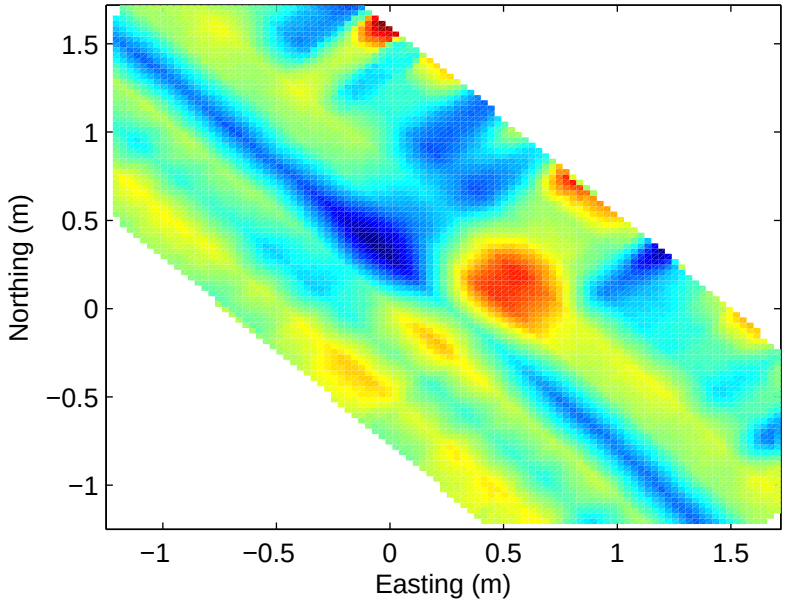

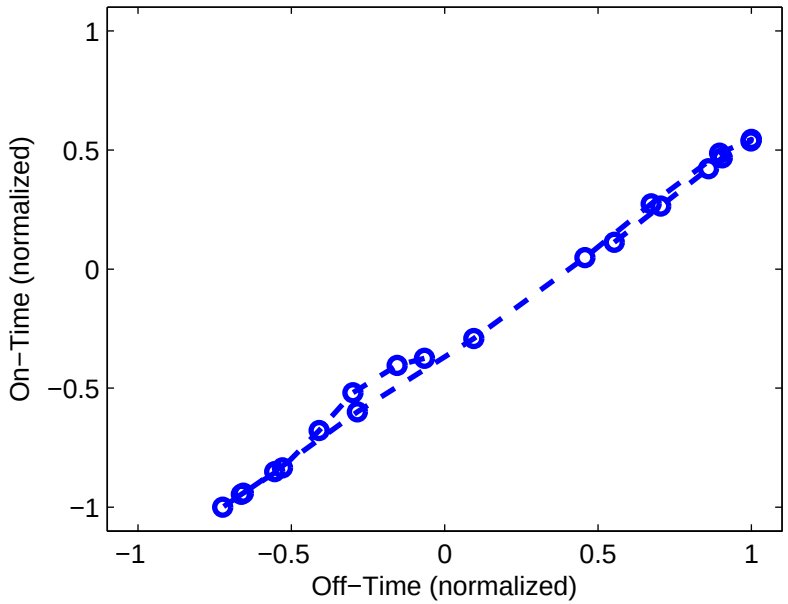

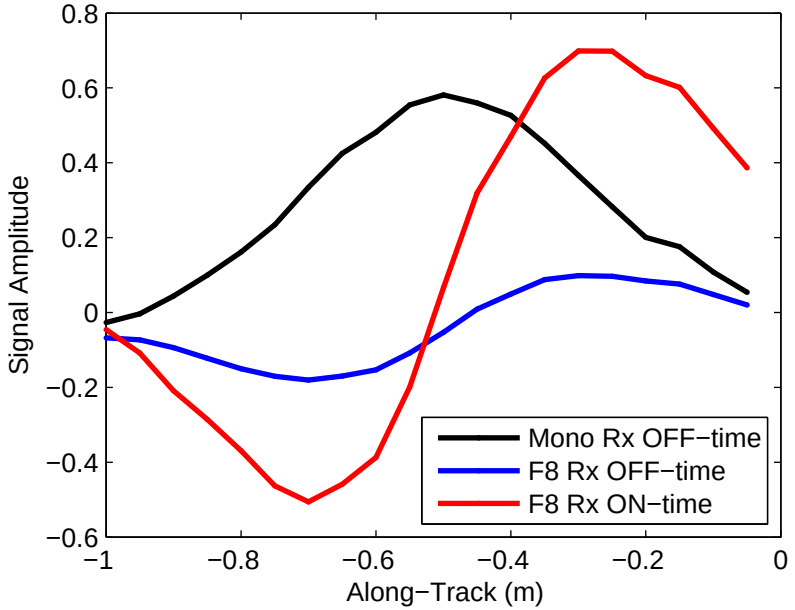

2.54 cm diameter steel rod, 60 cm depth

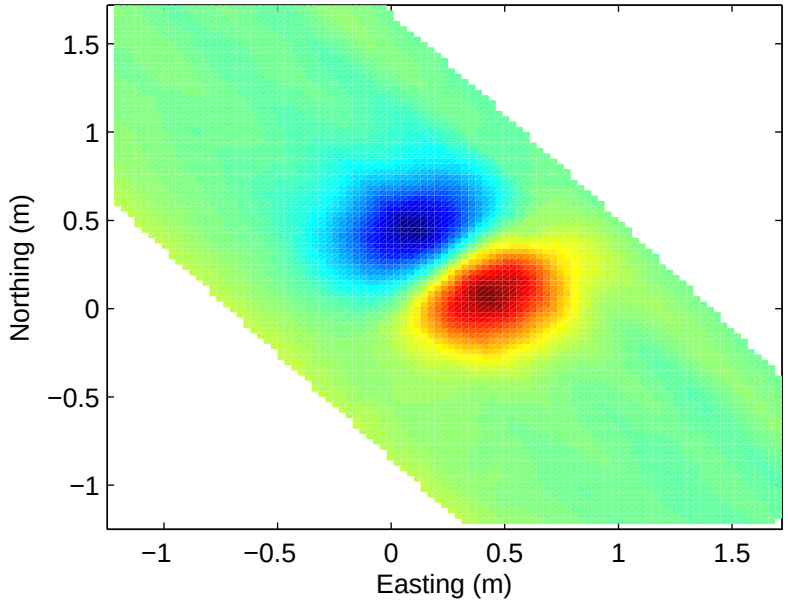

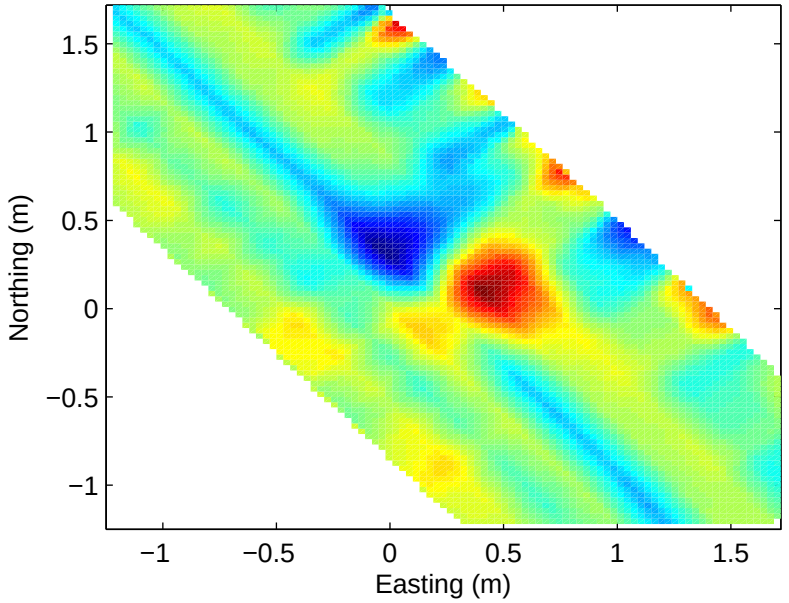

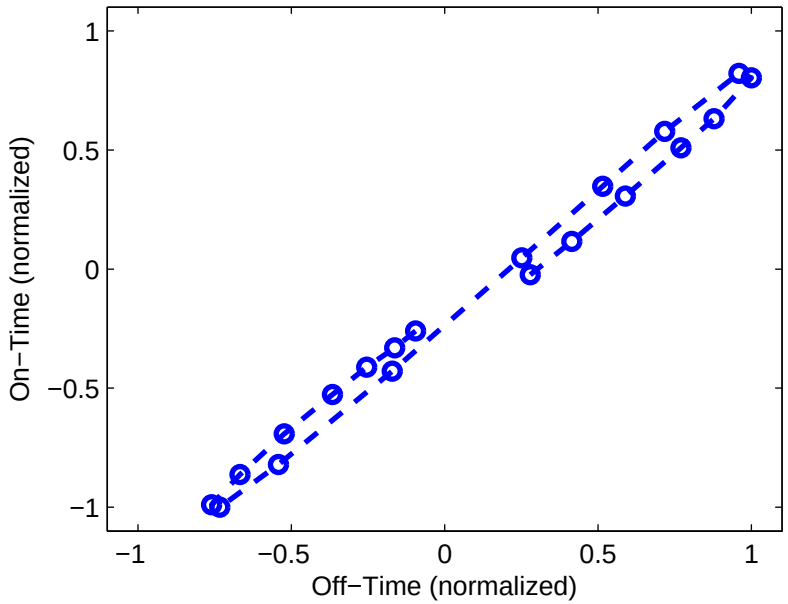

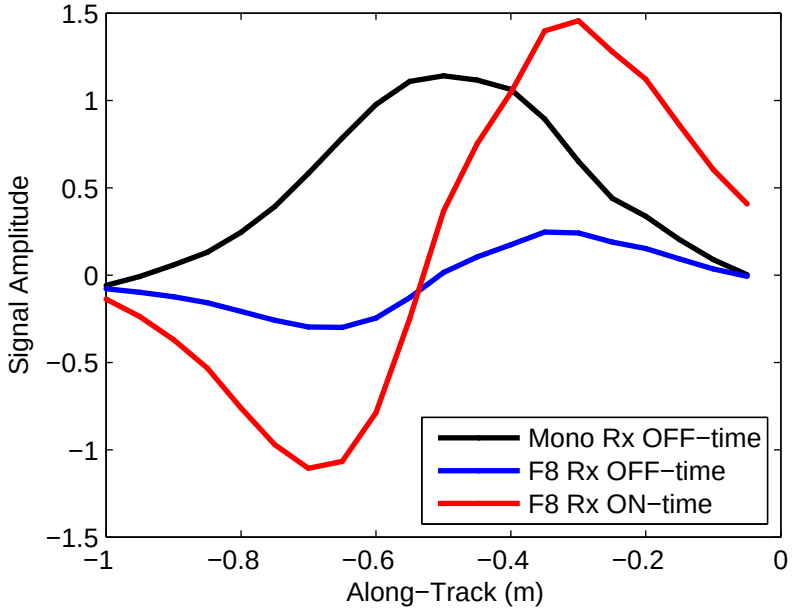

2.54 cm diameter steel rod, 60 cm depth

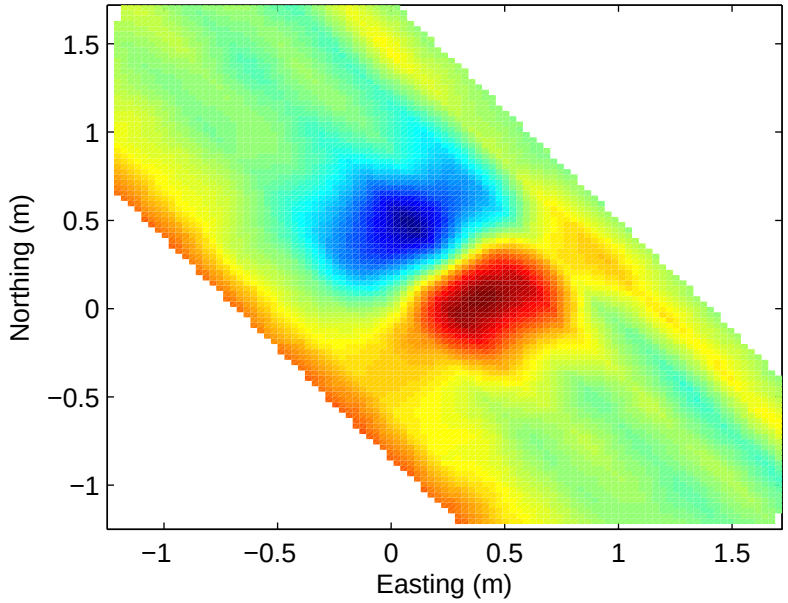

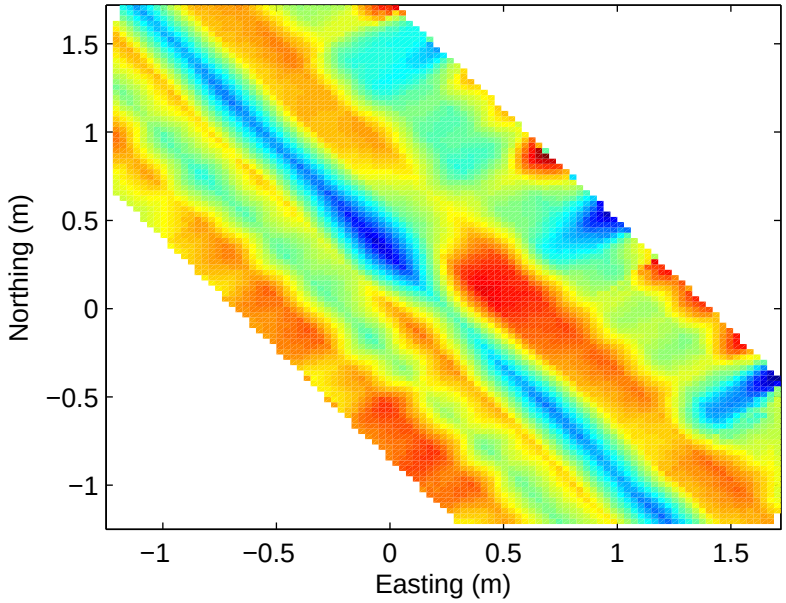

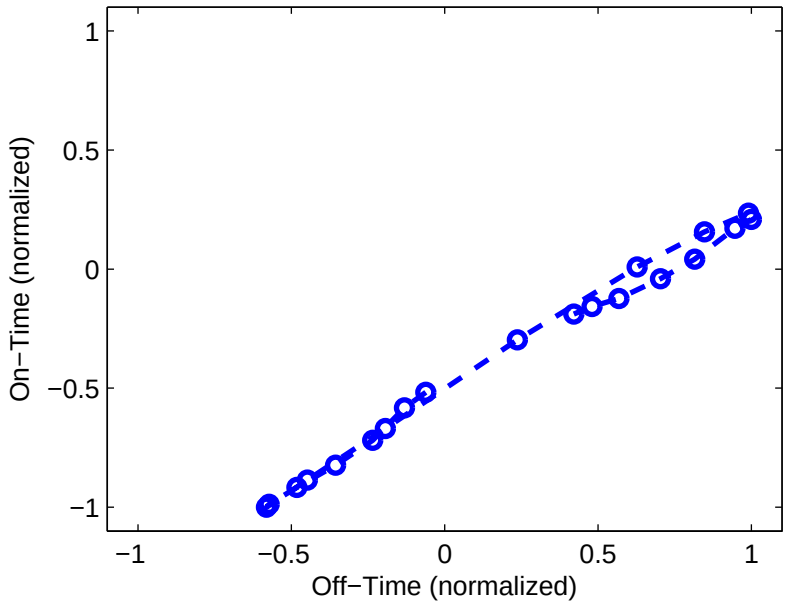

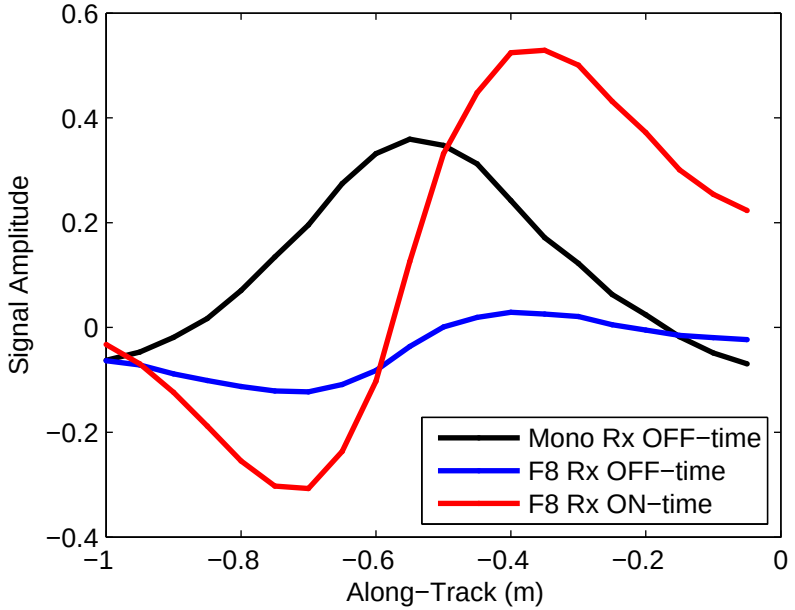

2.54 cm diameter aluminum rod, 30 cm depth

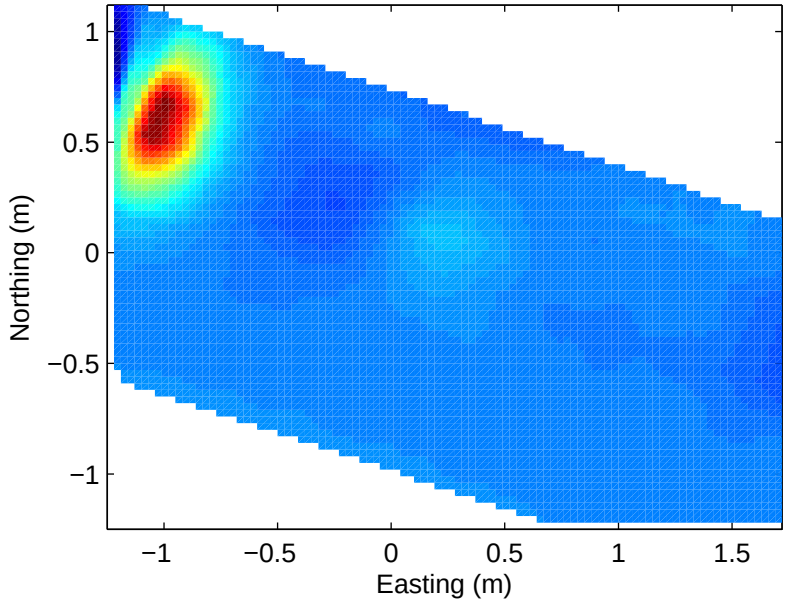

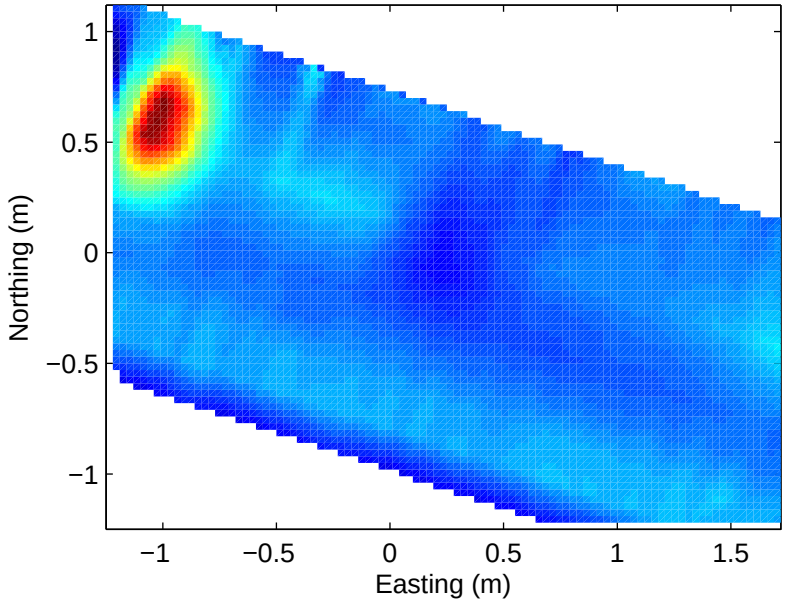

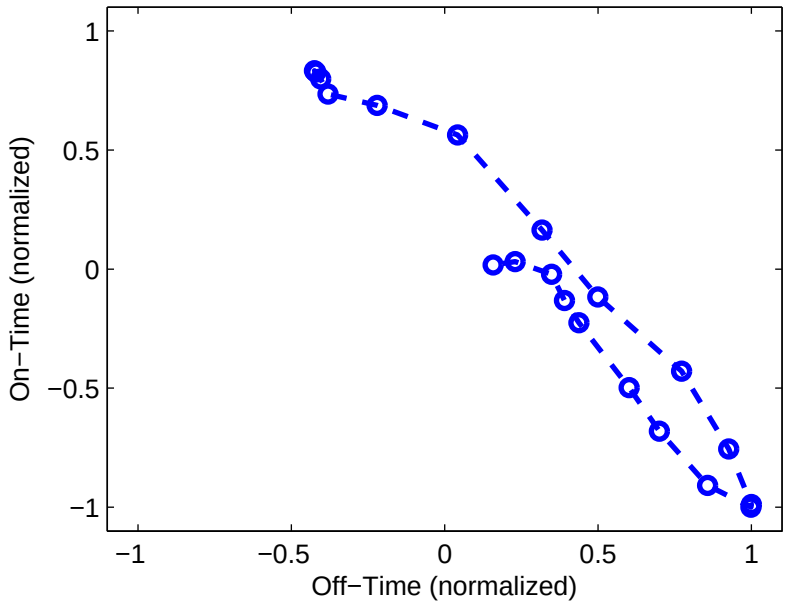

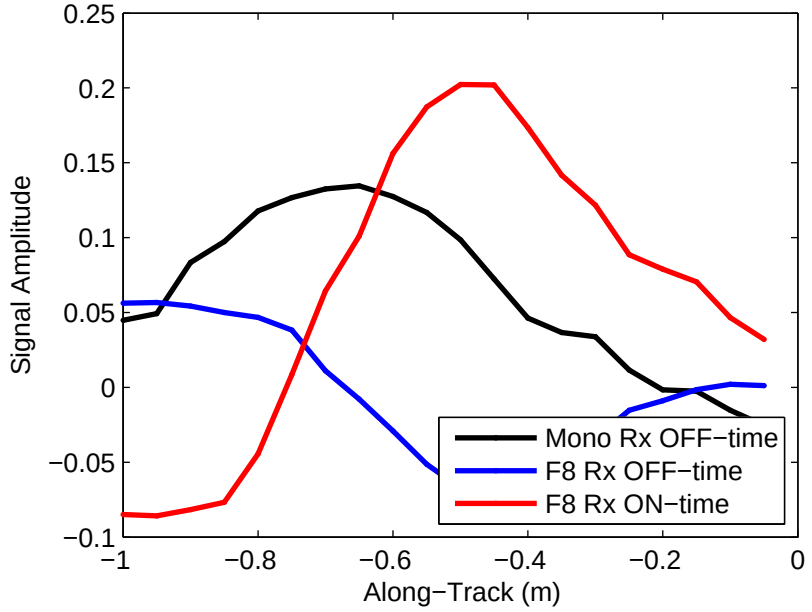

2.54 cm diameter aluminum rod, 30 cm depth

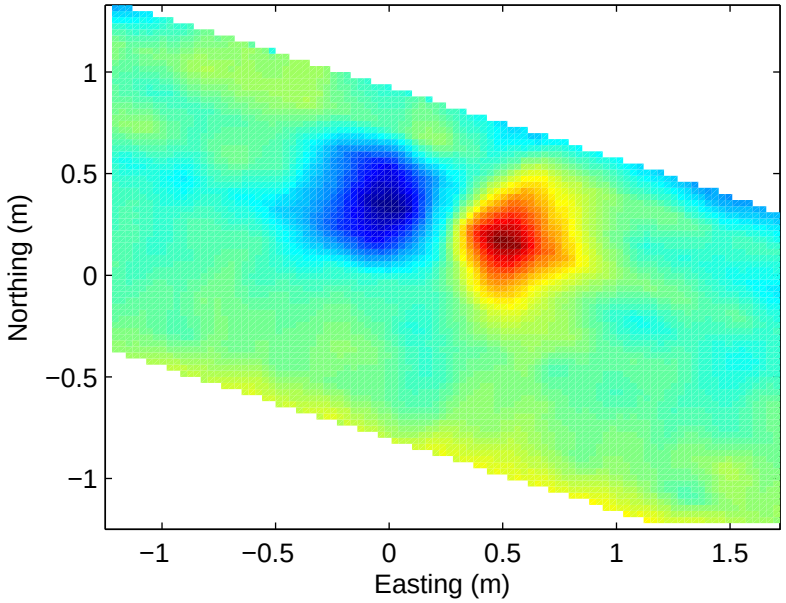

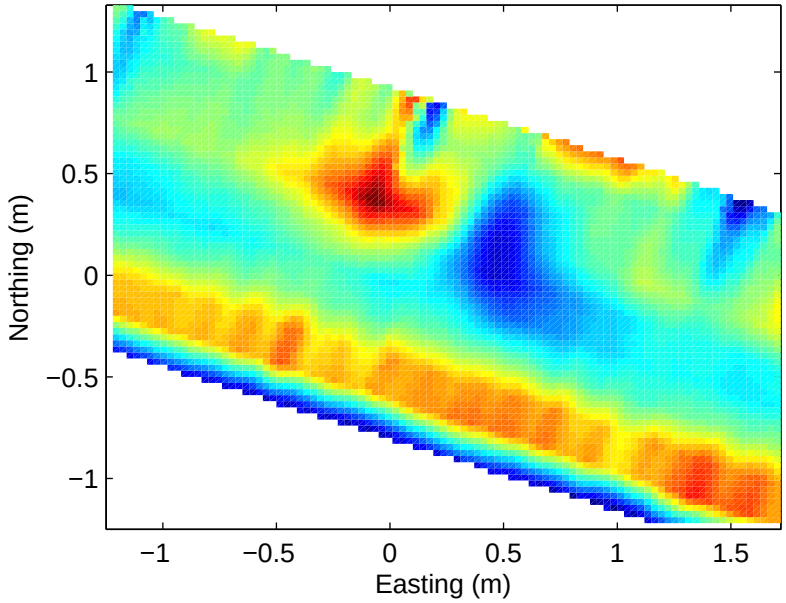

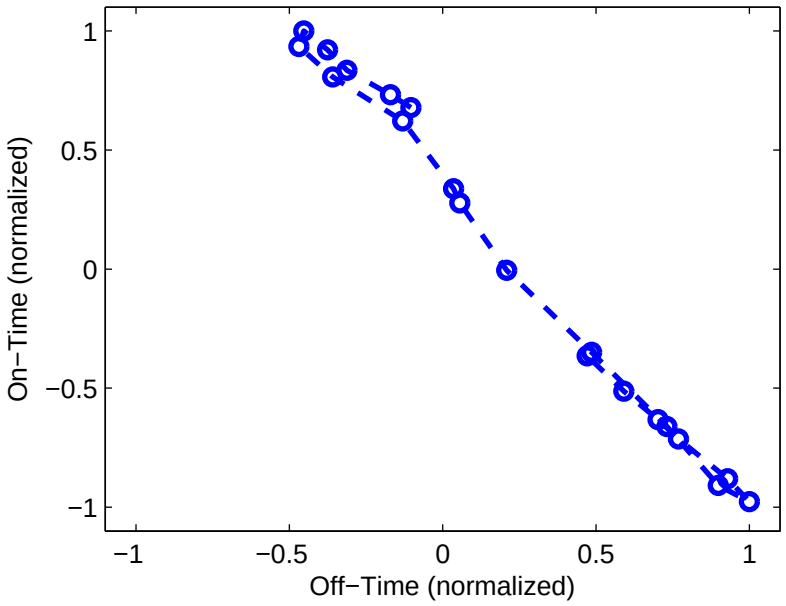

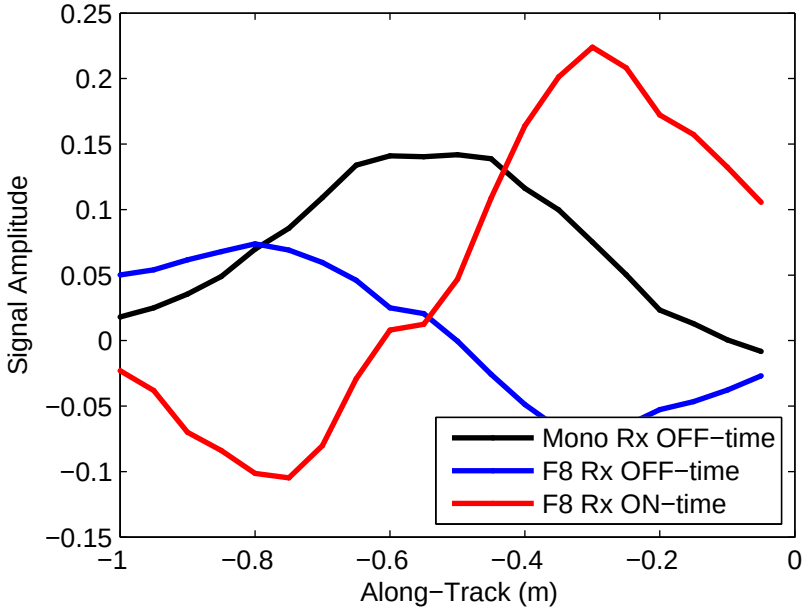

2.54 cm diameter aluminum rod, 30 cm depth

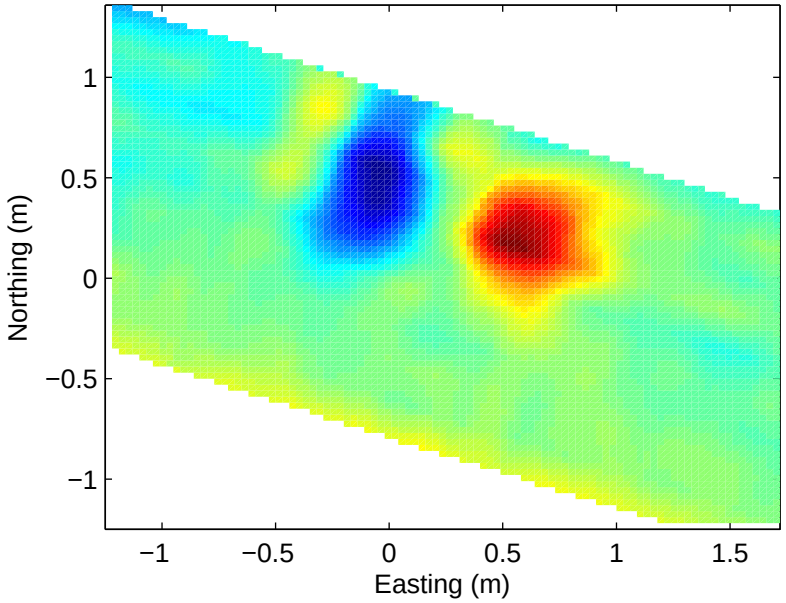

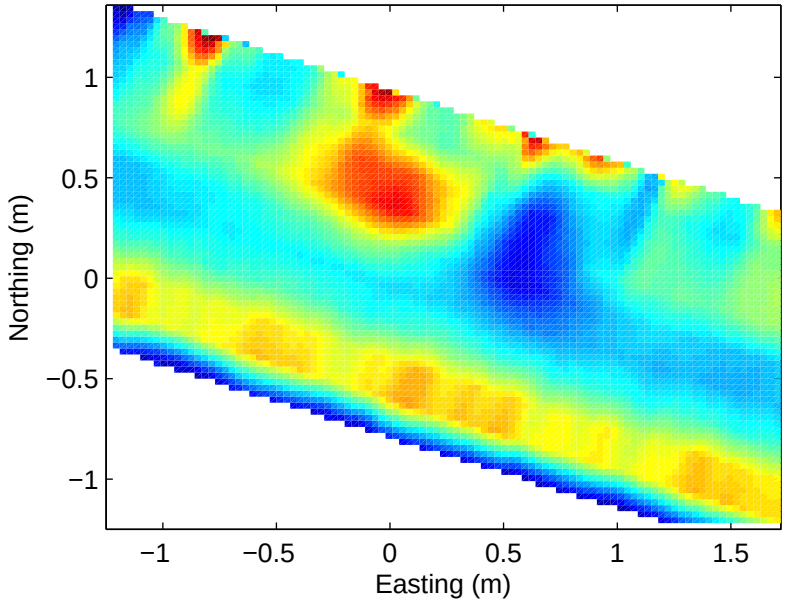

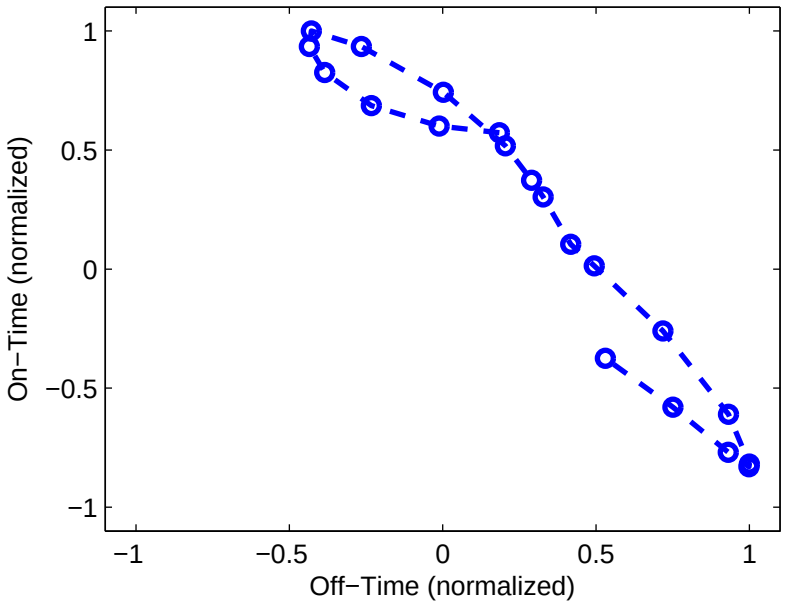

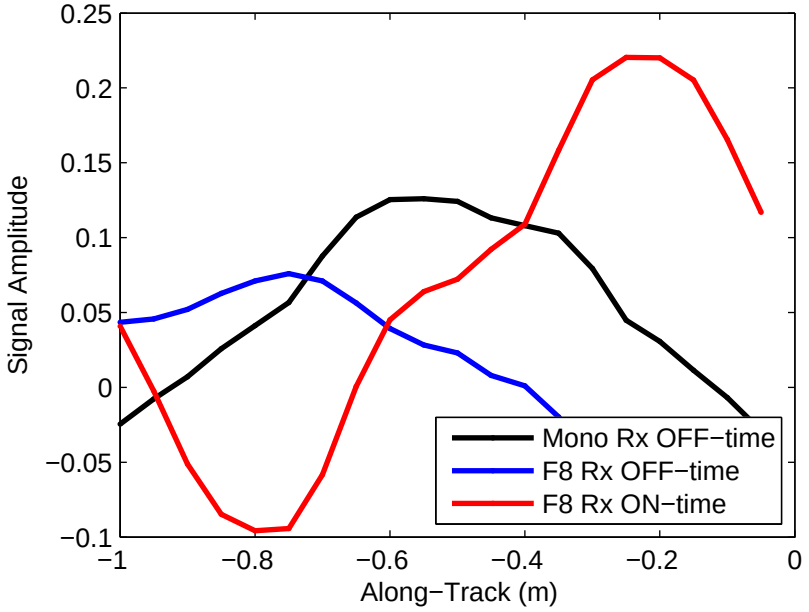

7.6 cm diameter aluminum disc, 30 cm depth

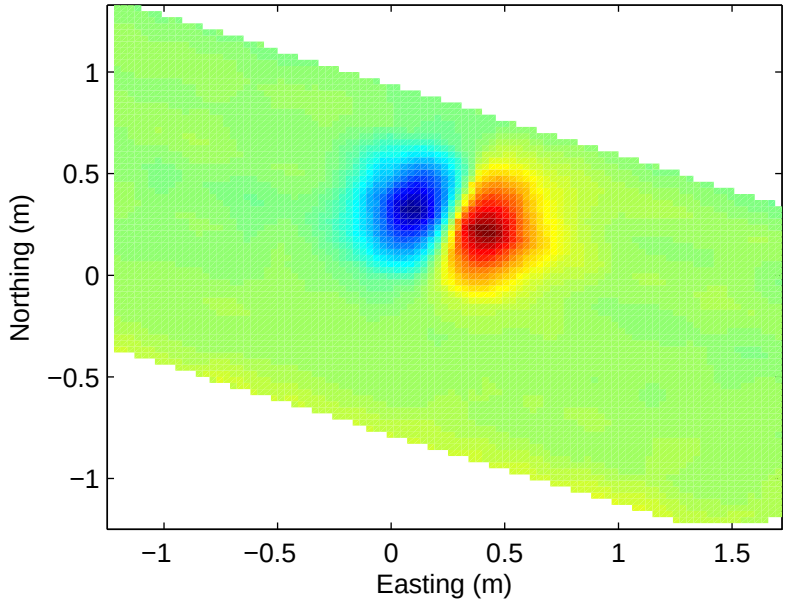

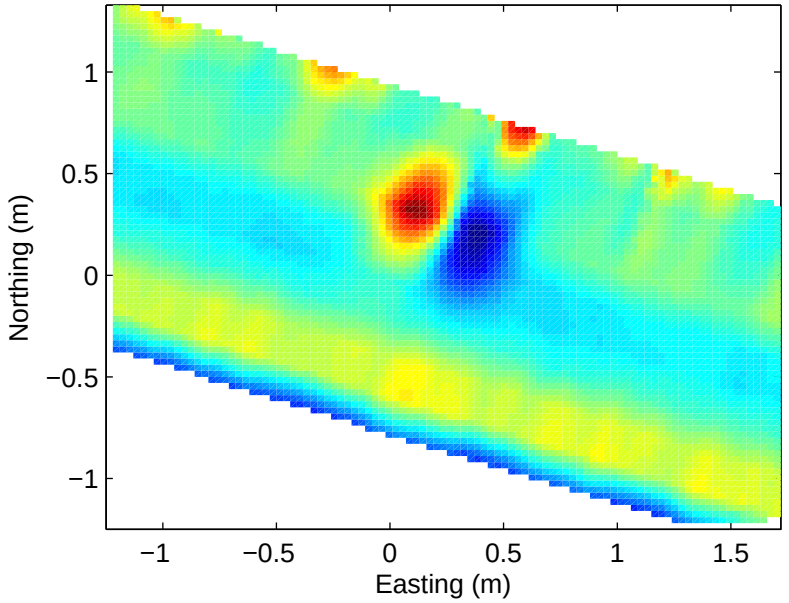

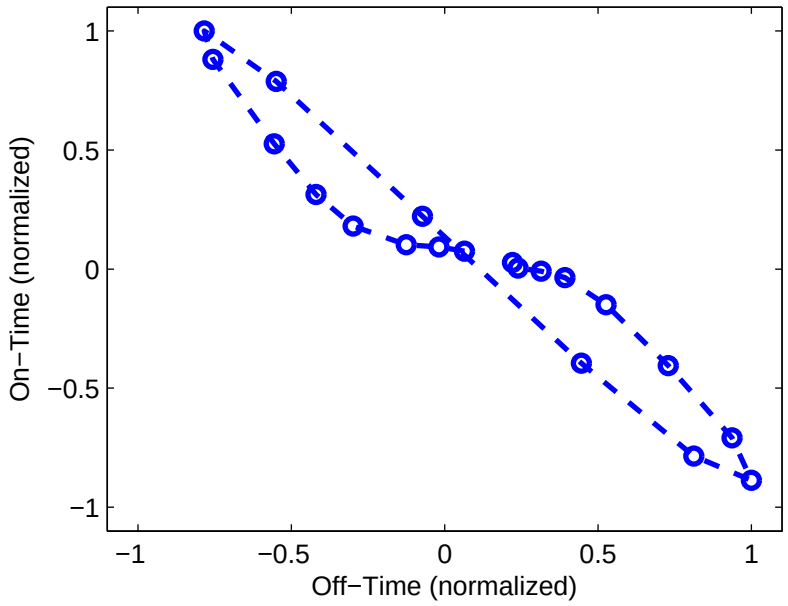

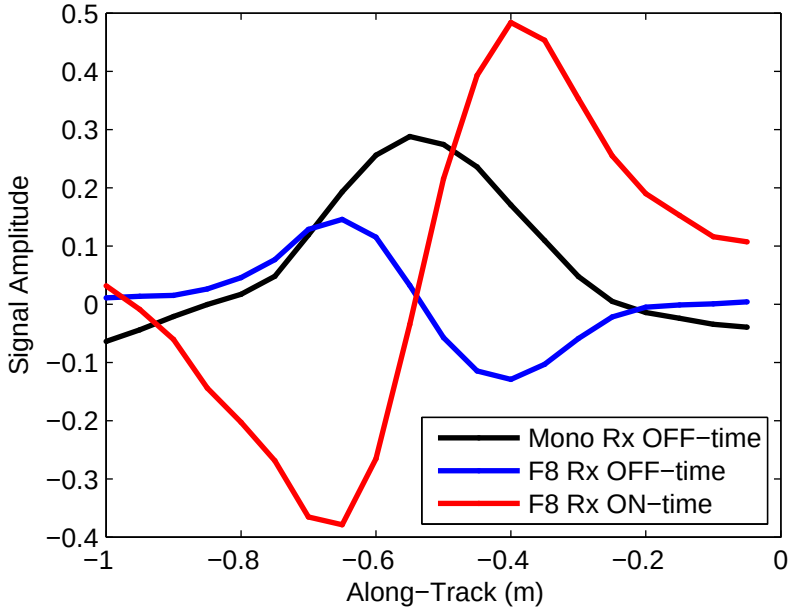

11.5 cm diameter aluminum disc, 30 cm depth

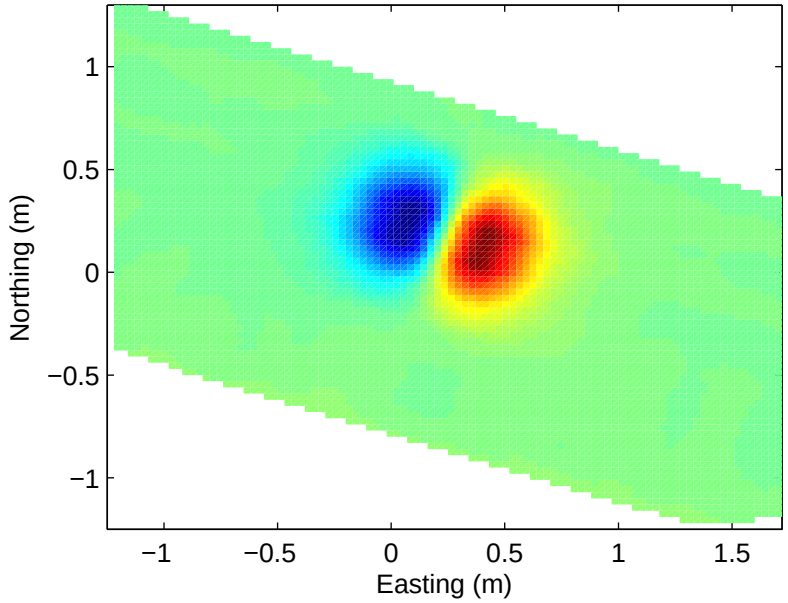

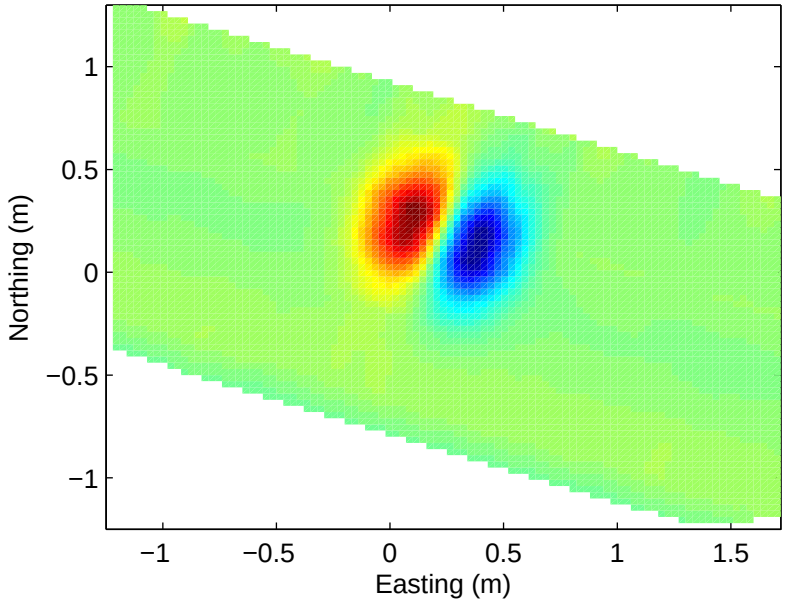

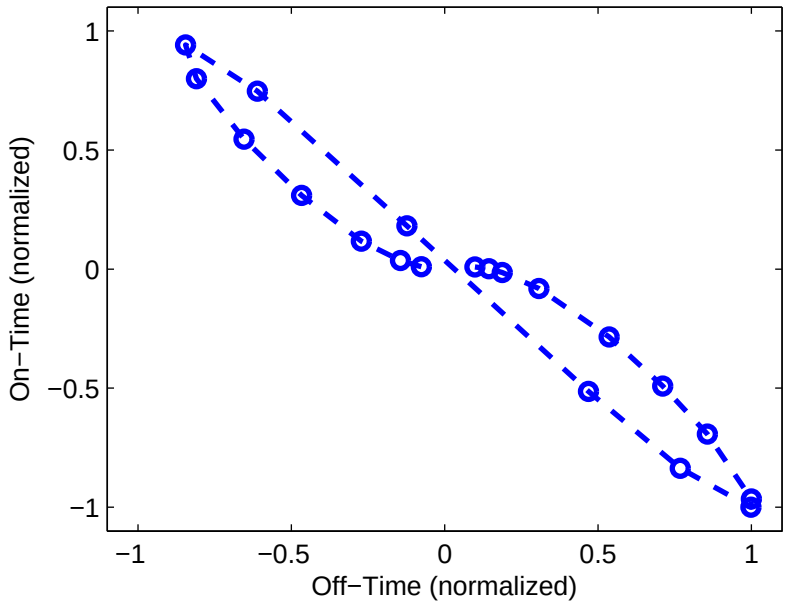

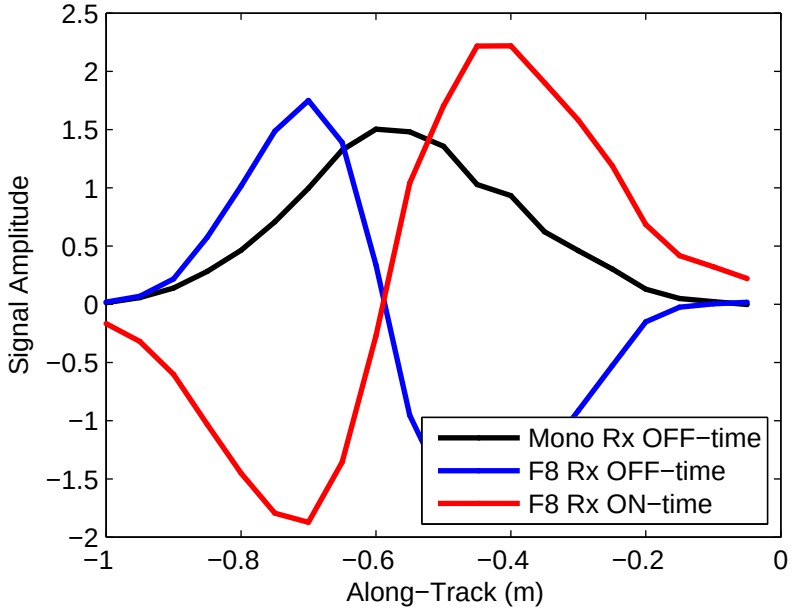

15.25 cm diameter aluminum disc, 30 cm depth

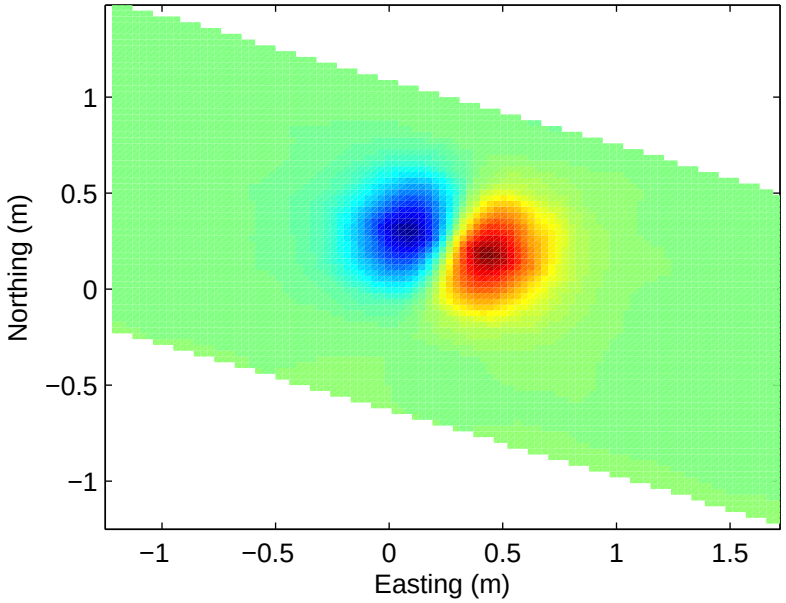

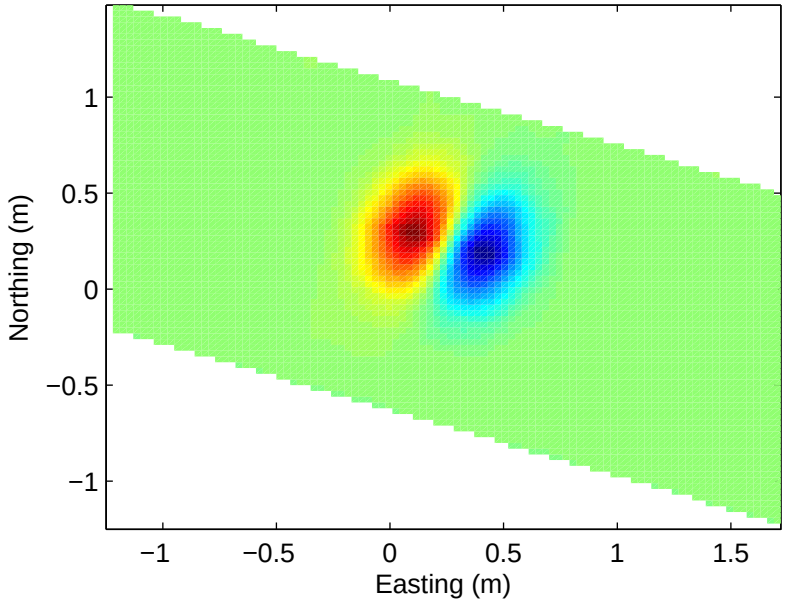

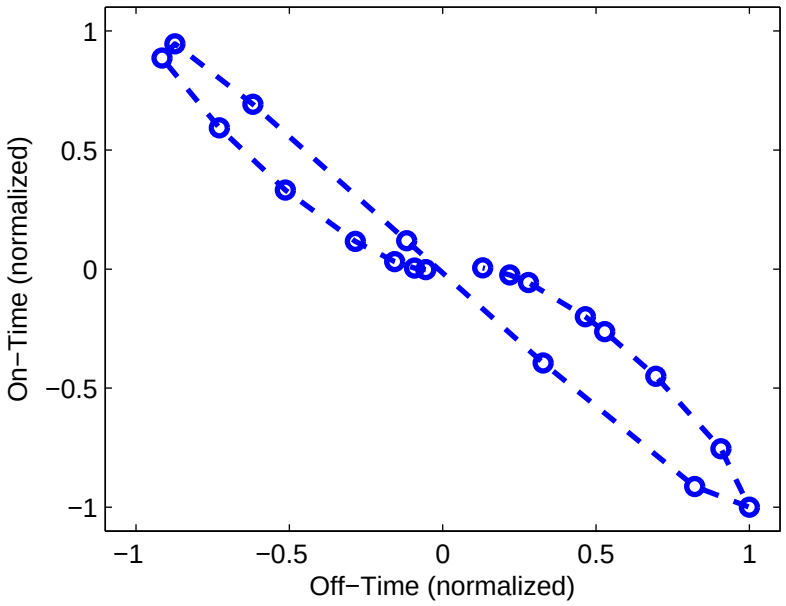

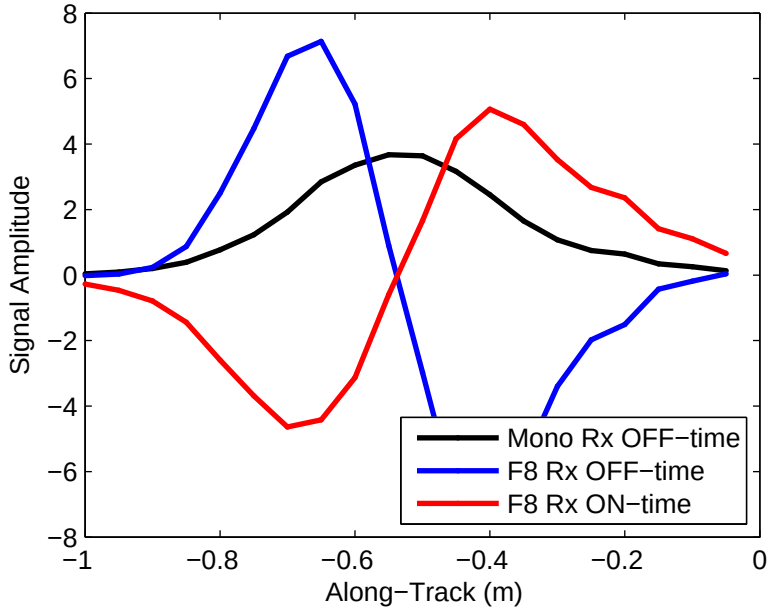

7.6 cm diameter aluminum cylinder, 30 cm depth

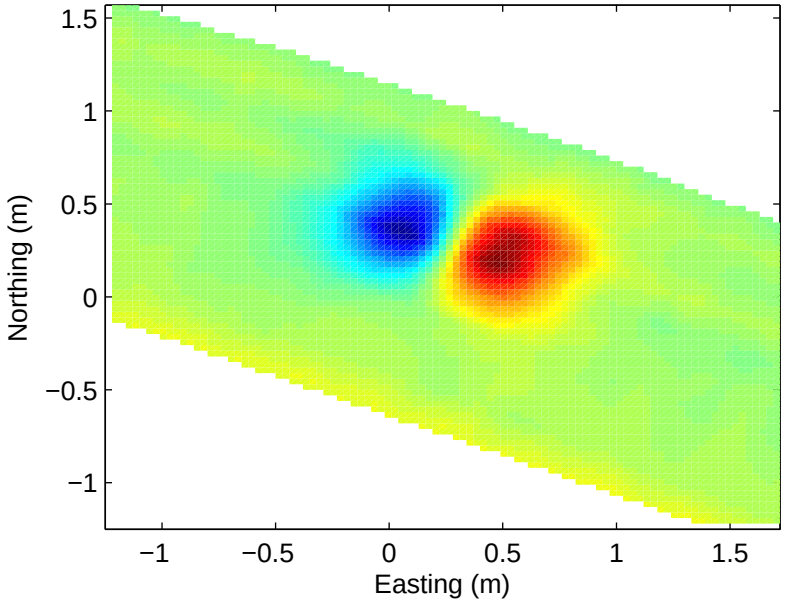

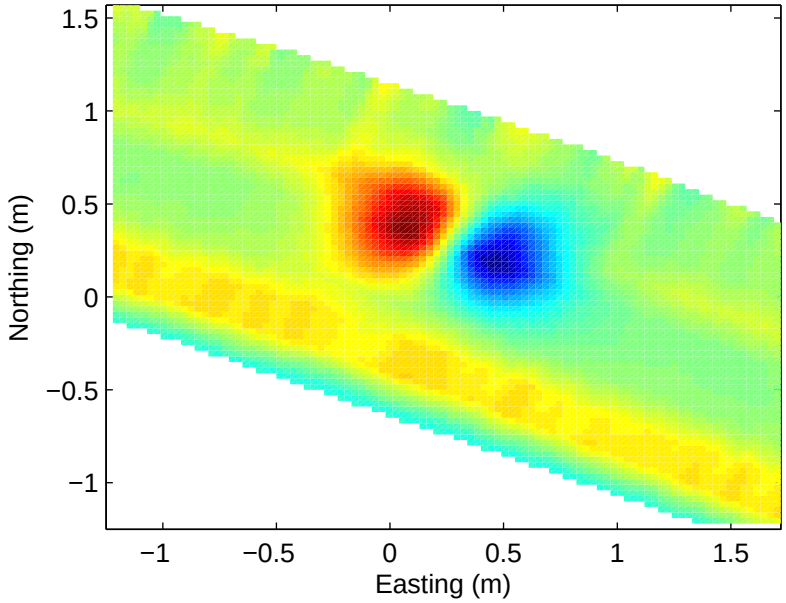

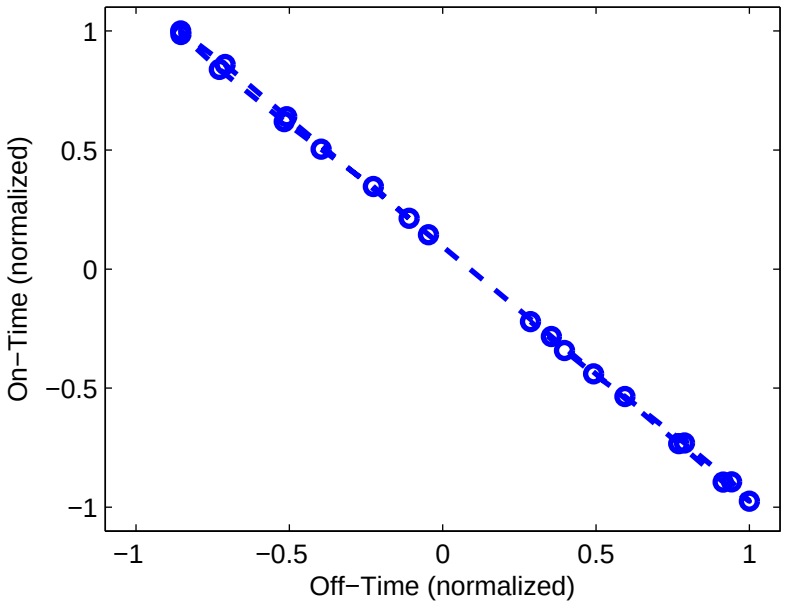

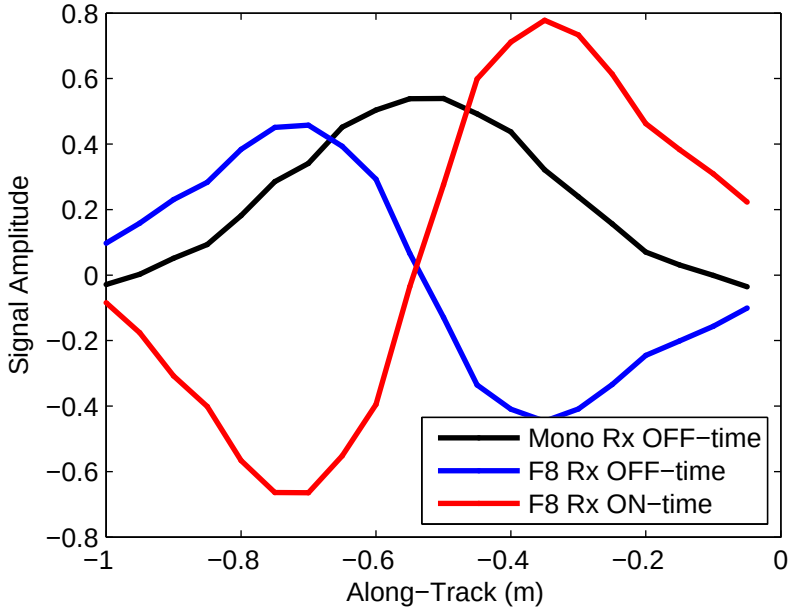

11.5 cm diameter aluminum cylinder, 30 cm depth

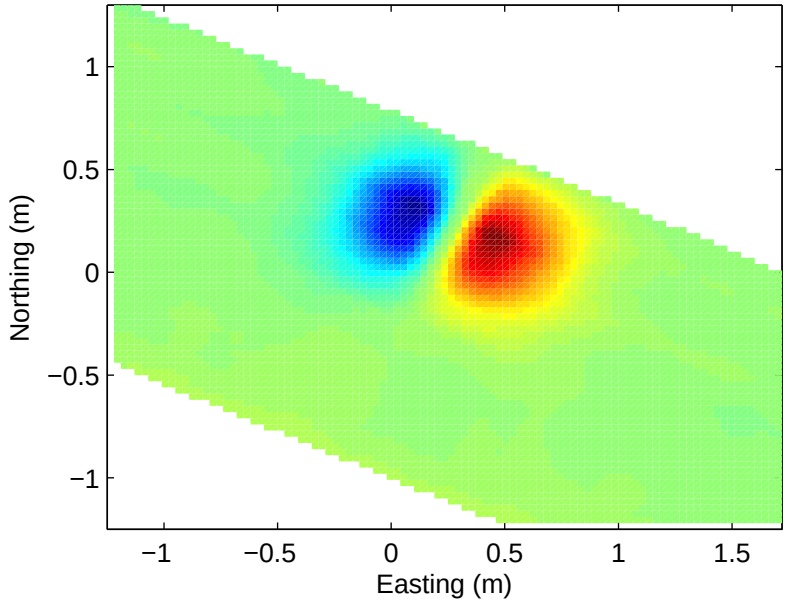

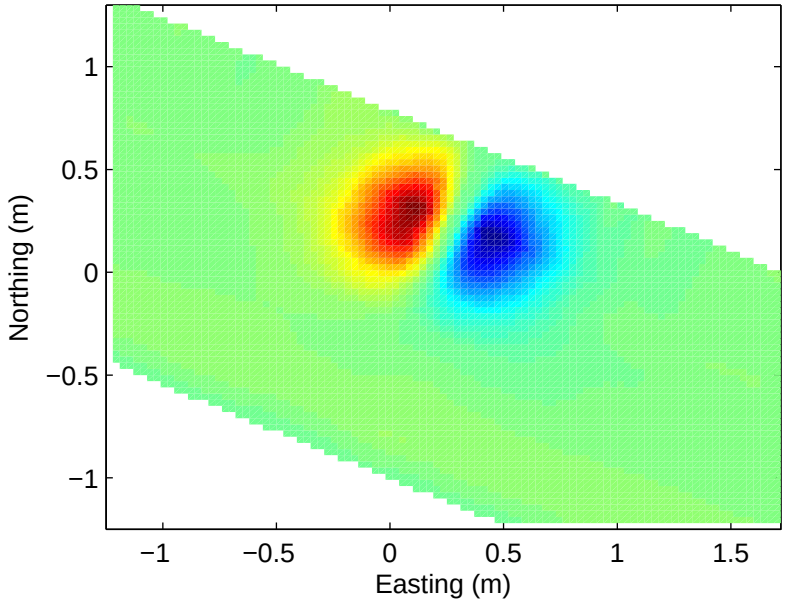

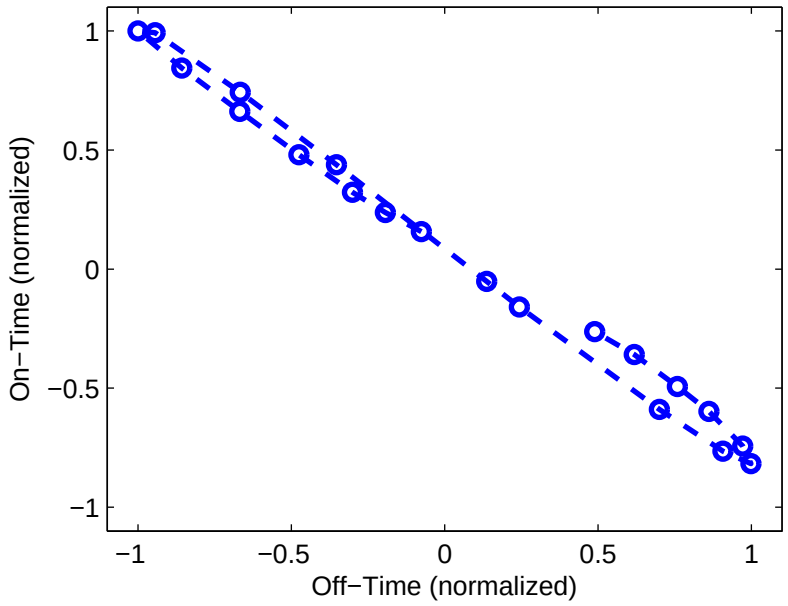

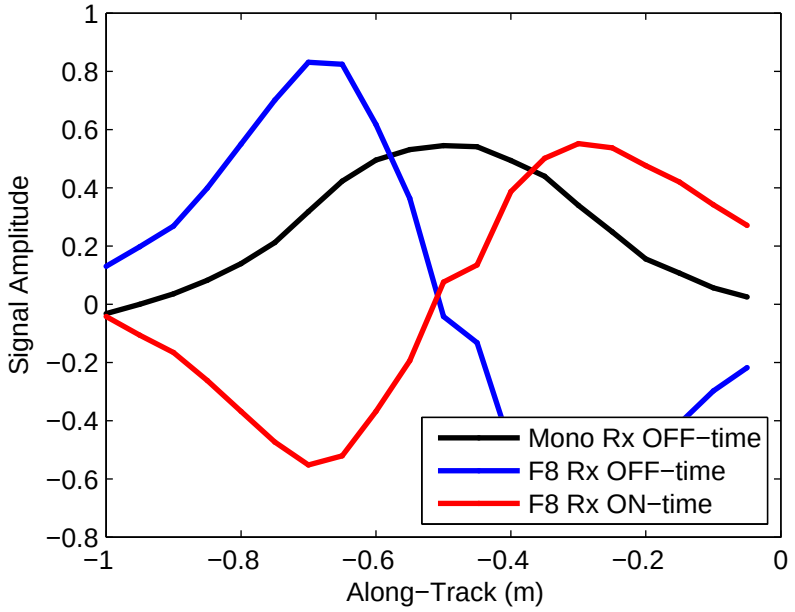

15.25 cm diameter aluminum cylinder, 30 cm depth

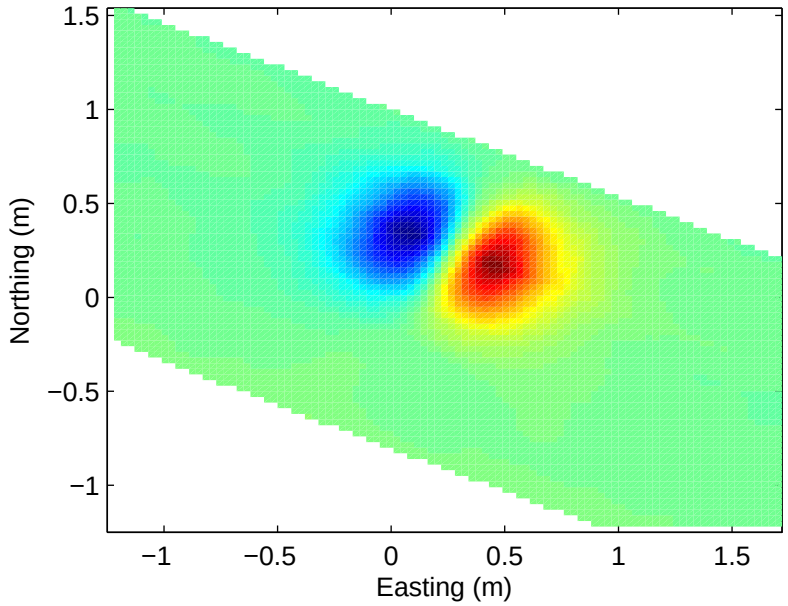

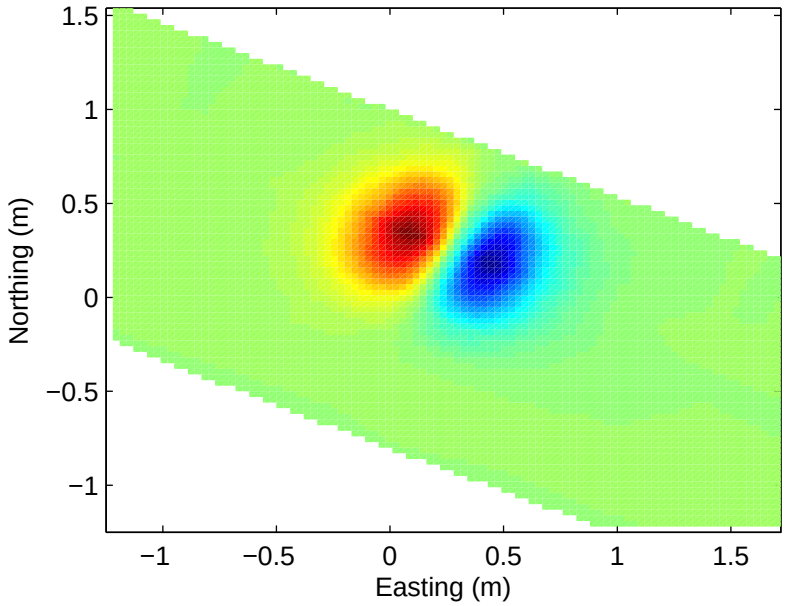

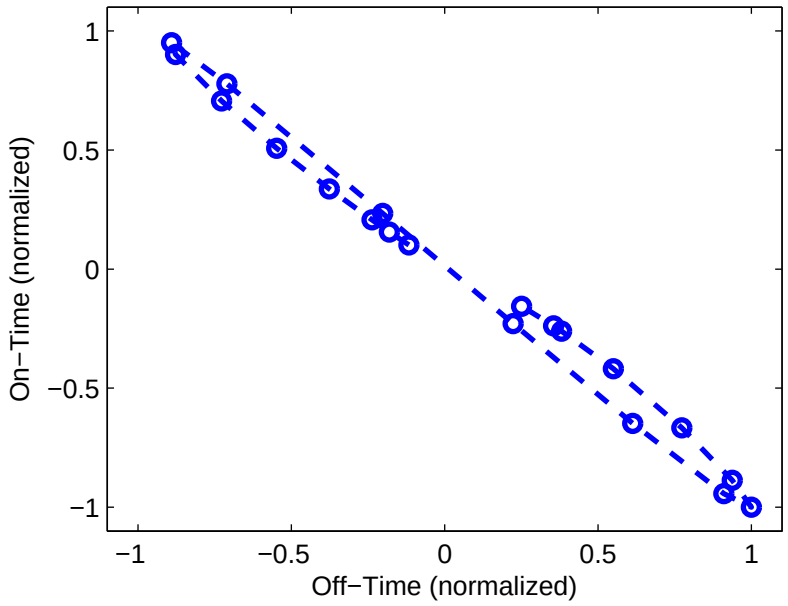

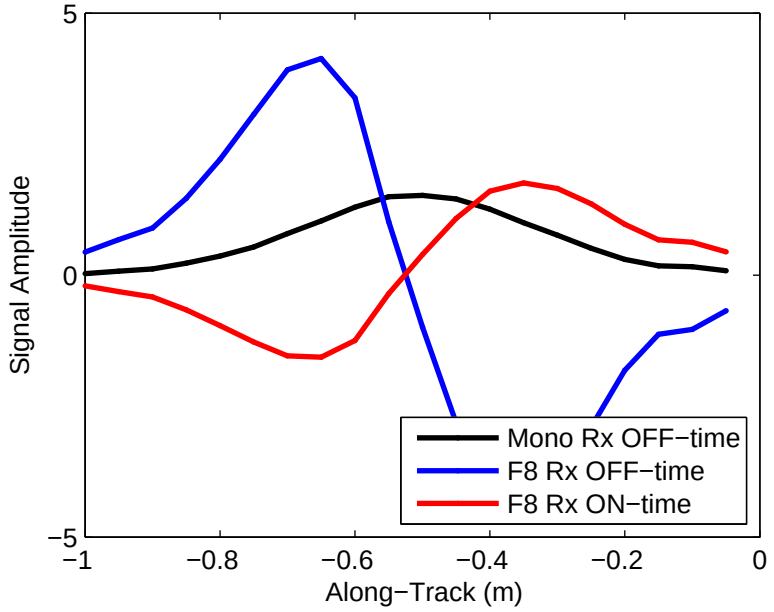

2.54 cm diameter aluminum rod, 45 cm depth

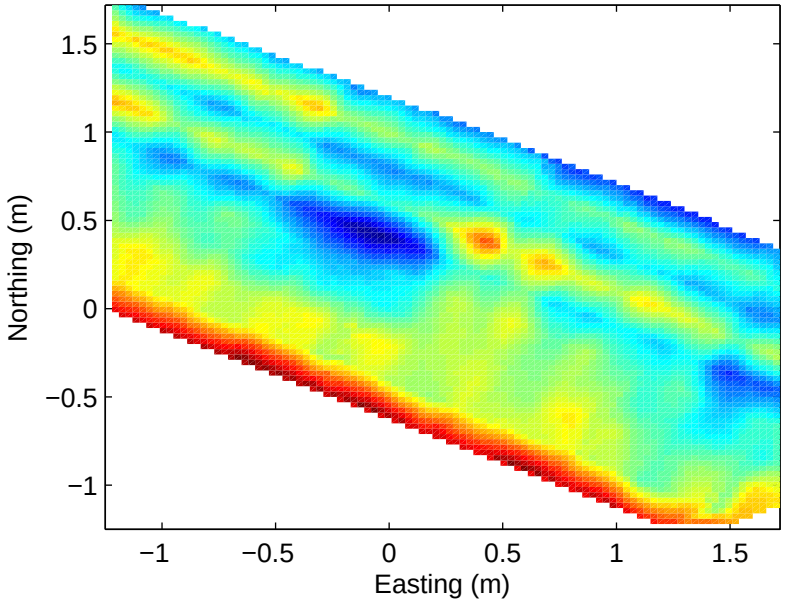

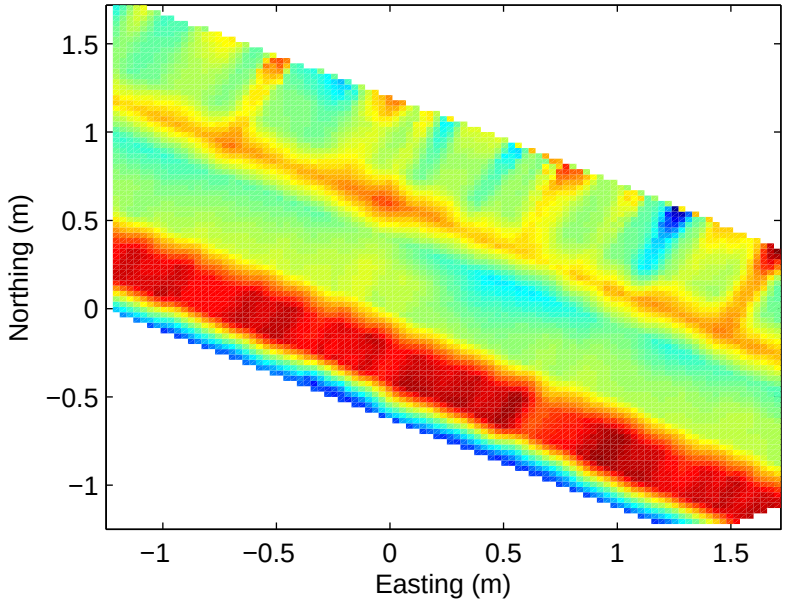

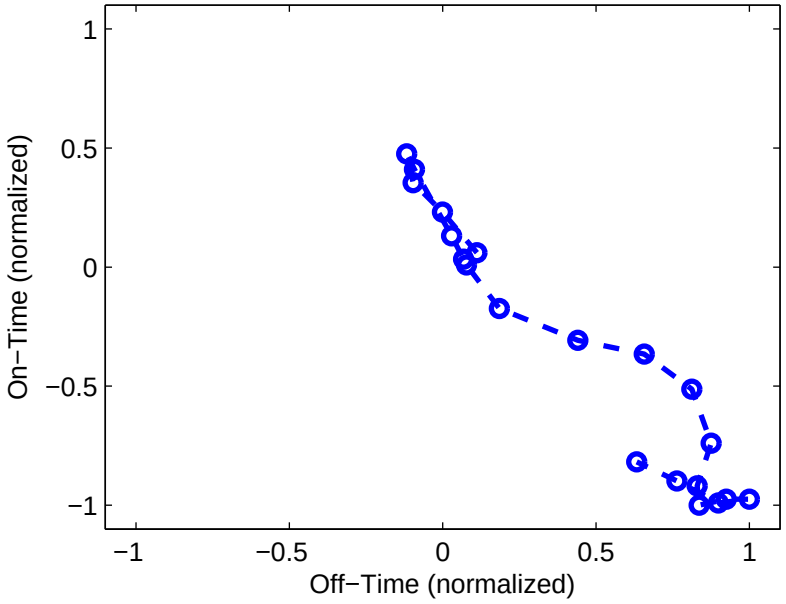

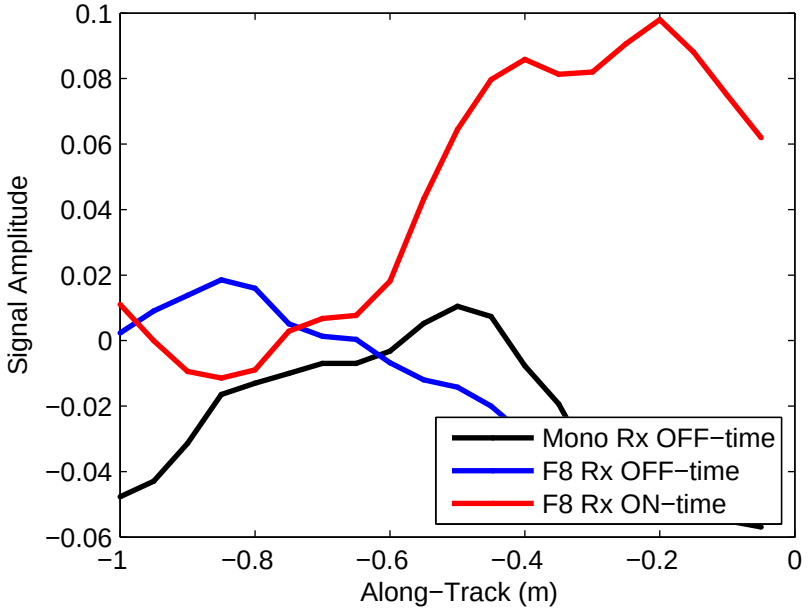

2.54 cm diameter aluminum rod, 45 cm depth

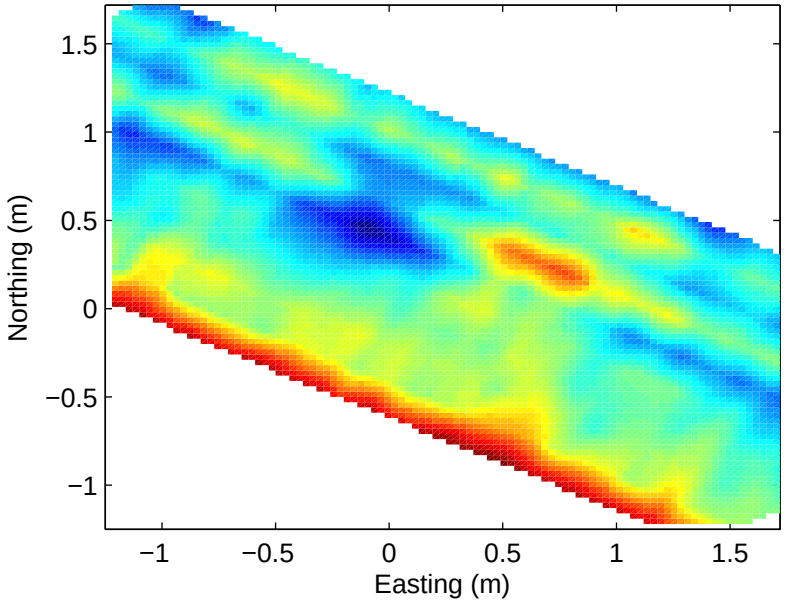

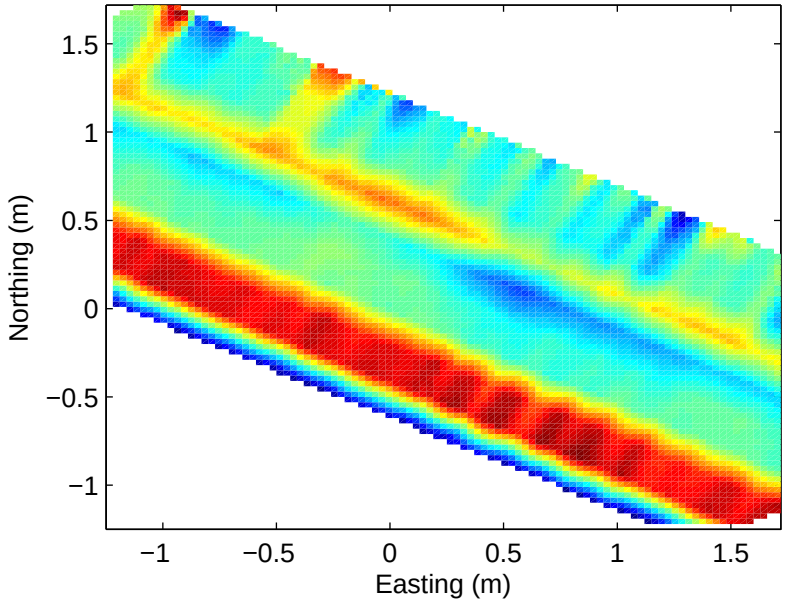

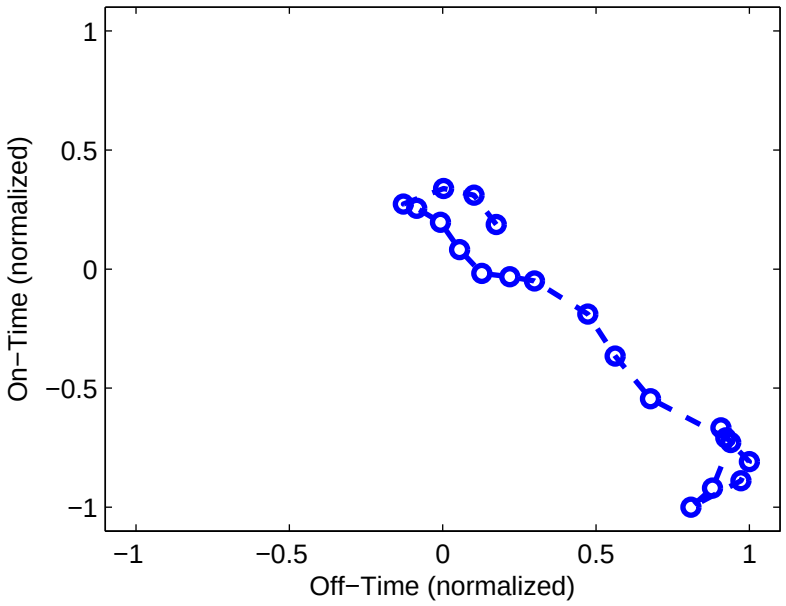

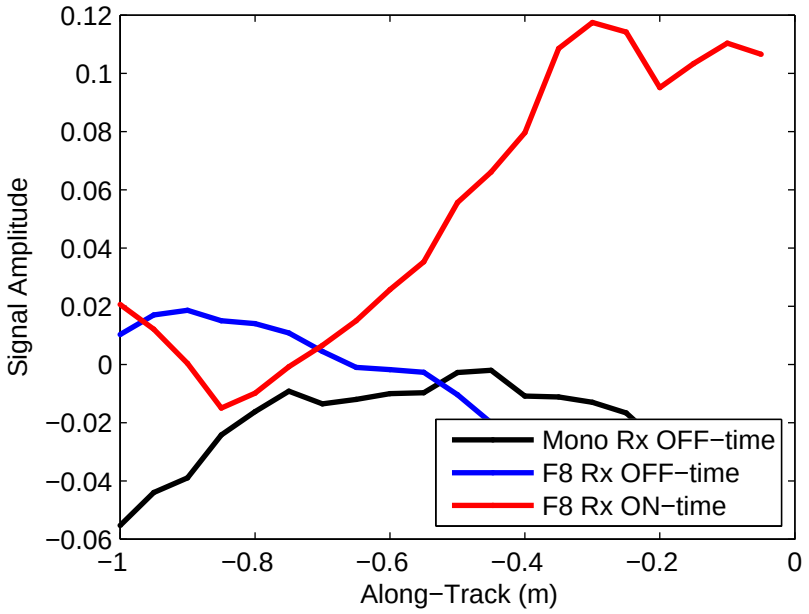

2.54 cm diameter aluminum rod, 45 cm depth

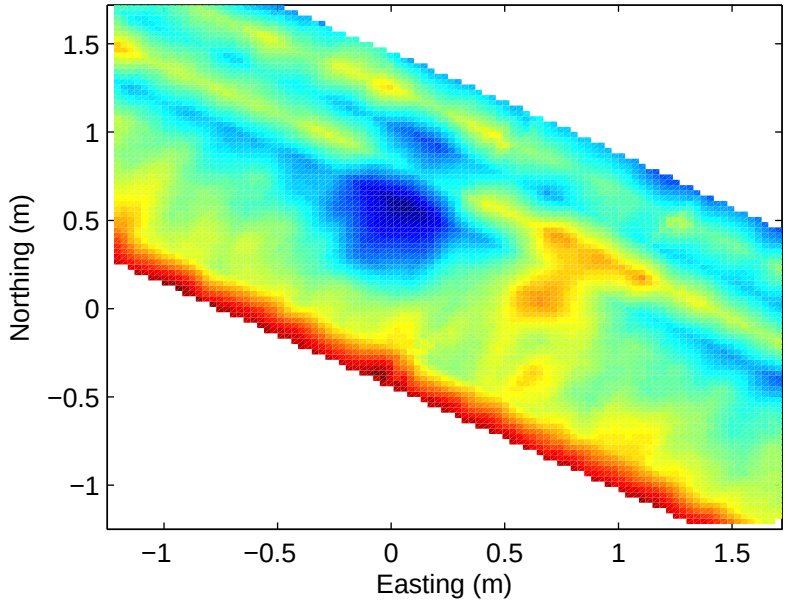

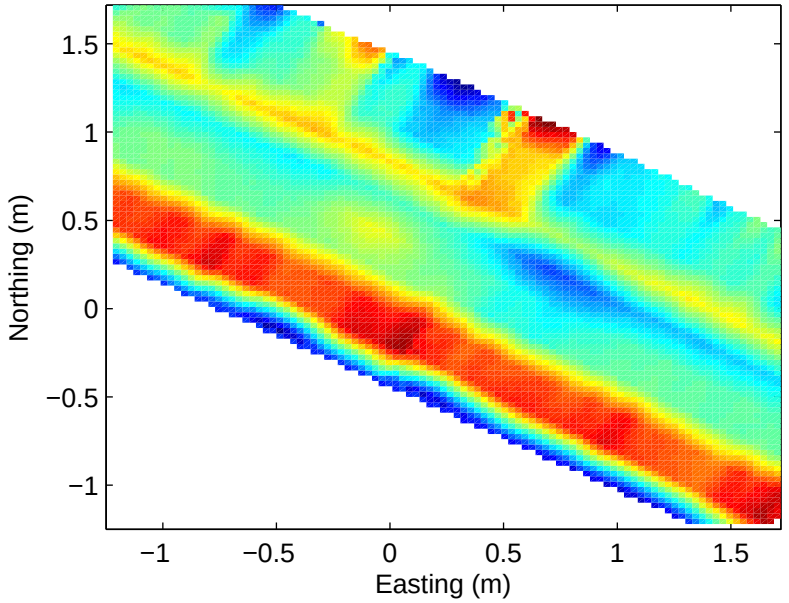

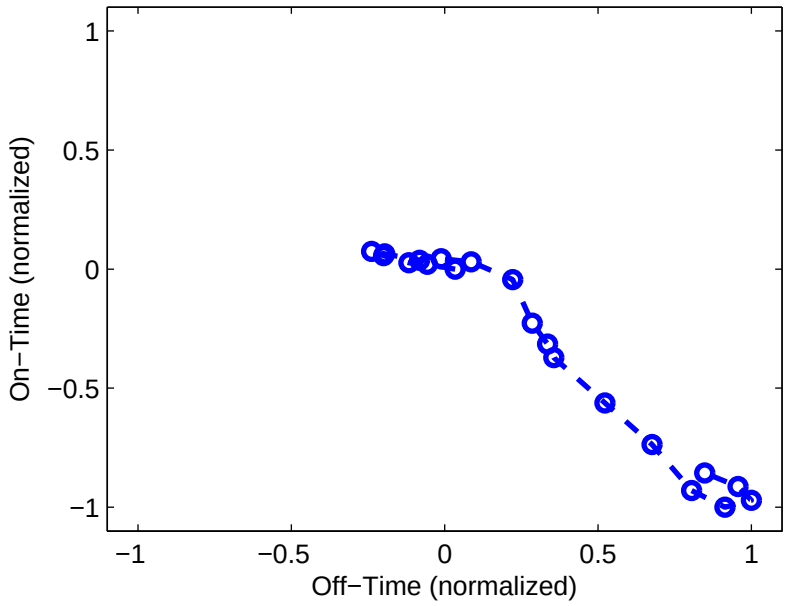

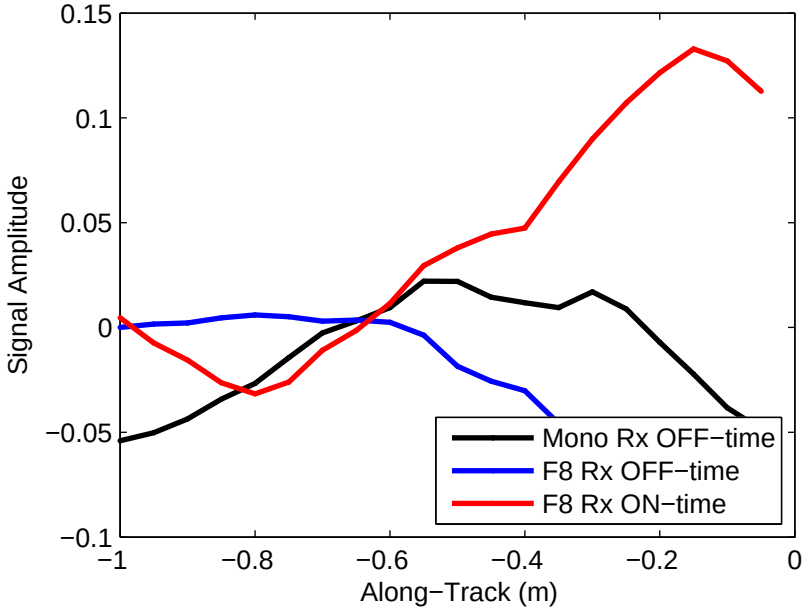

7.6 cm diameter aluminum disc, 45 cm depth

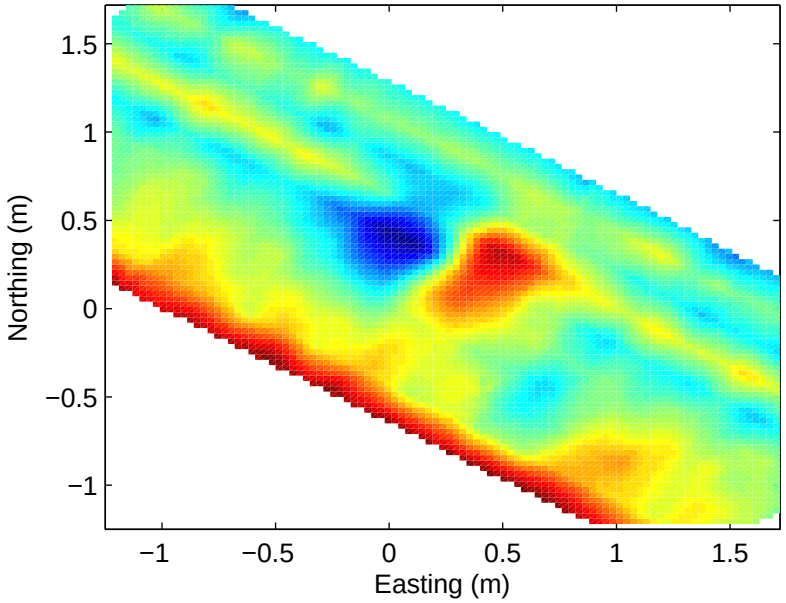

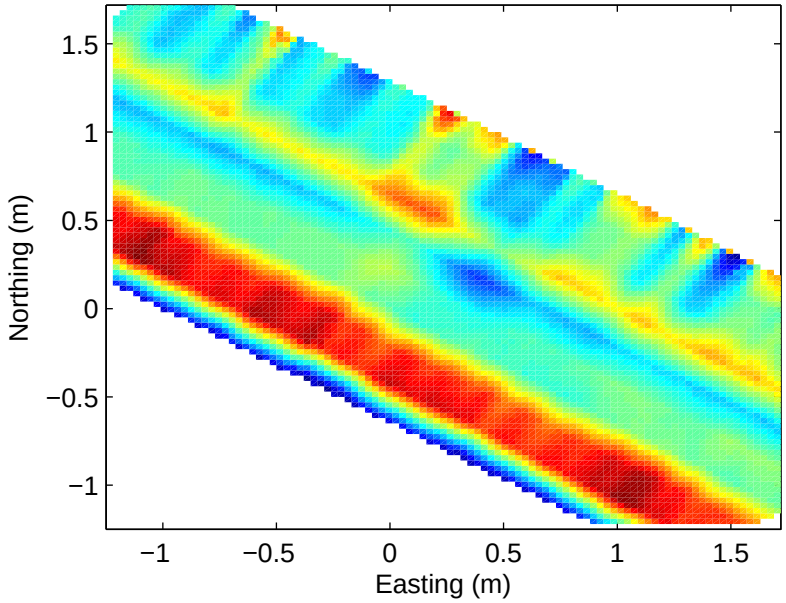

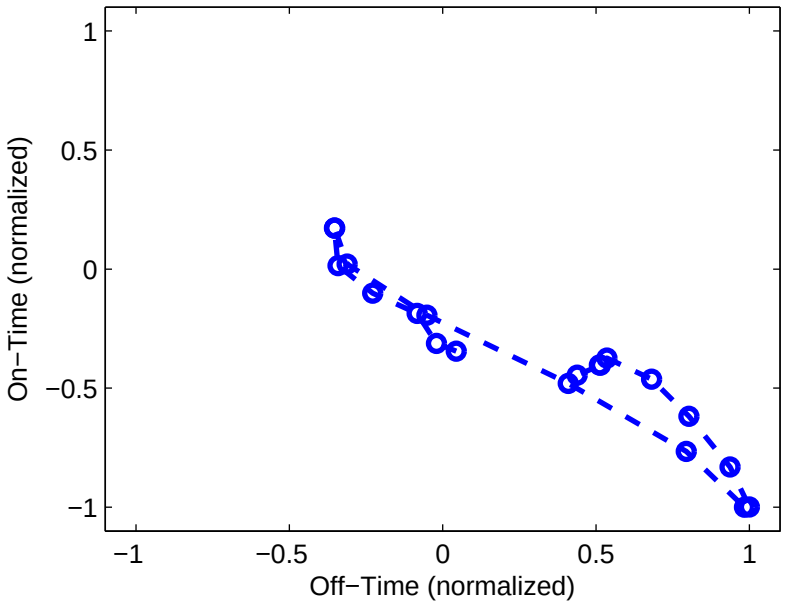

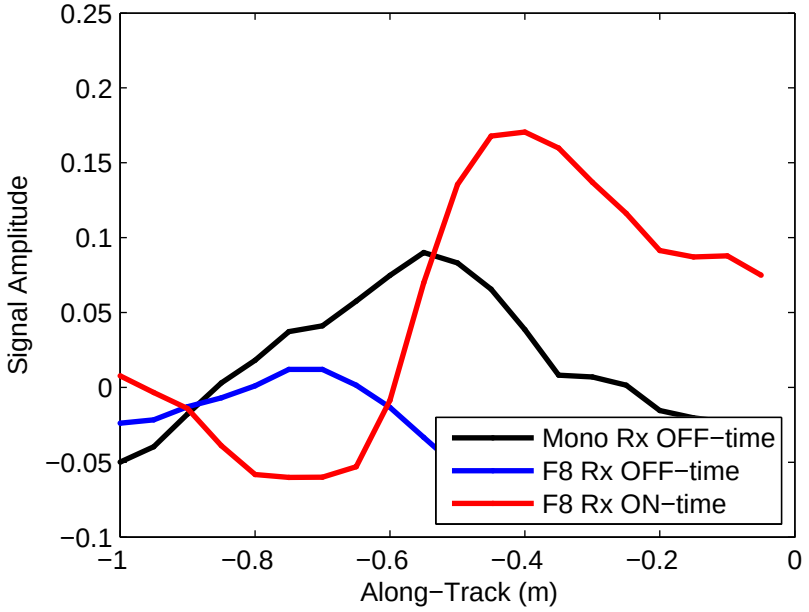

11.5 cm diameter aluminum disc, 45 cm depth

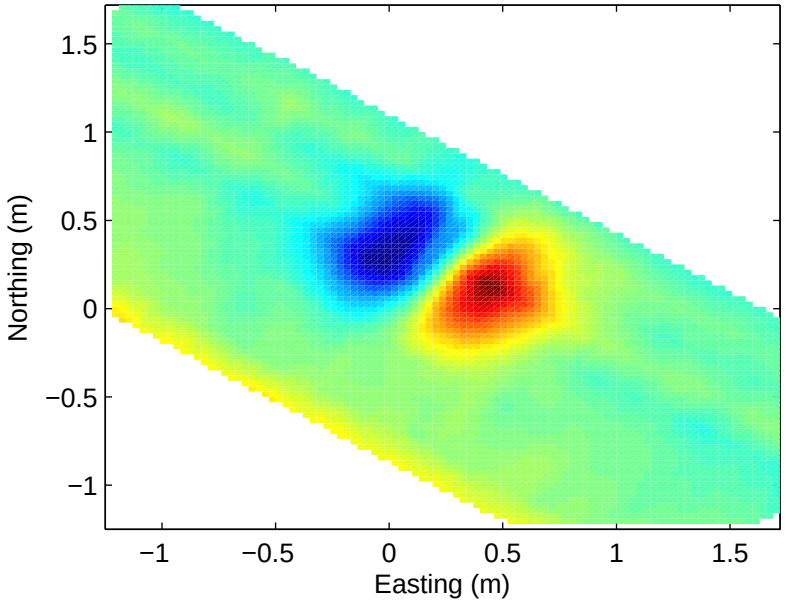

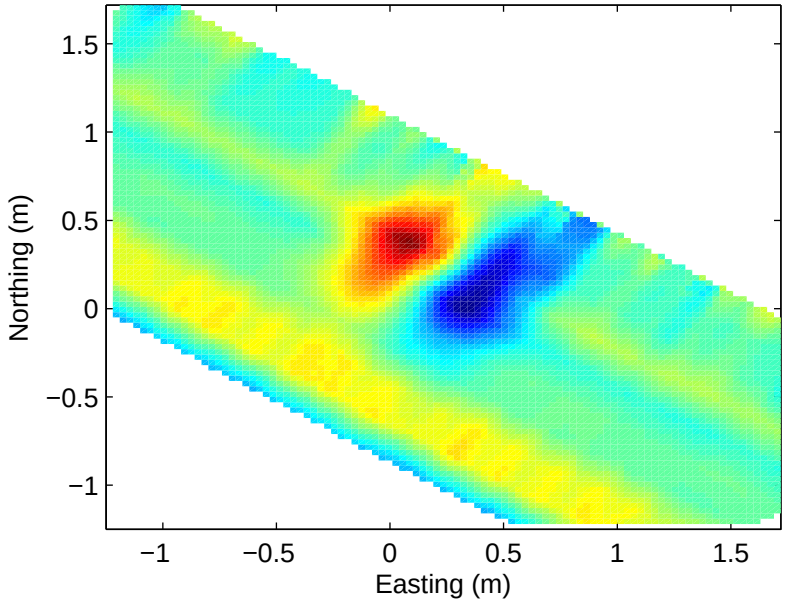

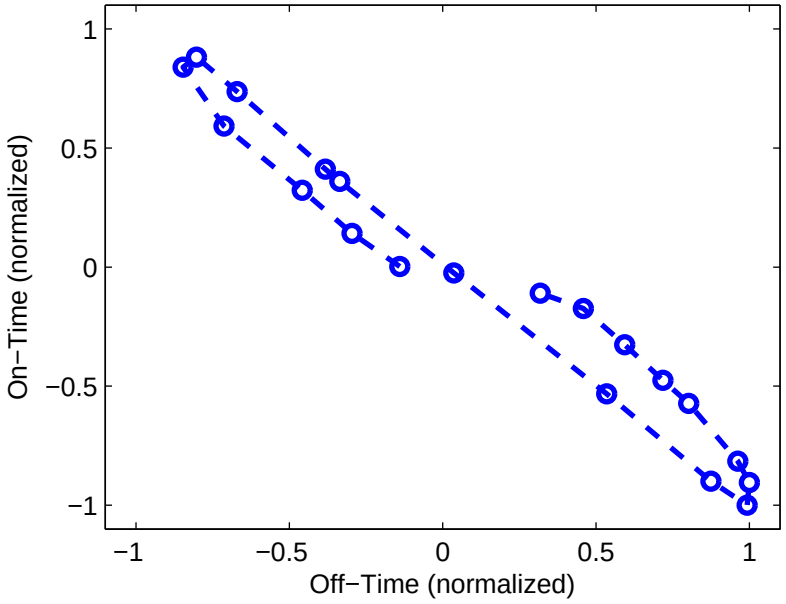

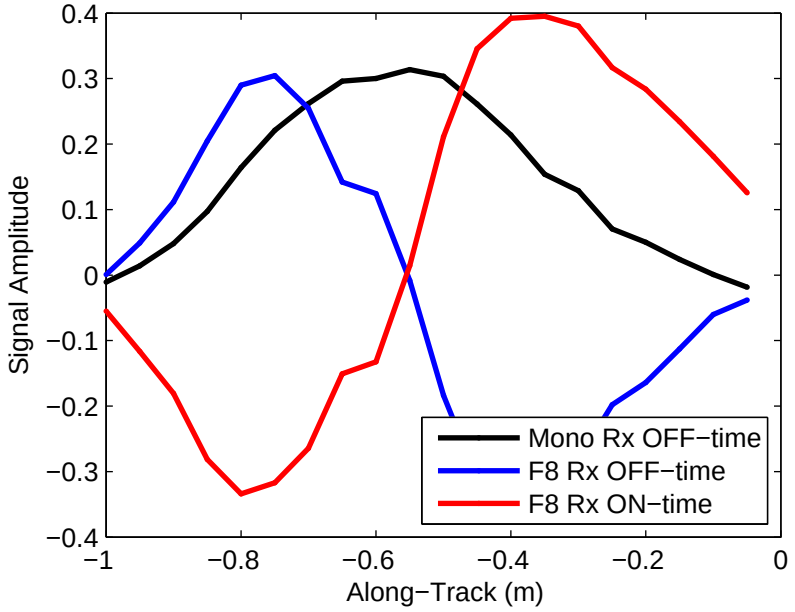

15.25 cm diameter aluminum disc, 45 cm depth

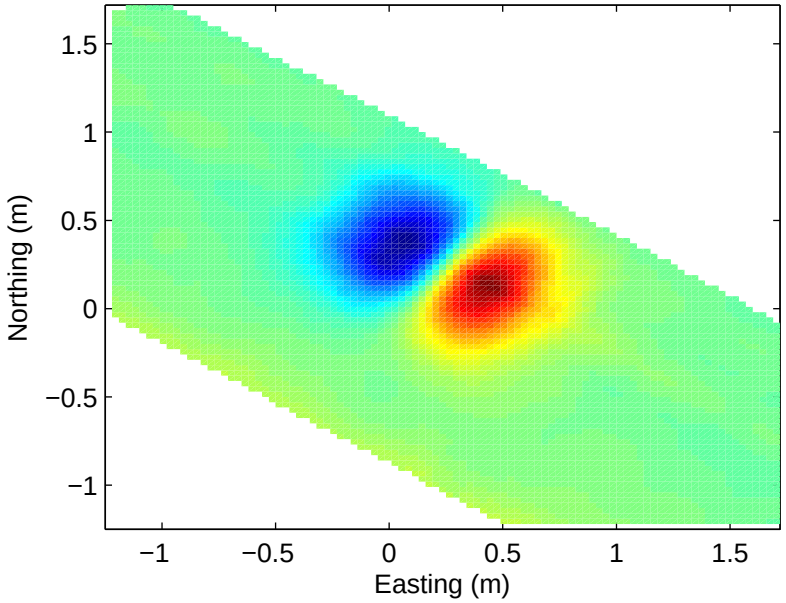

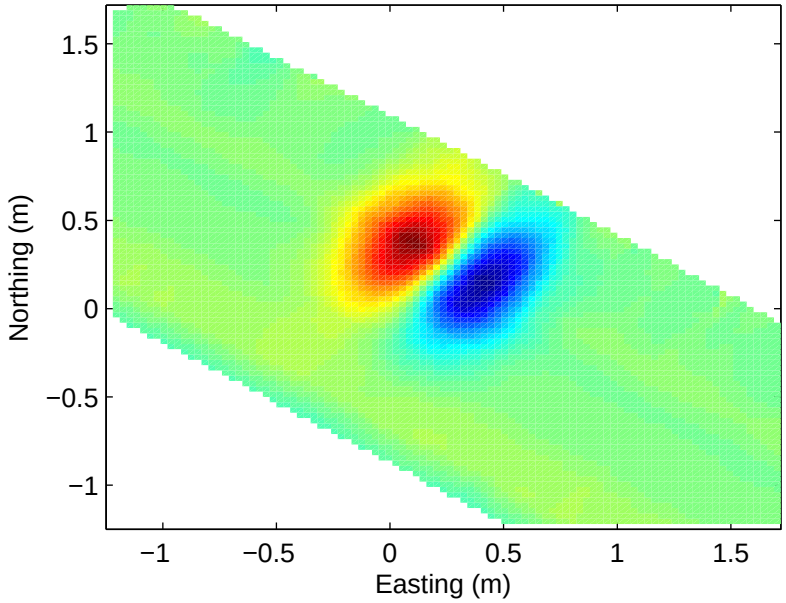

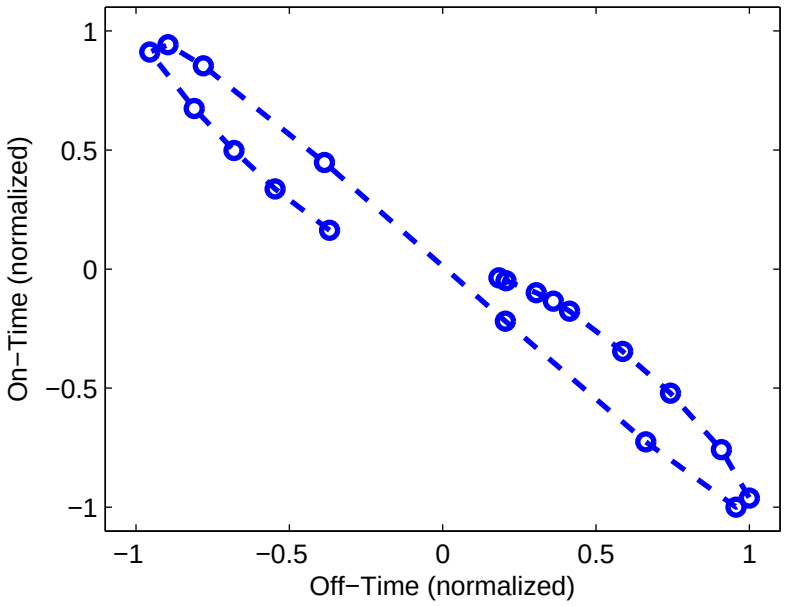

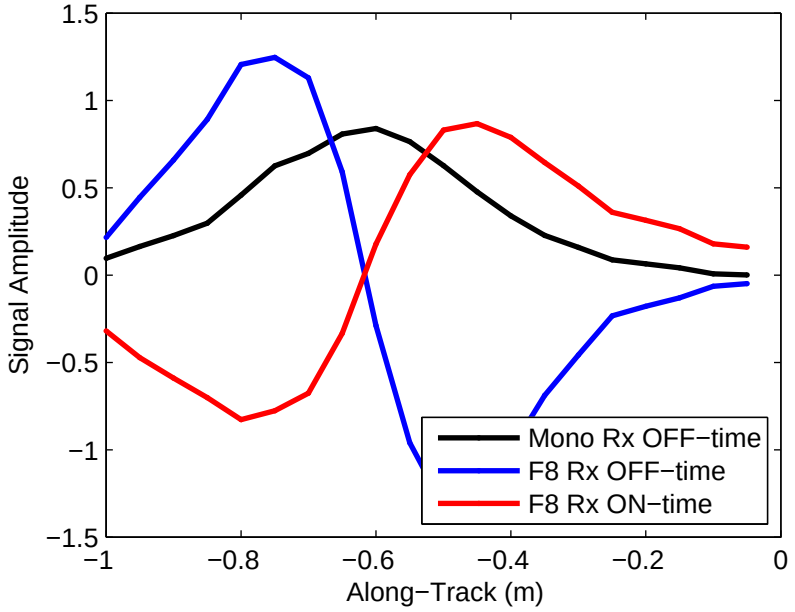

7.6 cm diameter aluminum cylinder, 45 cm depth

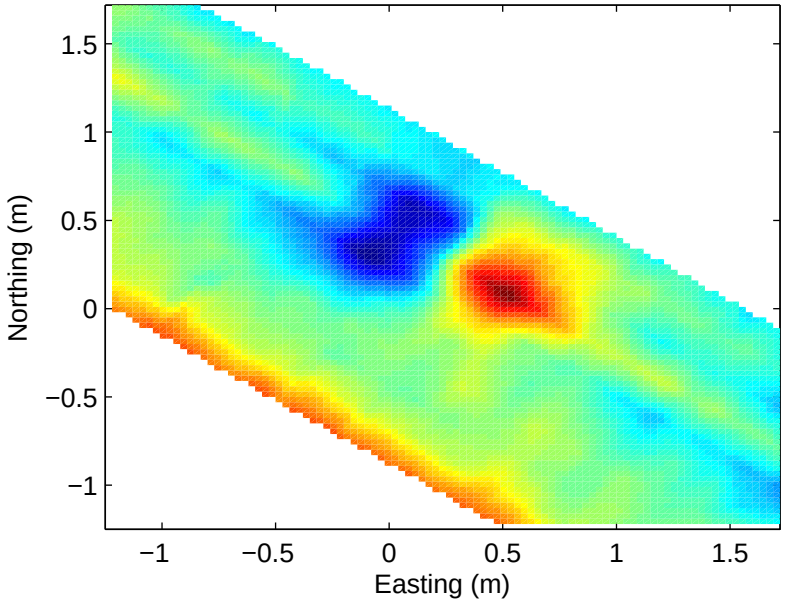

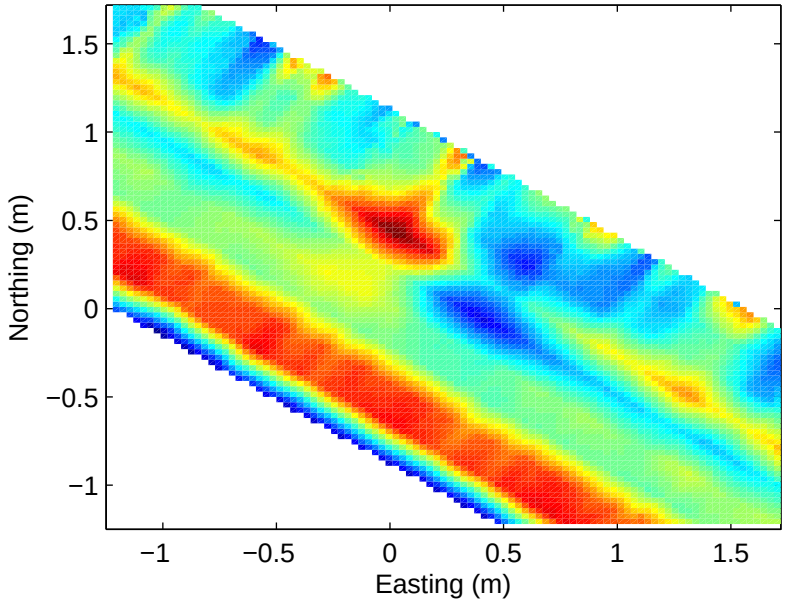

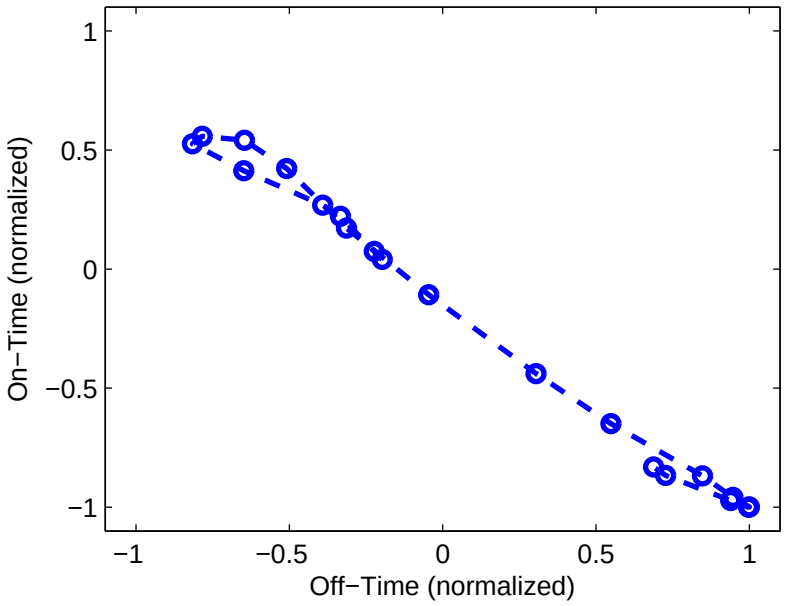

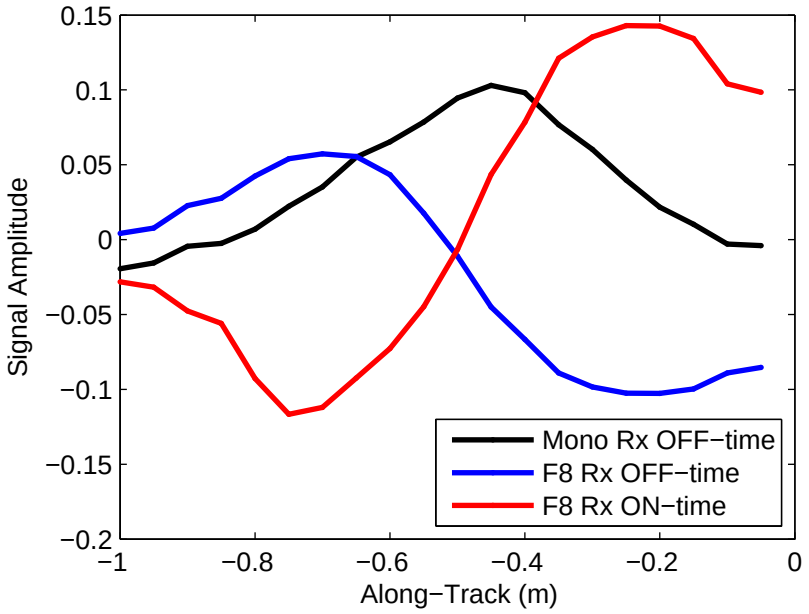

11.5 cm diameter aluminum cylinder, 45 cm depth

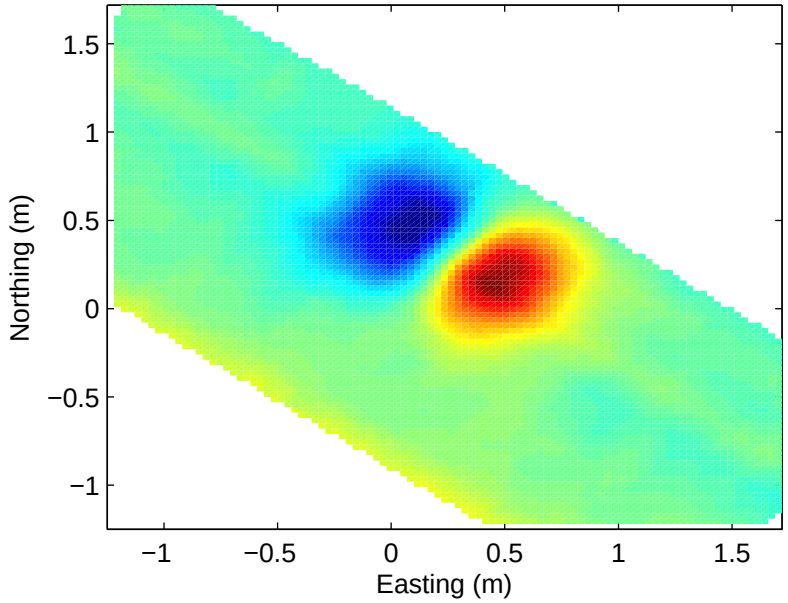

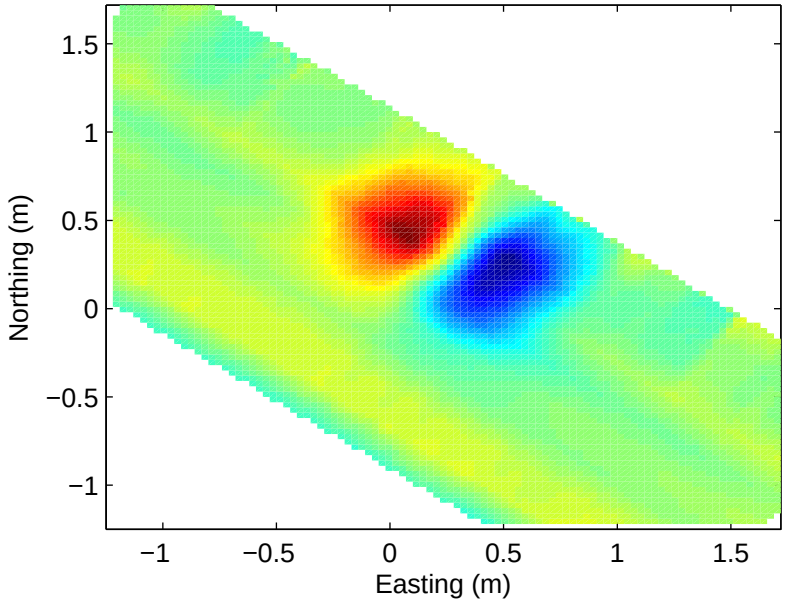

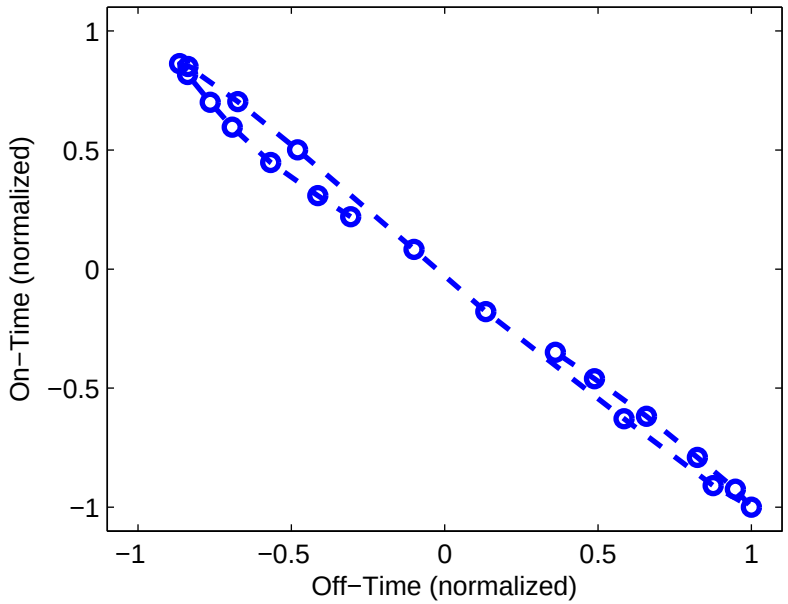

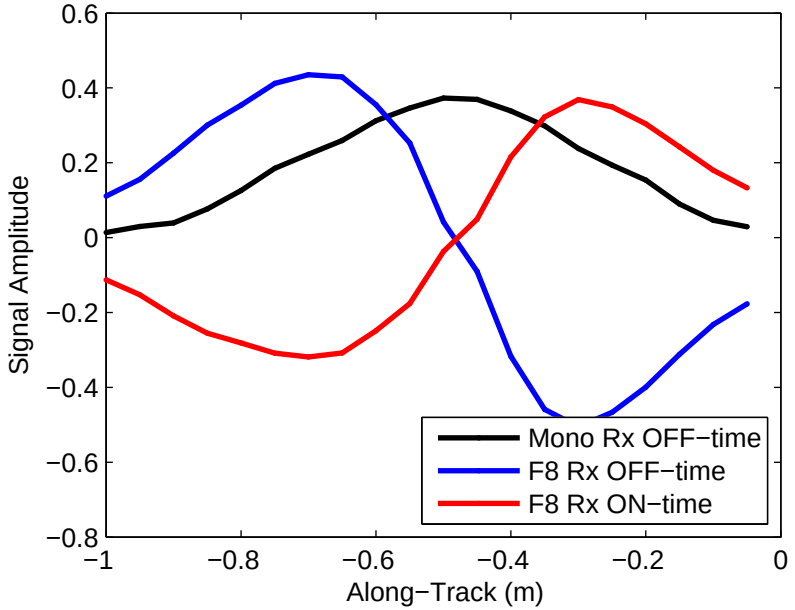

15.25 cm diameter aluminum cylinder, 45 cm depth

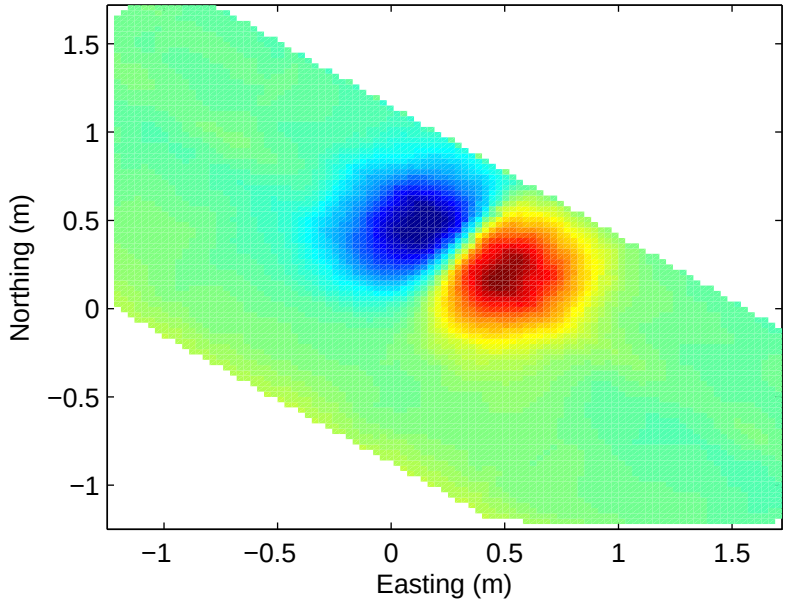

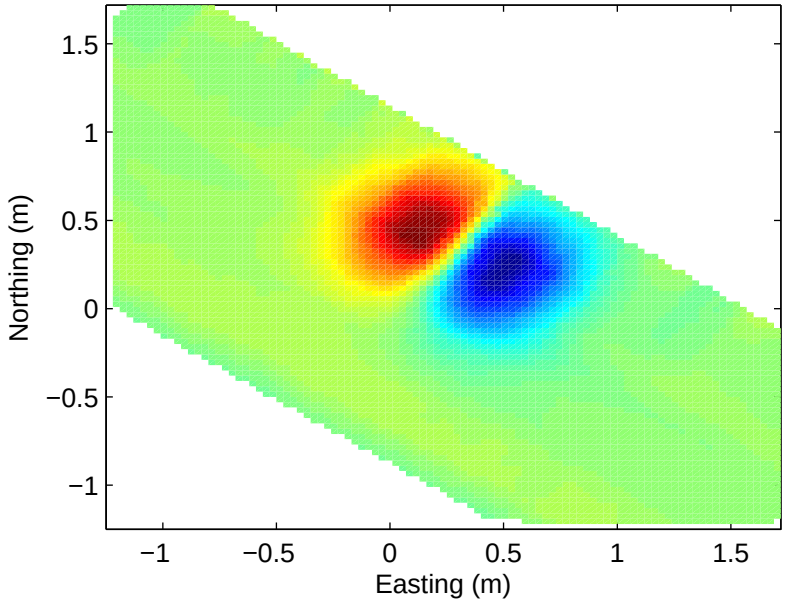

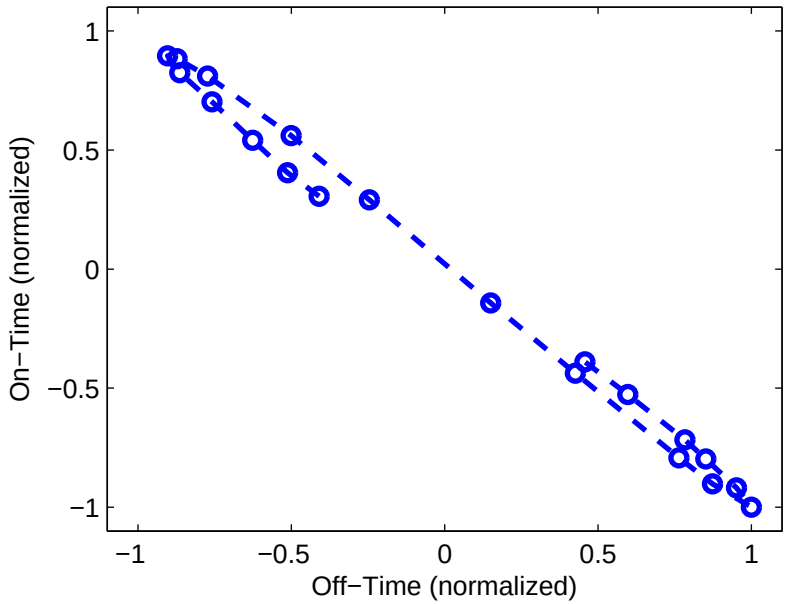

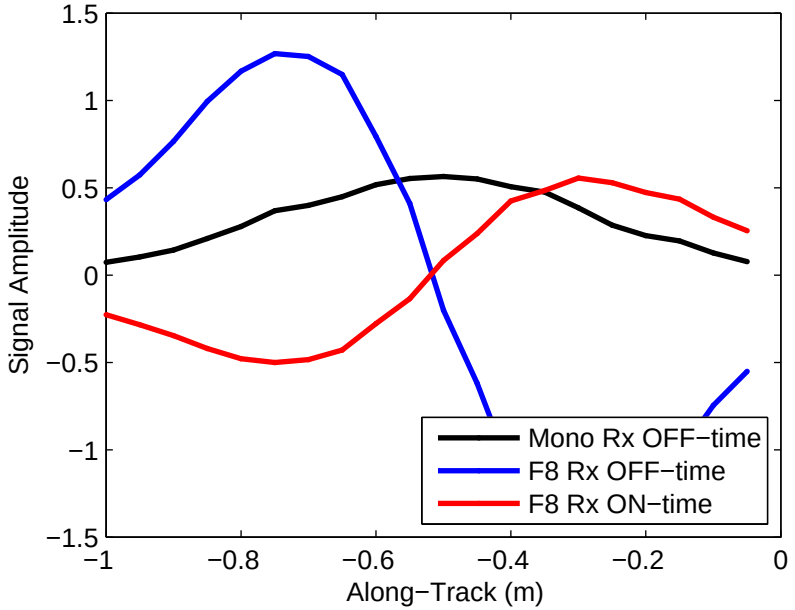

2.54 cm diameter aluminum rod, 60 cm depth

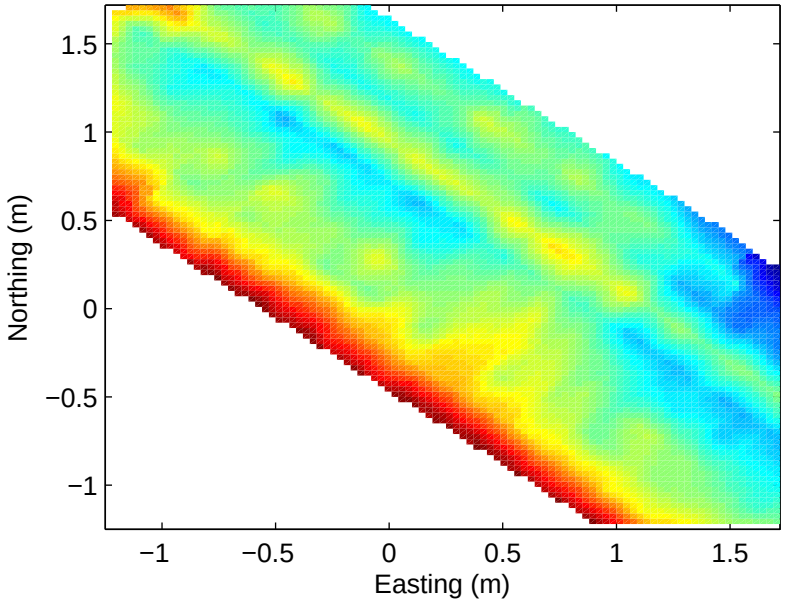

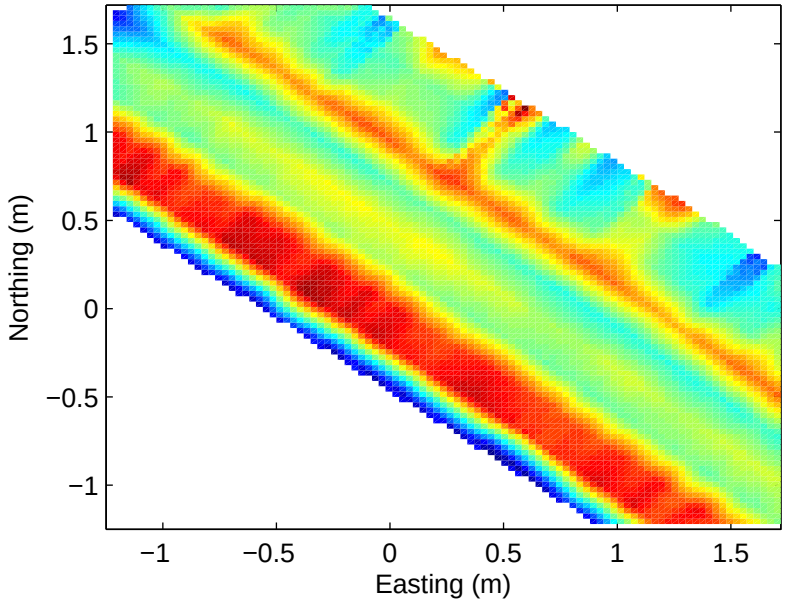

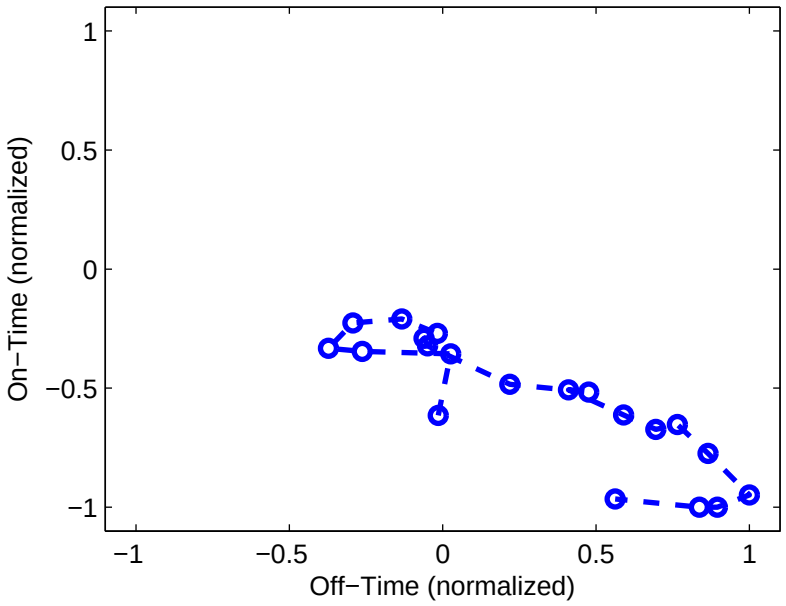

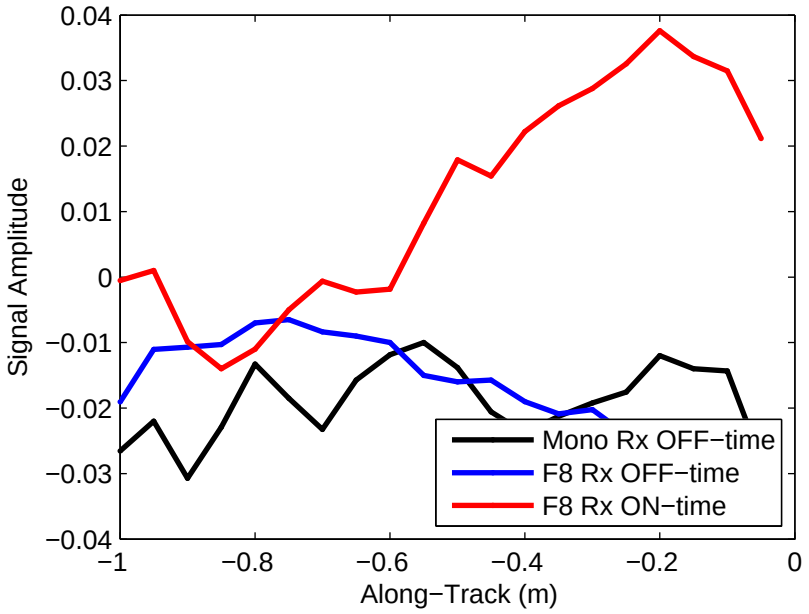

2.54 cm diameter aluminum rod, 60 cm depth

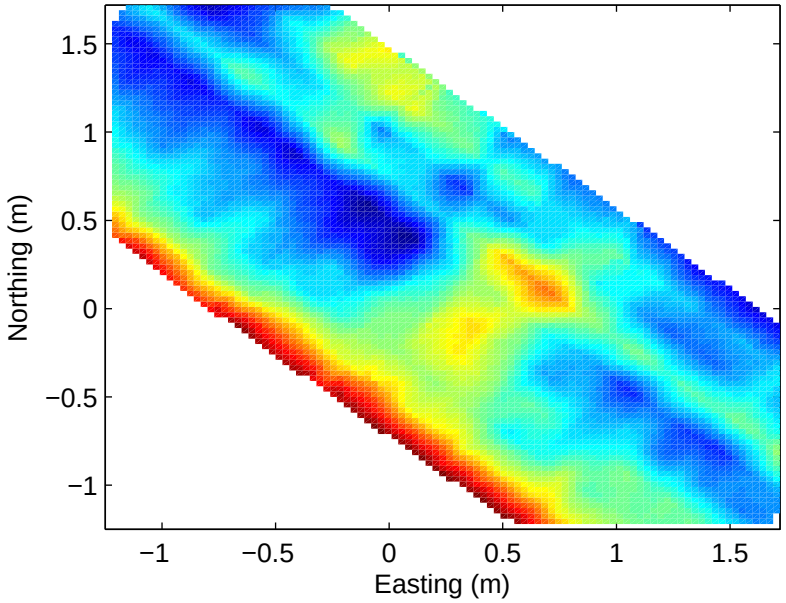

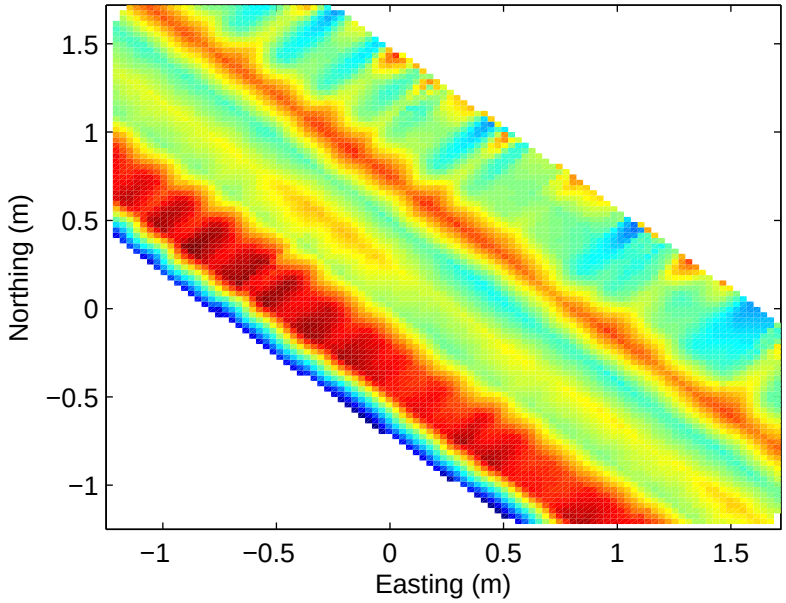

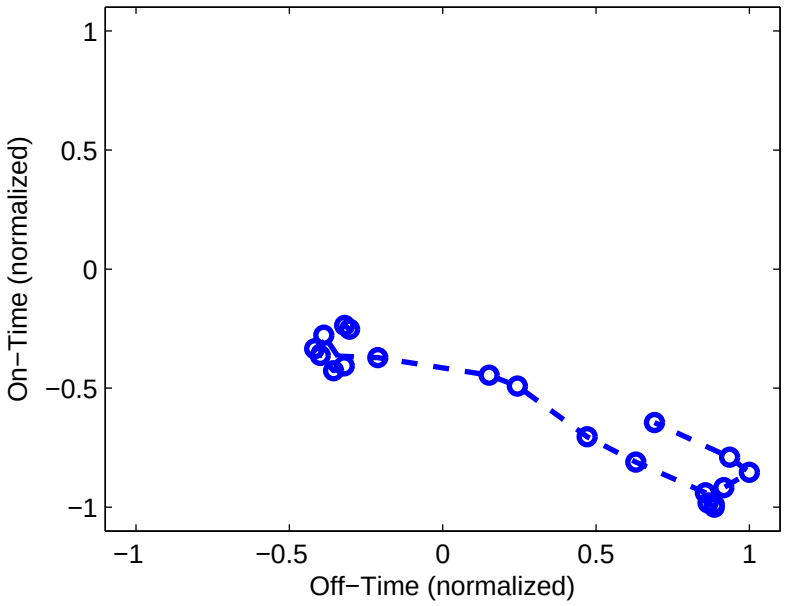

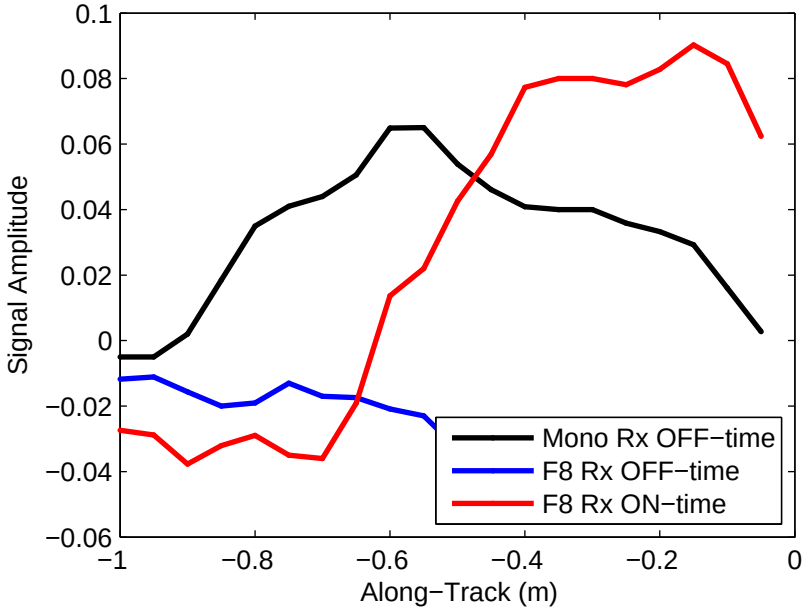

2.54 cm diameter aluminum rod, 60 cm depth

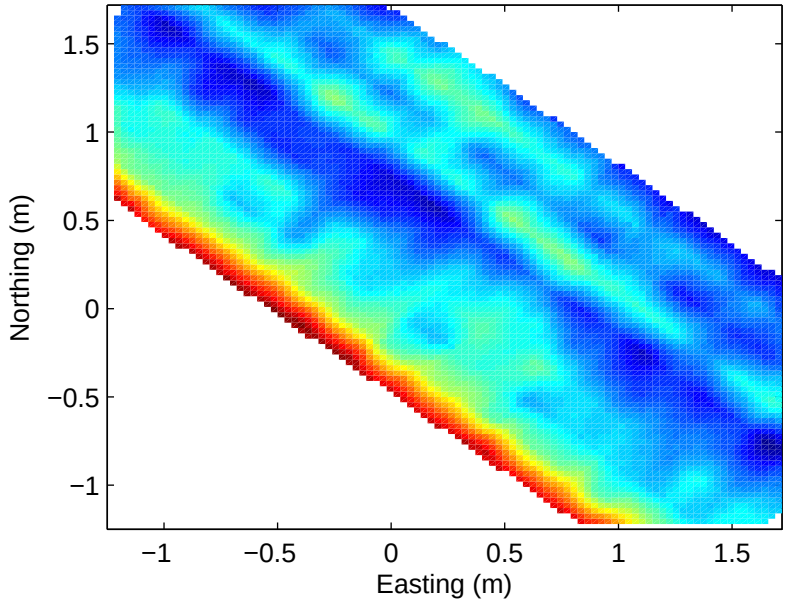

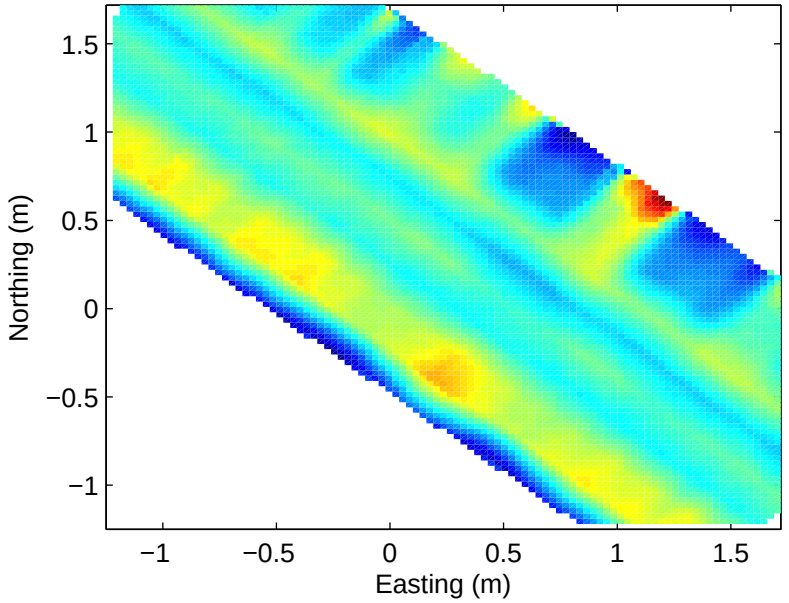

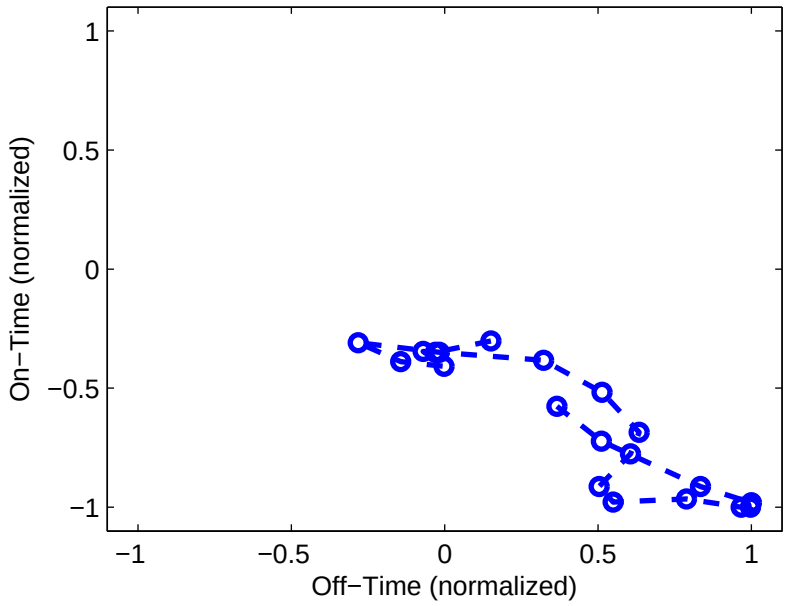

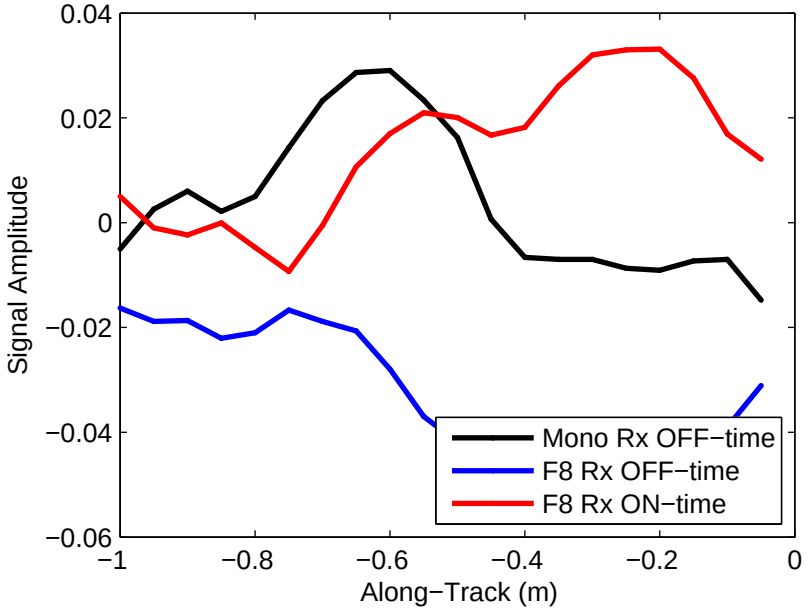

7.6 cm diameter aluminum disc, 60 cm depth

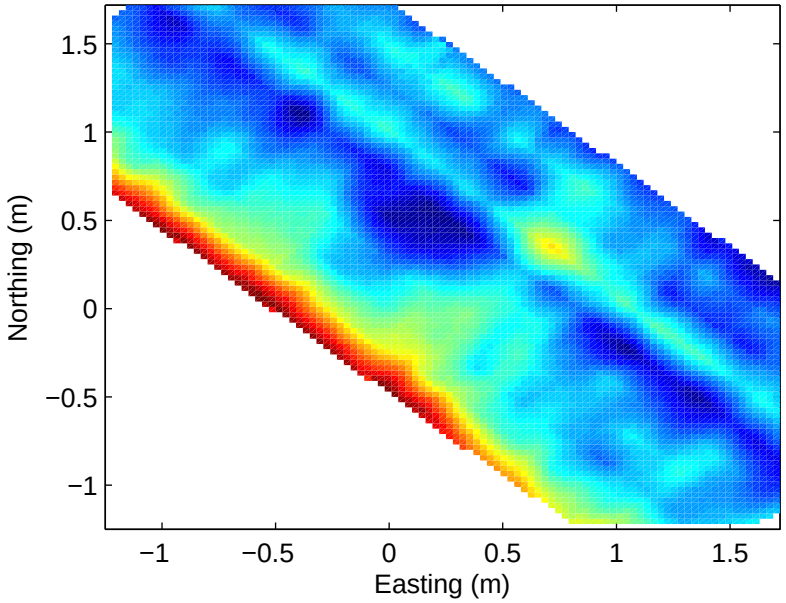

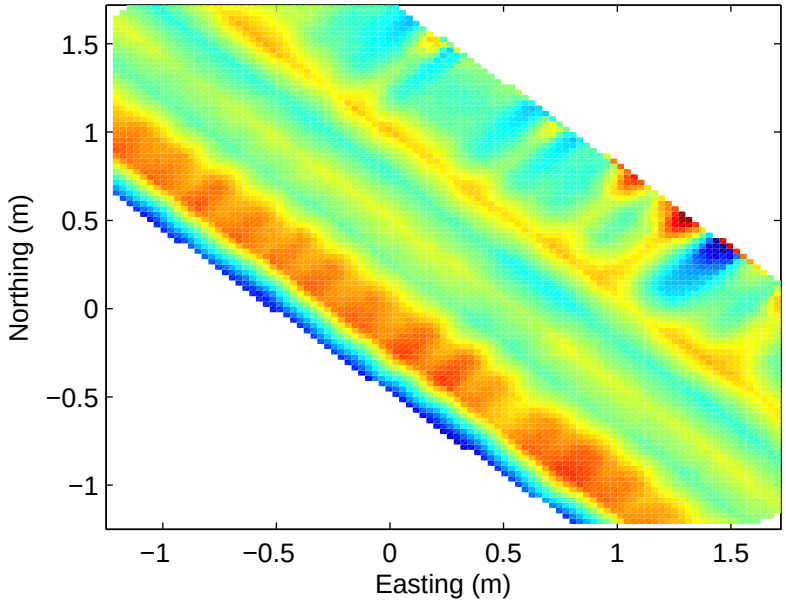

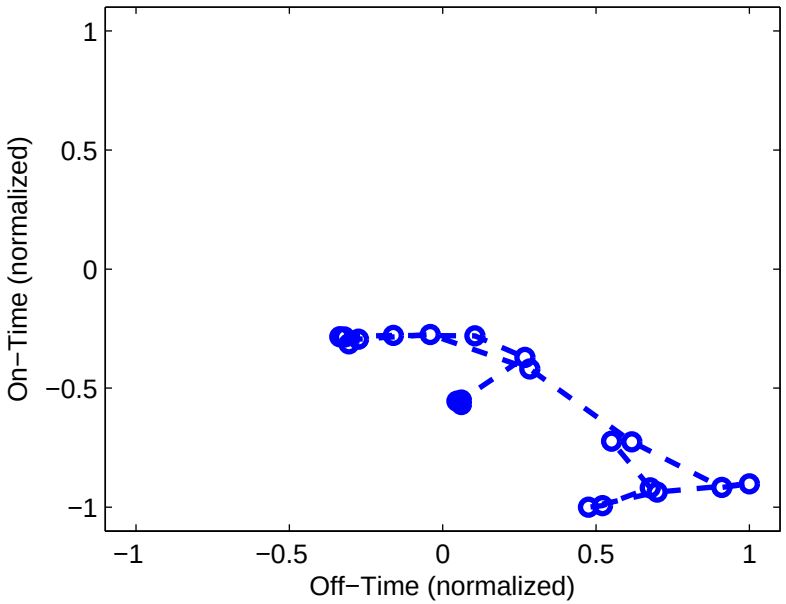

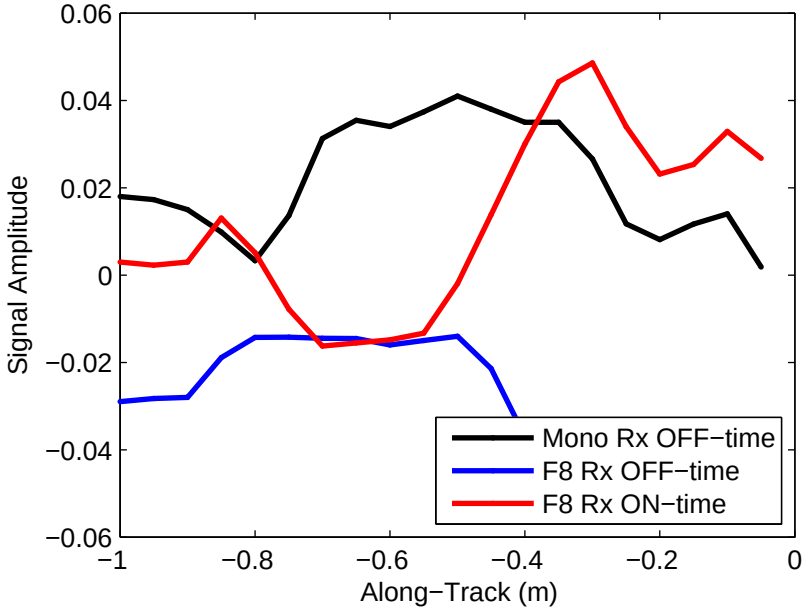

11.5 cm diameter aluminum disc, 60 cm depth

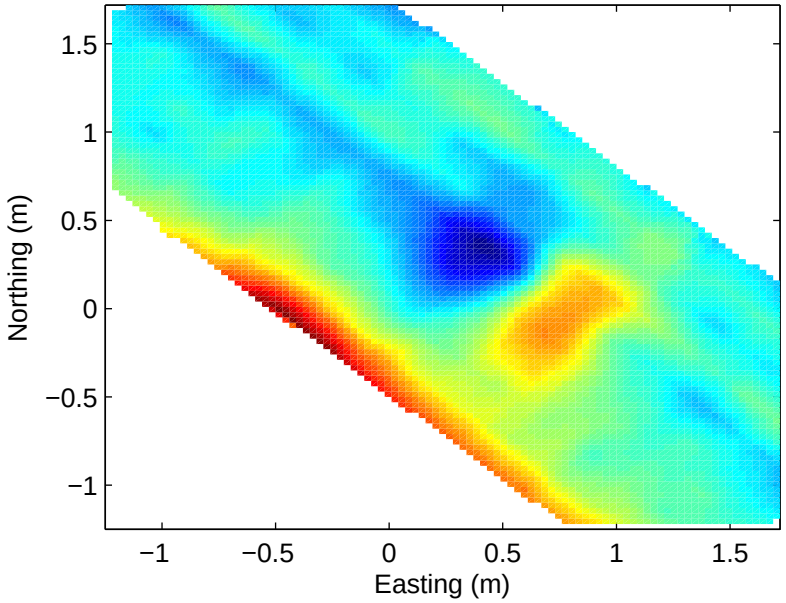

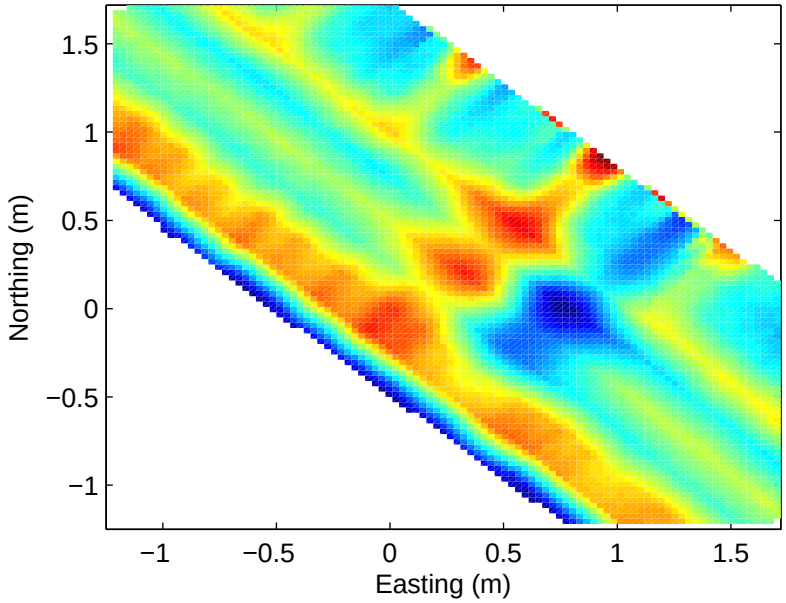

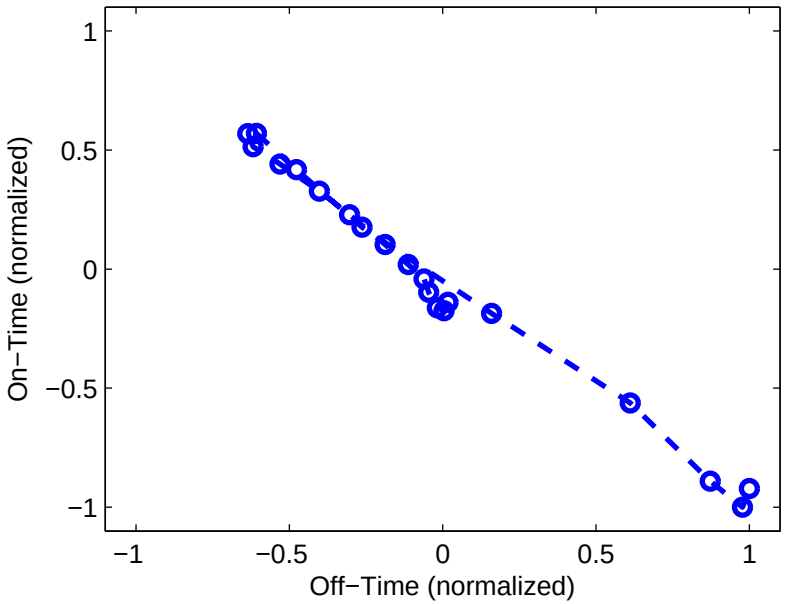

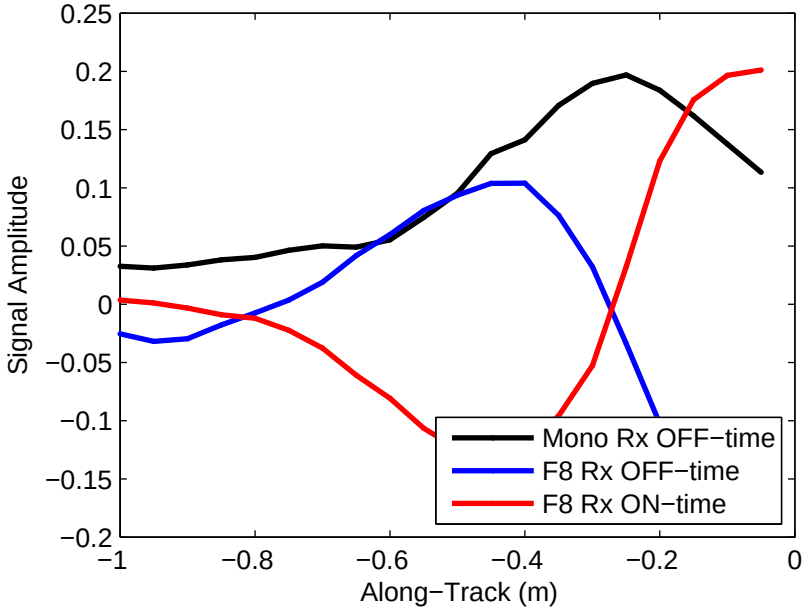

15.25 cm diameter aluminum disc, 60 cm depth

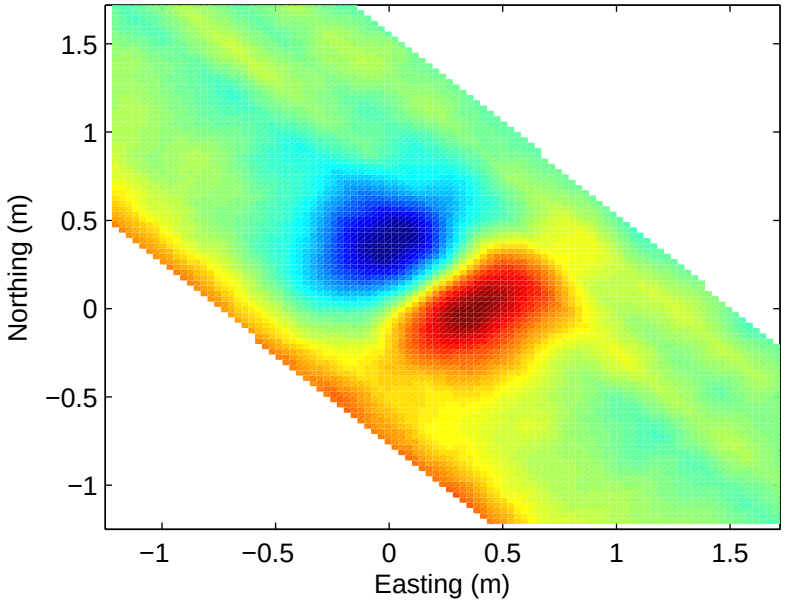

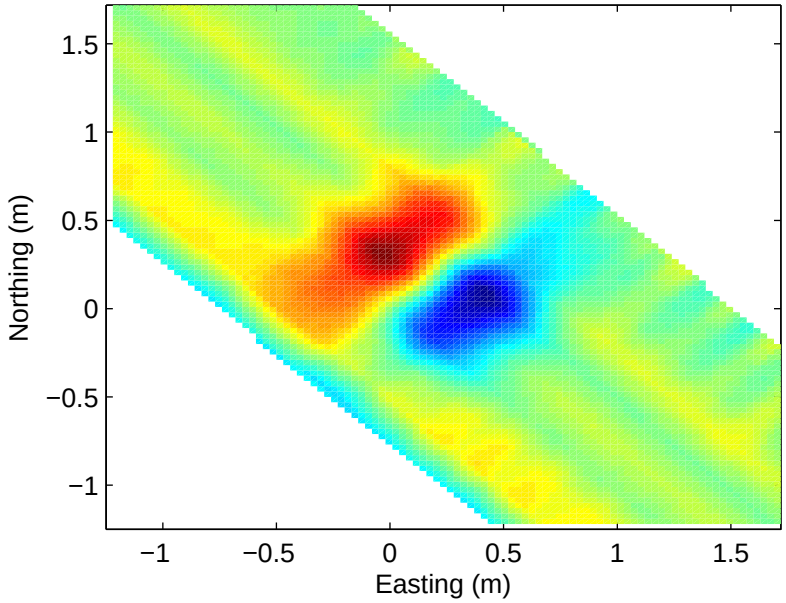

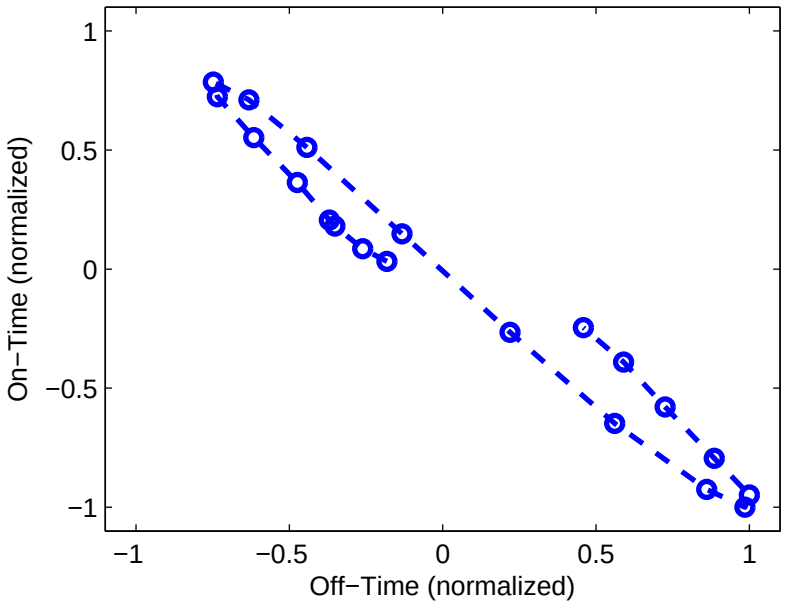

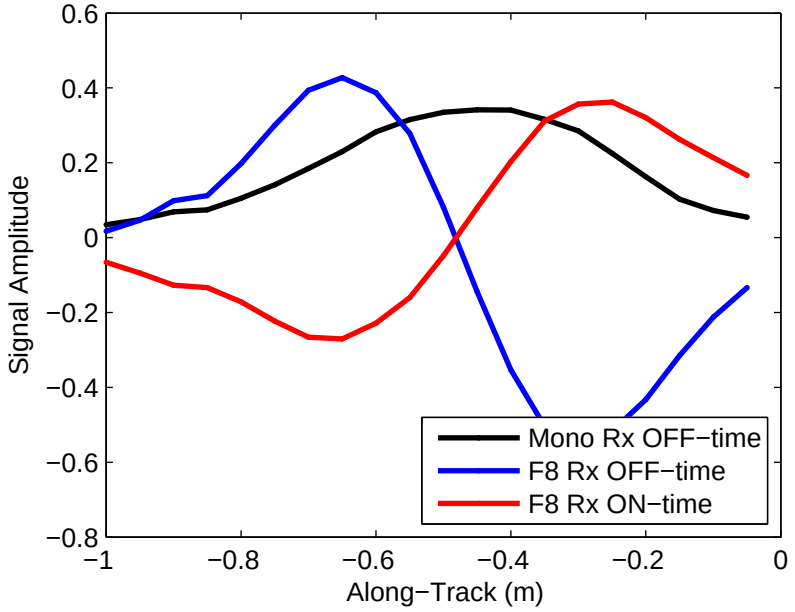

7.6 cm diameter aluminum cylinder, 60 cm depth

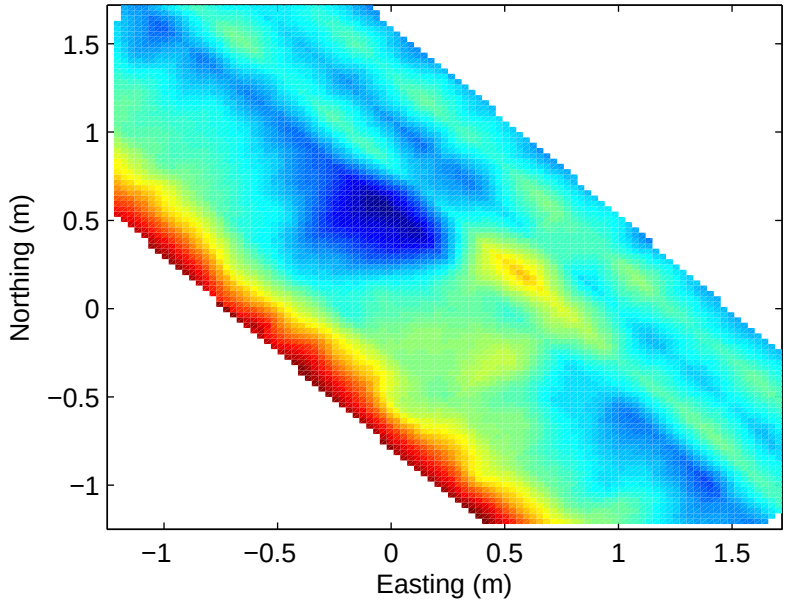

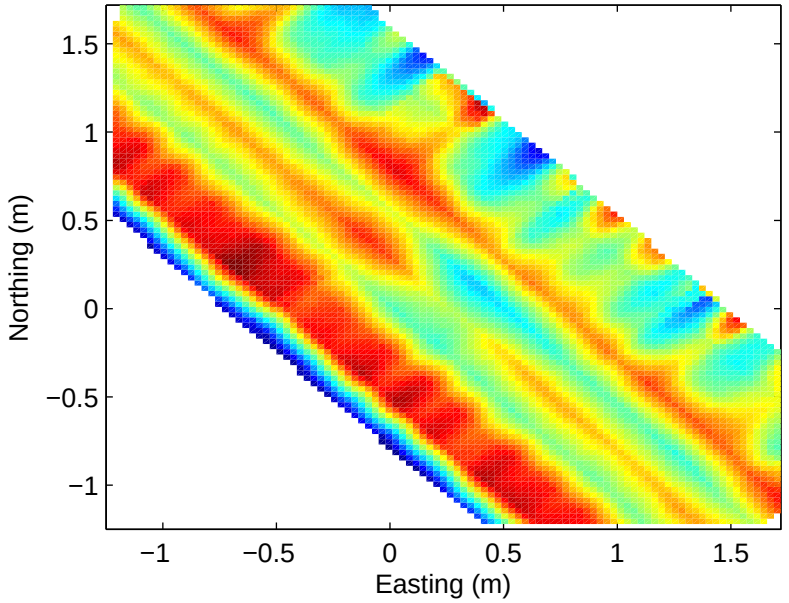

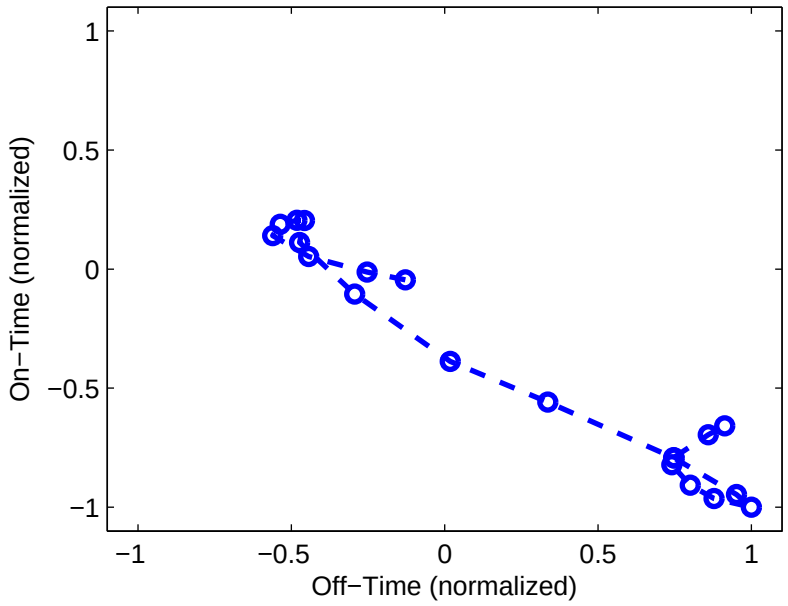

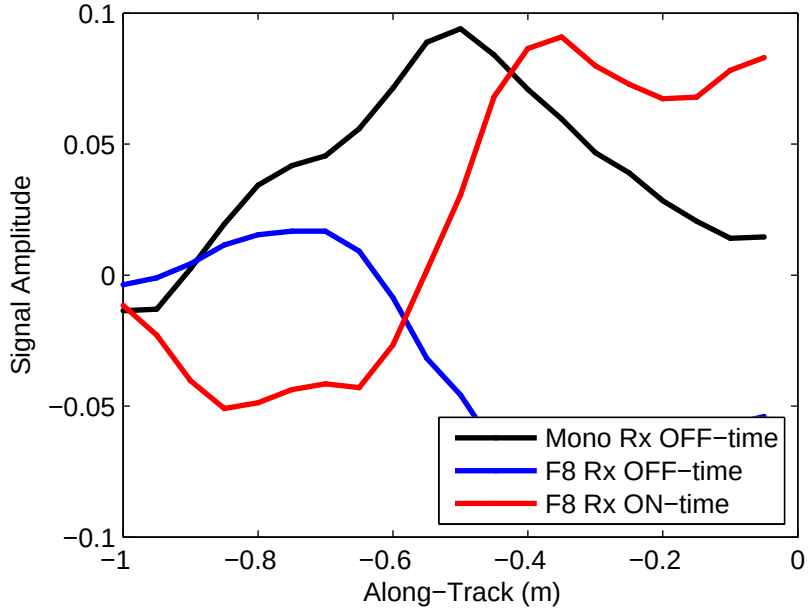

11.5 cm diameter aluminum cylinder, 60 cm depth

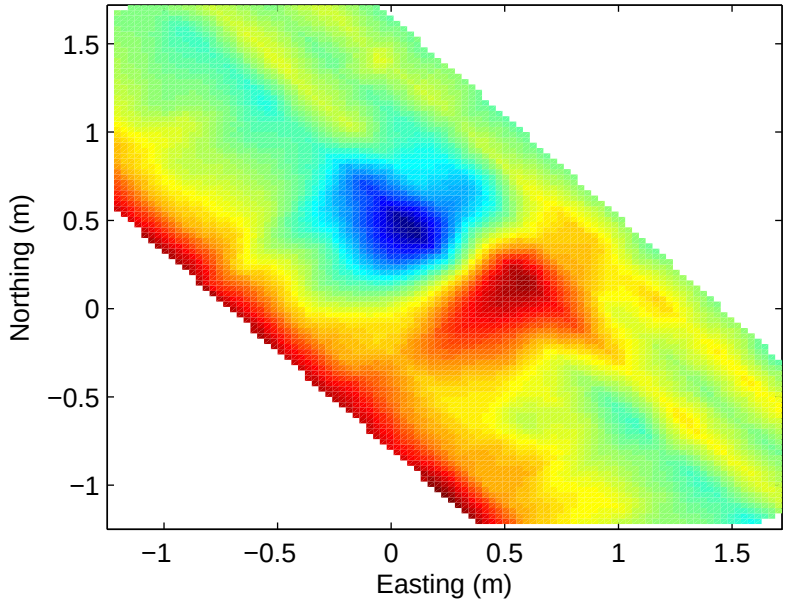

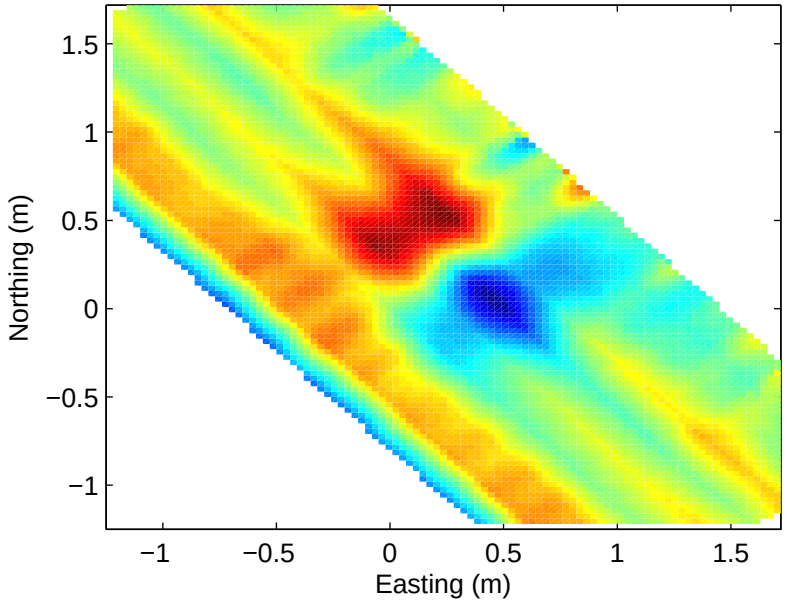

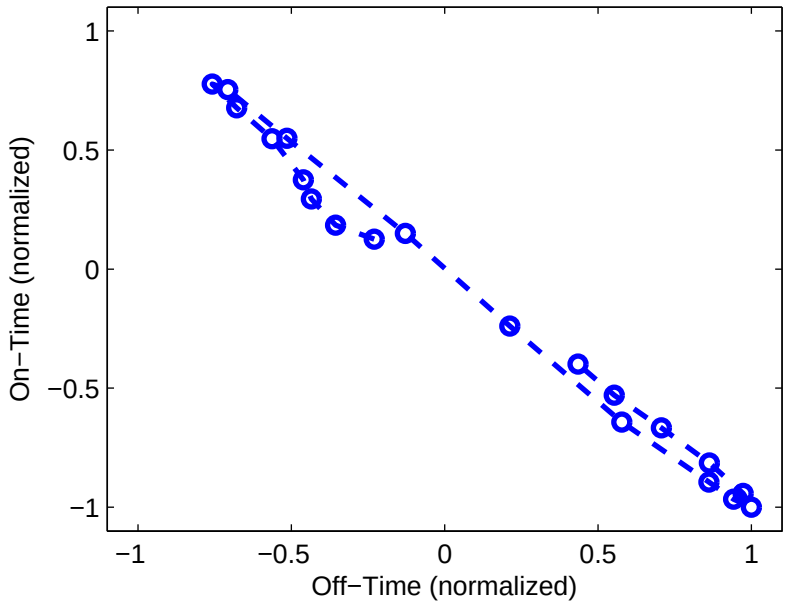

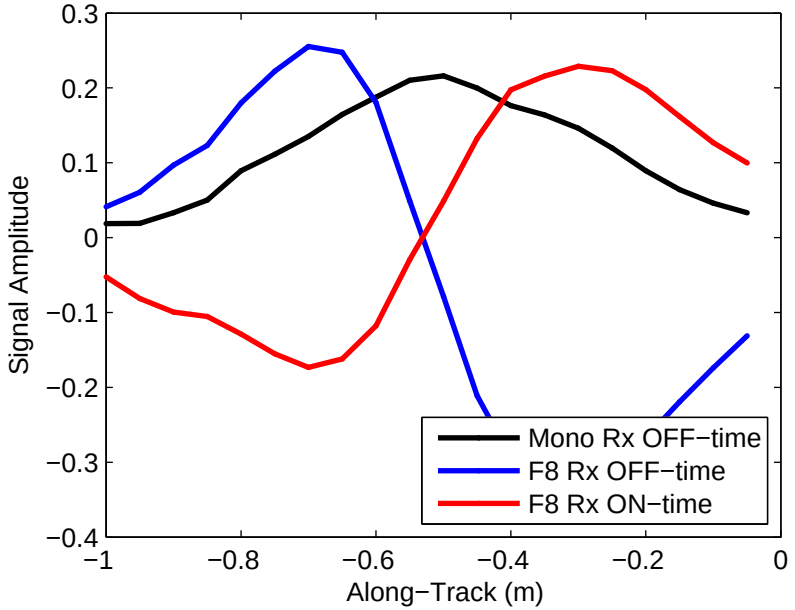

15.25 cm diameter aluminum cylinder, 60 cm depth